The Development of Particle Image Velocimetry for Water Wave Studies

a thesis by

Callum Gray

for the degree of

Doctor of Philosophy

Department of Physics

University of Edinburgh

1989

Abstract

A wave measuring facility based on particle image velocimetry is described. The most important aspects of recording the flow field and the subsequent evaluation of the records is considered from a theoretical and practical point of view. The main sources of error are discussed and the performance of the system evaluated in terms of reliability and accuracy. Measurements of the internal kinematics of an extreme plunging breaker are made and the results shown to compare well with velocities predicted from a numerical model of a similar wave. The flexibility of the technique is illustrated with two further applications to vortex shedding behind a cylinder towed through a tank of stationary water and acoustic streaming within a cylindrical glass tube.

Acknowledgements

I would like to thank the following people for their help and advice in this work. Dr Clive Greated for his encouragement, assistance and advice at all stages of the project, Dr. Norman Fancey and Dr. Bill Easson for helpful conversations and useful comments, Dr. John Sharpe and David Skyner for advice and collaboration in the Acoustics and Wave studies respectively. Thanks also to Frank Morris for providing technical support in the design and construction of the wave flume and who maintained and adjusted the laser.

Finally, I would like to thank my Mum and Dad for their support and encouragement. To both this thesis is dedicated.

Declaration

This thesis has been composed by myself and, except where stated, the work contained is my own.

.....

Callum Gray

Contents

Chapter 1

General Introduction

1.1 Experimental techniques in fluid dynamics

Experimental techniques are essential in fluid dynamics research. The complexity of even the simplest flows make flow measurement necessary for verification of numerical equations of motion as well as quantitative investigation of flows for which no reliable computational schemes exist. The development of flow measurement techniques has therefore evolved into a significant field of research in its own right.

Qualitative insight into complex flow situations is made possible by flow visualisation techniques. Methods such as Schlieren photography, Shadowgraphy, Interferometry and Holography reveal variations in refractive index within the flow, induced by changes of temperature, pressure or density. Velocity, streakline, streamline, and pathline information is communicated to the experimentalist by means of Particle tracing, smoke wire, direct injection, and spark tracing methods. This information is important for insight into the large scale structures as well as the fine detail present in most flows of interest. Flow visualisation also provides guidance in the interpretation of more quantitative point measurements and the design of experiments. The detail and quality that can be achieved with such methods is illustrated in books such as Van Dyke (1984)[120] or Japan Soc.

Mech. Eng (1988)[96].

Velocity is typically the most useful measureable quantity and devices such as Pitot tubes have been widely used to provide point velocity measurements. However, the spatial and temporal resolution of these instruments is low. Hot-wire and hot-film anemometers have also been used extensively and to a certain extent overcome the problem of frequency response associated with the Pitot tube. However, the measurements made using these devices is comparative rather than absolute and require calibration leading to considerable uncertainty in the final velocity estimate. Further to this, the physical intrusion of the probe in the fluid affects the flow that is being measured.

A class of optical point measuring tools have developed from the initial experiments of Yeh and Cummins, 1964[124]. A cross-beam Laser-Doppler-Anemometer utilises the interaction of suspended microscopic particulate matter with a light pattern set up at a point within the flow. This light pattern is set up within the flow by interference of coherent light from a laser. The evolution of this technique has been rapid and diverse and is now a standard method of obtaining high precision point velocity measurements. This method and its various refinements are well documented in Durst et.al. (1976)[43] and Durrani and Greated (1977)[42].

Because Laser-Doppler-Anemometry (LDA) is an optical technique, the limitations of probe interference exhibited by earlier devices are avoided. Sophisticated multicomponent configurations of the LDA have been devised and used to resolve all three components of velocity at a point. In order to determine the spatial structure of flow velocity however, it is necessary to move the LDA probe region throughout the flow [45]. For steady and precisely repeatable flows this is feasible but for random or non-repeatable flows this procedure is limited in its ability to resolve any useful spatial structures. In such cases point measurements have to be interpreted in conjunction with flow visualisations.

The detail present in such flow photographs has prompted many workers to

consider quantitative analysis of visualisation images and techniques that have recieved attention in the past include Streak-photography-analysis and tracking of flourescent tracers [74,50]. Both these and similar techniques involve measurement of the travelled distance of tracer particles in a known time interval. Streak photography analysis has probably attracted the most attention [37,33] resulting in a moderate degree of success. Particles introduced into an essentially two-dimensional flow field are illuminated by an intense sheet of light, typically from a laser, and then over a short time interval imaged onto a recording medium (photographic, video etc.). The analysis of such flow records requires the use of highly sophisticated image analysis techniques [1], and typically result in only moderate measurement accuracy. The main difficulties occur because streaks may lie very close to each other and may even cross. Further problems occur when rapidly moving particles move out of the plane of illumination, resulting in anomalously short particle trajectories. The finite width of the streak must also be taken into account when estimating the travelled distance from a tracer streak length.

[1] A good general review is given by Hesselink [60].

1.2 Speckle photography in fluid dynamics

In 1977-78 a number of workers published results illustrating the application of Scattered Light Speckle Photography (SLSP) to the measurement of flow velocities, [15],[41],[58], [68]. SLSP had previously been used to measure the small scale elastic distortion of solid objects [10,26]. The principle of the technique is quite simple. Coherent light from a laser is used to illuminate the surface of a solid object, or a region within a transparent body that has been seeded with tiny impurities. The scattered coherent illumination is then imaged onto photographic film where the random phase relationship of the scattered light leads to the formation of a speckle pattern [52]. Movement of the scattering object will cause the speckle pattern to move in space and so, as long as the motion of the object is perpendicular to the axis of the imaging lens, two similar but displaced speckle patterns can be recorded photographically. This photographic record of the in-plane displacement of the object is called a "specklegram". Quantitative analysis of the specklegram is possible either by point analysis with a narrow probe laser beam [23] or by a full field spatial filtering technique which displays contours of equal displacement [24].

The local analysis technique utilises optical processing of small regions of the film where displacement is assumed to be constant. A narrow laser beam passed through the film generates speckle displacement or Youngs fringes in the back focal plane of a lens (see figure 1.1). The orientation and periodicity of these fringes can then be related back to the recorded speckle pattern displacement and thus the object motion. The full field technique first described by Celaya, Jonathan and Mallick[24] utilises spatial filtering in the Fourier plane of the specklegram to reveal fringes of equal displacement in the second image plane.

In the preliminary applications of SLSP to fluid dynamics, a surface was generated within the fluid by illuminating a heavily seeded flow with an intense sheet of laser light. The speckle field generated by the random interference of scattered

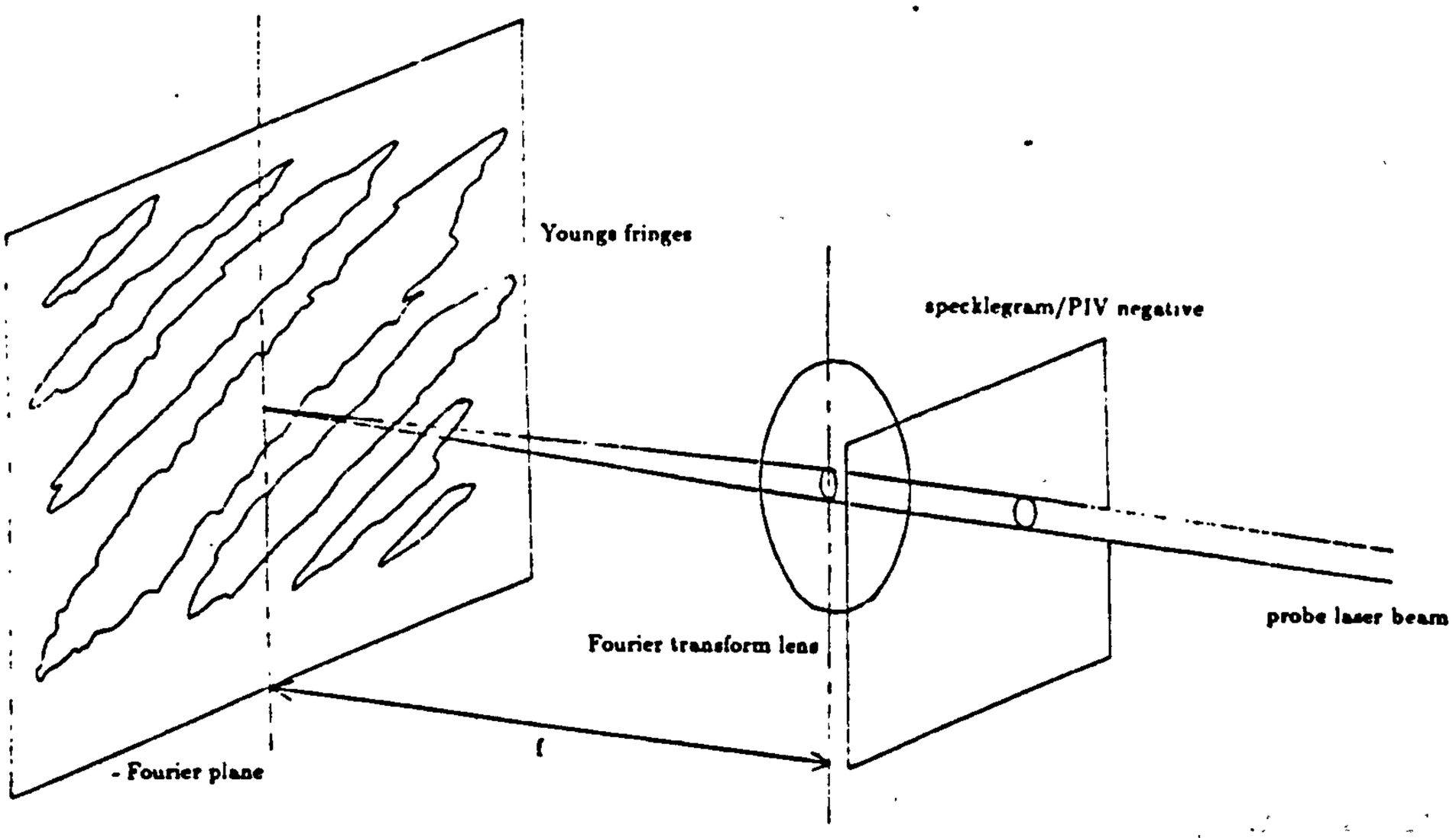

Figure 1.1: Optical processing of a "Specklegram" to generate Youngs fringes

laser light was recorded photographically two or more times[2] (see figure 1.2) to generate a specklegram that could be evaluated using either of the methods described above. Barker and Fourney[15] measured the laminar velocity distribution across the the diameter of a circular pipe. Illumination was provided by a Q-spoiled ruby laser and the resulting specklegram analysed by the Young's fringe method to yield the radial velocity distribution of the pipe. It is suggested in this paper that decorrelation of the speckle pattern due to out-of-plane motion or turbulence would lead to loss of measurement and a more sensitive speckle interferometry technique (SLSI) is suggested as a solution [3]. Applications of the speckle photography technique for measuring velocities along a circular tube are also reported by two other groups. Simpkins and Dudderar[41] measured the velocities by the Young's fringe method whereas Grousson and Mallick[58] employed full field spatial filtering as well as point measurement in their com-

[2]Iwata, Hakoshima and Nagata imaged resolved particle images rather than generating a speckle pattern from overlapping images. They also used multiple exposures to artificially increase the seeding density within their flow.

[3]Application of the SLSI technique to solid body motion had been published [82] but no reported application of this technique to fluids has been found.

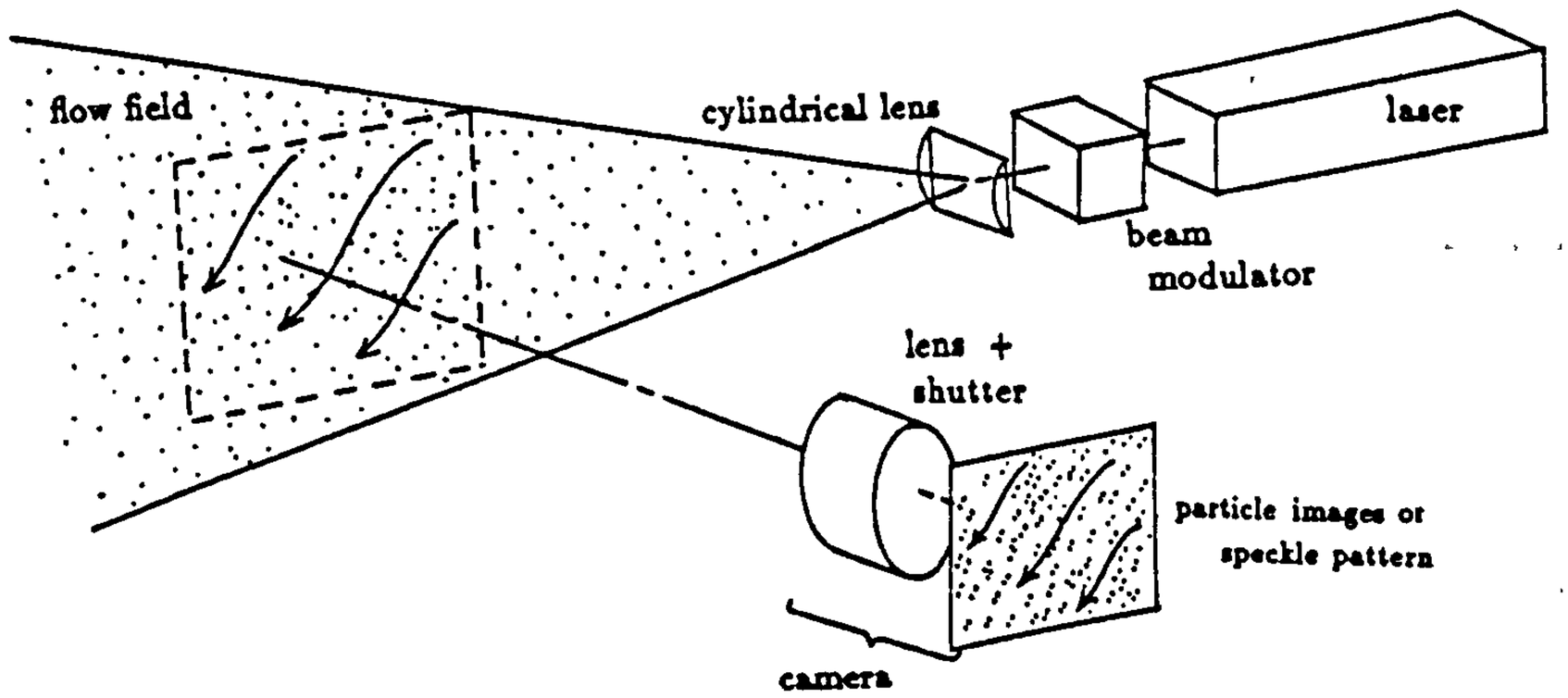

Figure 1.2: Arrangement for recording in-plane displacement of flow field

parison with simple theory. The first applications of this technique cited above were to simple one-dimensional slow steady flows but illustrated the potential of the technique for measuring the instantaneous distribution of velocities in fluids.

Further applications of Speckle photography to fluid flows were reported soon after the introduction of the technique to fluid dynamics. Simpkins and Dudderar followed up their initial work with an application to unsteady convection within a Bénard cell [113]. Iwata, Hakoshima and Nagata[68] measured velocities within a convective cell using multiple exposures and resolved particle images[4].

An important point that should be made here concerns the nature of the random pattern recorded from the light scattered from within the flow. In most of the initial experiments the recorded image was a classical speckle pattern. Small out-of-plane motion of the scattering particles between illuminating pulses changes the random intensity pattern recorded on the photographic film and ultimately leads to decorrelation of the separated speckle patterns and therefore loss of measurement at that point. This problem is avoided by reducing the seeding density resulting in a pattern of resolved particle images, in which case

[4]Iwata et al also measured the instantaneous flow velocity distribution within a similar cell using double exposure holographic technique[68].

the particles have to move completely out of the light sheet before total decorrelation occurs. Consequently, most fluid dynamics applications of this technique adopt the particle image mode of operation. Further advantages of this latter approach include improved optical penetration, lower seeding cost, and reduced risk of altering the fluid characteristics by the large seeding density required to generate a speckle pattern. This factor has altered the terminology concerning this method. Laser Speckle Velocimetry (LSV) has been used because of the technique's close links with SLSP but a more popular name for the technique is Particle image velocimetry (PIV) [97]. I will use PIV unless explicitly referring to a speckle technique.

1.2.1 Evaluation of flow records

To date, the development of speckle photography applied to fluid flow has been considerable. Measurements are no longer confined to slow flows or small areas [79,111]. Automatic analysis systems have been developed that are capable of point-by-point evaluation of the double exposure flow field record over thousands of points [7,93,86,13]. These systems process the photographic flow record by a variety of different numerical processing techniques using flow data from the Fourier plane of the film in the case of Young's fringes and the image plane when the speckle pattern or particle image data is used directly.

Fourier plane analysis

Initial processing schemes were intended more for the analysis of solid body displacement specklegrams [87,66,73,80] than for fluid dynamics applications. The motivation for such work is the limited accuracy, resolution and speed associated with a manual analysis of fringe patterns generated from specklegrams or PIV negatives. Automatic processing of the Young's fringes presents the possibility of a rapid and accurate evaluation of the velocity information contained on the

film and the subsequent calculation of derivative quantities such as strain or vorticity.

Ineichen et.al.[66] proposed a semi-automatic system where the speckle displacement fringes are manually aligned parallel to the lines of a Video camera and then digitally integrated along their length. This step compresses the amount of data required for further analysis and smooths the speckle noise that is superimposed on the fringes. The DC bias on which the fringes sit is estimated by integration perpendicular to the fringes and then subtracted from the 1-D fringe data. The autocorrelation of this de-biased signal is then calculated to further increase the signal to noise ratio for subsequent measurement of fringe periodicity. Estimated accuracy attainable with this system is 1% and 1deg for fringe separation and orientation respectively. Kaufmann et. al. [72] employ a similar 1-D integration technique but perform the integration optically using a cylindrical lens arrangement. Detection of the resulting 1-D fringe signal is performed using a linear photodiode array. Orientation of the fringes is achieved manually and measured using a sin-cos potentiometer to better than 0.5deg for good visibility fringes. Fringe periodicity is measured from the Fourier transform of the de-biased fringe signal and accuracy of 1μm is quoted for good visibility fringes.

Meynart [91,89,92] in his work on Rayleigh Bénard flow uses the speckle photography technique to draw isovelocity contours by spatial filtering. Quantitative analysis of the flow record is also performed using a 1-D fringe analysis technique similar to those described above. Additionally, a fringe processing technique based upon calculation of the average autocorrellation in a number of different directions is discussed. This technique gives the fringe frequency in a number of different directions, and combined with the knowledge that the fringes are straight, allows the fringe direction as well as the fringe periodicity to be calculated without user intervention. This fully automated system is used in an application of the speckle technique to study vortex pairing in a low-Reynolds number jet (Re=2300), Meynart (1983) [93]. This is a much cited publication and represents a key piece of work in the development of PIV. It illustrates the

potential of the technique for precise measurement of instantaneous velocities and calculation of vorticities over extended regions of an unsteady flow. Similar systems based on multidirectional correlation techniques are discussed by Erbeck [47], Reynolds et al [104], and Robinson [105]. Robinson also describes a fully automatic 1-D integration system where the direction of integration is determined by comparing the sum of pixel values in a number of radial directions about the centre of the fringe pattern. The main limitation of such systems is that for low fringe density (less than five fringes) the accuracy and reliability with which the fringe spacing and direction can be determined is significantly reduced. This problem is compounded by the noise and low visibility of fringes typical of flow displacement records. A more natural approach to the evaluation of fringe periodicity and direction in the presence of noise is transformation of the fringe intensity distribution to the spatial frequency domain. The energy associated with the fringes is thus concentrated about two symmetrically of the fringe intensity distribution. adjacent points in the frequency plane while the speckle noise is distributed randomly This approach is suggested by Robinson [106], and Adrian [6] but they emphasise the computationally expensive nature of the calculation.

A fully automatic fringe analysis system based upon 2-D Fourier analysis of fringe intensities is described by Huntley (1986) [64]. Digitisation of the diffraction patterns is performed using a mechanically scanned linear photodiode array with digital processing of the intensity data on a microcomputer. The performance of the system is analysed by recording the accuracy and reliability with which fringes of known frequency and visibility are evaluated. It is shown that for good visibility fringes the displacement and orientation of speckle patterns can be determined to within 0.1 μm and 0.1deg respectively. Reliability is 100% for fringes down to 7% visibility where uncertainties are increased to 0.3 μm and 0.4deg for displacement and orientation respectively. This accuracy and reliability is impressive but, as noted above, requires considerable computation compared with 1-D integration and multi 1-D correlation techniques. Commercially available hardware is available for the rapid calculation of 2-dimensional Fourier transforms and can transform large (512*512) arrays in under a second.

This suggests that for many applications where high visibility fringes are not guaranteed the two-dimensional transform technique will probably be preferred.

Image plane analysis

Evaluation of PIV negatives and specklegrams are not confined to the analysis of Youngs' fringe patterns. Numerical processing of 2-D intensity data from the image plane of displacement records has been achieved using a variety of techniques. Adrian and Yao (1984)[123] performed particle displacement measurements directly from the particle image pairs over small local regions of a PIV negative by integration of the digitised image intensity distribution in two orthogonal directions. The resulting pair of 1-D records are then numerically processed by correlation and Fourier transform techniques to resolve the mean particle displacement in the x and y directions. Particle image tracking [21] has been used to locate possible particle images within a local area after filtering and thresholding of the digitised flow record. Statistical techniques are then used to link the centres of the located particle images to give the flow direction and magnitude. These techniques assume that there is a reasonable amount of information per local interrogation spot relating to the flow direction and magnitude. In certain cases where the signal to noise ratio is low due to low contrast images, decorrelation between images etc. maximum use of the available image data must be made. In such cases full 2-D autocorrelation of the local image plane intensity data is most appropriate [6,9]. and produces two displacement correlation peaks, symmetrically displaced about a central self correlation peak. This appears to put the displacement information in the same form as 2-D Fourier analysis of Youngs fringes discussed above. The Youngs fringe intensity pattern, detected in the back focal plane of a biconvex lens, is the power spectrum of the photographic density distribution within the region of film illuminated by the interrogating laser beam. The power spectrum and the autocorrelation function form a Fourier transform pair by the autocorrelation theorem/Wiener-Khintchin relation [22] and so 2-D Fourier analysis of the fringes and autocorrelation in the image plane are actually equivalent.

An alternative method for the analysis of flow records proposed by Collicott and Hesselink (1986)[28] utilises displacement information from a line on the photograph rather than a point. The technique described as "Anamorphic optical processing" performs a 1-D optical Fourier transform on a coherently illuminated strip of the film and one dimensional imaging in the direction perpendicular to this using an arrangement of cylindrical lenses. This allows simultaneous measurement of the velocity component perpendicular to the illuminating strip along the whole length of the analysis area. Processing of the generally curved fringes produced in this manner is achieved by multiple 1-D correlation.

1.3 Development of the PIV technique

Present work in PIV is directed at improving the accuracy, resolution and applicability of the technique. Velocity measurements should be of sufficiently high accuracy and resolution to permit calculation of derivative quantities such as vorticity, and streamlines and so afford a complete description of the flow field being investigated. In pursuit of this goal many different aspects of the operation of PIV have been investigated and reported in the literature.

Work by Adrian and Yao (1984)[5,4] has considered the scattering power and concentration of seed materials neccessary for optimal operation of a Particle image velocimetry system. Seeding is discussed in terms of the opposing requirements of increasing size for photographic detectability and decreasing size for maximum positional accuracy and resolution.

A two step photographic process is described by Pickering and Halliwell[102,101,100] and illustrates the reduction in speckle noise in Youngs fringes that can be achieved by contact printing a negative flow record.

The influence of the pedestal function in the evaluation of Youngs fringes has been considered by a number of workers. It has been shown that this bias function causes a shift in the positions of the fringe maxima and in fringe patterns of low visibility a similar but reduced shift in fringe minima. Kaufmann (1981) [71] showed that this effect was less pronounced when fringe processing was performed by Fourier transform techniques. Subtraction of the pedestal function prior to processing of fringes is usually adopted to reduce the influence of this bias and extend the lower limit of measurable fringe density [98,99,64]

It can be seen that the evaluation techniques described above allow the magnitude and direction of the flow to be determined across a PIV negative. However, there is no information present on the film from which the sense of the flow can be determined. Particle tracking and flourescent tracer techniques can label the direction of the flow unambiguously by means of coded illumination and tracer

tails respectively. For many flows the direction can be inferred from *a-priori* information but this is difficult if not impossible for more complex flows. Two different solutions to this problem have been proposed. Adrian et. al. [8,81,7] describe a technique first suggested by Ewan (1979)[48] whereby the imaged flow field is subjected to a shift between exposures so that the largest negative displacement appears as a small but positive displacement. Thus, positive and negative velocities result in measured displacements above and below this "pedestal" displacement. Negative and zero velocities are then resolved when the known shift is subtracted. This is analagous to a technique that is used in crossbeam Laser Doppler Anemometry where a Phase Shifter is used to superimpose a known positive velocity on all the measured velocities. An alternative approach to resolving this directional ambiguity has been reported by Coupland et al (1987)[32,31] where Image plane holography is used to label the first and second images recorded in the flow. Reconstruction of the first and second images independently, by illumination of the flow record with two separate reference beams, allows the two sets of particle image positions to be detected and then cross-correlated to determine an unambiguous particle displacement. A further advantage of this approach is the added immunity of the resulting flow information from anomalous random connections when less than three complete particle image pairs are present within the analysis area.

An implicit assumption in the pointwise analysis of Particle image flow records is that the velocity and therefore particle pair separation does not vary significantly within the local analysis area. For most practical applications of PIV this assumption is only partially satisfied. Real flows have velocity gradients and turbulence, both of which will lead to a range of particle separations within the probe region. When fringe analysis is adopted in the evaluation of such flow records the fringe visibility will vary across the fringe pattern caused by the slight decorrelation of the two similar but displaced particle image patterns. It has been shown that, excluding all other sources of fringe decorrelation and a statistically complete set of particle image separations, it is possible to relate the fringe visibility distribution to the velocity distribution within the probe region.

Ewan (1979)[48] commented on this possibility and Hinsch et al (1984)[61] have since investigated the use of fringe visibility to measure the velocity probability density distribution. Further work by Arnold et. al. [11] has experimentally investigated this principle by taking double exposure photographs of a seeded airflow in a low turbulence wind tunnel with a small controlled degree of turbulence. The resulting flow records were analysed using a 20mm diameter probe beam, to ensure a statistically complete set of particle pair separations and the visibility distribution measured across the fringe pattern. Turbulent intensities were then shown to compare well with simultaneous measurements made with a hot wire probe.

Real time recording and processing of double exposure flow records have been achieved using a reusable photorefractive material to record a double exposure displacement pattern with instant analysis of the flow record using a conventional probe laser beam to generate Youngs fringes, Collicott and Hessellink (1988) [29]. The photorefractive material $Bi_{12}GeO_{20}$ (BGO) stores the images as spatial variations in the refractive index and can be quickly erased and used again. This offers the possibility of accurate real time measurement of velocities when combined with high speed digital processing techniques.

The possibility of measuring three components of velocity has also been considered using stereo photography, De Almeida Dias Delgado, (1986) [36] and Holographically, Royer, (1988) [107].

The possibility of very high speed processing of PIV films using purely optical techniques has been realised. Photorefractive materials such as Bismuth silicon oxide (BSO) has been used to optically compute the 2-D autocorrelation [125] so avoiding the need for slow digital analysis. Optical correlation based on the use of a spatial light modulator as a frequency plane filter has also shown potential as a method of rapidly evaluating PIV flow records [126] with the accuracy and reliability associated with the autocorrelation approach to film analysis.

1.4 Application of PIV to Water Waves

It can be seen that the Laser Speckle/Particle image technique has considerable potential in experimental fluid mechanics. A standard of experimental data previously unattainable due to the limitations of conventional point measurement techniques has been shown to be available in a number of preliminary experiments and the increasing affordability of high intensity laser light sources and powerful computers has prompted a number of researchers to apply this novel technique to a wide variety of flow situations.

The work discussed in this thesis describes the development and evaluation of a PIV system for measuring the internal kinematics of laboratory generated breaking water waves. Previous experimental studies based on more conventional measuring techniques have had a number of difficulties and limitations associated with them. The main difficulty is due to the transient nature of the wave breaking and the limited number of simultaneous measurements that can be made with propeller meters, hot-wire or LDA probes etc. In the past it has been necessary to make individual measurements at different positions within successive waves to buid up a complete velocity map[45]. This requires that individual measurements be made over very short time intervals ($\approx 1ms$) and assumes that the wave is completely repeatable. Sophisticated signal gating and processing techniques allow the velocity within a short instant to be made accurately and elaborate timing systems are used to ensure that individual measurements are made at the same phase position as measurements at other positions. However, exact repeatability of individual waves is doubtful although advanced wave generation techniques do ensure a fair degree of repeatability. Successful application of the PIV technique would avoid such experimental complications and most importantly would be independant of wave repeatability allowing random events to be investigated.

The following chapters consider in detail the theoretical and practical aspects of a PIV wave measuring facility that has been developed by the author. Chapters 2

and 3 consider the recording and evaluation of PIV flow records in a general way that is not particular to wave measurement but introduces several novel features that have been developed in the application of PIV to waves. Uncertainty and errors associated with both the recording and analysis procedures are identified in Chapter 4. The most significant sources of error are considered in some detail and permit an estimate of the accuracy associated with the final velocity measurements to be quoted. Chapter 5 examines the resulting velocity data and describes procedures used to remove anomalous data values, interpolate missing points and calculate vorticity. A complete description of the wave generation facility, flow recording procedure and film processing is described in Chapter 6. Wave measurements are made from a series of negatives that were taken at equal time intervals through the breaking of a typical deep water wave and the results are shown to be consistent with what is known about such waves. Two further applications of the PIV technique are described in Chapter 7. Firstly the use of an incoherent illumination system for the measurement of surface flows and secondly the measurement of Acoustic streaming using PIV. Finally, Chapter 8 identifies some of the advantages and limitations of the PIV technique and in the light of these considers the direction that future work should take.

Chapter 2

Photographic flow recording for PIV measurement

The measurement of velocity inescapably involves the measurement of a travelled distance in a known time interval or vice versa. In the case of particle image velocimetry the instantaneous velocity of a region within a flow is estimated by photographically recording, over a short time interval, the travelled distance of particles which have been introduced into the flow. The arrangement shown in figure 2.1 illustrates the basic principle of the recording process where the motion of the tracer particles is imaged onto a recording medium as as a random distribution of particle image pairs.

The motion of a particle represents the flow as seen from a Lagrangian viewpoint where the position (x, y, z) of the particle is a function of time t and its initial position (x', y', z') at $t = 0$ ie. $x = f(x', y', z' : t), y = f(x', y', z' : t), z = f(x', y', z' : t)$. The velocity as a function of position x, y, z and time t, ie. $\underline{v}(x, y, z : t)$ represents the Eulerian velocity and is the most commonly used viewpoint in fluid dynamics where,

$$\underline{v} = v_1 i + v_2 j + v_3 k \tag{2.1}$$

and v_1, v_2, v_3 represent the components of velocity in the x, y, z directions respectively. The relationship between the Lagrangian particle position and a single

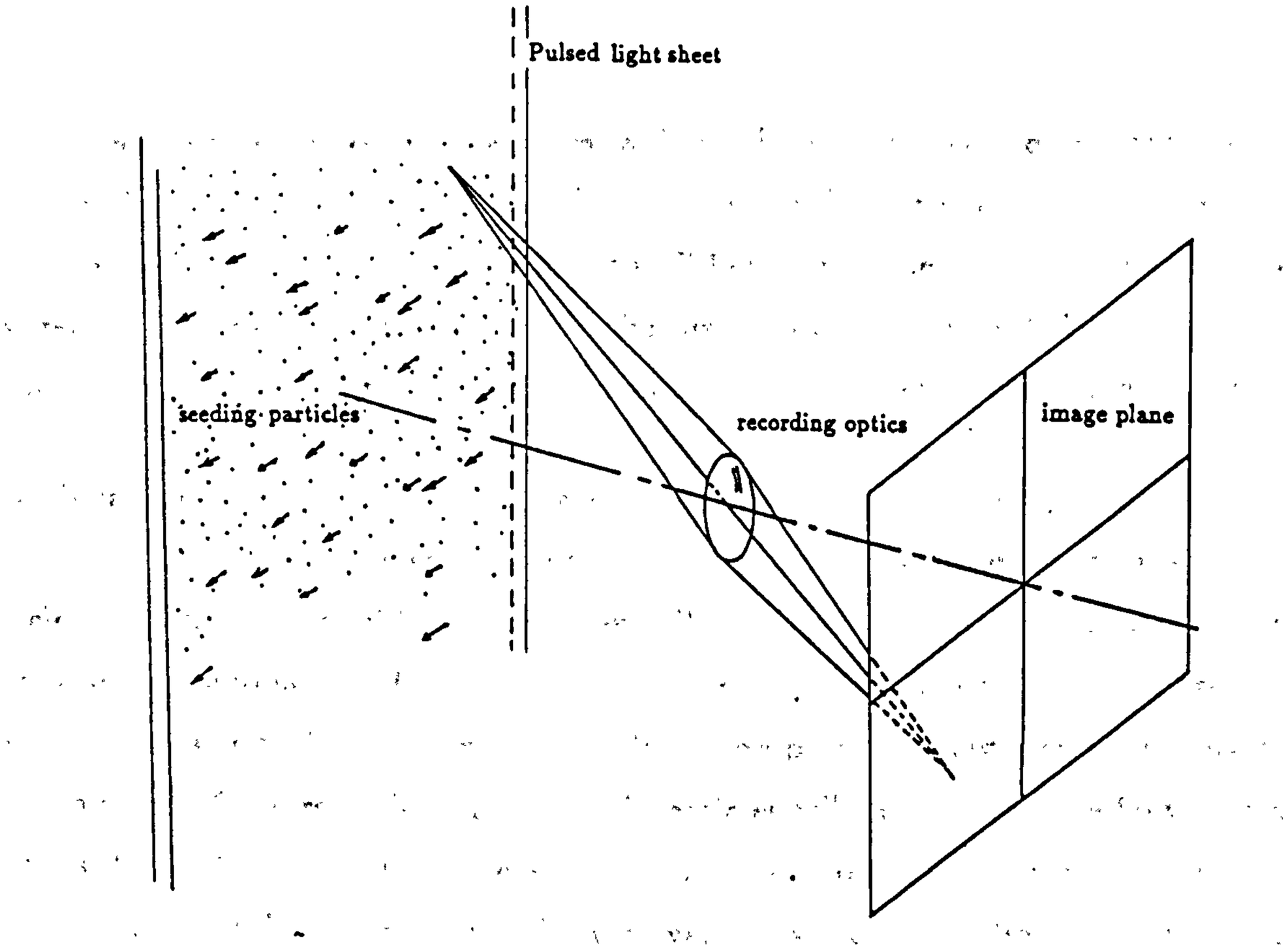

Figure 2.1: photographic recording of the in-plane motion of a flow field

component of the Eulerian velocity is embodied in the expression,

$$v_i = \frac{dx_i}{dt} = \lim t_1 \rightarrow t_2 \frac{x_i(t_1) - x_i(t_2)}{t_1 - t_2} \tag{2.2}$$

where $x_i(t_1), x_i(t_2)$ are the coordinates , in the x,y or z direction, of a single particle at t_1 and t_2. For a time interval $t_1 - t_2$ that tends to zero the ratio of the travelled distance over the time of travel will closely approximate the instantaneous Eulerian velocity. In practice, the time interval need only be small compared to typical Eulerian time scales of the flow for the measured velocity to closely approximate the instantaneous velocity.

A double exposed flow record obtained from a seeded flow will therefore be a random distribution of particle image pairs where the local instantaneous velocity at time $t \approx (t_1 - t_2)/2$ is proporional to the separation of any particle image pairs that may be found at that point.

Beyond the approximation between the instantaneous Eulerian velocity and the measured Lagrangian motion of the tracer particles, the precision with which

instantaneous velocities can be measured will be limited by the accuracy with which the fluid displacement and the time interval between exposures can be determined. Typically, the time interval T between pulses can be measured to a very high degree of accuracy while the major source of uncertainty resides in the measurement of the fluid displacement at a particular point within the flow.

An ideal recording system would produce a double exposure image of the seeded flow that had a very dense concentration of perfectly recorded very small particle images. This would give an essentially continuous distribution of velocity information across the flow record where, no matter how small a local area of the film was considered, there would always be particle image pairs relating to the motion of the recorded flow. Small particles will respond to the flow better and will produce smaller particle images on the recording medium. This would permit smaller displacements to be resolved thus increasing both the temporal and spatial resolution of the flow record. Additionally, the position, and therefore separation, of particle images will be more accurately measureable if they are small. It can be seen therefore, that practical recording systems should aim to record as high a concentration of small particle images as is possible.

Listed below are the main factors that control how close to this ideal practical measurements can come

Flow characteristics: max/min velocity, refractive index, area

Seeding: material,dimensions,concentration, light scattering efficiency

Recording medium: sensitivity,resolution, noise, size

Light source: power, wavelength, directionality

Recording optics: resolution,image distortion,magnification,aberations

Exposure parameters: pulse duration, pulse separation, number of pulses

The choice of components and parameters for recording a flow field will often be a compromise reflecting the limited sensitivity and resolution of the recording

medium, the power and form of the light source, the scattering efficiency of tracers, financial limitations etc. The final configuration of the flow recording system will thus be dependent upon the resources available and the priorities of the user concerning accuracy, measurement area and resolution. The following sections consider in more detail the parameters outlined above and the details of the flow recording facility that has been developed for the measurement of velocities under breaking waves.

2.1 Seeding considerations

Particle Image Velocimetry like Laser Doppler Velocimetry relies upon the interaction of light with particulate matter suspended within, and assumed to follow the fluid motion. In Laser Doppler measurements the light scattered from one or more particles within a small intense spatial pattern of light is monitored to determine the time dependent velocity of the flow in one direction at that point. In contrast PIV measurements rely upon capturing spatial information over a very short time interval throughout an extended region of a flow field and typically encompasses many thousands of particles. This raises questions concerning the precision with which the particle motion matches that of the fluid, the detectability of particles during the small timescales and large areas involved, and the optimum seeding concentration required for good resolution and accuracy.

2.1.1 Particle motion in fluid

An implicit assumption in the recording of PIV photographs is that the particles introduced into the flow faithfully follow the motion of the fluid and that the flow is not perturbed by the presence of the tracer particles. Consideration of the relative motion between particles and flow has been given in experimental studies utilising Laser Doppler Anemometry and a number of different effects

have been identified.

Inertial effects A difference in the density of the particles and the fluid will result in a delayed response of the particle to fluid acceleration. This effect is only significant when the density difference is large or when high frequency fluctuations of the flow are important. In liquid flows with reasonably matched seeding densities this is unlikely to be a problem. Large differences in density are most commonly found in air flows and this effect may become apparent at high frequencies. For small particles the power spectrum $\Phi_u(\omega)$ of the fluid flow is related to the power spectrum of the particle velocity $\Phi_v(\omega)$ in an approximate manner [42],

$$\Phi_v(\omega) = |a_m|^2 \Phi_u(\omega) \tag{2.3}$$

where

$$|a_m| = \frac{K_\nu}{(K_\nu^2 + \omega_m^2)^{1/2}} \tag{2.4}$$

and

$$K_\nu = \frac{36\mu_0}{(2\rho_p + \rho_0)d_p^2} \tag{2.5}$$

where the flow velocity is varying sinusoidally , and ω_m is the frequency of oscillation, d_p is the particle diameter, μ_0 is the fluid viscosity and ρ_p and ρ_0 are the particle and fluid densities respectively. The complex amplitude of the particle oscillation is a_m. It can be seen from the expressions above that the real amplitude $|a_m| = (a_m a_m^*)^{1/2}$ will decrease rapidly at high frequencies.

Gravity Differences in density between the seeding and the fluid can also cause settling, or upwards drift of the particles. For small particles the velocity of this drift is given by the expression,

$$V_v = \frac{d_p^2 g}{18\mu_0}(\rho_p - \rho_0) \tag{2.6}$$

where g is acceleration due to gravity. Again, unless ρ_p and ρ_0 differ significantly the settling velocity will be negligible. However, a settling velocity that is not significant compared with the flow velocities, but which

can still be detected, may cause difficulties in maintaining the required seeding density for the duration of an experiment.

Spatial averaging of turbulence This will occur if the particle diameter is larger than the dimensions of the eddies in a fluid, causing a filtering out of very small scale motions. This will not be important for the majority of experiments but may become significant in small scale studies of turbulence.

Other effects such as the Magnus effect and Shear flow lifting force are due to particle spin and the effect of motion in large velocity gradients respectively but their effect is small in non-extreme flows even compared to Inertial and gravity effects. For the measurements in waves pollen particles with an average diameter of $50\mu m$ were used. When introduced into the flow the particles remained suspended for several hours without visible settling. This suggests that the response of the particles in the relatively low accelerations in waves will be very good.

2.1.2 Light scattering efficiency

Light scattered from particles moving within the illuminated region of the flow is collected using camera optics and imaged onto the recording medium. The mean exposure on the film plane is $E = \mathcal{I}t$, where $\mathcal{I}$ is the mean image intensity and t is the exposure time. The time t should be short enough to freeze the motion of the particles within the flow while the exposure E must exceed that required to generate an image density, after development, that is greater than the gross fog level of the film [34]. Thus, successful recording of the flow field will be dependent upon the intensity of the particle images and the threshold exposure E_0 required to record an image. The light intensity $\mathcal{I}$ reaching the film will be a function of the illumination intensity, the scattering efficiency of the particles, the solid angle through which light is collected (lens f number) and any light losses associated with propagation through the fluid and past flow boundaries.

The illumination intensity is limited due to the cost and capabilities of laser light sources and is further reduced when the beam is expanded to form a sheet. The scattering efficiency of particles is very low perpendicular to the incident light, Kerker, 1969[75] and is dependent upon the shape, size, and material of the seeding. Selection of seeding size and material is therefore very important if the scattered light is to be sufficient to expose the photographic emulsion while forming an image that is small enough to be consistent with the desired accuracy.

A study of the scattering power of spherical seeding particles in a 0.2 to 15 μm range of diameters has been published by Adrian and Yao,1984[5] following similar studies for Laser Doppler measurement. Calculations of scattering efficiencies of polystyrene, glass and oil droplets were based on Mie scattering calculations and indicated that the mean scattering intensity increased rapidly for particles $\leq 1\mu m$ diameter and more slowly for particles $\geq 1\mu m$. Scattering efficiency is also shown to be strongly dependent upon the ratio of the particle refractive index n_p to the fluid refractive index n_0 giving considerably more scattered light for larger values of $\frac{n_p}{n_0}$, as in air flows, where the n_0 is low. The detectability of the different particles is optimised to obtain the minimum particle image diameter and maximum mean intensity at the film plane and Adrian quotes $10\mu m$ polystyrene particles in water and $5\mu m$ oil or glass spheres in air as best. These values are dependent upon film type, laser intensity and wavelength, and the f number of the recording optics.

Such a study clearly illustrates the most important aspects of the scattering and recording process involved in PIV but extrapolation of the results to other systems employing different seeding can be done only on a comparative basis. It is difficult to quantify the scattering efficiency of opaque non-spherical or random shaped seeding particles. The fact that the particles may be polydisperse will also complicate the analysis. The use of monodisperse spherical latex or polystyrene particles is feasible for small scale flow experiments but this becomes costly when large volumes have to be seeded. Alternative seeding materials that have been used in PIV studies include tobacco smoke, Aluminium dust,

Aluminium oxide, Hydrogen bubbles, milk, sawdust, Latex paint, Conifer pollen etc. Almost all of these particles have an irregular shape and computation of their scattering efficiencies is generally not possible and so a more empirical approach is required for estimation of their detectability. The choice of seeding material and dimensions for a given experiment will be based upon the opposing trends that on the one hand require large particles for increased scattered light intensity and efficient resolution both by photographic film and camera optics and on the other require small particle images for accuracy.

2.1.3 Seeding concentration

The first experiments illustrating the possibility of full field velocity measurements in fluids emulated the laser speckle photography technique from which PIV was derived. High concentrations of seeding particles resulted in unresolved particle images overlapping with random phase to produce a speckle pattern in the film plane limiting the techniques ability to measure in-plane velocities when the flow is three-dimensional.

Reducing the seeding density, so that in general particle images are resolved from each other, will reduce the dependence of the recorded intensity pattern on the positional relationship between particles. Total decorrelation of the random pattern of particle images will then only occur when the out-of-plane motion results in particles moving completely out of the plane of illumination between exposures, typically 0.5-5mm. Generation of purely 2-D flows is difficult and limits the number of fluid dynamically interesting flows that can be studied and so increased resistance of measurements to out-of-plane motion is a significant advantage. However, the displacement information is no longer continuously distributed over the flow record and velocity informatiom occurs only where particle image pairs have been recorded. In certain cases this can lead to signal dropout akin to that experienced in Laser Doppler studies for fluids with very low seeding densities.

Questions are thus raised concerning the optimum seeding density for different flows and configurations of measurement system. The source density $S.D.$ is a dimensionless quantity [4] that has been defined as,

$$S.D. = C\Delta z d_e^2/M^2 \tag{2.7}$$

where C is the volume concentration of detectable particles, Δz is the illumination sheet thickness, M is the image/object magnification, and d_e is the diameter of a particle image including diffraction (see section 2.4.1). The source density represents the average number of particles that exist within a volume defined by the thickness of the light sheet and the area in the object plane that corresponds to a demagnified particle image. Essentially it gives a measure of the number of overlapping images, where $S.D. \gg 1$ results in a speckle pattern at the image plane and $S.D. \ll 1$ gives, in general, resolved particle images. For a particle image diameter $d_e = 20\mu m$, a magnification of M =1 and Δz=1mm, a volume concentration of approximately 2.5×10^{12} particles/m^3 is required to achieve the threshold of speckle with a source density of 1. If the recording optics were close to being diffraction limited and were operated at f5.6[1] the seeding would then constitute ≈0.3% of the total fluid volume. At this concentration optical penetration of light into the flow will be significantly reduced and it is possible that the high concentration of particles will affect the characteristics of the fluid. It can be seen therefore, that seeding concentrations should be well below that required to form speckle.

For very low seeding densities individual particle image pairs will tend to be separated by distances greater than typical lengthscales of the flow and so considerable high frequency spatial information will be lost. Point analysis of the film with a narrow laser beam in regions that contain a single pair of particle images result in Youngs fringes[2] with little noise and very high visibility (figure 2.2). The analysis of such fringes is simplified because of their clarity but spatial resolution is limited to the diameter of the laser beam. For higher seeding

[1]The limitations imposed by diffraction at the lens will be discussed separately in a later section.

[2]A more formal description of the production of Youngs fringes and the optical arrangement used is given in Appendix 1.

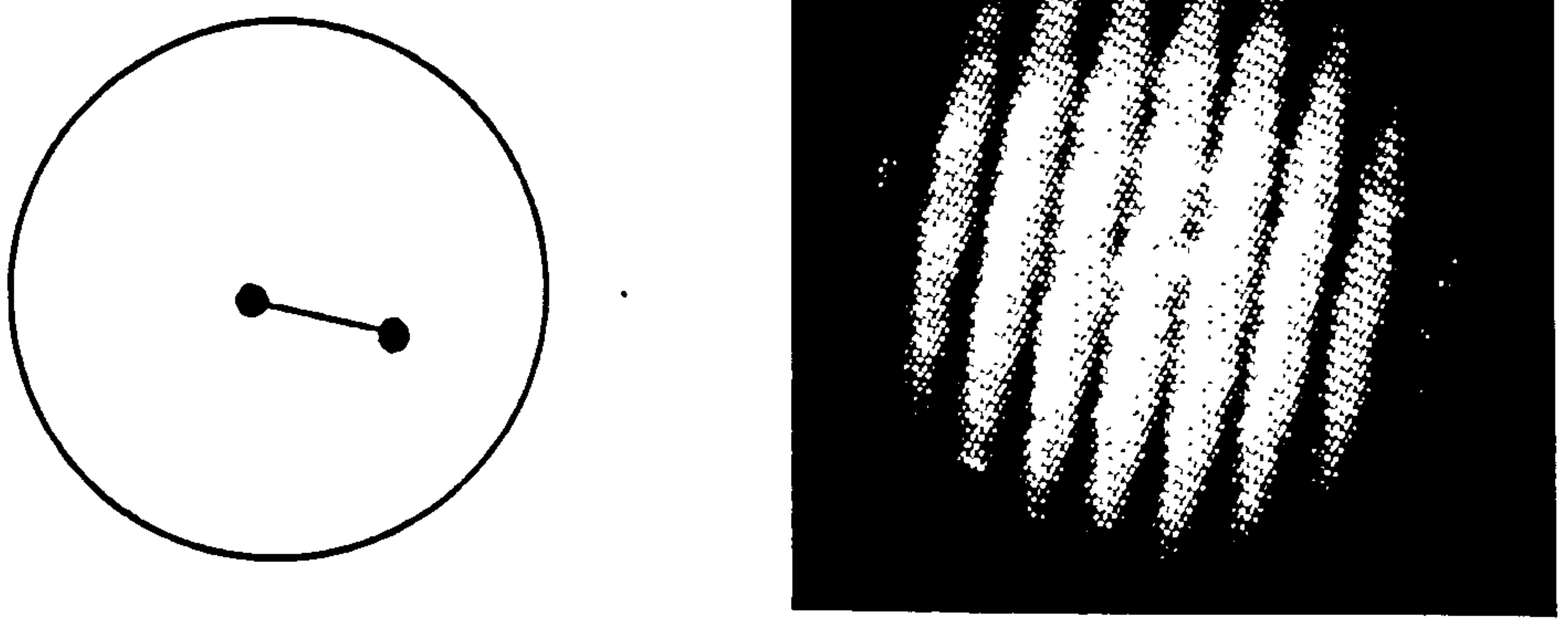

Figure 2.2: Noise free fringe pattern (right) generated from a single pair of particle images (left).

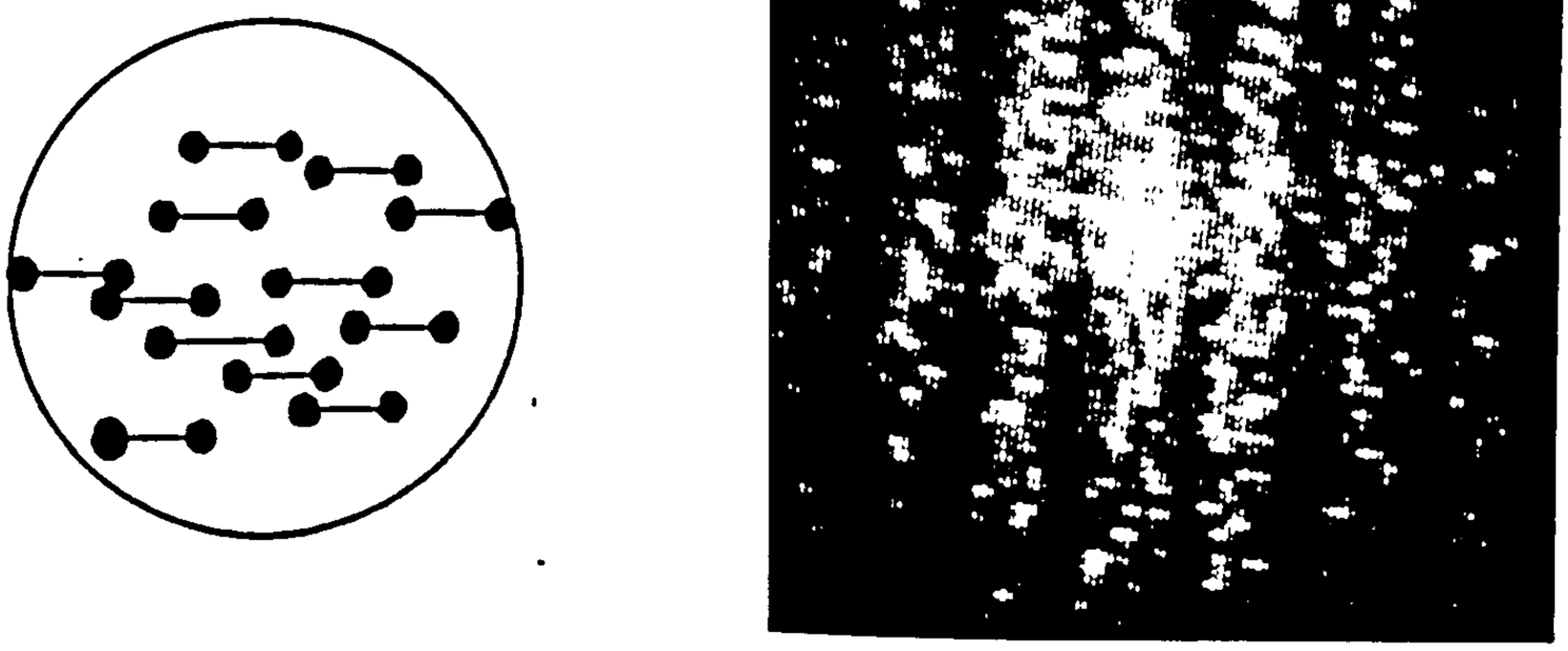

Figure 2.3: Fringe pattern with speckle noise (right) derived from the randomly positioned particle image pairs shown on the left.

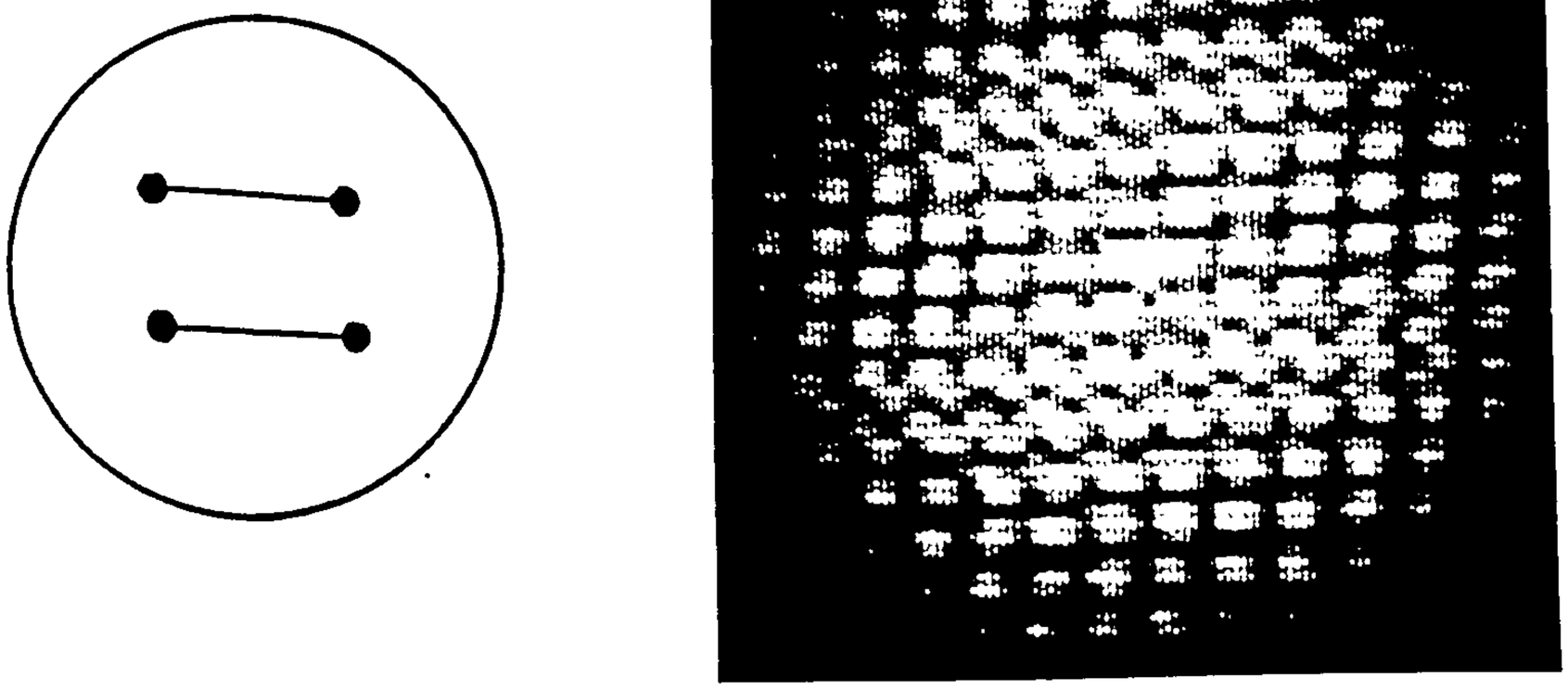

Figure 2.4: Crosshatch fringe pattern (right) generated from ambiguous situation of exactly two pairs (left).

densities many particle image pairs will exist within the laser probe region and the Youngs fringes are degraded by the presence of "secondary speckle" noise (figure 2.3, right). This speckle noise is due to the random distribution of particle image pairs within the local measurement area (figure 2.3, left). When the probe laser beam is passed through the film light diffracted from every particle image interferes with similarly diffracted light from every other image within the analysis area. Interference between all particle images produces a large number of overlapping fringe patterns similar to that produced in the single pair case. The fringes that are generated from particle image pairs whose displacement is due to the flow will all combine in phase to produce the visible fringes while all the random pairings of particle images will result in a random interference pattern i.e. speckle.

The two situations described above correspond to two extremes in the particle image mode. A low seeding density, producing a high visibility signal wherever a particle pair exists and the high seeding density producing an almost continuous

signal but degraded by the random phase relationships between particle image pairs.

Between these two extremes is a particular seeding concentration that leads to loss of measurement due to the same number of random pairings to valid pairings occurring within the probe area. An example of this can be seen in figure 2.4. The probe area, shown on the left, contains exactly two pairs of particle images and as such there is insufficient information from which an unambiguous velocity estimate can be made[3]. This is reflected in the fringe pattern generated from such a pair where the two strongest correlations produce two equally strong fringe patterns superimposed to form a crosshatch pattern.

It can be seen from these considerations that the optimum seeding density is one that results in high image density negatives without producing a speckle pattern. The seeding density should be sufficiently high that the mean number of particles per analysis area never drops below 6 so that if the random particle image pattern follows a Poisson distribution the probability of obtaining $\leq$ two particle image pairs per interrogation spot is less than 5% [4].

For an average of six or more particles per interrogation spot ie.

$$C\Delta z\pi\left(\frac{D}{2M}\right)^2 \geq 6 \tag{2.8}$$

the C required is given by,

$$C \geq \frac{24M^2}{\Delta z\pi D^2} \tag{2.9}$$

where C is the number of particles per unit volume, M is magnification , Δz is the laser sheet thickness, and D is the diameter of the interrogation area. With $M = 0.1$, $\Delta z = 2mm$, $D = 1.0mm$ approximately 4×10^7 particles/m^3 are required to give a source density less than 1 but high enough to give reliable measurements continuously over the flow photograph.

[3]This ambiguity is avoided if the first and second particle images can be identified eg. Holographically[31].

[4]This does not take account of the probability of the first or second of the images from either pair existing out side the probe area. This is considered in section 2.2.

2.2 Exposure parameters

The choice of exposure parameters is based on the nature of the flow to be measured and the required spatial resolution. The flow photograph is analysed over a large number of discrete points where the particle displacement within each local probe area is assumed to be constant [5]. The probe region is usually circular and centred on the measurement point and the diameter of the probe region is chosen to be small compared to the smallest scales of motion represented on the flow negative. Consequently, the maximum particle separation must be smaller than the diameter of the analysis spot while being large enough that the particle separation can be measured accurately.

2.2.1 Pulse separation

Equation 2.2 embodies the relationship between the time dependent position of the marker particle and the measured velocity showing that it approaches the instantaneous Eulerian velocity as the time between exposures T tends to zero. However, T should be large enough that the particle motion in that time is large compared to the absolute uncertainty associated with locating the centre of a particle image. The upper limit on measureable particle image displacement will be imposed by the dimensions of the probe spot. The maximum measureable particle image separation within a probe region of diameter D is that which permits a correlation between the first and second particle images of each pair within the probe region. Figure 2.5 shows that the area within the circular probe region that contributes to the displacement correlation decreases as the particle separation increases and drops to zero when the displacement d equals D. The ratio of the crosshatched region to the total probe area is given by

$$R = 1 - \frac{2}{\pi}\sin^{-1}\frac{d}{D} - \frac{2d}{\pi D^2}\sqrt{D^2 - d^2} \tag{2.10}$$

This rapid decrease in useful probe area is shown in figure 2.6 below. Additionally,

[5] The limitations of this approximation are discussed in chapter 5.

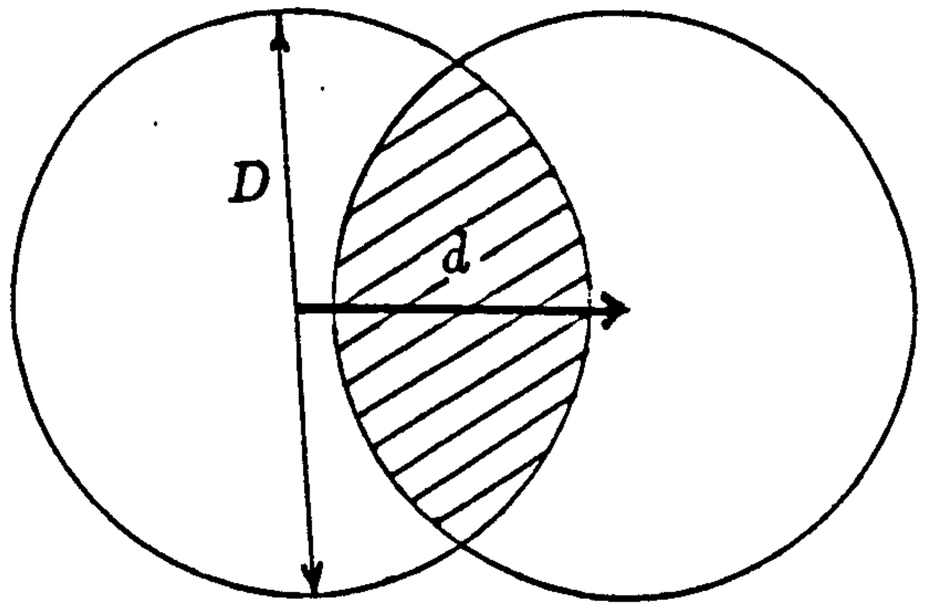

Figure 2.5: Crosshatched region indicates area of possible correlation within the probe area

it is neccessary that 3 or more particle pairs exist within this region in order that an unambiguous correlation in the flow direction can be detected. The particle image pairs are distributed randomly and to a good approximation will follow a Poisson distribution [17] and so the probability of 3 or more particles existing within a given area is given by

$$P(n \geq 3) = \sum_{n=3}^{\infty} \frac{(\lambda s)^n}{n!} \exp^{-\lambda s} \tag{2.11}$$

where $P(n \geq 3)$ is the probability that 3 or more particles exist within the area s and λ is the rate parameter or the mean number of particle images per unit area. Substituting the useful correlation area into equation 2.11 gives us the probability of obtaining ≥ 3 particle pairs within the probe region as a function of displacement and image density (see figure 2.7). The three lines on the graph illustrate the situation for image densities of $\lambda = 5, 10, 15$ particles per probe spot.

It can be seen that for particle image separations approaching the probe diameter D the probability of a succesful correlation existing within the analysis region drops rapidly to zero. Thus the maximum permissible particle displacement

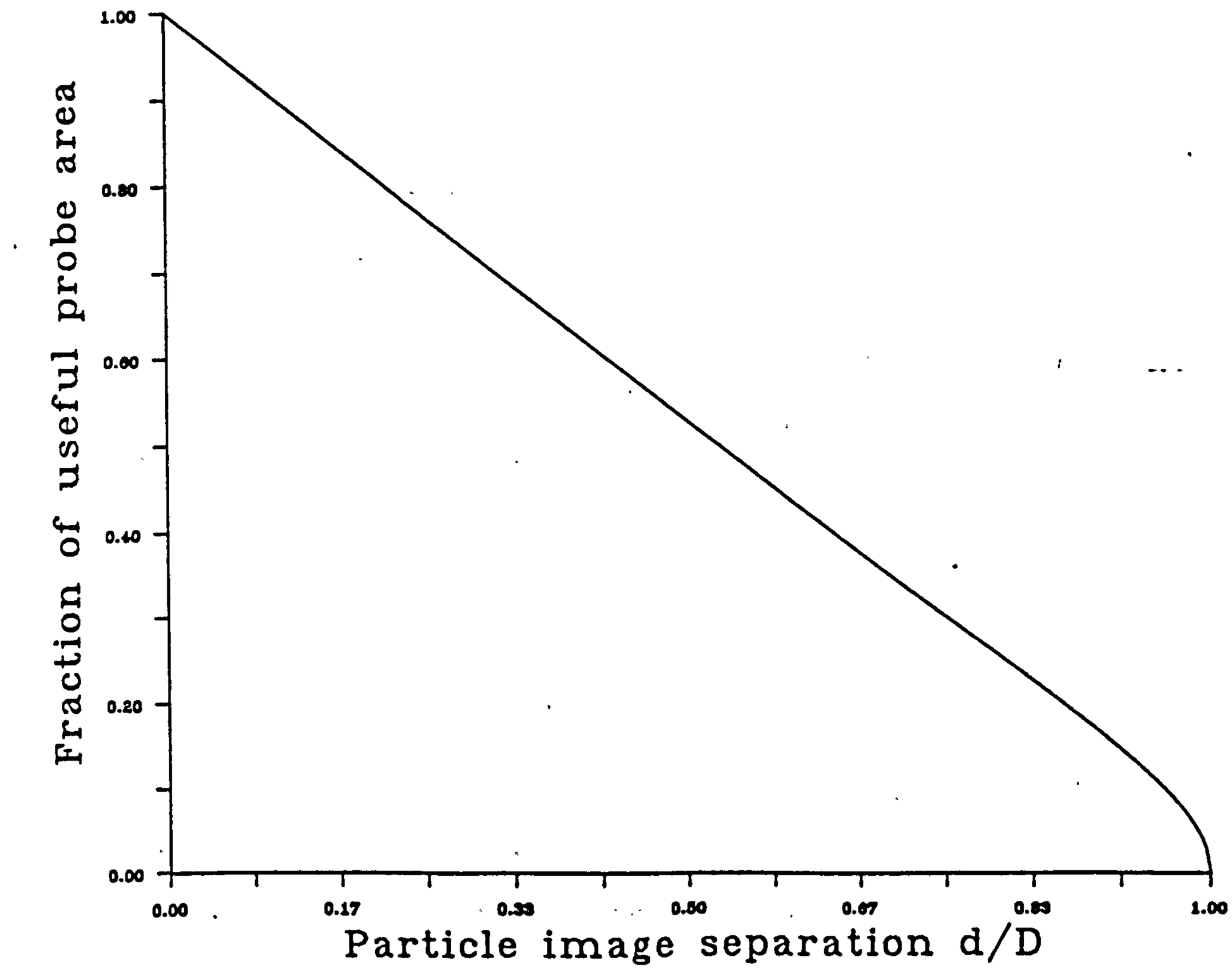

Figure 2.6: Useful probe area as a function of particle displacement

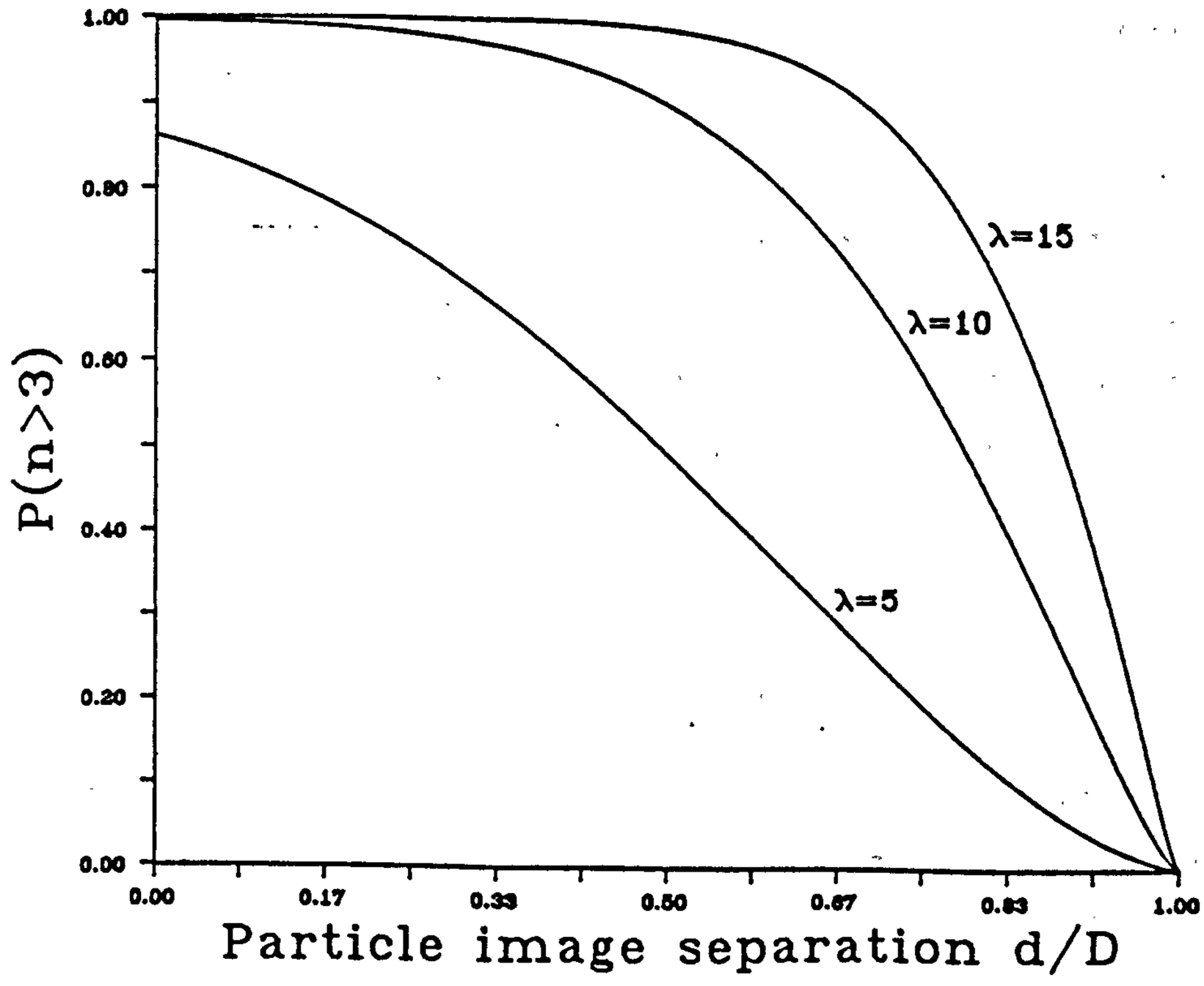

Figure 2.7: Probability of ≥ 3 pairs existing within probe area as a function of particle image displacement and image density.

will be significantly less than the probe diameter D especially for lower particle image concentrations.

A further consideration when deciding upon the pulse separation T is the maximum resolvable spatial frequency for a probe diameter D and a transforming lens of focal length f_l[85].

Figure 1.1 illustrates the generation of displacement fringes in the Fourier plane of a multi exposed flow record. The separation of the fringes is given by,

$$d_f = \frac{\lambda_a f_l}{M v_{max} T} \tag{2.12}$$

where λ_a is the wavelength of the illuminating beam, f_l is the focal length of the lens, M is the magnification of the image recording optics, and v_{max} the largest expected velocity. The fringe period d_f must be larger than the diffraction limited point response of the optical system which is given by.

$$d_s = \frac{3.83 \lambda_a f_l}{\pi D} \tag{2.13}$$

If $d_f \geq d_s$ then

$$TMv_{max} \leq 0.8D \tag{2.14}$$

indicating that the maximum particle image separation should be less than 0.8 times the probe diameter. The probability of obtaining more than three particle pairs at $\leq$0.8 times the probe diameter is 0.13, 0.45 and 0.73 for an average of 5,10 and 15 particle images per interrogation spot respectively. Thus, for particle separations less than $0.8D$, the fringes can be resolved in a diffraction limited system but the probability of obtaining 3 or more complete particle image pairs is low. In most situations therefore, the maximum measureable particle image separation will be significantly less than $0.8D$, ie. between 0.5-$0.8D$.

2.2.2 Exposure time

The exposure time used for recording particle images is chosen so that the motion of the particles in that time is very small. This ensures that the particle is

recorded precisely without blurring. It has been shown that velocity measurements are possible with relatively long exposure times[85] but results in particle images that are streaked in the direction of the flow. Such measurements will be of limited precision and the analysis of the flow record will be complicated due to the blurred particle images[111]. The use of a pulsed laser avoids any difficulties of this sort as the pulse time is sufficiently short (30-80ns) that the motion of all but extremely high velocity particles is arrested within the pulse time. Only when a CW laser is used does the pulse time become a variable parameter. The generation of pulsed planar illumination from a CW laser is discussed in the next section and a system that employs a scanning beam is described. This method of illumination allows a very short pulse time$\approx 3\mu s$ while maintaining a high illumination intensity. Pulse times of this duration are typically short enough to freeze particles travelling at up to several m/s.

2.2.3 Multiple exposures

When more than two exposures are used to record the flow the correlation in the direction of the flow is significantly increased. This is seen most vividly in the increased visibility of the Young's fringes that can be produced from PIV flow photographs which have more than two exposures. (see figure 2.8). This sharpening of the fringes comes about because of the presence of harmonic terms generated from the correlation between the first and third image, the second and fifth image etc. and also because of the density of image pairs recorded on the film. This aspect of the recording process is considered in greater detail in chapter 3 where the increased correlation in the direction of the flow is shown to result in increased reliability and accuracy.

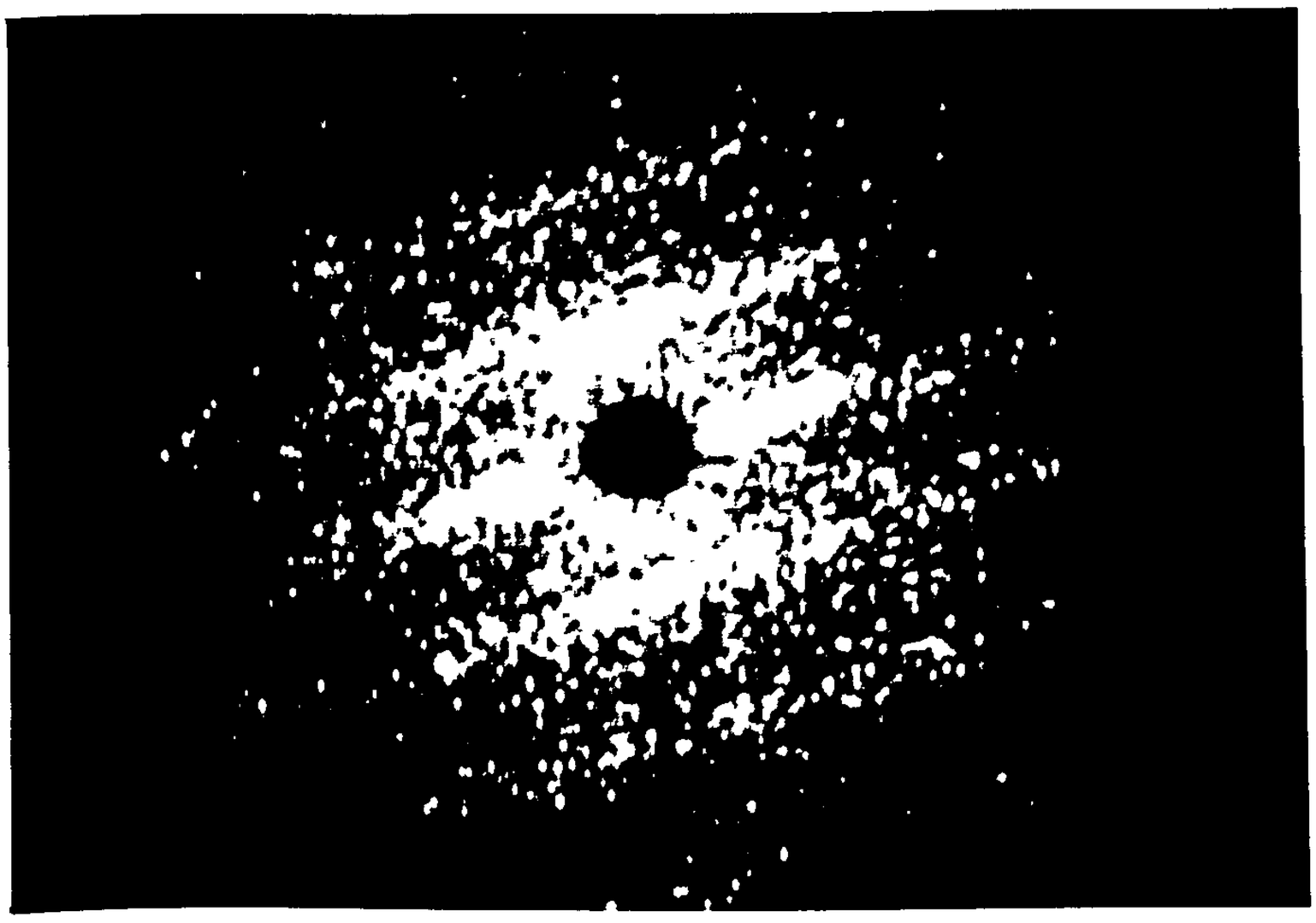

Figure 2.8: Youngs fringes generated from a multiply exposed flow photograph.

2.2.4 Dynamic range of velocity measurement

In most applications it is important that the measurement process is capable of evaluating an extended range of velocities. The velocity dynamic range is defined as,

$$\Delta v = \frac{v_{max} - v_{min}}{v_{min}} \tag{2.15}$$

According to the discussion above the maximum measureable velocity may be estimated to be,

$$v_{max} \approx \frac{0.6D}{MT} \tag{2.16}$$

and the minimum measureable velocity is that which corresponds to a particle pair being separated and no more ie. image centres are separated by one particle image diameter d_i.

$$v_{min} \approx \frac{d_i}{MT} \tag{2.17}$$

and so the dynamic range as defined above is

$$\Delta v \approx \left(\frac{0.6D}{d_i} - 1\right) \tag{2.18}$$

Thus, for a probe diameter of 0.75mm and particle image diameter of $20\mu m$ $\Delta v \approx 20$.

2.3 Illumination systems

The scattering efficiency of seeding particles perpendicular to the illumination is typically quite poor and combined with the limited sensitivity of high resolution photographic emulsions necessitates the use of a high intensity light source to succesfully record a flow field. Lasers have been the most common light source used in the past because of the highly directional and intense beam they produce. However, even with the light power available from a laser the scattered light reaching the recording medium is still of very low intensity. Expansion of the laser beam into a sheet of sufficient width to illuminate the region of interest within the flow will further reduce the intensity by two or three orders of magnitude, and when a CW laser is used the useful light is further diminished by the short pulse times required to record the particles without blurring.

The following section considers the expansion and modulation of a CW light source for illumination of a region covering several thousandcm^2 and velocities of severalms_{-1}. The use of pulsed laser souces has been avoided in the work described here due to the difficulties encountered in their use. Specifically, alignment of optics, safety, and the requirement that a single light source should be sufficiently flexible to be used for a large range of velocities and measurement areas.

For the measurements described in Chapter 6 it was necessary to illuminate an area within the wave tank 50-70cm wide. The most commonly employed method of producing such a light sheet is to use an arrangement of cylindrical lenses to expand the beam in one dimension. Temporal modulation of the beam is performed either by a mechanical chopper or an electro-optical device. Figure 2.9 illustrates a typical beam expansion system incorporating these methods. The limitations of such a system become apparent when high velocities, large areas or both are to be recorded.

A 25μm particle moving at 1 m/s will require a pulse time of less than 10 μs to

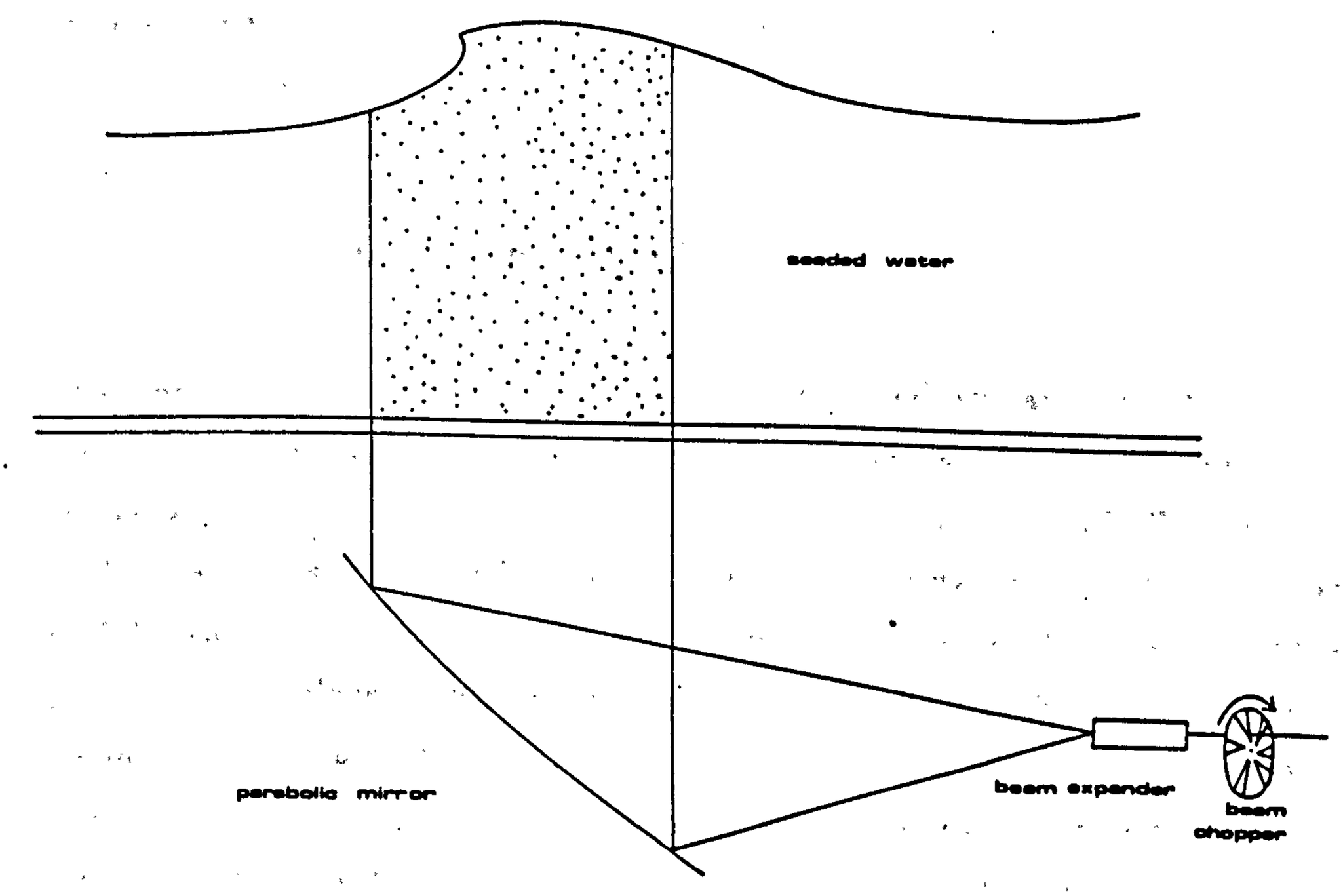

Figure 2.9: Beam expansion and modulation using cylindrical lenses and a mechanical chopper

confine its motion to less than half its own diameter. This is about 100 times shorter than the fastest shutter speed available on most cameras. Providing adequate exposure $E = \mathcal{I}t$ then requires that the light intensity is very high. It can be seen that the maximum measurement area, with a light source of limited power, is reduced as the maximum expected velocity in that region increases. Also, the chopping of the laser beam at a low mark-to-space ratio means that only a small fraction of the available light power is being used. An alternative, more efficient, method of illuminating a planar region within a flow field is described below.

2.3.1 Scanning beam illumination

The illumination system described here was developed primarily for the recording of flow fields under laboratory generated water waves. However, the principle of the technique will permit a wide range of flows to be efficiently illuminated. High intensity, short duration light pulses are imparted to the flow field by rapidly scanning a laser beam through the region of interest. The seeding particles within the plane of interest are illuminated by the very high intensity laser beam for the time that it takes the finite width of the beam to pass a single particle. Figure 2.10 illustrates the configuration of such a system set up to illuminate water waves. The scanning frequency is the time between pulses for the chopped system.

Assuming that the exposure time t is short enough to freeze the motion of the particles within the flow region the exposure for a chopping system similar to that illustrated in fig. 2.9 is given by.

$$E = CIt \tag{2.19}$$

where I is the average intensity of the expanded sheet of laser light, t is the exposure time and C is a constant which accounts for the fraction of the incident light that is scattered and imaged for a given magnification and lens aperture. The exposure from a scanning system illuminating the same area with the same

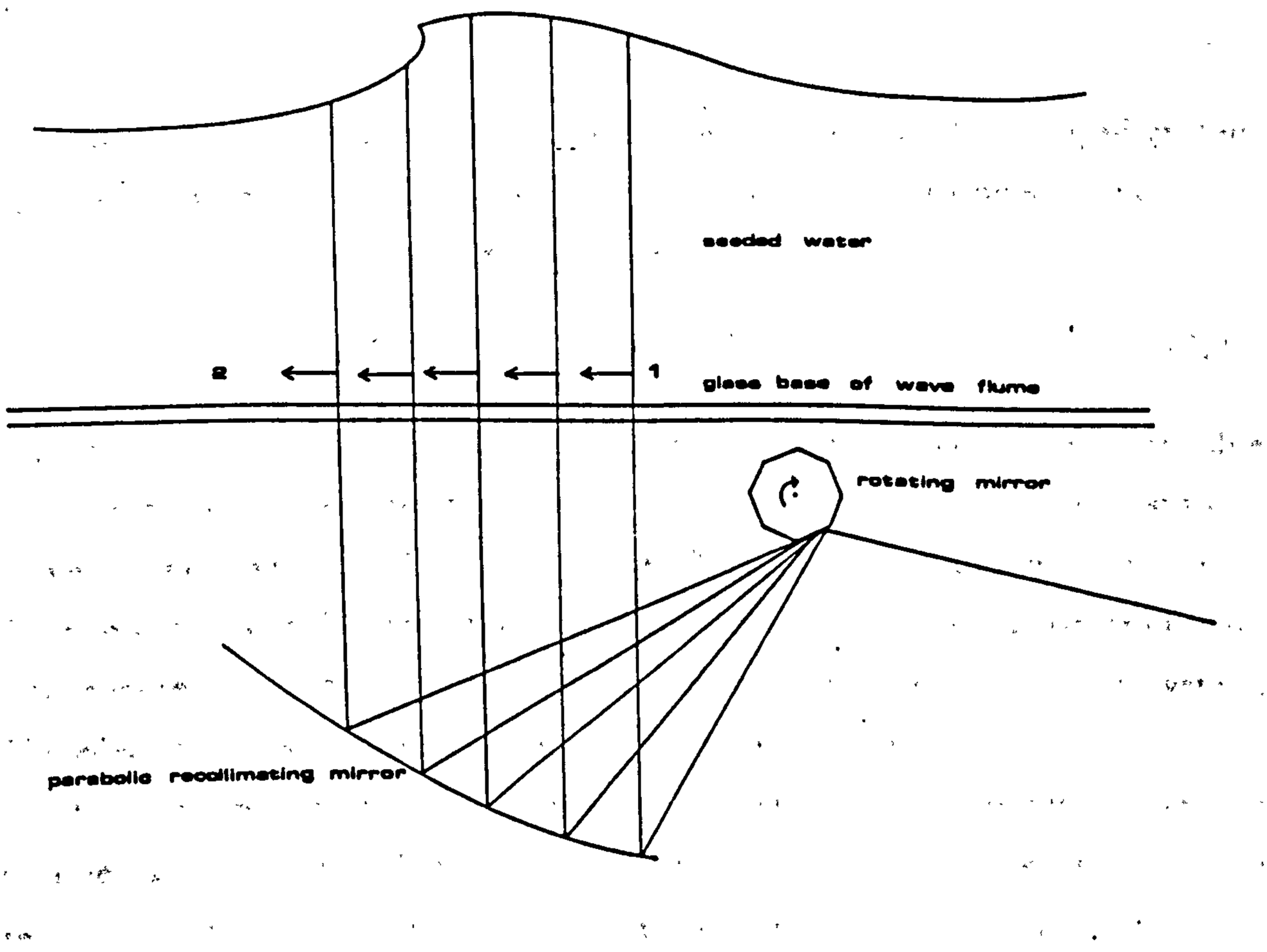

Figure 2.10: Scanning beam system incorporating rotating octagonal mirror and parabolic collimating dish

pulse separation is given by,

$$E' = CI't' \tag{2.20}$$

where I' is the average intensity of the unexpanded beam and t' is the time that it takes the beam to pass any point within the measurement area. The intensity of the unexpanded laser beam I' is given by,

$$I' \approx IL/d, \tag{2.21}$$

L is the width of the measurement area, and d, is the diameter of the scanning beam.

$$t' \approx Td,/L \tag{2.22}$$

T is the scanning period and the time between pulses for the chopped system ie. $T = Rt$ where R is the ratio of the pulse separation to pulse duration ie. $R = T/t$. Therefore E' can be expressed as

$$E' \approx CI(L/d,)t(d,/L)R = CItR \tag{2.23}$$

So, for the same laser power and the same area of illumination the exposure value is increased by R over that provided by a modulated, expanded beam system. Meynart and Lourenco, (1985)[94] quote 20 as being a minimum value for R. Therefore, the scanning system offers the equivalent of at least an order of magnitude more useful light power over a conventional chopped illumination system. The effective exposure time is also reduced in most cases ie. if $(L/d,) > R$ then $t' < t$. Therefore, for the same laser power one has the option of measuring over a larger area and/or higher velocities as well as permitting the use of higher resolution film and thus smaller and more accurately measureable particles.

The most obvious drawback of this system of illumination is the extended time taken to record the whole flow field. The scanning method of illumination is analogous to a focal plane shutter where different parts of the image are exposed at different times depending upon the horizontal position in the illumination area. When the speed of the shutter is not large compared to the speed of the object there will be a stretching or compression present in the final recorded image. The same is true for the scanning beam. If the scanning frequency is too

low then the image of the flow field will be stretched or compressed compared to the flow itself, depending upon the direction of the scanning beam relative to the direction of the flow. The expression that relates the positions of the particles at consecutive illuminations becomes,

$$v_x = \frac{x_1(t_1) - x_2(t_2)}{t_1 - t_2} \tag{2.24}$$

where $t_1 = t_0 + \frac{x_1}{L\nu}$ and $t_2 = t_1 + \frac{1}{\nu} - \frac{1}{L\nu}(x_1 - x_2)$, $x_1(t_1)$ and $x_2(t_2)$ are the x positions of an illuminated particle within the measurement area, t_0 is the time of the beam initially entering the measurement area at $x = 0$ and ν is the scanning frequency. The mean measurement time $t = (t_1 + t_2)/2 = t_0 + \frac{1}{2\nu} + \frac{1}{L\nu}\left(\frac{x_1+x_2}{2}\right)$ varies according to the horizontal position within the measurement area. The approximate time between exposures and the time taken for the beam to cross the flow field is $1/\nu = T$ and so it can be seen that this effect is going to be small as T is chosen to be small compared to typical timescales of the flow. The time taken to doubly expose the whole flow with a scanning beam is $2T$. So, as long as the flow does not change significantly in $2T$ the difference between measurements using a conventional system and a scanning system will not be significant.

It can also be seen that the time between exposures $t_2 - t_1 = \frac{1}{\nu} - \frac{1}{L\nu}(x_1 - x_2)$ depends upon the horizontal distance travelled by the particle between exposures $\Delta x = (x_1 - x_2)$. The horizontal component of motion of the flow field will enlarge or reduce the distance and therefore time that the beam has to travel to arrive back at the same particle for a second exposure

$$\Delta t = \frac{L - \Delta x}{L\nu} \ , \tag{2.25}$$

where Δx is given by,

$$\Delta x = v_x \Delta t \tag{2.26}$$

where v_x is the average velocity of the particle in the time between exposures Δt. Therefore,

$$\Delta t = \frac{1}{\nu(1 + v_x/L\nu)} \tag{2.27}$$

The horizontal and vertical components of velocity are given as,

$$\frac{\Delta x}{\Delta t} = v_x = \frac{\Delta x \nu}{(1 - \Delta x/L)} \tag{2.28}$$

and

$$\frac{\Delta y}{\Delta t} = v_y = \Delta y \nu \left(1 + \frac{\Delta x}{(L - \Delta x)}\right) \tag{2.29}$$

It can be seen that v_x and v_y can be calculated exactly if Δx is known in both magnitude *and* direction. However, the error imposed upon the final velocity measurement if the corrected velocity is not calculated is very small. For a particle displacement of 1.5mm over a horizontal scanning length of 60 cm the magnitude of the error is $< 0.25\%$.

2.3.2 Apparatus

The scanning beam system is implemented using a rotating mirror and a parabolic recollimating mirror. The laser used is a Spectra Physics 171 Argon Ion which has a maximum power of 15 watts. The beam is directed onto the rotating octagonal mirror which reflects the laser beam through an accurately repeatable 90 deg arc. The angular sweep of the beam is then reflected up into the measurement area by the parabolic mirror with the rotating mirror at its focus to produce a constant velocity scanning beam within the measurement area. The rotating mirror is a commercially purchased unit (Lincoln Lasers octagonal mirror) with its relatively slow motor replaced by a low vibration/high speed dc motor (figure 2.11). The rotational speed of the motor and therefore scanning rate is controlled by altering the input voltage and measured using a digital storage oscilloscope receiving a signal from a phototransistor positioned at the end of the parabolic mirror (see figure 2.12).

The parabolic mirror is milled from a solid piece of aluminium and given a highly reflective coating by bonding a long length of perspex that has been front silvered with Aluminium. The silvered surface is generated by evaporation of Aluminium within an evacuated evaporation chamber and produces a reflec-

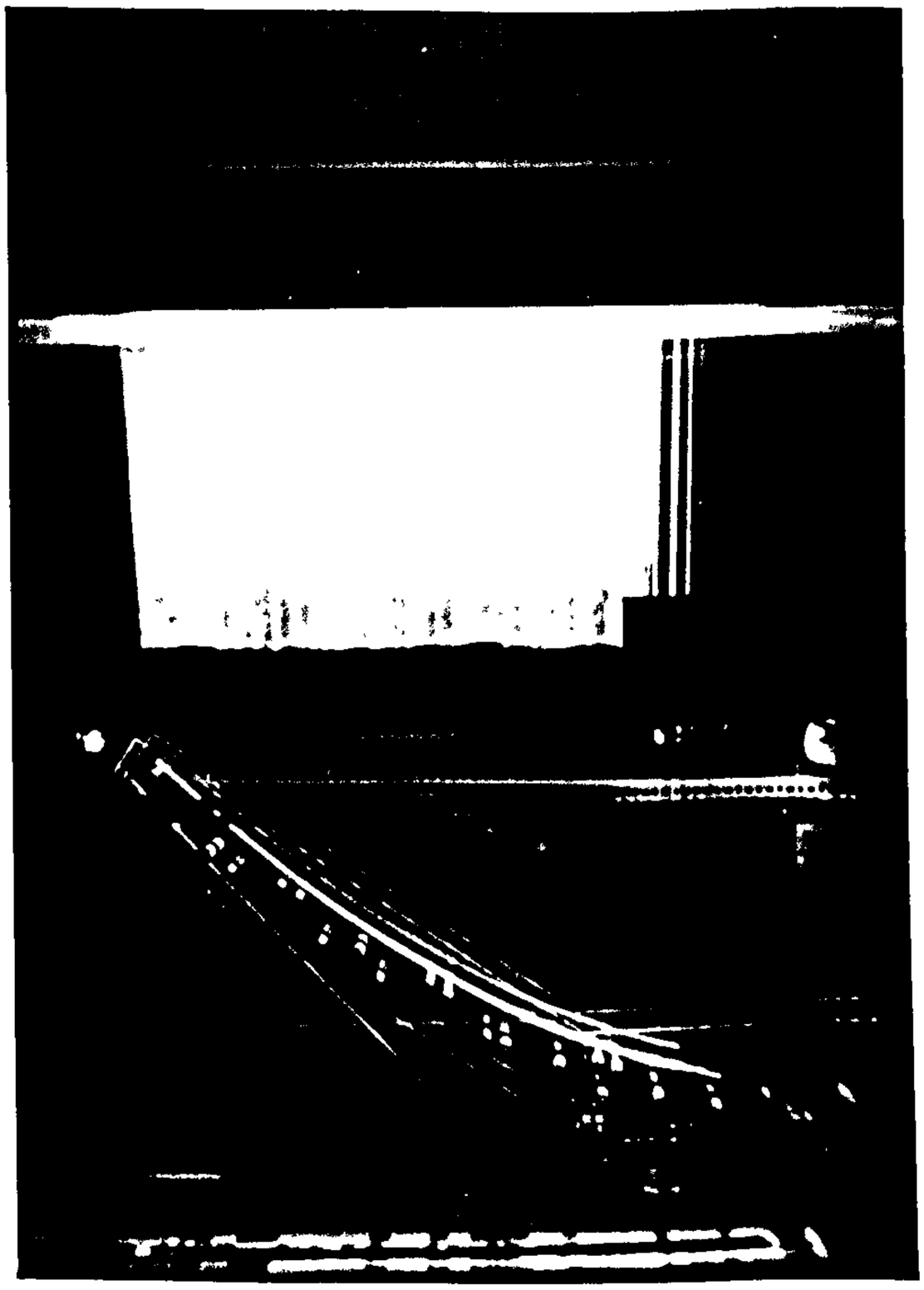

Figure 2.11: Octagonal rotating mirror mounted below the wave tank and at the focus of the parabolic collimating mirror

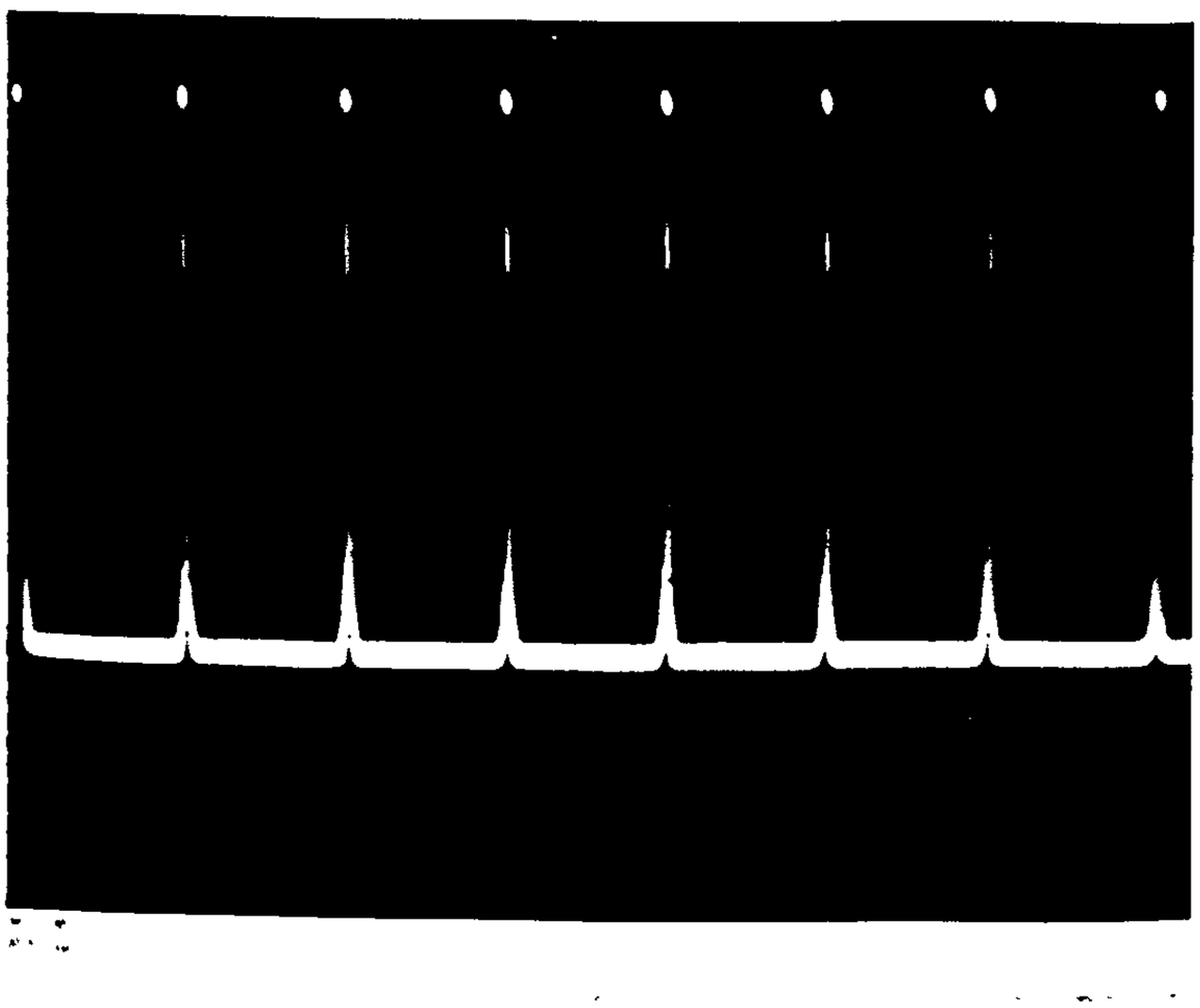

Figure 2.12: Oscilloscope trace showing the phototransistor signal from which the scan rate ν is measured.

tive surface of approximately 91-92% reflectivity for wavelengths of 450-550 nm Kingslake, 1965[76].

2.4 Imaging and Recording

Accurate measurement of particle displacements rely upon precise imaging and recording of the particle positions. The image formed by an ideal lens would be an exact point-by-point reproduction of the object which in our case is a random distribution of tracer particles moving in the plane of a narrow measurement volume (figure 2.1). Deviation of the actual particle image shapes or positions from the ideal are due to diffraction of light at the lens aperture, aberations due to the limitations of lens design and manufacture [76], or errors in lens construction. The precision with which the diffraction and aberation degraded image is recorded is further compromised by the limited spatial frequency response, nonlinearity and noise associated with the recording medium.

PIV measurements are generally performed using a photographic emulsion with either a celluloid backing for most 35mm or 120 formats or glass when a plate camera is used. Photographic recording is used in preference to other media such as thermoplastic films or Video (Vidicon or CCD) as it offers the best compromise between sensitivity, resolution, and cost. However, a fundamental disadvantage associated with photographic recording is the time penalty imposed by the development process. The use of a Video camera would provide the spatial information in a form that can be digitised for processing on computer very quickly but is limited in resolution (typically 512*512 pixels) restricting its use to very small areas. Films such as Kodak Holographic can resolve approx. 1250 line pairs/mm while remaining relatively sensitive. However, short exposure times and limited illumination intensities generally makes the use of more sensitive films necessary. This is not such a limitation as it may seem since modern films such as T-MAX 100/400 provide good sensitivity 100-400 ASA with good resolution 125-200 lines/mm, depending on contrast.

2.4.1 Lens evaluation

The suitability of a lens for recording the positions of point images such as seeding particles is determined by its spread function (the luminance blur associated with the image of a point source) and the overall image distortion (deviation of the geometry of the image compared to the flat object field). The point spread function represents the fundamental limit on the ability of the lens to reproduce fine detail and for high quality lenses is ultimately limited by the effect of diffraction at the lens aperture. The use of larger apertures reduces the effect of diffraction and for a perfect lens will result in a smaller point source image. However, the limitations of the optical components become significant in the non-axial regions of the lens used at small f nos. and aberations will begin to distort and widen the Point Spread Function (PSF). A comprehensive overview of procedures used to test objectives such as camera lenses is given by Shannon, 1969[76] where the effect of chromatic, astigmatic and spherical abberations on the point response of a lens are illustrated and techniques capable of identifying them described. A detailed analysis of the effect of lens aberations is not taken on here but it is important to recognise that lens aberations will compromise the accuracy of velocity measurements made with PIV.

Particle imaging considerations

The accuracy with which the separation of a particle image pair can be measured is limited by the size of the particle images themselves. In general the position of a large particle image is less precisely measurable than that of a small image. It is important therefore that the imaging lens system and photographic emulsion used to record the particle positions is capable of resolving particles that are small enough to be consistent with the desired accuracy. Diffraction at the lens aperture and aberations associated with the lens will tend to spread small features of the image over a larger area. The level of aberations present in the image of a given lens will tend to be a function of its cost. Sophisticated design

and manufacturing processes are capable of producing optical components that are very nearly diffraction limited and so the lens aperture represents the most fundamental limit on the resolving power of an optical imaging system.

The Optical transfer function (OTF) is a complex weighting factor applied by the lens system to the spatial frequencies present in the object plane and decreases to zero, past a limiting frequency, beyond which the lens does not transfer any information. This is consistent with the blurring of small image detail as higher spatial frequencies required to form sharp edges in the image plane are lost due to the upper limit of the OTF. The decreasing response of the lens system used for the measurements described in Chapter 6 is shown in figure 2.13. This shows the Modulation Transfer Factor, which is the magnitude of the OTF, for three different spatial frequencies across the image plane [6] and shows a clear decrease in the response of the lens to higher spatial frequencies. The effect of limited frequency response of a lens in the imaging of small point sources such as seeding particles can be more easily seen by considering the point spread function (PSF) which is the Fourier transform of the OTF and represents the response of the imaging system to a point source in the object plane (ie. impulse response),

$$\mathcal{T}(k_x, k_y) = \mathcal{F}(\mathcal{S}(x, y)) \tag{2.30}$$

where $\mathcal{T}(k_x, k_y)$ is the OTF of the lens system, $\mathcal{S}(x, y)$ is the point spread function and $\mathcal{F}$ represents a Fourier transform.

For a diffraction limited lens with a circular aperture the PSF is the Airy intensity distribution,

$$I(r) \propto \left(\frac{J_1\left(\frac{2\pi a r}{\lambda f}\right)}{r} \right)^2 \tag{2.31}$$

where $I(r)$ is the intensity a distance r from the centre of the image of a point source. J_1 is a first order Bessel funcion, f is the focal length of the lens, λ the wavelength of light and a the radius of the lens aperture.

For a point source in the object plane the intensity distribution in the image plane of a diffraction limited lens will be similar to that represented in figure

[6] The MTF is shown to vary with image height ie. distance from the image centre.

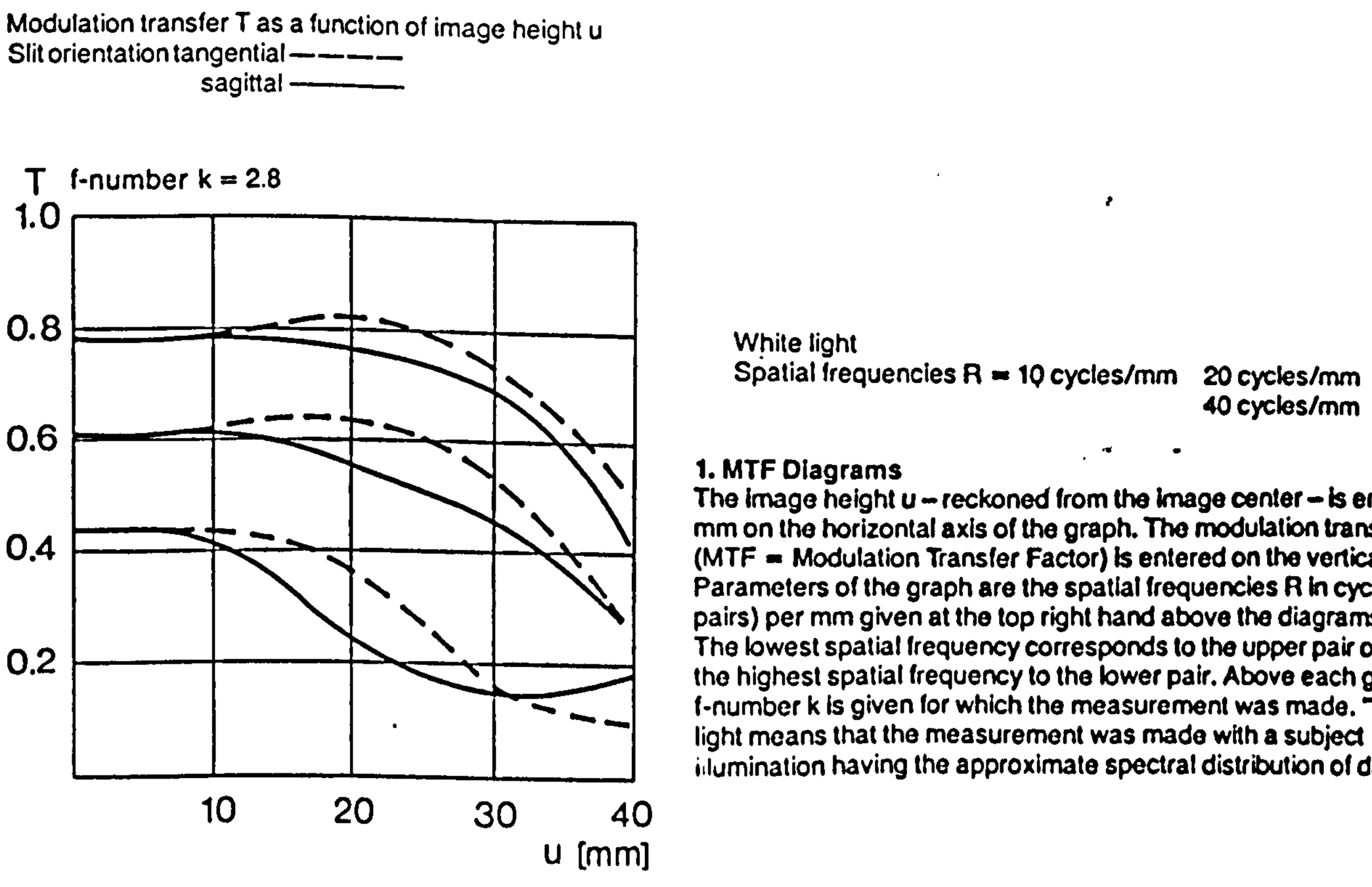

Figure 2.13: Modulation transfer function for Zeiss Planar T* f2.8 80mm lens

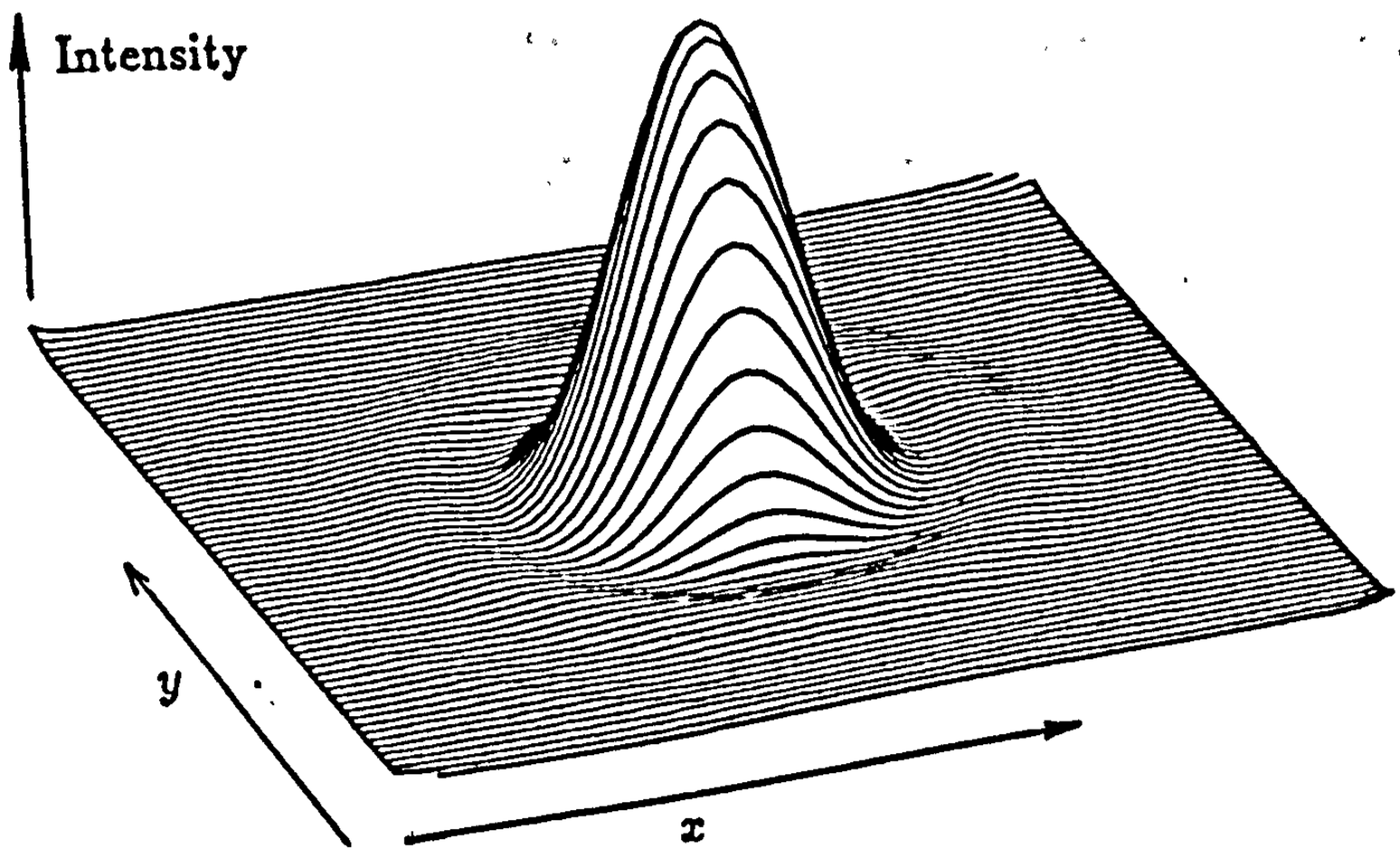

Figure 2.14: Airy intensity distribution or point spread function for a diffraction limited lens

2.14 where 95% of the image resides within the central spot. Therefore, it is reasonable to consider the radius of the diffraction spread function to be the distance between the centre and the first minimum. This occurs when the argument of the Bessel function= 3.832. For a diffraction limited imaging system operating with a magnifcation M the diameter of the diffraction spot d_d is given by[7],

$$d_d = 2.44(1+M)f\#\lambda \tag{2.32}$$

where $f\# = f/a$ is the f number of the lens.

Any real image, which can be considered to consists of a large collection of point sources of light, will be the ideal image convolved with the Point spread function. The particles used to seed the flow are small and so the PSF will affect the final image relatively more than the imaging of a larger object. This will enlarge the imaged particle and the diameter of a particle image can be approximated by[7],

$$d_e = \sqrt{M^2 d_p^2 + d_d^2} \tag{2.33}$$

where d_p is the particle diameter.

Smaller seeding particles will begin to closely represent point sources of light and consequently reducing the size of the seeding much past the dimensions of the PSF will not reduce the diameter of the image but will only reduce the average intensity of the image.

Image field distortion

The illuminated region over which velocity measurements are made consists of a thin *slab* within which the seeding particles are imaged using a lens with a depth of field that extends through the thickness of the measuring volume. The recorded image from such a set-up should ideally be related to the measurement area by a scale factor M which is the magnification of the recording optics. In practice the relationship between object and image is complicated by distortion.

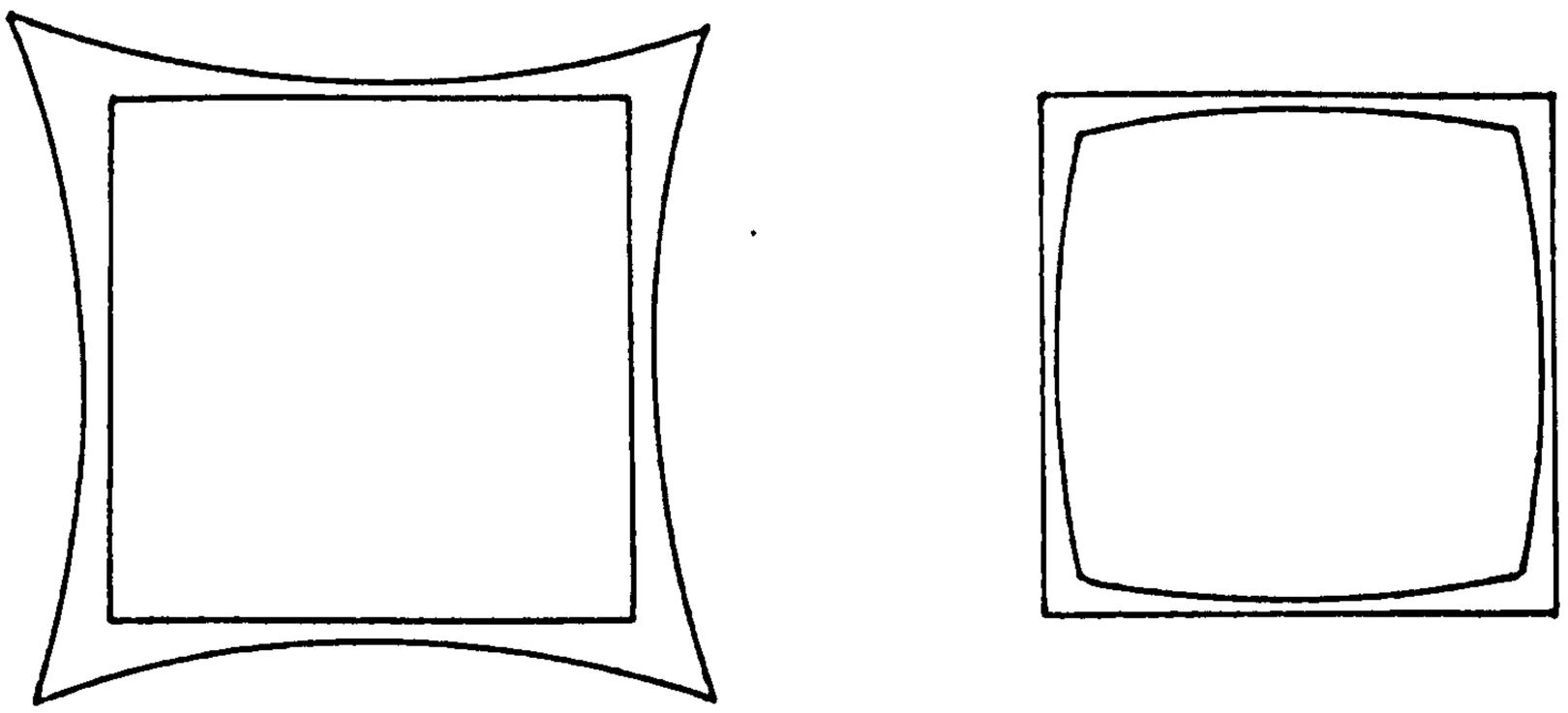

Figure 2.15: Image distortion,left, positive *pincushion*, right, negative *barrel*

If one considers a light beam entering a lens obliquely from an object point to one side of the lens axis the principal ray of the beam will pass through the image plane at height H' (where image height is defined as distance from the optical axis). For an imperfect lens this will differ from the ideal image height H'_0. The difference between H' and H'_0 is a measure of distortion usually given as a percentage of H'_0 and is often expressed as a power series.

$$H' - H'_0 = aH'^3_0 + bH'^5_0 + \cdots \tag{2.34}$$

A positive value of distortion leads to an image of a square that is pincushion shaped and everywhere too large, whereas negative distortion produces a barrel shape which is everywhere too small (figure 2.15).

Point measurements made from a film which exhibits distortion will not correspond to the desired point if it is assumed that M relates image and object fields. If the precise nature of the distortion is known then a scheme to relate point measurements from the film to exact points within the measurement area can be devised. This will considerably complicate the analysis of PIV records and a more acceptable solution to the problem is to use a lens which has a low enough level of distortion that the mismatch between image/object points can be neglected.

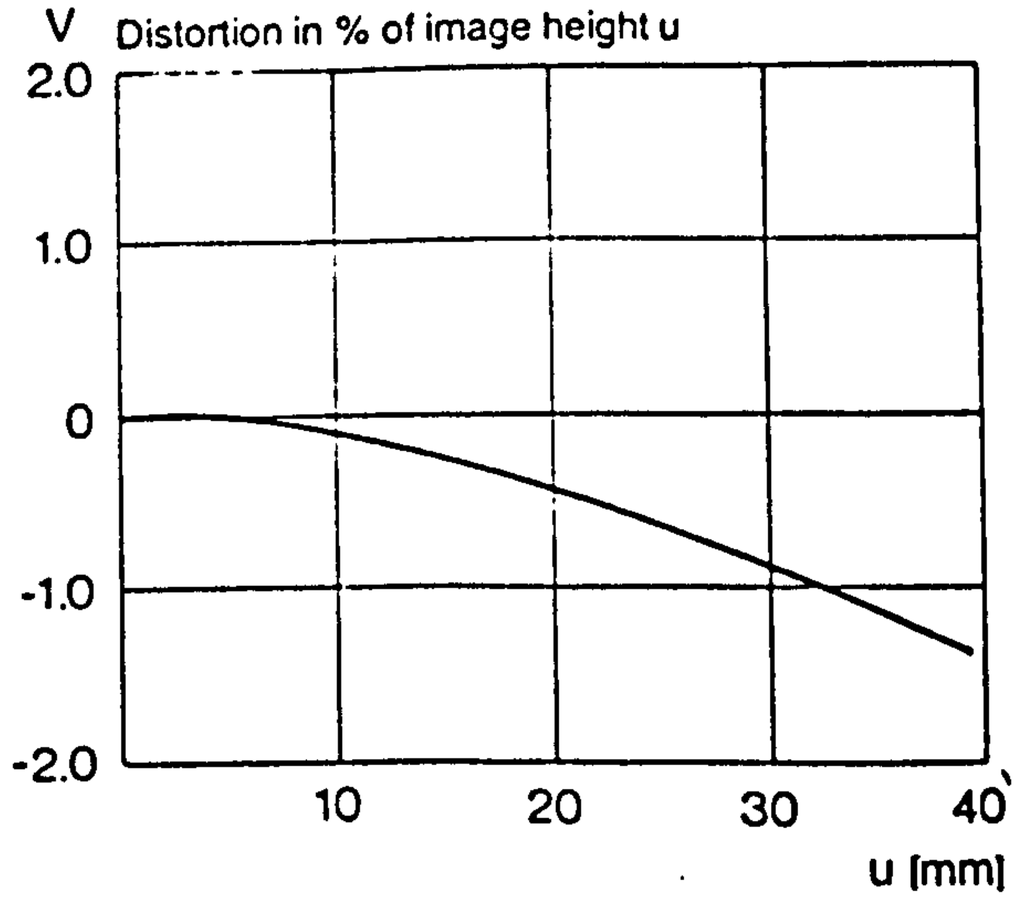

3. Distortion
Here again the image height u is entered on the horizontal axis in mm. The vertical axis gives the distortion V in % of the relevant image height. A positive value for V means that the actual image point is further from the image center than with perfectly distortion-free imaging (pincushion distortion); a negative V indicates barrel distortion.

Figure 2.16: Distortion in % of image height

The measurements described in Chapter 6 were made using a *Zeiss Planar T** f2.8, 80mm lens. Figure 2.16 shows the distortion in % of image height[3] and shows that the furthermost corners of the image plane for a 120 negative size is approximately -1.5% of the image height ie. 39.95mm*-1.5%=-0.6mm. The % distortion reduces smoothly to zero at the centre of the image so, for central regions of the image the positional accuracy can be good enough for all but very high accuracy measurements. This lens also has an extremely flat image field which avoids loss of focus at the outer regions of the image.

2.4.2 Recording medium

The photographic emulsion used to make the wave measurements was T-MAX 100[1] on a 120 film format (56.5*56.5 mm^2). This modern film is characterised by its good sensitivity (100 ASA) and resolution (200 lines/mm at 1:1000 contrast)[1] and as such is highly suited as a recording medium for PIV measurements where high resolution is required for precise recording of imaged particles and good sensitivity required to ensure that images are successfully recorded despite low image intensities and short exposure times.

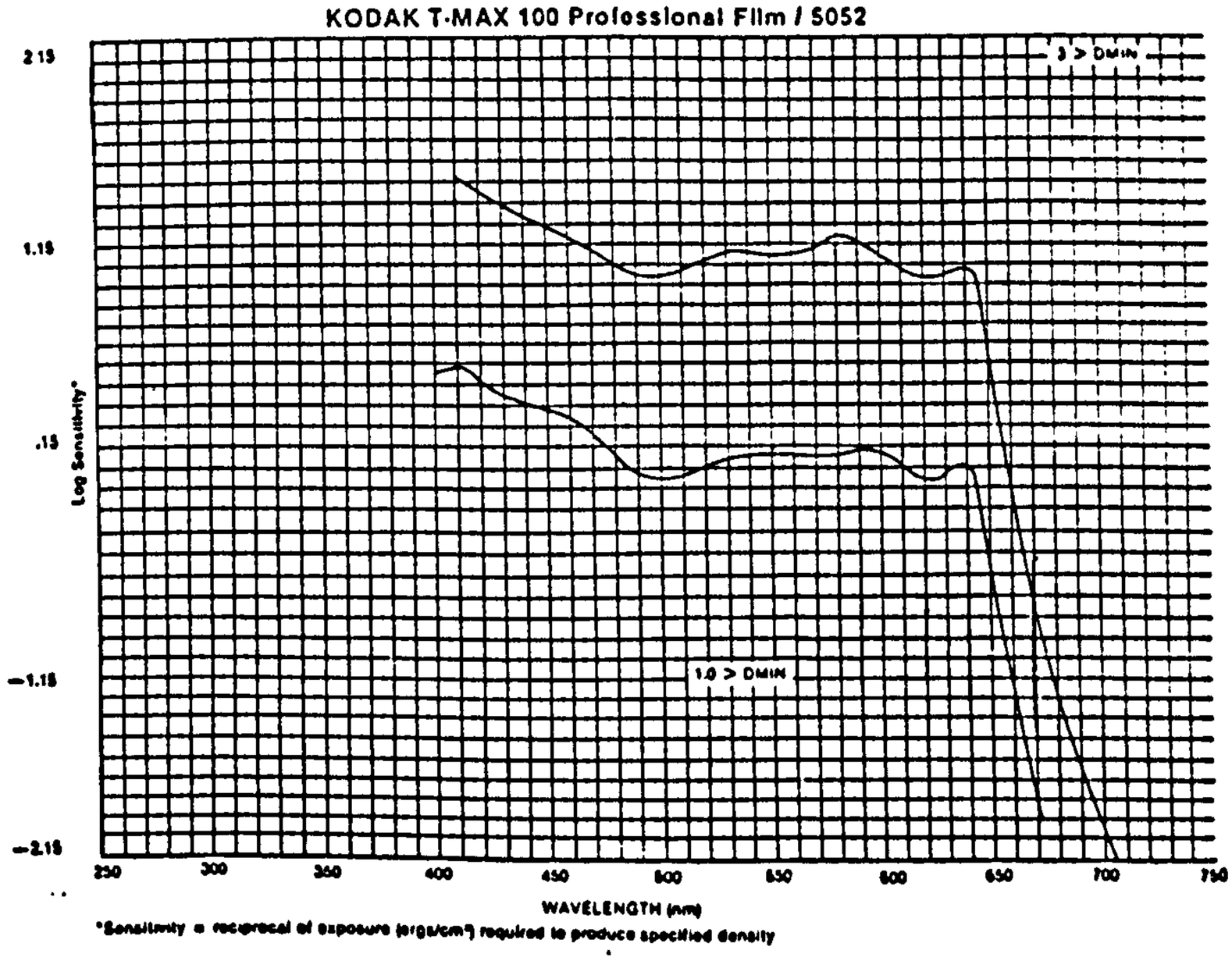

Figure 2.17: Spectral sensitivity of T-MAX 100 emulsion (Taken from Kodak T-MAX technical specifications).

Emulsion sensitivity

The Argon Ion laser used for illumination in the scanning system described above has a maximum useable power output of 15 Watts over 8 lines from 514.5 nm-457.9nm. Figure 2.17 shows this to be well within the main region of spectral sensitivity of the emulsion. As mentioned earlier in this chapter it is difficult to calculate the scattering efficiency of the randomly shaped and sized pollen grains so the illumination intensity required to give well recorded particle images was found experimentally by exposing a number of frames at different illumination intensities and then inspecting the developed images under a microscope to determine the particle images with the best contrast. It should be noted here that the correct illumination intensity for successfull recording of images also depends upon the scanning rate of the illumination system and the image object magnification. Thus, for different configurations of these two variables it is

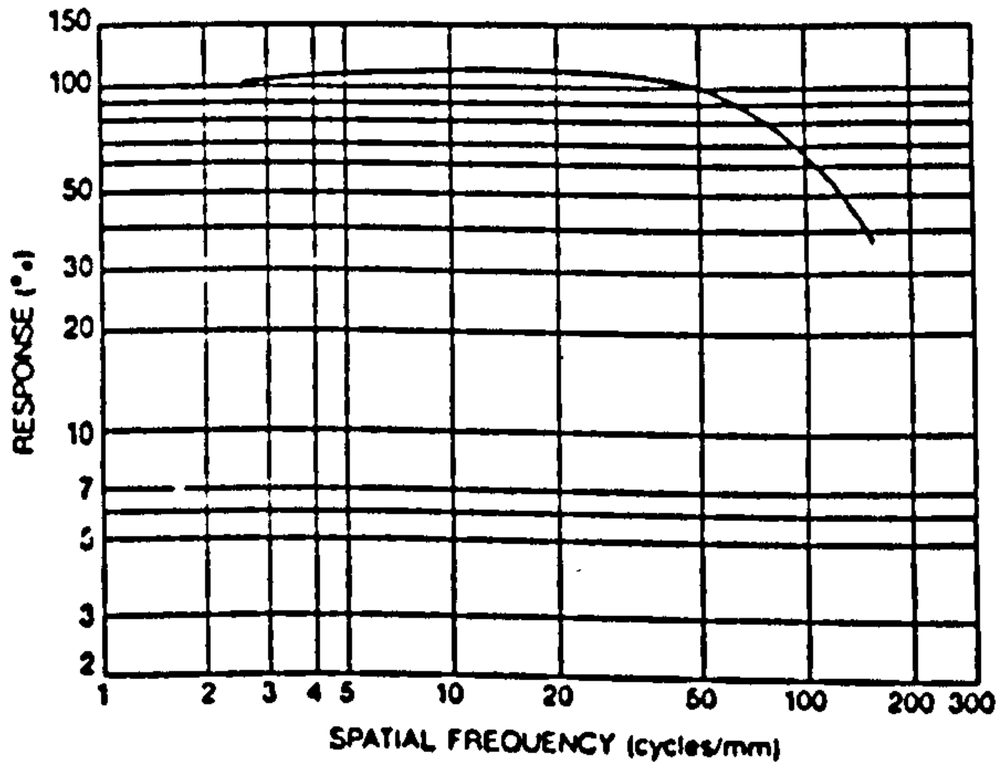

Figure 2.18: Modulation Transfer Function for T-MAX 100 (taken from Kodak data sheet).

neccessary to adjust the illumination intensity to account for variation in these parameters.

Spatial resolution

The exact spatial resolution of the film differs for different image contrasts, the limit being somewhere about 200 lines/mm for contrasts above 1:1000. It can be seen from the film MTF shown in figure 2.18 that like the lens there is an upper limit on the detail that is resolvable and which will produce an impulse response function similar to that exhibited by the lens. It is important therefore to consider the effects of the limited resolution of the lens/emulsion combination. It has been proposed [9] that an approximate value for the recorded

image diameter may be calculated from,

$$d_l \approx (M^2 d_p^2 + d_d^2 + d_r^2)^{1/2} \tag{2.35}$$

where d_r is the diameter of the point spread function of the emulsion and may be approximated by the width of a line that is just resolved (i.e. $1/200mm = 5\mu m$). This is an approximate relationship and the contrast dependant resolution of the emulsion will tend to broaden particle images further.

Adjacency effects

A further limiting factor on the accuracy with which partical images may be recorded is due to adjacency effects. Adjacency effects arise due to uneven development of the latent image stored on the exposed emulsion and is caused by the development inhibiting agents produced as the developer becomes "spent" or used up. Obviously, developer will become exhausted more rapidly in regions of the latent image that have been highly exposed and if new developer does not diffuse into these regions development will slow down compared to those regions of image that are close to low-exposure regions of film. It can be seen from figure 2.19 that in the case of two closely situated particle images the region between the images has strong development followed by less rapid development as developer is consumed. The outside edges of the two images are close to regions of low development and so will continue developing at a greater rate. The net result of uneven development in this particular situation would be to cause an apparent drift of the particle image centres away from each other as strong development on the outside of the pair produces more silver grains and therefore greater photographic density. The obvious solution to this problem is to ensure that the developing solution is constantly in motion about the film which can be This is achieved by constant agitation of the developing tank during development. This speeds up the overall development of the film and so has to be compensated for with a slight reduction in the total development time. Normal procedure is, repeated inversion of the tank for 5 seconds every 30 seconds for 8 minutes with the developer at 20deg C. Experience has shown

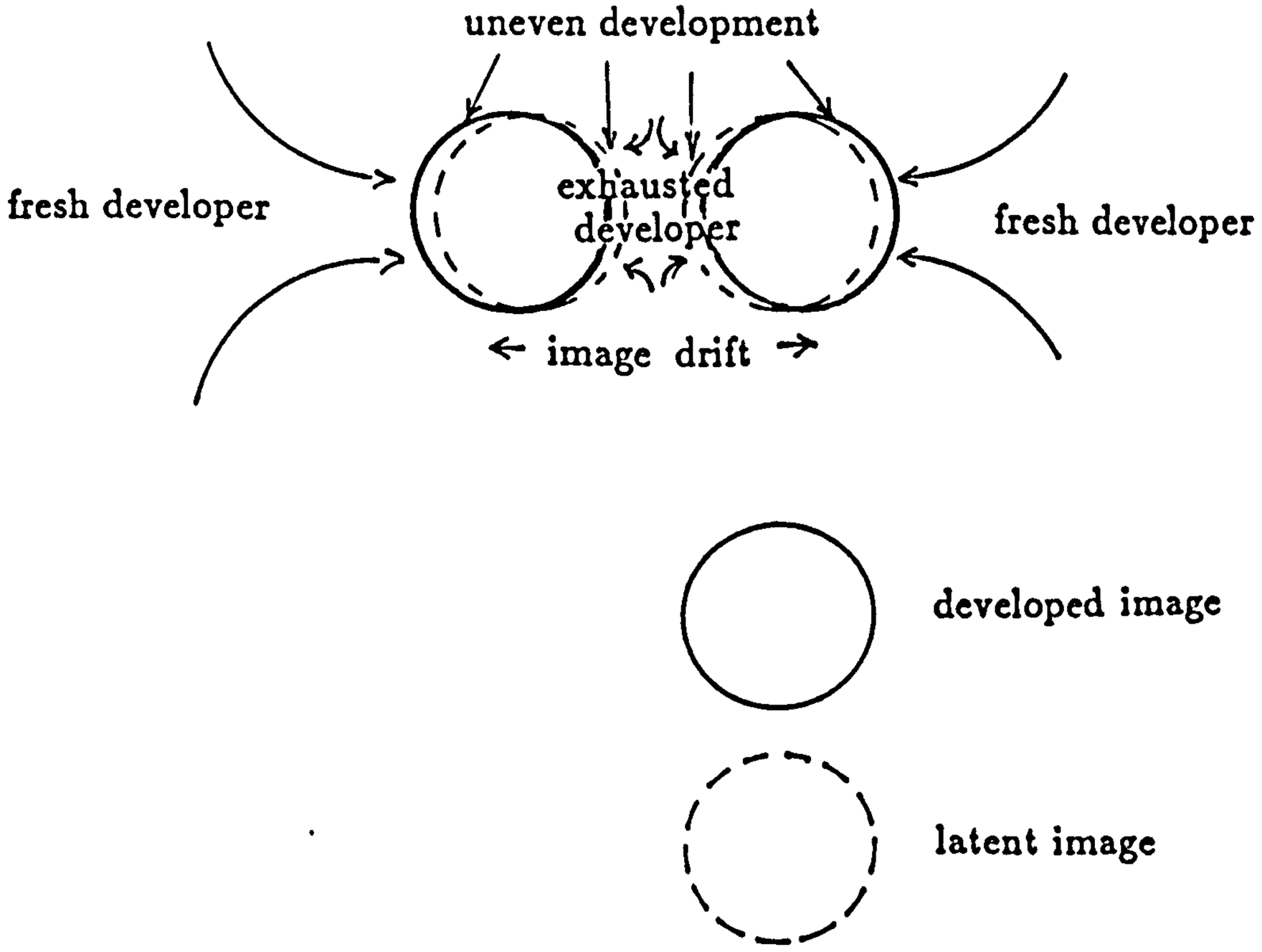

Figure 2.19: Uneven development due to adjacency effects influence the shape and therefore position of the image centre.

that a reduction of ≈60 seconds produces a similar development if the tank is constantly agitated.

In regions of film with a high particle image concentration it is possible that adjacency effects may introduce significant random errors. However, without an in-depth study of this effect it is difficult to estimate the importance of such errors. Additionally, there will be a distortion of the particle images on a microscopic scale due to the finite size and random positions of the silver grains that constitute the particle images. Effects such as these are fundamental and will ultimately lead to an accumulated random error in the precision with which the particle positions are recorded on the film. Further research in this area is required to determine the relative influence of these and other possible limitations of the photographic recording process.

2.4.3 Refraction effects

A further source of image distortion which is not associated with the lens is that due to the refraction of light at the fluid/glass/air boundaries when the fluid has a different refractive index to air. This will cause the recorded position of a particle to differ from its real position (see figure 2.20).

For particles away from the centre of the measurement area the shortest optical path length is not a straight line. Thus scattered light entering the camera lens from this off-axis region will appear to come from a point that is further from the centre of the flow field. For a small field of view such that $\theta_0 \approx \sin\theta_0 \approx \tan\theta_0$ the difference between the recorded image position and the image of the same point without distortion can be approximated as,

$$x_i' - x_i \approx x_i \left(\frac{d_0}{d_3 + d_2 \frac{n_a}{n_g} + d_1 \frac{n_a}{n_w}} - 1 \right) \tag{2.36}$$

where the *true* image height is given by x_i and the distorted image height by x_i'. Therefore, for the approximate expression above, the distorted image will differ

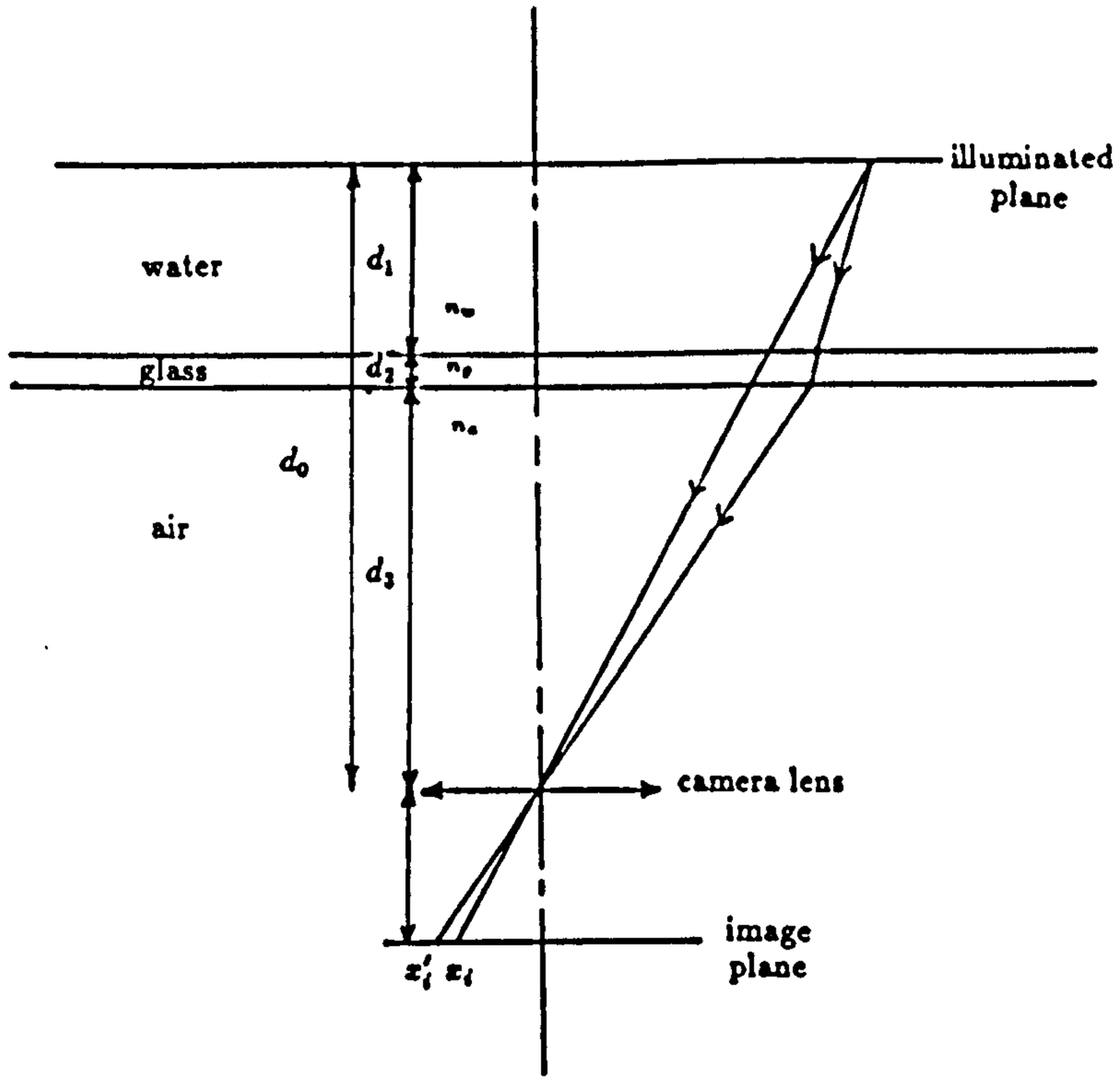

Figure 2.20: Ray path for refraction through fluid/glass/air interface

from an undistorted image by a constant factor ie. a magnification. This is true only for paraxial regions of the object plane. For regions that are imaged well off axis the distortion becomes progressively more positive producing pincusion distortion. An exact expression for the effect of refraction at the water/glass/air boundaries is less simple but has been calculated for a typical field of view used in the recording of the flow field under a wave and is shown in figure 2.22.

Verification of the above analysis was performed by photographing a flat perspex sheet positioned in the wave flume in the same position as the laser illumination. The same sheet was then photographed outside the tank the same distance away from the film plane of the camera. A number of vertical and horizontal lines etched onto the perspex prior to photographing the sheet were then accurately measured from the films using a travelling microscope and the two sets of coordinates compared (figure 2.21). The radial distance (image height) of a number of corresponding points from the two photographs were then compared and the difference plotted as a percentage of the out-of-the water *undistorted* image height. Figure 2.22 shows the measured distortion due to the refraction effects as a magnification which progressively increases in the outer regions of

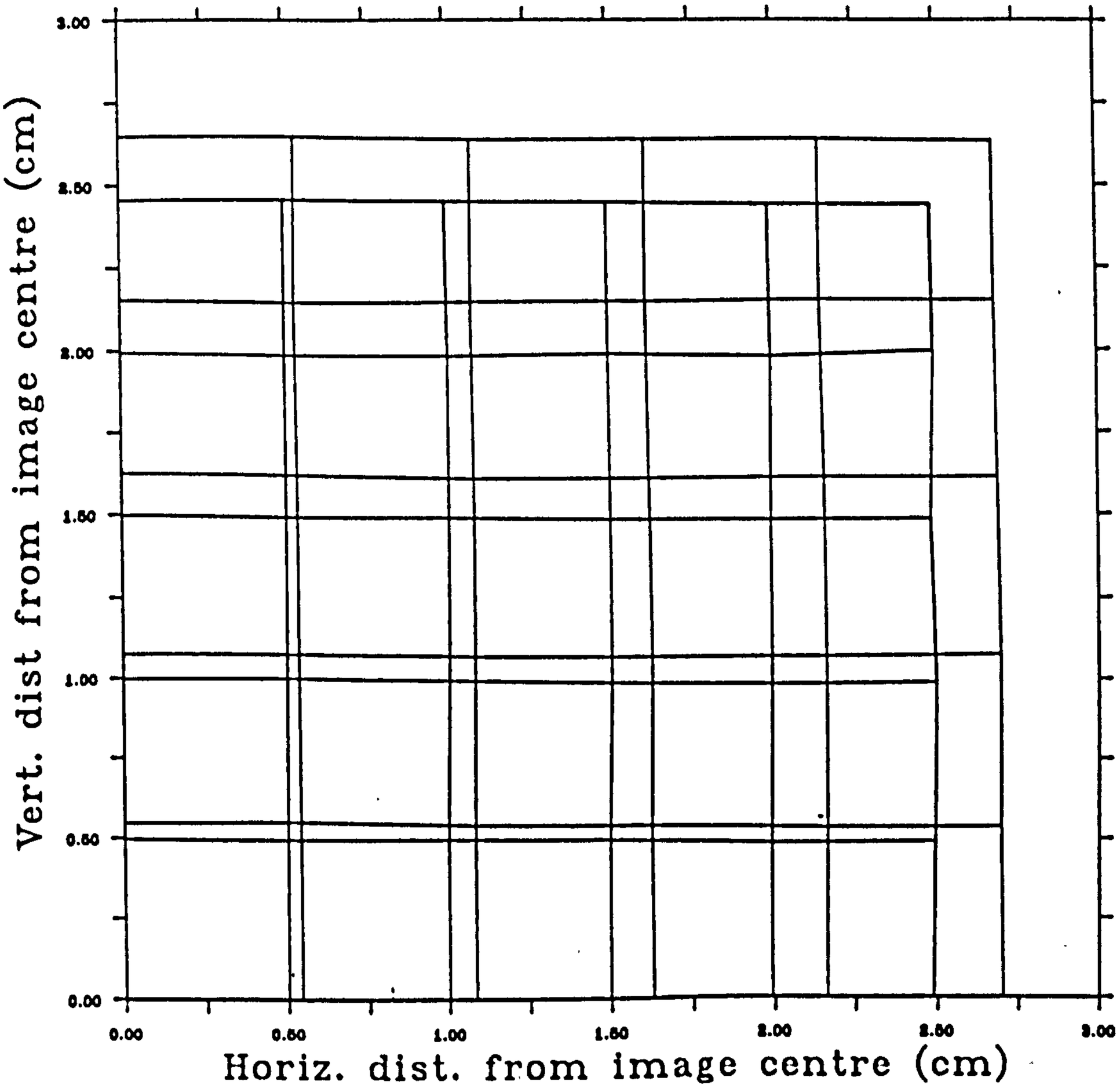

Figure 2.21: crossing points of photographed grid, in tank (large grid) and out of tank (small grid)

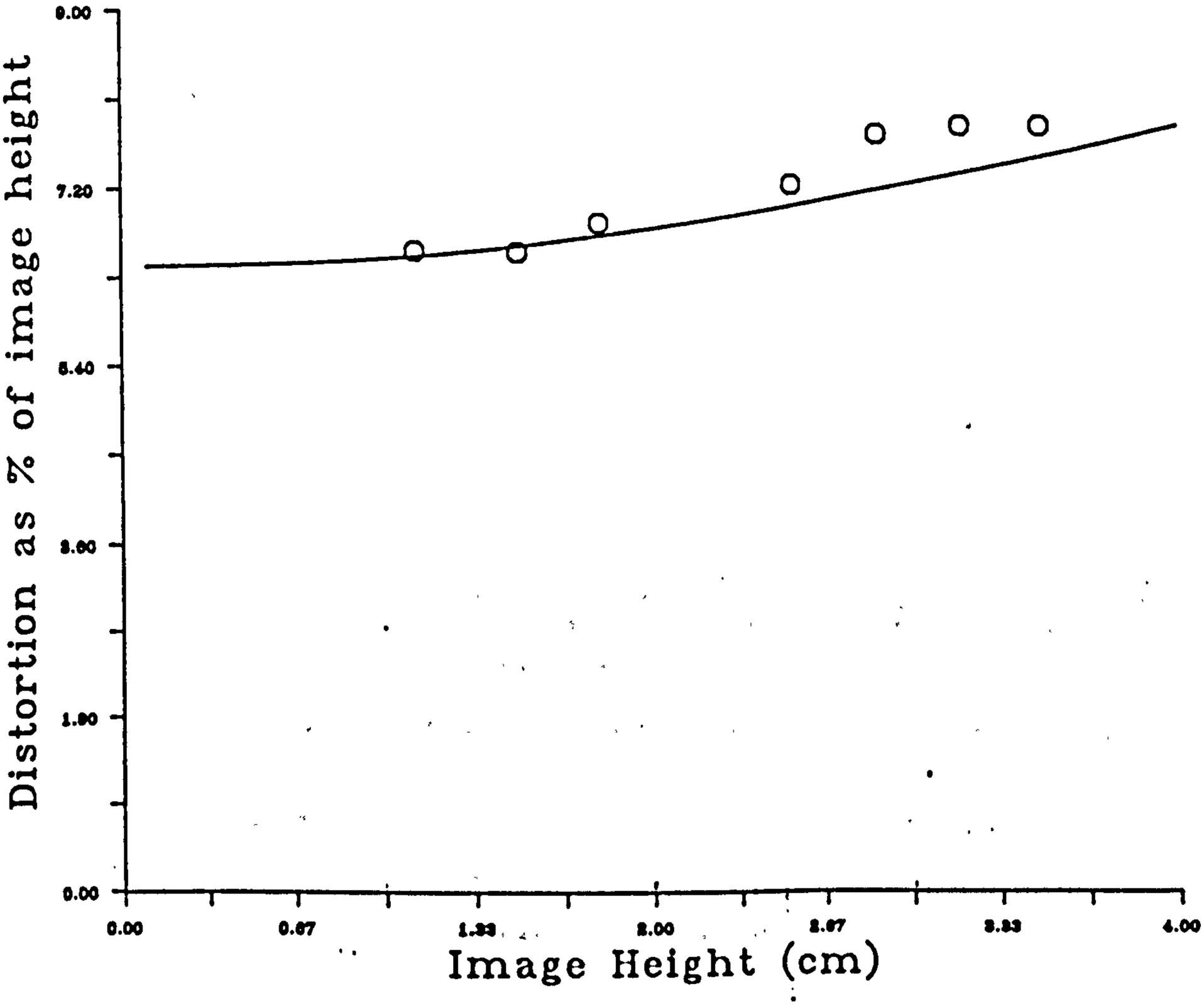

Figure 2.22: % distortion of the flow field image due to refraction effects calculated (line) and measured (points)

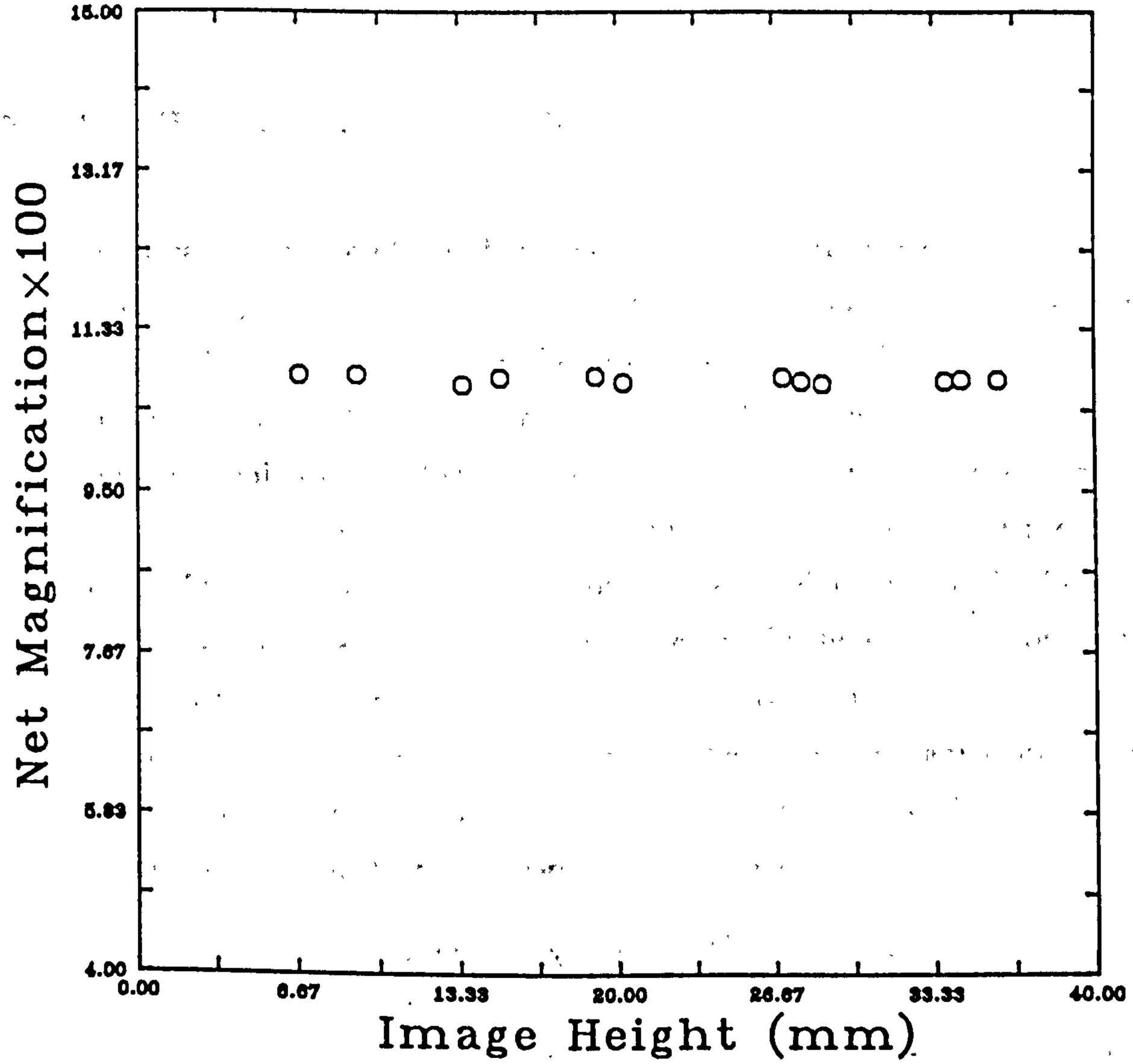

Figure 2.23: Measured magnification across the image plane.

the image as predicted. For most applications this effect can be assumed to constitute a constant magnification. For high precision measurements however, it may be desirable to compensate for this effect.

The influence of the combined lens distortion and distortion due to refractive effects is shown in figure 2.23. The measurements suggest that little distortion is present across the image. Conveniently, the distortion due to refraction effects is opposite in sign and similar in magnitude to the distortion inherent in the camera lens. The resulting distortion of the system is extremely small and if the mean of the measured values is taken as M the standard deviation is only 0.3% of this value.

2.4.4 Three-dimensional flow fields

The photographic image of the flow field used in PIV measurements is a two-dimensional image and as such can only contain two components of displacement information. In most applications the flow is assumed to be two-dimensional with the two components of velocity in the plane of the illumination and image. Three-dimensionality of the flow will, in extreme cases, result in particles leaving the measurement volume and so no displacement information will be present at that point of the negative. For smaller out-of-plane velocities the third component of displacement can generate significant errors in the evaluation of the two in-plane components. Particles that are imaged away from the centre of the film plane result in out-of-plane motion being recorded as an in plane displacement [116]. The measured displacements Δx_m, Δy_m are related to the real particle displacements Δx, Δy, Δz for a magnification M by

$$\Delta x_m = -M(x + \Delta x)(1 + \frac{\Delta z}{d_0 - \Delta z}) + Mx \tag{2.37}$$

$$\Delta y_m = -M(y + \Delta y)(1 + \frac{\Delta z}{d_0 - \Delta z}) + My \tag{2.38}$$

where d_0 is the distance from the illuminated flow field to the lens and x,y are the coordinates of the particle positions relative to the intersection of the optical axis of the camera lens and the measurement plane (see figure 2.24).

By substituting some typical values for the variables in the expressions above it is possible to illustrate the magnitude of this effect. For $M = 0.1$, $y = 250mm$, $\Delta y = 1.5mm$, $\Delta z = 1.0mm$, $d_0 = 900mm$, $x = 250mm$ and $\Delta x = 1.5mm$ the measured values of Δx_m and Δy_m are both $0.1779mm$. Thus an error of $\approx$20% is introduced into the measurements of the particle displacements due to an out-of-plane component of velocity of similar magnitude to the in-plane components.

A solution to this problem is to record the flow from two different positions and using trigonometry resolve the third component of motion from the two different sets of measurements[116]. Alternatively, the influence of out-of-plane motion

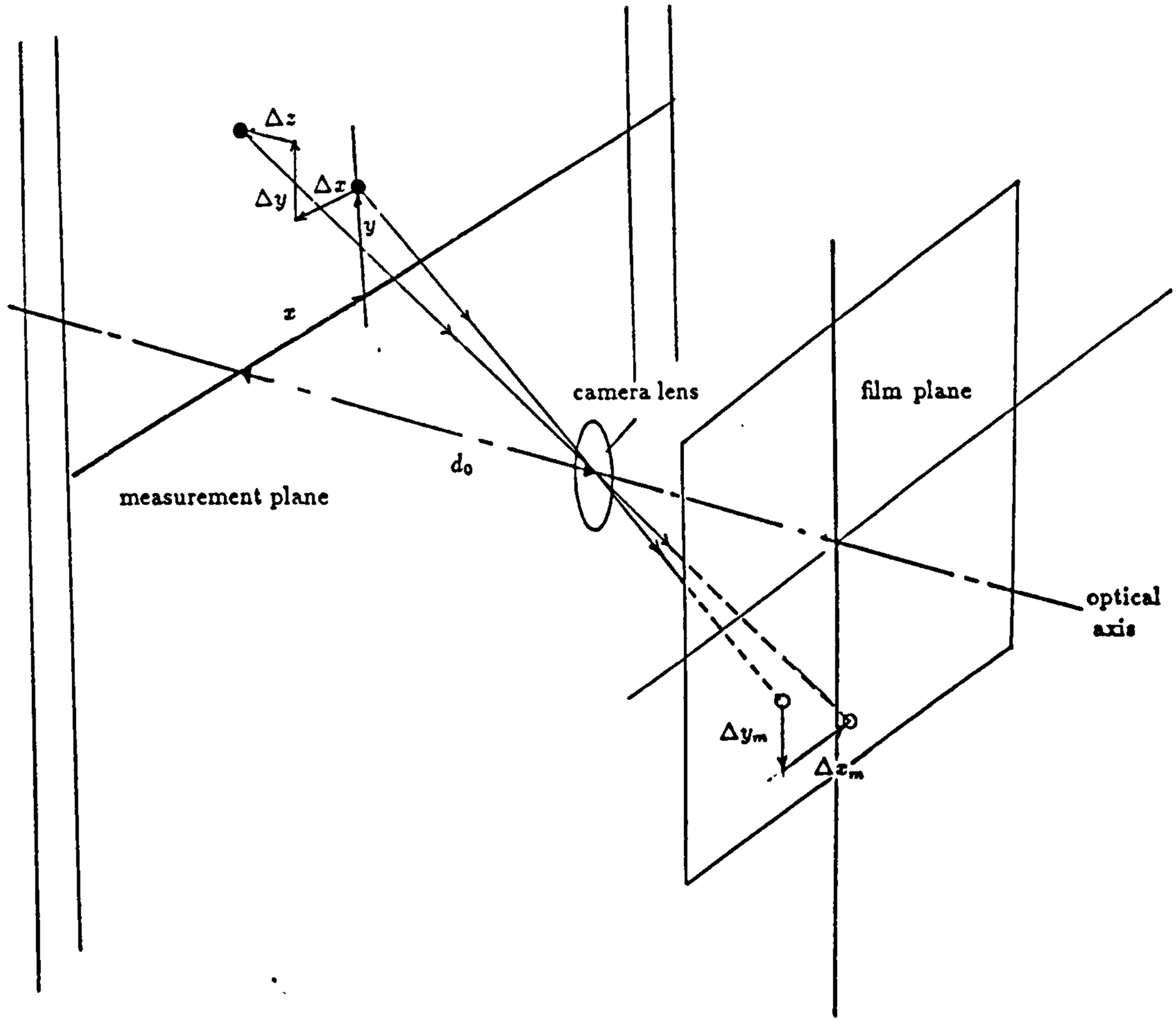

Figure 2.24: Two-dimensional imaging of three components of motion resulting in a systematic error in the measurement of the two in-plane components from the negative.

can be minimised by ensuring that the out-of-plane motion is small, reducing the thickness of the light sheet or limiting the field of view of the camera.

Chapter 3

Flow photograph analysis

Evaluation of PIV negatives involves measurement of particle image displacements over the complete area of flow recorded on the film. This represents a complex and tedious task if it were to be performed manually and consequently much of the research effort in PIV has been directed towards the development of automated film analysis systems [87,66,90,64,7].

This chapter describes one such system for automatic evaluation of two components of velocity over the area of a flow negative. The mean particle displacement within a small local region of the negative is reliably determined from the 2-dimensional autocorrelation of the photograhic density distribution over that area. The autocorrelation and the Young's fringe intensity pattern are Fourier transform pairs and this relationship is utilised to efficiently calculate the autocorrelation function. Young's fringes are detected using a CCD array camera and digitised rapidly using a real time image digitiser interfaced to a microcomputer which also performs the analysis of the fringe data. A Fast Fourier transform algorithm is used to transform the fringes to the autocorrelation plane where the mean particle image displacement can be detected with maximum immunity from noise. Measurements are made at discrete points on a regular grid over the whole film. This is achieved by transportation of the film relative to the probe laser beam by two orthogonally mounted microtranslation units. The resulting array of velocity data is then output either to the computer screen for inspection

or to a file where it can be further analysed or transferred to a plotter.

3.1 Theory

Measurement of particle displacement, and therefore velocity, from a typical high image density PIV negative is complicated by the dense random distribution of particle image pairs that contain the velocity information. Within small local regions of the negative, over which the fluid velocity is approximately constant, the recorded flow will consist of two similar but displaced random patterns of resolved particle images. Measurement of the mean displacement between these two separated sets of images is most reliably determined by autocorrelation of the local particle image distribution, where the autocorrelation $R(s)$ is given by,

$$R(s) = \int g(r)g(r+s)dr \tag{3.39}$$

and $g(r)$ is the 2-D pattern of images on the flow negative. Integration is over the area of the circular probe beam. This could be achieved by digitising small regions of the flow negative and performing the above operation numerically. A more efficient method however, is to employ the Autocorrelation theorem (Wiener-Khinchin relation) which relates the autocorrelation of a signal to its power spectrum by Fourier transform [22].

$$R(s) = \mathcal{F}.\mathcal{T}.[I(k)] \tag{3.40}$$

where $\mathcal{F}.\mathcal{T}.$ represents a Fourier transform and $I(k)$ is the power spectrum, which in the case of a PIV negative can be obtained optically as the Youngs fringe pattern discussed in previous chapters. The optical arrangement for achieving this is shown in Appendix A and utilises the Fourier transforming properties of a converging lens. With the PIV negative in front of the lens, illuminated by a narrow collimated beam of spatially coherent, monochromatic light, the intensity pattern in the back focal plane of the lens will be proportional to the power spectrum of the illuminated region of film. Neglecting speckle noise and assuming all particles to be identical the intensity distribution of the Youngs fringe pattern will be given by (see appendix A),

$$I(k) = S(k)\sum_{l=1}^{N}\{1+\cos(kd_l)\} \tag{3.41}$$

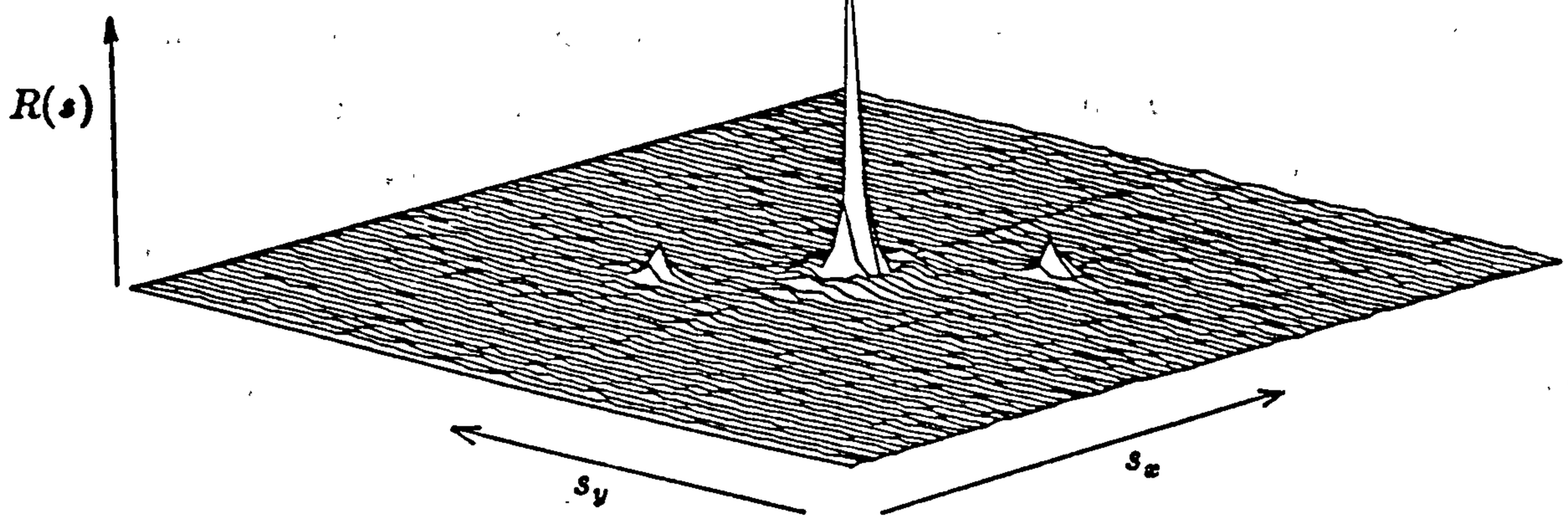

Figure 3.1: Two-dimensional autocorrelation function $R(s)$ calculated from a Youngs fringe intensity pattern.

where $k = \frac{2\pi r_f}{f\lambda}$, f is the focal length of the Fourier transform lens, λ is the wavelength of the probe laser beam, r_f is the position in the Fourier plane and N is the number of complete particle image pairs within the probe area. $S(k)$ is the diffraction halo that results from a single particle image and d_l is the separation of the l^{th} particle image pair. ie.

$$S(k) = \mid \mathcal{F}.\mathcal{T}.[h(r)]\mid^2 \tag{3.42}$$

where $h(r)$ is a particle image. Calculating the Fourier transform of $I(k)$ then gives,

$$R(s) = H(s) * \left[N\delta(s) + \frac{1}{2}\sum_{l=1}^{N}[\delta(s+d_l) + \delta(s-d_l)]\right] \tag{3.43}$$

where $\oplus$ and $*$ represent autocorrelation and convolution operators respectively and $H(s) = [h(s) \oplus h(s)]$. Thus, neglecting a noise term due to the random particle positions within the measurement area and a slowly varying background function due to the finite interrogation diameter, the function $R(s)$ consists of three components (see figure 3.1)

$$R_c(s) = NH(s) * \delta(s) \tag{3.44}$$

$$R_{d+}(s) = \frac{1}{2}H(s) * \sum_{l=1}^{N} \delta(s - d_l) \tag{3.45}$$

$$R_{d-}(s) = \frac{1}{2}H(s) * \sum_{l=1}^{N} \delta(s + d_l) \tag{3.46}$$

R_c is the sum of the autocorrelation of each particle image with itself. R_{d+} and R_{d-} are symmetricaly positioned peaks about the centre peak R_c and result from the correlation across the the interrogation region about the mean displacement. The presence of two identical peaks is due to the 180 degree directional ambiguity inherant in PIV records of this sort. Various techniques to resolve this ambiguity have been proposed and are discussed in Chapter1. For analysis purposes however, either peak can be considered as they both contain identical information.

If the particle image pairs within the probe region are all uniformly displaced from each other the signal peaks R_{d+}, R_{d-} will be similar to R_c but half the height and centred on $s = +d$ and $s = -d$, where d is proportional to the separation of the particle images. In most situations however, the small but finite probe area will encompass a small range of particle displacements due to turbulence and/or velocity gradients. Figure 3.2 illustrates this situation in 1 dimension and shows that the position of the peak will, in general, not correspond to the mean particle displacement within the probe region. It is shown below that the mean particle displacement is actually given by the position of the centroid of R_{d+}.

If one considers a function $f(s)$, that represents a signal distribution similar to R_{s+}, then its zeroeth and first moments m_0 and m_1 are given as,

$$m_0 = \int f(s)ds \tag{3.47}$$

$$m_1 = \int sf(s)ds \tag{3.48}$$

and its mean,

$$\eta = \frac{m_1}{m_0} \tag{3.49}$$

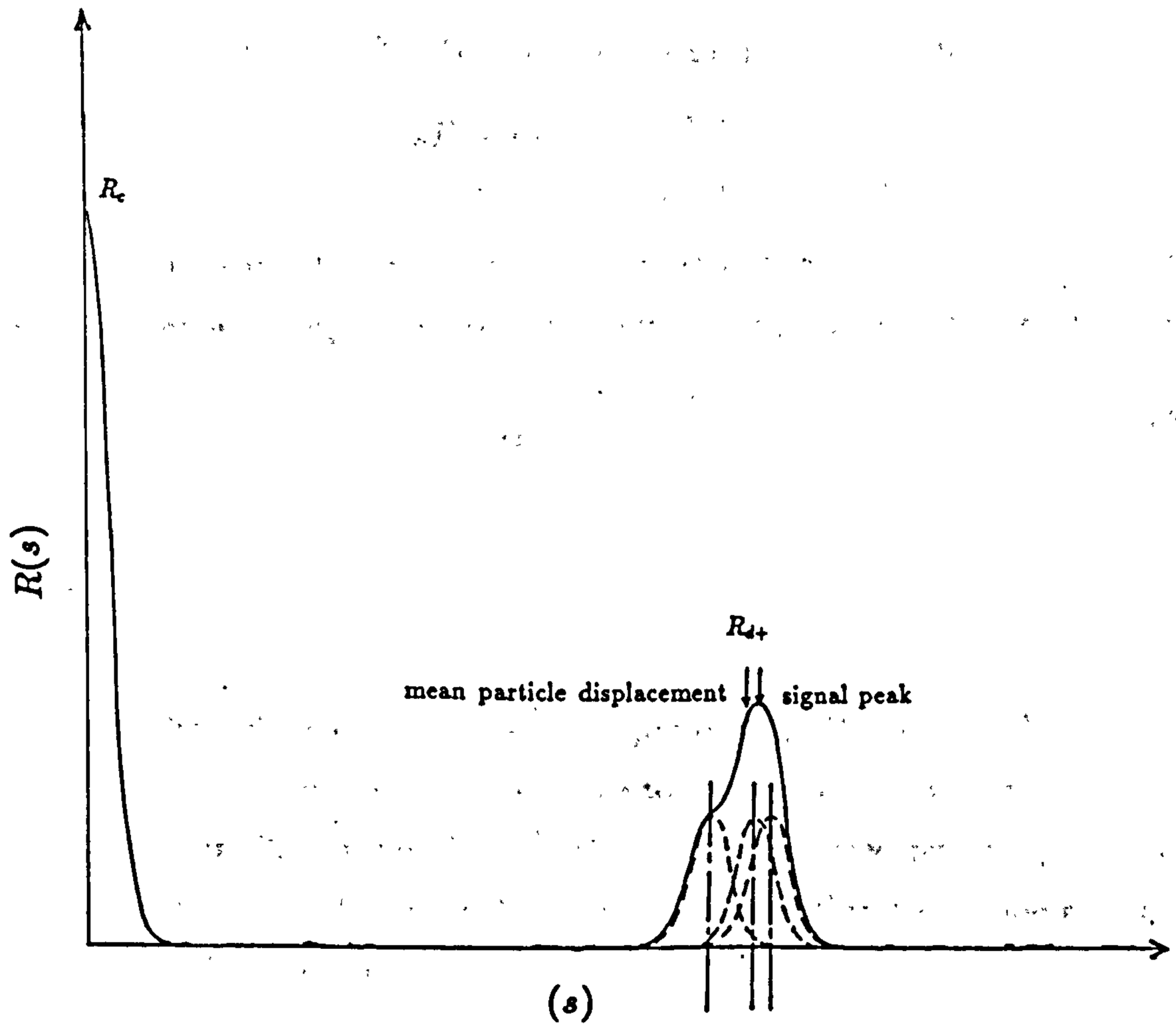

Figure 3.2: Discrepancy between signal peak R_{d+} maximum and mean particle displacement introduced by random spread of particle separations within probe region

Suppose now that $f(s) = f_1(s) * f_2(s)$ where $*$ represents a convolution then their mean values are related by,

$$\eta = \eta_1 + \eta_2 \tag{3.50}$$

Thus, for $R_{d+} = H(s) * \sum_{l=1}^{N} \delta(s - d_l)$ the mean η_{d+} is given by,

$$\eta_{d+} = \frac{\int sH(s)ds}{\int H(s)ds} + \frac{\int s \sum_{l=1}^{N} \delta(s - d_l)ds}{\int \sum_{l=1}^{N} \delta(s - d_l)ds} \tag{3.51}$$

The first term is equal to zero as $H(s)$ is symmetrical about zero while the second term, upon integration, can be seen to equal the mean particle displacement.

$$\eta_{d+} = \frac{\sum_{l=1}^{N} d_l}{N} \tag{3.52}$$

Fringe Visibility

In general, the height of the correlation peaks R_{d+}, R_{d-} will be less than that predicted in the theory above. This is due to the reduced visibility of the Youngs' fringes (see figure 3.3), where $V = \frac{I_{max} - I_{min}}{I_{max} + I_{min}}$ and is caused primarily by decorrelation of the two sets of displaced particle images within the probe region. The main sources of decorrelation can be identified as,

- Non-uniform particle displacements within the interrogation area.
- Different densities of particle images due to differences in intensity of the recording pulses. This is usually due to out-of-plane of particles to outer, less intense regions of the illumination sheet.
- Extreme out-of-plane motion shifting particles out of the illumination plane completely, resulting in only a single particle image and no correlation at all for that pair.
- Particle pairs which have only one particle image within the probe area. This is especially significant for large displacements.

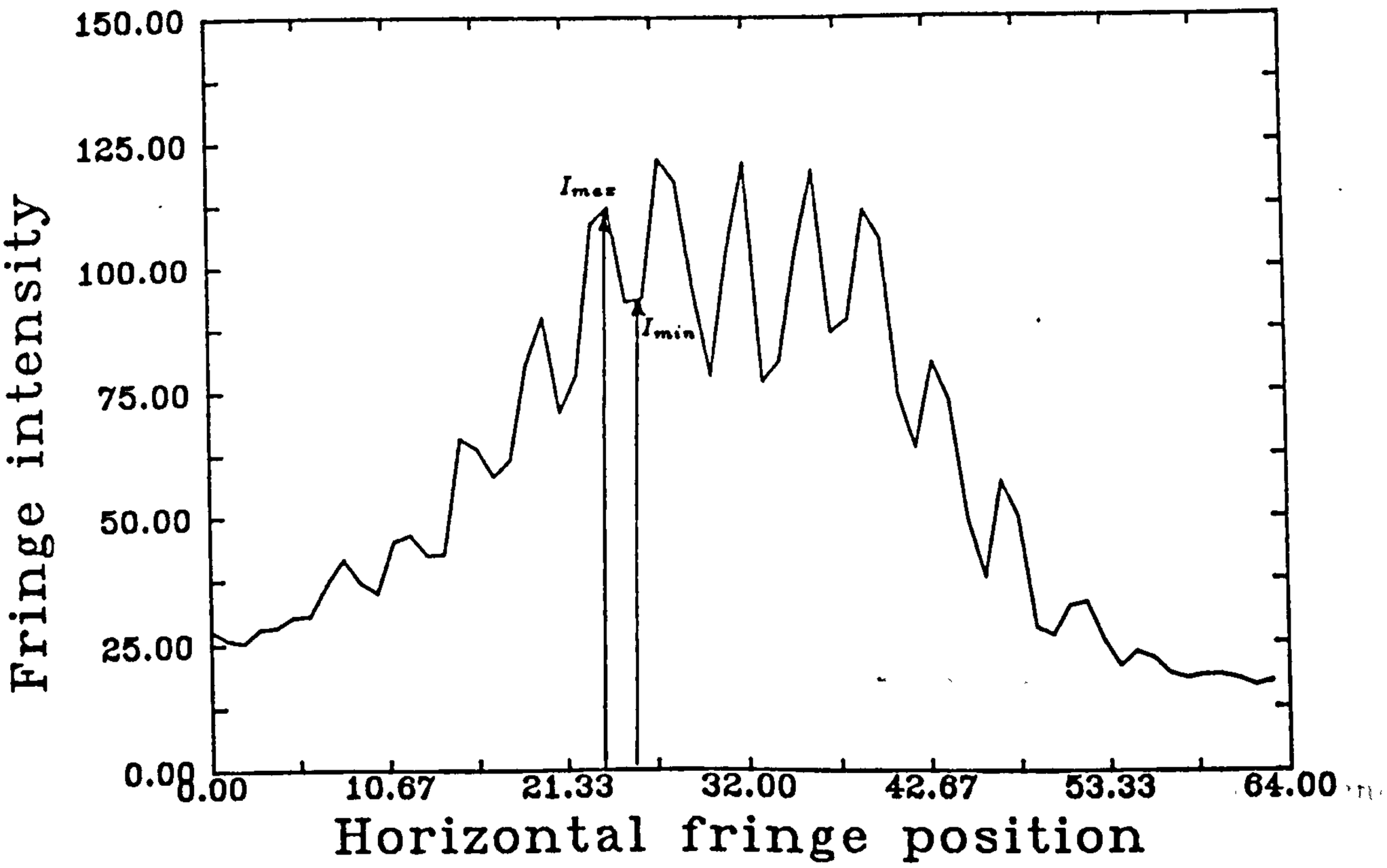

Figure 3.3: Reduced visibility fringe pattern due to partial decorrelation of the particle images within the probe region

- Noise associated with the photographic film eg. non uniform thickness/ refractive index, grain noise and spatial noise in the probe laser beam will also affect the fringe visibility.

In extreme cases the reduction in fringe visibility brought about by the above factors will be so great that the signal peaks in the autocorrelation plane will not be discernable above the random background noise. In this situation there will be a "dropout" in the velocity measurement from the film.

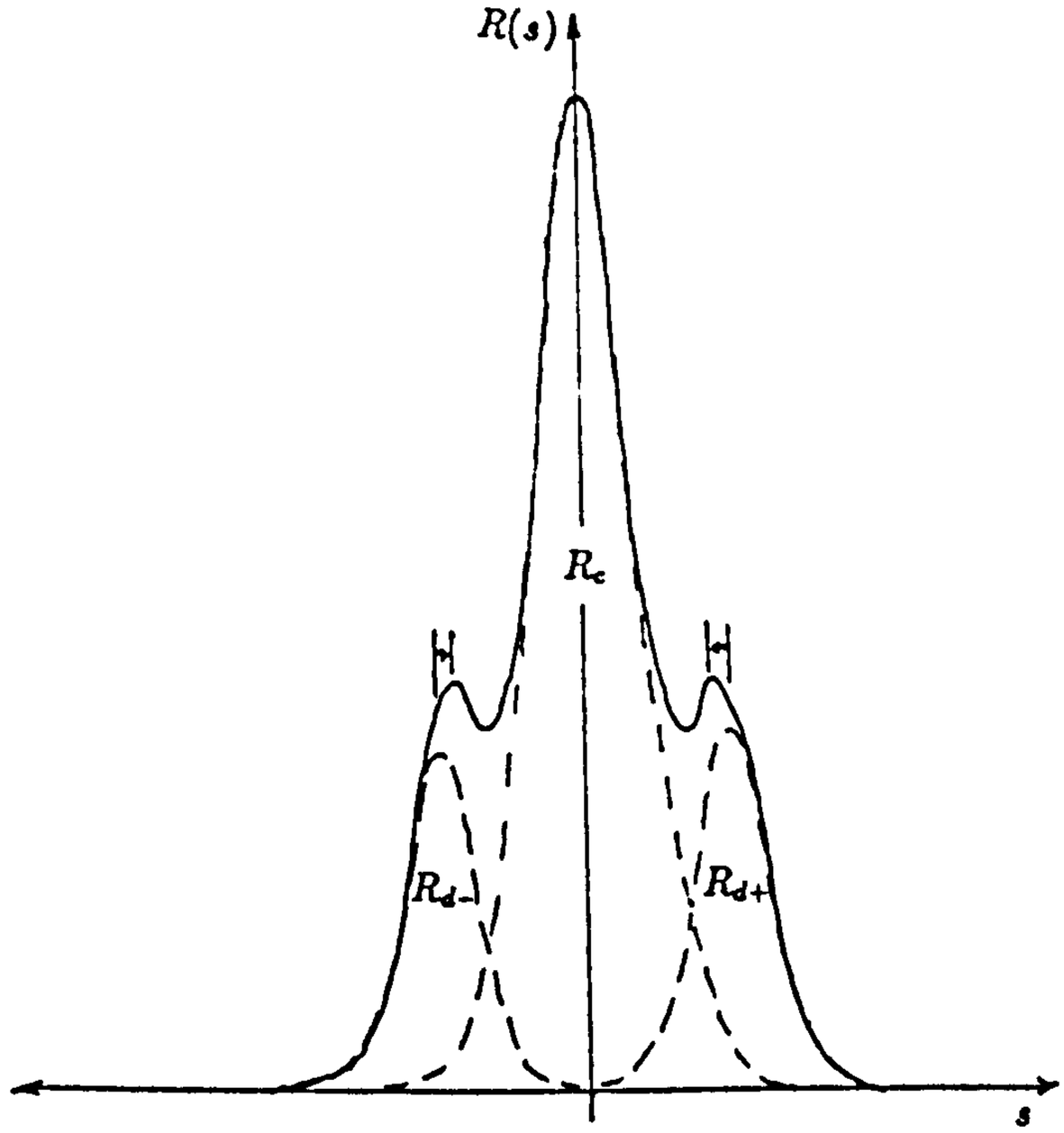

Figure 3.4: Shifting of signal peaks R_{d+}, R_{d-} due to close proximity of the central peak R_c.

Pedestal removal

It is clear from equation 3.41 that, for small particle displacements d, the signal peaks R_{d+}, R_{d-} will begin to impinge upon the centre peak R_c. For very small displacements and reduced fringe visibilities the signal peaks may not be resolved at all. In less extreme cases the detected centroid of the signal peaks will be shifted towards the centre due to the overlapping self correlation peak (see figure 3.4).

It has been shown by various authors that subtraction of the pedestal function $S(k)$ from the fringe pattern $I(k)$, prior to Fourier transformation, will suppress the central peak in the autocorrelation plane, significantly aiding the resolution and detection of small particle separations [66,99,64].

With fringe visibility defined as in the previous section it can be shown that a

fringe pattern of visibility V will have the form [99,62],[2]

$$I(k) = \frac{S(k)}{1+V}\{1 + V\cos(kd)\} \tag{3.53}$$

Subtraction of $\frac{S(k)}{1+V}$ gives

$$I'(k) = \frac{V}{1+V}S(k)\cos(kd) \tag{3.54}$$

which upon Fourier transformation gives

$$R'(s) = \frac{V}{1+V}H(s) * \{\delta(s-d) + \delta(s+d)\} \tag{3.55}$$

Thus, if $S(k)$ and the visibility V is known, it should be possible to suppress the central peak in the autocorrelation plane. $S(k)$ can be approximated by averaging a number of diffraction patterns from a single exposure negative of the same imaged flow. The ratio $\frac{1}{1+V}S(k)$ is then calculated indirectly knowing that the $s = 0$ position in the autocorrelation plane is equal to the dc component of the fringe pattern which is to be zeroed, ie.

$$\int I'(k)dk = \int I(k)dk - \frac{1}{1+V}\int S(k)dk = 0 \tag{3.56}$$

and so assuming that $I(k)$ and $S(k)$ are the same height then the visibility V can be calculated.

$$V = \frac{\int S(k)dk}{\int I(k)dk} - 1 \tag{3.57}$$

This approach to pedestal subraction assumes that the visibility is constant across the fringe pattern. This is a reasonable assumption in many cases but for fringe patterns that are generated from a local region of film that have a range of particle separations contained within it the fringe visibility becomes a function of k [1]. Pedestal subtraction in the manner described above will then only suppress the $s = 0$ component of the autocorrelation plane but will leave a low frequency "crater". This can be seen in figure 3.5.

---

[1]It has been proposed that this variation in fringe visibility be used to measure second order parameters such as vorticity [35] and the turbulence probability distribution within the probe area [62].

[2]In reference [99] Pickering and Halliwell include a scaling factor $\frac{I(0)}{B(0)}$ in equation 3.53 above. This represents the ratio of the intensity of the fringe pattern and the pedestal function at their central $k = 0$ position and is included to scale the pedestal shape to the actual intensity of the fringe pattern. For eq. 3.53 this is not included as the function $S(k)$ is assumed to be scaled already.

Multiple exposure PIV

The use of more than two exposures was discussed briefly in chapter 2 and it was seen from an example fringe pattern that multiple exposures have the effect of increasing the visibility and sharpness of the Youngs fringe pattern. This comes about through an increase in the particle image pair density on the negative and a significant increase in the degree of correlation in the direction of the flow, compared to the random background noise. A similar approach to that taken in Appendix A can be used to show that the Young's fringe intensity distribution, generated from a negative containing N exposures, will have the form,

$$I(k) = S(k)\left\{N + 2\sum_{n=1}^{N-1} n\cos\left[(N-n)kd\right]\right\} \tag{3.58}$$

where all the displacements between exposures d are identical. For $N = 2$ this expression reverts to the equal displacement, double exposure form (3.41), as expected. It can be seen that the fringe pattern resulting from an N exposure flow record consists of a $\cos(kd)$ fundamental and $N-2$ harmonic terms at integer multiples of the fundamental frequency. These harmonic terms sharpen the primary maxima of the fringe pattern and give $n-2$ secondary maxima, which due to their small relative intensity are seldom visible above the speckle noise. Fourier transformation of $I(k)$ to the autocorrelation plane then gives,

$$R_m(s) = H(s) * \left\{N\delta(s) + \sum_{n=1}^{N-1} n\left[\delta(s-(N-n)d) + \delta(s+(N-n)d)\right]\right\} \tag{3.59}$$

which consists of a self correlation peak at the origin plus $N-1$ signal peaks at equally spaced displacement intervals of d, diminishing linearly in amplitude. Ideally, the n^{th} signal peak will be $\frac{N-n}{N}$ the amplitude of the self correlation peak (figure 3.5). In practice, however, the signal peak amplitudes will be lower than this theoretical value due to the decorrelation effects discussed above. Furthermore, the finite probe diameter will impose a bias against larger displacements up to the limit discussed in chapter 2. This will tend to further reduce the amplitude of the higher order signal peaks. Figure 3.5 shows an example of an autocorrelation function resulting from a point measurement on a four exposure flow record.

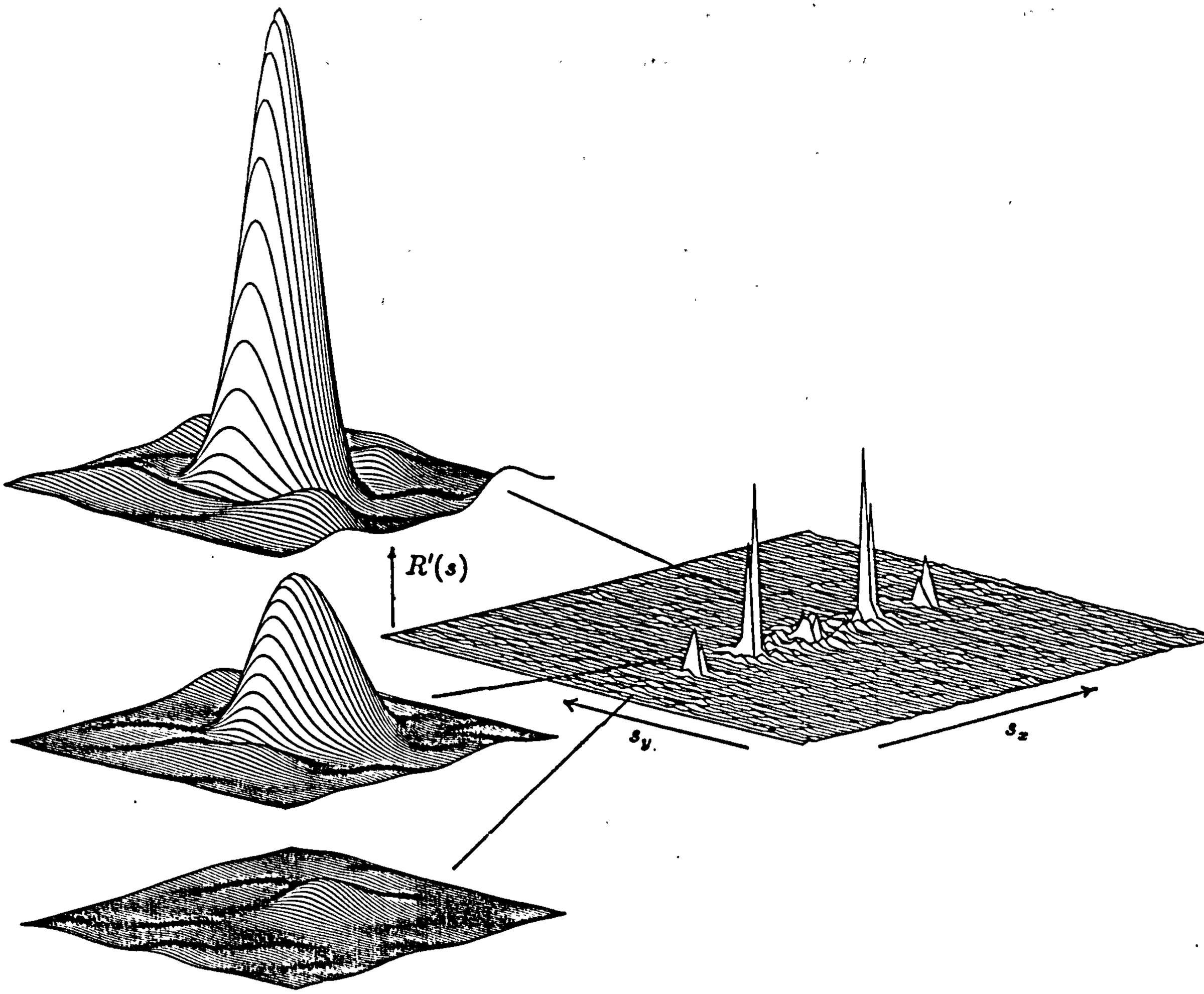

Figure 3.5: Autocorrelation function for a 4 exposure PIV negative showing the fundamental and two harmonic peaks.

The use of multiple exposures in recording a flow field will improve the accuracy and reliability with which the resulting flow record can be analysed. The ratio of particle image pairs to the total number of particle images is increased dramatically as the number of exposures are increased. This gives a corresponding increase in the amplitude of the primary correlation peak from which the displacement measurement is made. Furthermore, there is the possibility of utilising the "harmonic" peaks to measure the mean displacement between peaks rather than just the position of the first peak. It is important, however, to limit the number of exposures when the flow to be measured is highly unsteady so that the total exposure time does not exceed typical timescales of the flow.

3.2 System description

Optical processing hardware

The Power spectrum $I(k)$ is obtained from a small local region of a PIV negative using the optical processing system shown in figure 3.6. The beam from a 2mW Hughes Helium Neon laser is passed through spatial filter L_1, S_1 to limit the spatial noise present in the probe beam. A second small circular stop S_2 positioned on the optical axis ahead of the spatial filter controls the solid angle of the diverging beam reaching the collimating lens L_2. Horizontal adjustment of S_2 then allows the resulting probe beam diameter to be adjusted from $\approx$ 2mm-0.6mm. The tailored probe beam then passes normally through the PIV negative which is positioned on two orthogonally mounted translation stages. These permit precise positioning of the negative in two dimensions. The diffracted light from the transparency is then collected by the Fourier transforming lens L_3, which is positioned close behind the film to limit vignetting of the diffracted light by the finite lens diameter[51]. The light amplitude distribution in the back focal plane of the lens is then proportional to the spatial Fourier transform of the amplitude transmission distribution of the interrogated region of film, apart from a phase factor which does not alter the detected intensity distribution. The high mean transmittance of the negative results in a high intensity spot at the origin in the Fourier plane. This is stopped from the CCD array, which is positioned at F, by a small optical stop S_3. Removal of the high intensity DC peak avoids damaging the camera and reduces light scattering at the array surface[2]. Control of the beam intensity is by means of crossed polarisers P which are positioned in front of the laser but behind the spatial filter.

[2]Contact printing of the PIV negative (as described in Chapter 1[100]) has the effect of significantly reducing the mean transmittance of the flow record and so reduces the intensity of the central spot avoiding the need for a stop here.

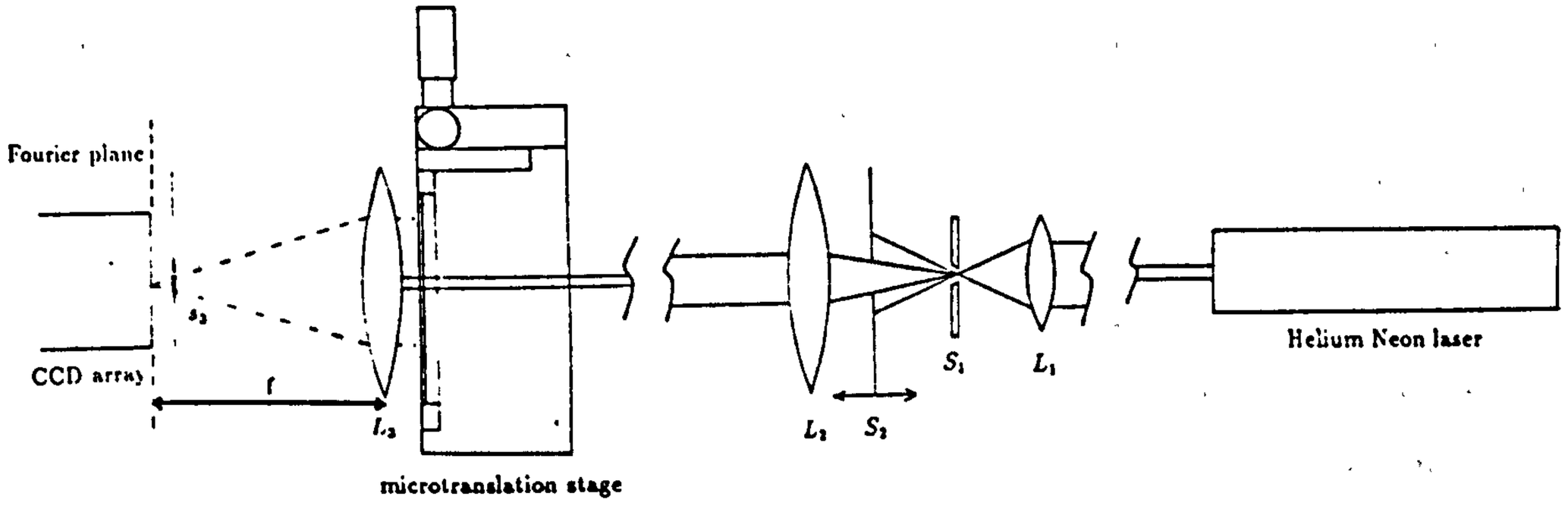

Figure 3.6: Optical processing section of automatic PIV analysis system

Image capture and film positioning

The arrangement used to control the aquisition and processing of the data is shown in figure 3.7. A Panasonic WV-CD20 CCD array camera interfaced to a Watford electronics real-time image digitiser is used to digitise the Youngs fringe pattern $I(k)$. The camera is used with its lens removed and is positioned so that the CCD array is located the back focal plane of lens L_3. A CCD array camera is used in this system as the image sensor because of the need for precise and repeatable image recording. Images aquired with a standard video camera, based on a raster scanned Vidicon tube, would be subject to random distortions of up to a few % introducing unacceptable errors into the measured displacements.

The CCD is an array of precisely positioned photodetectors (256*512) which permit the continuous power spectrum $I(k)$ to be discretely sampled at each of these points. By the sampling theorem [22] this would permit detection of spatial frequencies of up to 128 cycles vertically and 256 horizontally across the

region occupied by the CCD array. There are typically between 3 and 30 fringes within the halo function $S(k)$ that windows the fringes and so the full resolution is considerably greater than that required to represent the information carrying fringes. Sampling over fewer, more widely spaced points, would reduce the amount of memory required and more importantly reduce the computation time required to transform the discrete power spectrum to the autocorrelation plane. However, the spatial frequency content of the fringe pattern extends well above that of the fringes, and is associated with the speckle noise, arising primarily from the random particle pair positions and phase/amplitude noise inherant in the photographic medium. Sampling at a frequency that is lower than this noise will lead to aliasing of that part of the signal into the autocorrelation function. It has been shown however, that undersampling of fringe patterns derived from Laser speckle photography displacement records does not unduly contaminate the useful part of the fringe spectrum [64], and so a low sampling rate 64*64 is adopted here so that the amount of data to be processed is reduced as far as possible. In practice, the array of 64*64 discrete image values are obtained by averaging blocks of 4*4 pixel values from the 256*512 values detected by the CCD. This process performs a crude low pass filtering operation and so further reduces the possibility of aliasing corrupting the displacement measurement.

Two Micro-controle UT100 translation stages are used to control the position of the negative relative to the probe laser beam. The negative is clamped between two square brackets which itself is mounted on the vertical translation stage projecting forward so that the film can be positioned close to the Fourier transforming lens L_3 (see figure 3.6). The vertical stage is precisely mounted perpendicularly ontop of the horizontal stage allowing the negative to be moved to any position across its $56.5 * 56.5mm^2$ area to within $0.5\mu m$. Each stage is driven by a drive board (Micro-controle PMB68). These are interfaced to an Archimedes 440 microcomputer through a custom built interface to the user port of the computer (see figure 3.7). The software used to control the motion of the film generates a train of pulses which can be addressed to either translation stage and which ramps up in frequency to the maximum drive speed of

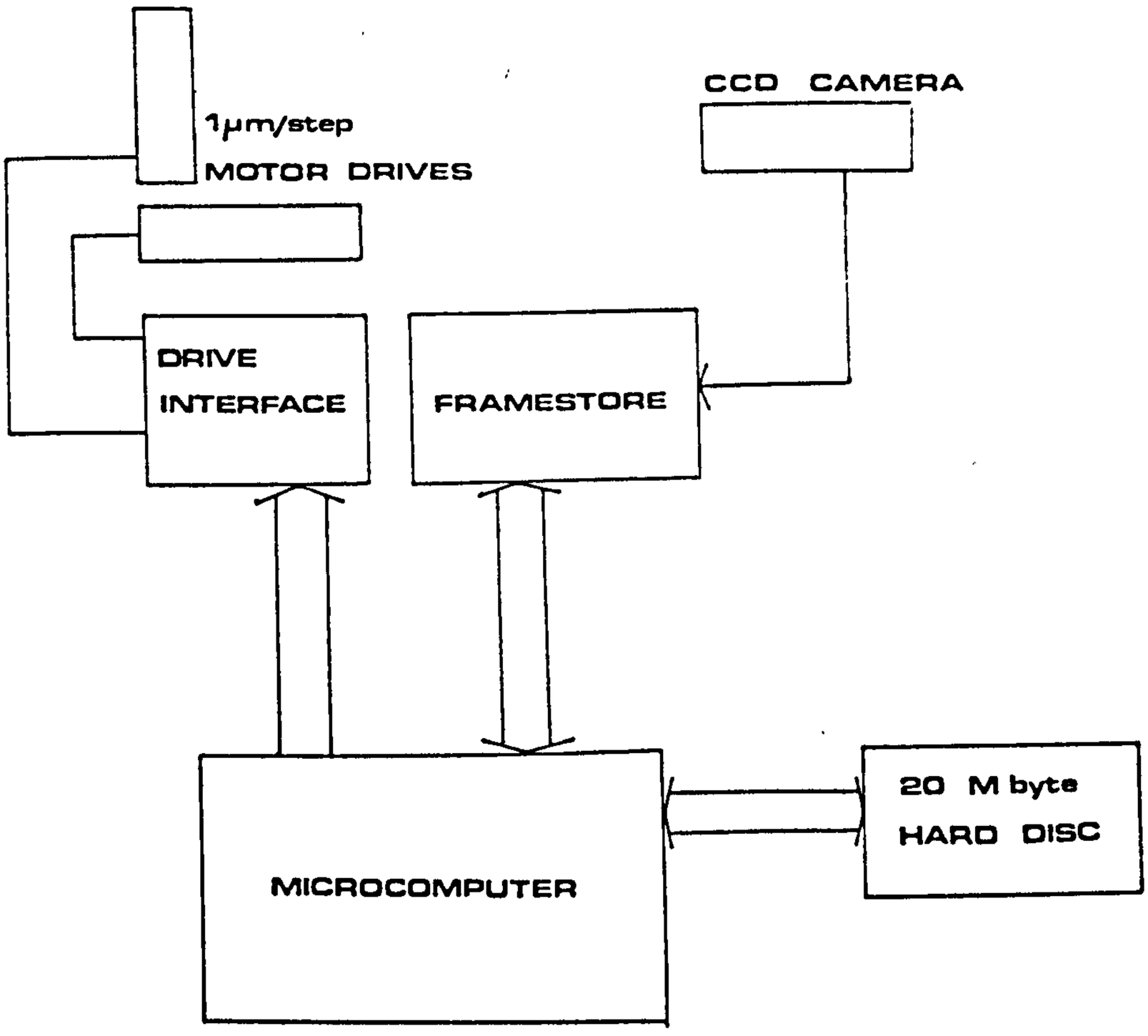

Figure 3.7: Block diagram of analysis system hardware

$\approx 2mm/s$. Ramping of the signal ensures that the translation stages do not miss any steps due to inertia of the drive mechanism. This is particularily important in this application where the stage may have to start from rest several thousand times, in which case missed steps each time would lead to an accumulating positional error of the probe beam relative to the film.

Analysis software

The analysis program used to control the optical processing rig is written in BBC BASIC and performs the fringe analysis routine in 80 seconds including film transport and image aquisition. . The procedure for analysis of a PIV negative begins with registration and levelling of the film relative to the probe beam. This is achieved by aligning the beam with a central datum

mark on the transparency which, in the case of the water wave application, is a $4 * 4cm$ cross marked on the glass wall of the tank. Traversing the film across until it coincides with another datum mark horizontally displaced along the glass wall ensures that the horizontal on the analysis rig coincides with the true horizontal. The film is then traversed to a chosen origin and given the dimensions and grid spacing of the region to be analysed. The X/Y stages then move the film through the desired grid of points and an image is captured at each point. Numerical processing of the power spectrum obtained at each point then measures the mean particle displacement within the region of the flow that has been recorded on the PIV negative. At certain points, corresponding to regions outside the flow and where insufficient information is present on the film a spurious value will be obtained. These values are identified and then removed. The procedure used to do this is discussed in Chapter 5.

Image processing algorithm

Section 3.1 shows how the mean particle displacement within a small local region of a PIV negative can be derived from its autocorrelation function. Assuming that sufficient information is present within the probe region (ie. three or more particle image pairs) a signal peak that is spread over several sample points in the discrete autocorrelation plane will be detectable above the random noise. A precise estimate of the mean particle displacement can then be made by calculation of the centroid of the signal distribution in the local area about the detected peak.

The discrete autocorrelation function $R(s_m, s_n)$ is calculated efficiently by Fast Fourier transforming the columns and then the rows (or vice versa) of the discrete power spectrum $I(k_i, k_j)$. This is done efficiently using a Fast Hartley transform [22] from which the discrete Fourier transform is easily calculated. The discrete Hartley transform of a function $f(\tau)$ is defined as,

$$H(\nu) = \frac{1}{N} \sum_{\tau=0}^{N-1} f(\tau) \left\{ \cos(\frac{2\pi\nu\tau}{N}) + \sin(\frac{2\pi\nu\tau}{N}) \right\} \qquad (3.60)$$

The complex discrete Fourier transform is defined as,

$$F(\nu) = \frac{1}{N} \sum_{\tau=0}^{N-1} f(\tau) \exp(-\frac{i2\pi\nu\tau}{N}) \tag{3.61}$$

and is related to $H(\nu)$ by $F(\nu) = E(\nu) - iO(\nu)$ where, $E(\nu) = \frac{H(\nu)+H(N-\nu)}{2}$ and $O(\nu) = \frac{H(\nu)-H(N-\nu)}{2}$. Calculating the discrete Fourier transform (DFT) in this way is typically twice as fast as with a DFT algorithm when the data to be transformed is real. The discrete Hartley transform (DHT) has no complex multiplications , which take four times longer than real multiplications, and so, for transformation of the power spectrum $I(k_i, k_j)$, gives a significant reduction in computation time over a DFT. A fast Hartley transform algorithm [22] was then used to calculate the DFT of the rows then columns of $I(k_i, k_j)$ to get the discrete autocorrelation function $R(s_m, s_n)$.

Rather than Fourier transform $I(k_i, k_j)$ the transform of $I'(k_i, k_j)$ is taken where,

$$I'(k_i, k_j) = I(k_i, k_j) - \frac{c_1}{c_2} S(k_i, k_j) \tag{3.62}$$

where $S(k_i, k_j)$ is an approximation to the pedestal function discussed in section 3.1 and is obtained by averaging the power spectrum from a single exposure negative of the flow over 40 different positions on the film. The values c_1, c_2 are given by $c_1 = \sum_{k_i,k_j} I(k_i, k_j)$ and $c_2 = \sum_{k_i,k_j} S(k_i, k_j)$ and ensure that $\sum_{k_i,k_j} I'(k_i, k_j) = 0$. This means that the $s = 0$ in the correlation plane is zeroed but will only suppress the whole central peak R_c if the fringe visibility is constant over the fringe pattern. In general this is not true and so the above operation will only partially cancel the central self correlation peak leaving a small rim. This aspect of the analysis procedure requires further work to estimate, more precisely, the form of the function to be subtracted from $I(k_i, k_j)$ so that the whole of the central peak can be cancelled.

The signal peaks R_{d+}, R_{d-} are generally situated over several grid points due to the finite diameter of the particle images recorded on the flow negative. This permits the approximate position of R_{d+} to be found by searching for the position (s_{xm0}, s_{yn0}) of the maximum correlation value of $R(s_{xm}, s_{yn})$. A precise estimate of the mean particle displacement is achieved by numerically calculating the

position of the centroid of R_{d+}. This involves summation of the signal peak function over the area of $R(s_m, s_n)$ in which R_{d+} resides.

Using the widely spaced discrete points of the autocorrelation function a first estimate of the mean particle image displacement η_{1d+} can be calculated.

$$\eta_{1d+} = \frac{\sum_{s_{xm},s_{yn}}(s_{xm}, s_{yn})R(s_{xm}, s_{yn})}{\sum_{s_{xm},s_{yn}} R(s_{xm}, s_{yn})} \tag{3.63}$$

where the summation is over a small square area covering 16 grid points centred on (s_{xm0}, s_{yn0}) where the value η_{1d+} represents a first approximation of the mean particle displacement and is used as a centre point for a summation over a denser grid of interpolated points to give a high precision estimate of the mean displacement η_{2d+}.

Interpolation of the discrete autocorrelation grid points is achieved using a trigonometric interpolation scheme similar to that used by Huntley, 1986 [64]. The discrete power spectrum $I(k_i, k_j)$ and the autocorrelation function $R(s_{xm}, s_{yn})$ are Fourier transform pairs and so $I(k_i, k_j)$ can be used as the Fourier coefficients in the interpolation of $R(s_x, s_y)$ between grid points. Also, because these functions are separable in the x and y directions the interpolations can be performed as a number of one dimensional interpolations along equal s_x or s_y where,

$$\mid R(s_x, s_y) \mid = (FR^2(s_y) + FI^2(s_y))^{1/2} \tag{3.64}$$

and

$$FR(s_y) = \sum_{k_i=0}^{N-1} \cos(2\pi s_y k_i/N)R(k_i) + \sin(2\pi s_y k_i/N)X(k_i) \tag{3.65}$$

$$FI(s_y) = \sum_{k_i=0}^{N-1} \cos(2\pi s_y k_i/N)X(k_i) - \sin(2\pi s_y k_i/N)R(k_i) \tag{3.66}$$

where

$$R(k_i) = \sum_{k_j=0}^{N-1} I'(k_i, k_j)\cos(2\pi s_x k_j/N) \tag{3.67}$$

$$X(k_j) = \sum_{k_i=0}^{N-1} I'(k_i, k_j)\sin(2\pi s_x k_j/N) \tag{3.68}$$

Therefore the mean displacement in the x and y directions are evaluated as,

$$\eta_{2xd+} = \sum_{s_x}\sum_{s_y} s_x R(s_x, s_y) / \sum_{s_x}\sum_{s_y} R(s_x, s_y) \tag{3.69}$$

$$\eta_{2yd+} = \sum_{s_x}\sum_{s_y} s_y R(s_x, s_y) / \sum_{s_x}\sum_{s_y} R(s_x, s_y) \tag{3.70}$$

where $[(s_x - s_{x1})^2 + (s_y - s_{y1})^2] \leq rad^2$ and rad is the radius of a small circular region in the autocorrelation plane centred on $\eta_{1d+} = (s_{x1}, s_{y1})$ as calculated above. The value of rad is chosen to be about 2.5 grid spacings which defines a circular region that is typically slightly larger than the area occupied by the signal R_{d+}. Evaluation of $R(s_x, s_y)$ at quarter grid spacings gives an estimate of the mean displacement that differs from higher density estimates by a very marginal amount.

Figure 3.5 shows the three signal peaks present in the autocorrelation plane of a four exposure flow record. The small randomly positioned peaks about the signal peaks are due to the random correlations between non-related particle images within the interogation area. These will, in general, be small compared to the fundamental particle displacement correlation peaks R_{d+}, R_{d-} and so, in the calculation of the mean particle displacement, will alter the calculated mean displacement from the true displacement by only a small amount. However, this random noise present in the autocorrelation represents a fundamental limitation on the accuracy achievable with PIV. The two-dimensional analysis of the flow record ensures that this noise is evenly distributed about the autocorrelation plane allowing maximum immunity from the random correlations. Analysis techniques such as 1-D image compression [123] and 1-D fringe integration [?] tend to compress the random noise onto the signal, and so, although they can be evaluated much more quickly, they compromise accuracy. This has been shown to be the case in a recent experimental study that compares different methods of Young's fringe analysis [63].

The result of a successful measurement is two parameters s_x, s_y which are proportional to the mean particle displacement within the laser interrogation spot. The constant of proportionality that relates s_x, s_y to the displacement of the images on the PIV negative has been determined by calibration using a number of mock PIV negatives. Several precisely known displacements were measured (50-250μm) over $\approx$ 100 points, the mean taken and then plotted against the cor-

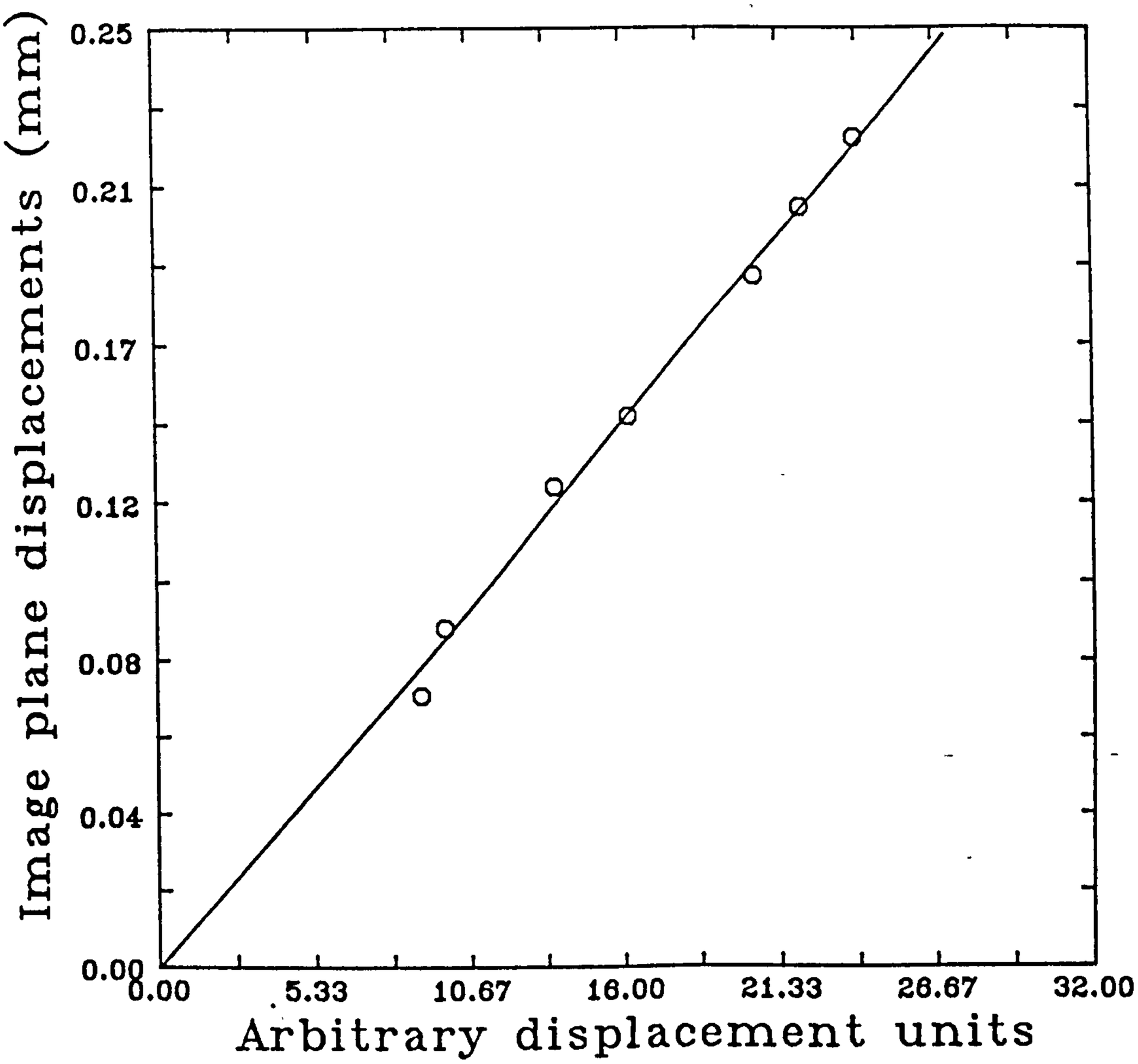

Figure 3.8: Real displacement(mm) of mock PIV negative v. measured displacement (s)

responding real displacement. (see figure 3.8). A least squares fit to the range of displacements measured gave a scale factor of $9.41 \pm 0.01 \mu m$/units. The values obtained in this way must then be further scaled using the magnification of the photographic image to give the true displacement and then by the time interval between exposures to give the velocity.

Chapter 4

PIV Measurement Accuracy

If velocities measured with PIV are to be of serious use they must be accompanied by an estimate of the uncertainty associated with each measurement. For the system described in Chaps. 2 and 3 the final velocity estimate will be the product of four different measurable quantities, given by,

$$\underline{v} = \frac{CM}{T}\underline{s} \tag{4.71}$$

where $\underline{s}$ is proportional to the mean particle image displacement within a given local interrogation area of a negative, C is a calibration factor that converts $\underline{s}$ to a real displacement value, M is the photographic magnification factor and T is the time between the illuminating pulses. Each of these values will have an uncertainty that will contribute to a total uncertainty associated with the final velocity estimate. The uncertainties in $\underline{s}, C, M$ and T are represented by $\sigma_{\underline{s}}, \sigma_C, \sigma_M$ and σ_T respectively and are combined to give $\sigma_{\underline{v}}$, the uncertainty in $\underline{v}$ thus,

$$\left(\frac{\sigma_{\underline{v}}}{\underline{v}}\right)^2 = \left(\frac{\sigma_{\underline{s}}}{\underline{s}}\right)^2 + \left(\frac{\sigma_C}{C}\right)^2 + \left(\frac{\sigma_M}{M}\right)^2 + \left(\frac{\sigma_T}{T}\right)^2 \tag{4.72}$$

The uncertainties in C, M and T will be small and estimating these quantities in no way represents a fundamental limit on the overall accuracy. In Chapter 3, C was estimated using a number of mock PIV negatives of precisely known displacement and shown to be be $9.41 \pm 0.01(\mu m)/unit$. The magnification M is determined by measuring the dimensions of the image of a regular grid that

has been positioned within the measurement area and photographed with the same photographic arrangement used to record the flow. Grid positions can be measured to within $0.02mm$ on the film and $\approx 0.25mm$ on the grid giving an approximate relative error of $\frac{\sigma_M}{M} \approx 0.001$.

The period of the scanning beam T and the approximate time between illuminations of the same particle is determined by detecting the scanning beam with a phototransistor and a digital storage oscilloscope (see figure 2.12) which allows the leading edge of the beam to be detected to within $2-3\mu s$ which for a $2-3ms$ scan period gives $\frac{\sigma_T}{T} \approx 0.001$. It is shown in Chapter 2 that the scanning beam system will introduce a displacement dependent error into the pulse separation. This error is small and can be accounted for if need be and so will not be considered in in the final error estimate. The displacement value $\underline{s}$ is determined from the correlation peak R_{d+} in the autocorrelation plane which is derived from small regions of the PIV negative. The recording of the particle motions and the subsequent measurement of their displacement undoubtably represents the major source of uncertainy in the final velocity measurement. This uncertainty can be attributed to a several separate sources,

1. Seeding particle dynamics ie. the ability of seeding particles to faithfully follow the flow being studied.

2. Characteristics of the optical recording system ie. the manner in which the physical motion of the seeding particles is transcribed onto photographic film or other recording medium.

3. Evaluation of velocity (particle displacement) at a given point on the flow record.

The first of these possible sources of error are considered early in Chapter 2 and for the majority of PIV experiments will be negligible. In the case of PIV measurement of water waves the relative motion between particles and surrounding

water will be of minute proportions as accelerations are of the order of g (acceleration due to gravity) and the density of seeding particles are, neccessarily, closely matched to that of water.

The characteristics of the recording system will vary from system to system depending upon the optical configuration and components used. The most important factors such as optical distortion of the imaged flow, the effects of 3-D motion, limited resolution etc. have been considered in Chapter 2 but will be briefly reconsidered here.

These errors can be divided up into systematic and random errors. The distortion of the imaged flow field due to limited lens quality and the influence of the glass walls of the tank will not change between measurements and so can be measured and accounted for in the final estimate of the velocity. Other effects such as distortion of the particle images due to grain noise, adjacency, shrinkage etc. cannot be individually accounted for here without detailed knowledge of their relative influence on the detectable shape and position of the particle images. Rather, a net estimate of their effect upon the measurement accuracy is made.

The third source of errors in PIV are those associated with measurement of the particle displacement from the flow negative. The analysis system described in the previous chapter measures the mean particle displacement within a small local area of the PIV transparency by autocorrelation of the amplitude transmission distribution across that local region of film. Several souces of error may be identified in this process -

- Distortion of the optically performed power spectrum $I(k)$ due to limited quality of the Fourier transforming lens and noise introduced by refractive index and film thickness variations across the negative[1].
- Quantisation errors associated with the digitised power spectrum data and

[1]It has been shown that phase noise associated with the film can be minimised by contact printing the negative to get a positive record of the flow[100].

rounding errors in the numerical calcuation of the autocorrelation function $R(s)$.

- The influence of random correlation noise in determining the centroid of the signal peak.

- The effect of the discrete and random sampling of an essentially continuous flow by the randomly distributed particles.

These factors will compromise the accuracy with which the flow velocity at a given point on the flow record can be measured from the film. All but the last two factors are functions of the quality of the components that make up the recording and and analysis equipment, and their influence on the final uncertainty can be minimised an appropriate choice of equipment. The last two factors are more fundamental in nature and are due to the manner in which the flow velocity information is represented on, and measured from, the recording medium.

For a flow field that does not vary across the local interrogation area, the detected position of the signal peak centroid will be affected in a random manner by the presence of nearby random correlation peaks. These small peaks can be seen in figure 3.5 and arise primarily due to correlations between non-related particle images. These peaks are randomly distributed about the correlation plane due to the random positions of the particle image pairs within the probe area.

For point measurement of the mean particle displacement over a spatially varying flow field there will be an additional random error associated with the random collection of particle displacements within the probe area. This is due to the discrete and random representation of the continuous flow field given by the motion of the particles present within the measurement plane of the flow. Different distributions of particle image pairs representing the same fluid motion will, due to their different positions within the interrogation area, give a slightly different measured mean displacement. This randomness will have a statistical distribution that is dependant upon the range of velocities present within the probe area and the concentration of particle images. Increasing the number of

particle image pairs within each interrogation area decreases the randomness of individual point measurements and in the limit of infinite image concentration the theoretically measureable mean displacement will closely approximate the mean motion of the fluid within that probe area.

Systematic errors are minimised by careful design and the use of high quality components. The random errors associated with the recording process arise from a number of different sources and are quantified experimentally along with the uncertainty associated with measuring the position of the correlation peak in the presence of random correlation noise. The influence of the finite probe area sampling a range of velocities is considered separately for a one-dimensional velocity gradient. This is important for the water wave measurements as turbulence is minimal before breaking but a strong velocity gradient is present through the wave profile.

It is mentioned in the footnote on page 95 that contact printing the PIV negative to produce a positive copy of the flow record reduces the influence of phase noise introduced by variations in the optical thickness of the film. This procedure is most effective for negatives of high mean transmittance, i.e. few particle images per unit area. For increasing concentrations of particle images the advantage of contact printing diminishes and for the measurements described in chapters 5 and 6 particle image densities were sufficiently high that no significant reduction in phase noise was attainable through contact printing.

4.1 Systematic Recording Errors

The relationship between the flow and the recorded PIV image is ideally just a scale factor M (A magnification factor). In practice there are a number of sources of distortion to consider.

1. Geometric distortion of the recording lens.
2. Refraction effects due to the air/glass/water interface.
3. Perspective and three-dimensionality of the flow

Image Distortion

Lens distortion and refraction effects can be considered together as they result in a combined distortion of the image field. In Chapter 2 the resulting distortion due to lens and refraction effects have been measured by photographing a regular grid and shown to result in minimal distortion across the image (see figure 2.23). However, the distortion present in the image will introduce errors into the measurements in two ways -

1. The regular grid positions of the probe beam across the PIV negative will not correspond to a regular grid of points across the imaged flow field but will be displaced by an amount depending upon the degree of distortion present.
2. The recorded particle displacement will be related non-linearly to the actual displacement in the flow due to the image distortion across the probe area.

The positional error of the probe beam will be more important as it depends upon the total distortion of the image at that image height. The effect of image distortion on the recorded particle displacement will be considerably less

as it depends upon the amount of distortion across the particle displacement (typically $\leq 300\mu m$) and so will negligibly small and can be neglected as the other errors considered below are considerably greater in magnitude. For high precision measurements however, the known distortion of the flow record can be used to correct for positioning and measurement errors.

Out-of-plane motion

It is shown at the end of Chapter 2 that out-of-plane motion of the flow will lead to considerable errors in the measurement of the two in-plane components of velocity. Errors of approx. 20% are shown to be possible in the off-axis regions of the image plane if the out-of-plane motion is of the the same order as the in-plane motion of the particles. Errors of this sort can be minimised by ensuring that the flow has only a small component perpendicular to the measurement plane. This is discussed further in Chapter 6, with regard to wave measurements, but at this point it suffices to say that wave motion perpendicular to the measurement plane is negligible. Furthermore, the most important measurements, under the wave crest, are made in the centre of the image where out-of-plane motion does not affect in-plane measurements to the same extent and the effects of distortion, discussed above, become negligible.

4.2 Random Errors

Random errors are introduced into velocity measurements from two distinct sources.

1. Practical limitations of the components used to record and measure the particle displacements ie. emulsion grain noise, adjacency effects, quantisation errors etc.

2. Fundamental limitations associated with the discrete and random distribution of particle image pairs influencing velocity estimates in two ways.

   - Degradation of measureable signal centroid by random correlation noise.
   - Effect of averaging spatially varying flow over discrete and random set of particle displacements.

The first source of errors will be wholly dependent upon the specific components of the recording and analysis rig and will vary depending upon the type of film, lens, developer, Video camera, image digitiser etc. The second, and more important, sources of error are more fundamental and are associated with the measurement method. Ideally, all these factors should be considered independently but for the purposes of this study it will suffice to examine the influence of random correlation noise simultaneously with the uncertainties associated with the specific hardware that has been utilised. This is acheived by making a large number of measurements from "mock" PIV negatives, similar to those used to calibrate the analysis rig. The variance of these measurements then give an indication of the measurement uncertainties for a constant in-plane displacement. The uncertainty associated with varying particle displacements within the probe region is examined independently in the next section using a computer simulation to model the random process.

4.2.1 Experimental measurement of random errors

A similar arrangement to that in Chapter 3 was used to produce a range of PIV displacement negatives of varying quality in order to evaluate the performance of the system for negatives that have varying degrees of random correlation noise. A flat perspex plate was dusted lightly with pollen grains and illuminated with an expanded laser beam. A double exposure photograph was taken, with an in-plane displacement between exposures. The degree of correlation in the direction of the displacement was reduced at various points across the negative by applying more seeding before exposing the film for the second time. Four negatives that showed a wide range of correlation strengths[2] were each analysed over approximately 2000 points covering the whole transparency. The strength of the correlation at each point was estimated by numerically calculating the correlation factor C_f which I have defined as the fraction of the total autocorrelation plane that contributes to the signal R_{d+}[3],

$$C_f = 2\frac{\sum_{s_{xm},s_{yn}} R_{d+}(s_{xm},s_{yn})}{\sum_{s_{xm},s_{yn}} R(s_{xm},s_{yn})} \tag{4.73}$$

The summation of the numerator is taken over the small circular region of the discrete autocorrelation plane that is used to calculate the signal centroid. Summation of the denominator was over the whole correlation plane. This gives an indication of how strong the displacement correlation is, compared to the background random correlations.

As the strength of the displacement correlation diminishes the estimate of the signal centroid will be increasingly affected by the presence of nearby random noise. The measurements made from the mock negatives were visually checked for spurious values using a graphical preview program (see Chapter 5). Anomalous values occur when insufficient information is present within the probe region to generate a detectable displacement correlation peak. The simple maxima

[2]The degree of correlation can be qualitatively estimated by viewing the visibility of the Young's fringe pattern generated from a given region of a negative.

[3]Refer back to definitions of R and R_{d+} given in Chapter 3

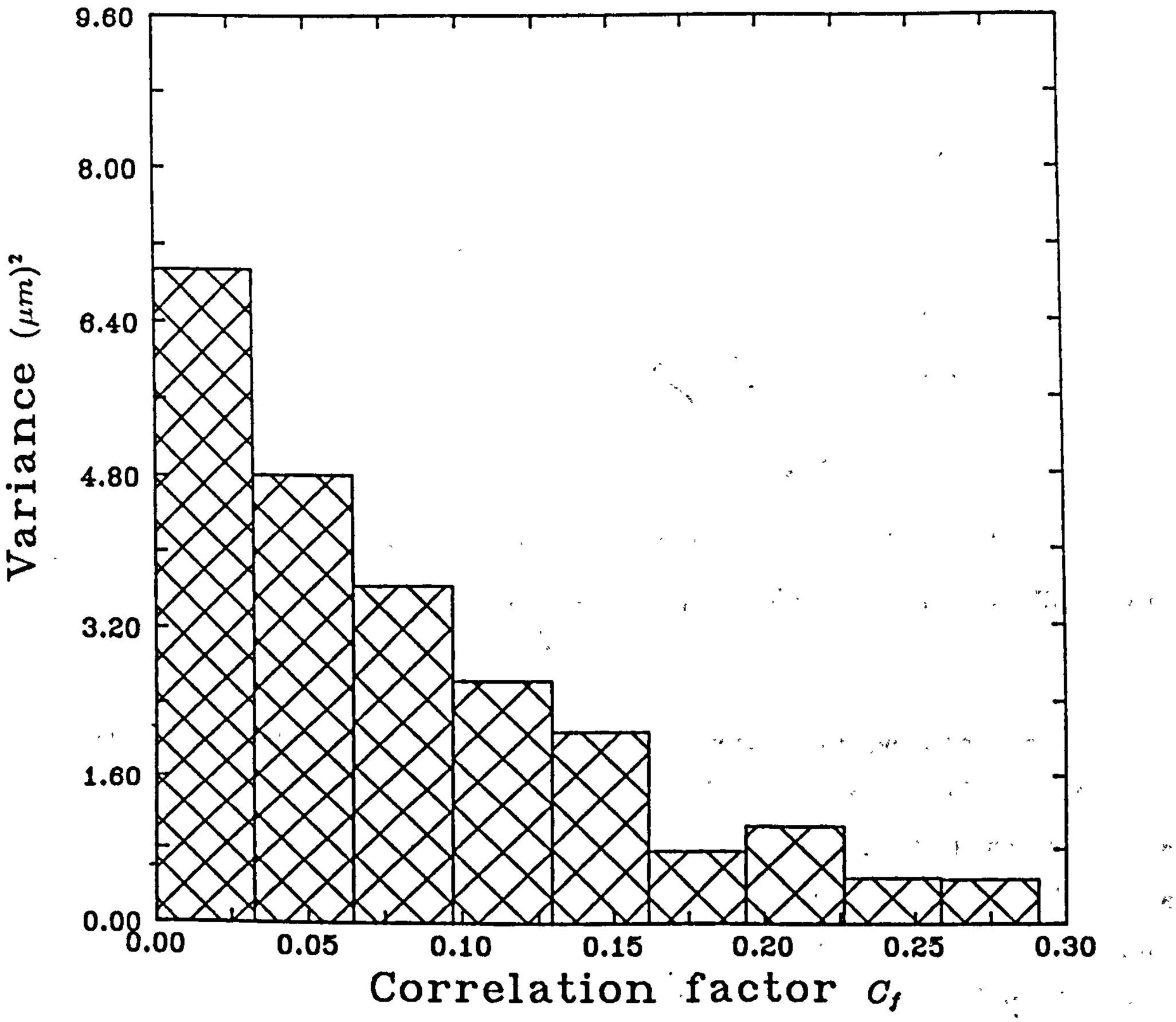

Figure 4.1: Histogram of the variance of displacement measurements with C_f.

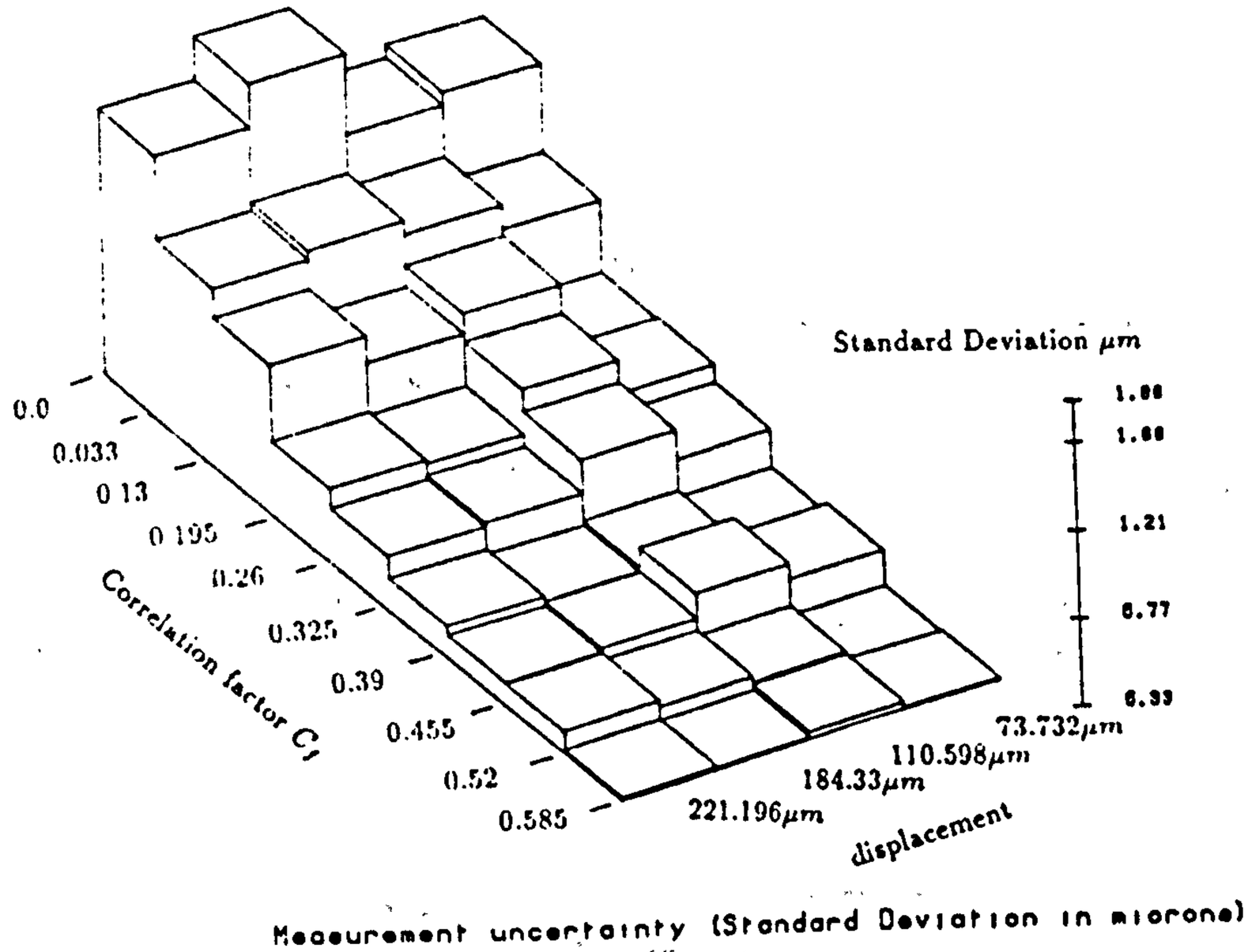

Figure 4.2: Standard deviation versus C_f for displacements of $73.732\mu m$, $110.598\mu m$, $184.33\mu m$ and $221.196\mu m$.

search described in Chapter 3 then locates a correlation peak that is not associated with the motion of the flow and which produces a displacement value that is inconsistent with the valid measurements made from the negative. These spurious values were removed, the remaining measurements calibrated to give displacement values, and then grouped into bands of varying C_f. The variance of each group was calculated and then plotted as a histogram (fig 4.1). The uncertainty for a displacement of $184.33\mu m$ decreases fairly consistently from $\sigma^2 = 6.92(\mu m)^2$ at $C_f = 0 - 0.033$ to $\sigma^2 \approx 0.5$ at $C_f = 0.22$. Beyond this point the uncertainty seems to vary little. Experience has shown that most PIV measurements will be made within the range of C_f shown.

This procedure was repeated for 3 further displacements of $73.732\mu m$, $110.598\mu m$ and $221.196\mu m$. The uncertainty distribution for the four sets of measurements is shown in figure 4.2 from which it can be seen that the absolute uncertainty varies in a similar manner for all four displacements.

The relative error as a percentage of the total displacement is shown in figure 4.3. It can be seen that the relative importance of the absolute uncertainty is greater

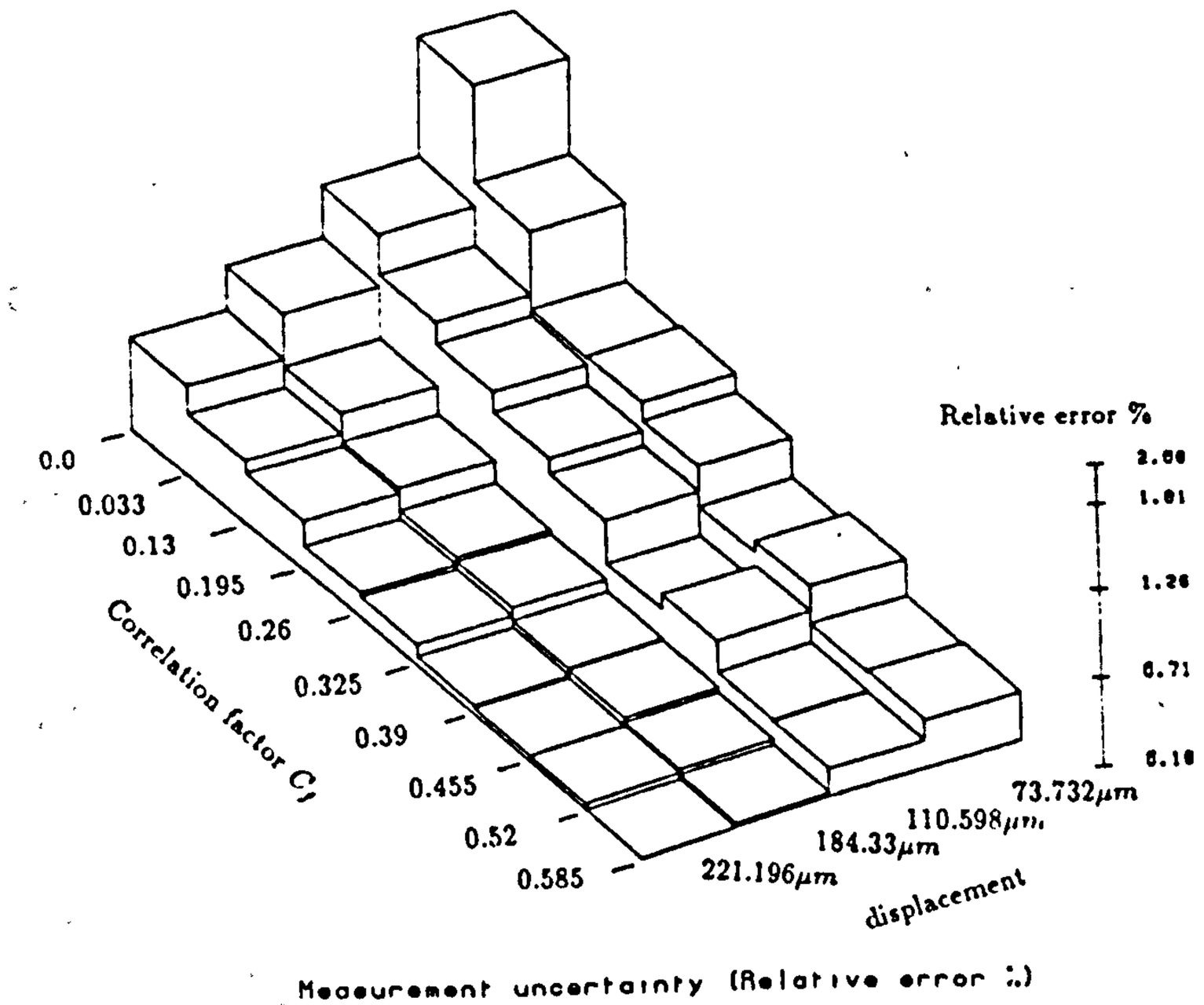

Figure 4.3: Relative uncertainty versus C_f.

for small displacements. For a displacement of $73.732\mu m$ and a correlation factor between 0.0 and 0.033 the relative error is $\approx$ 2%. At the other extreme, for a displacement of $221.2\mu m$ and C_f of 0.52-0.585 the relative error is $\approx$0.2%.

Measurement failure versus Correlation factor C_f

Of the 2000 or so measurements made across the mock negative approximately 200 appeared to be inconsistent with the majority of the similarly oriented vectors. The relative frequency of visually detected spurious vectors was plotted against their C_f values and are shown in figure 4.4. It can be seen that the probability of a measurement giving a spurious value becomes increasingly significant as the degree of correlation C_f associated with that measurement drops. It can be seen therefore, that the C_f value may be used to indicate the degree of confidence attributable to a given displacement value. This is considered further in Chapter 5.

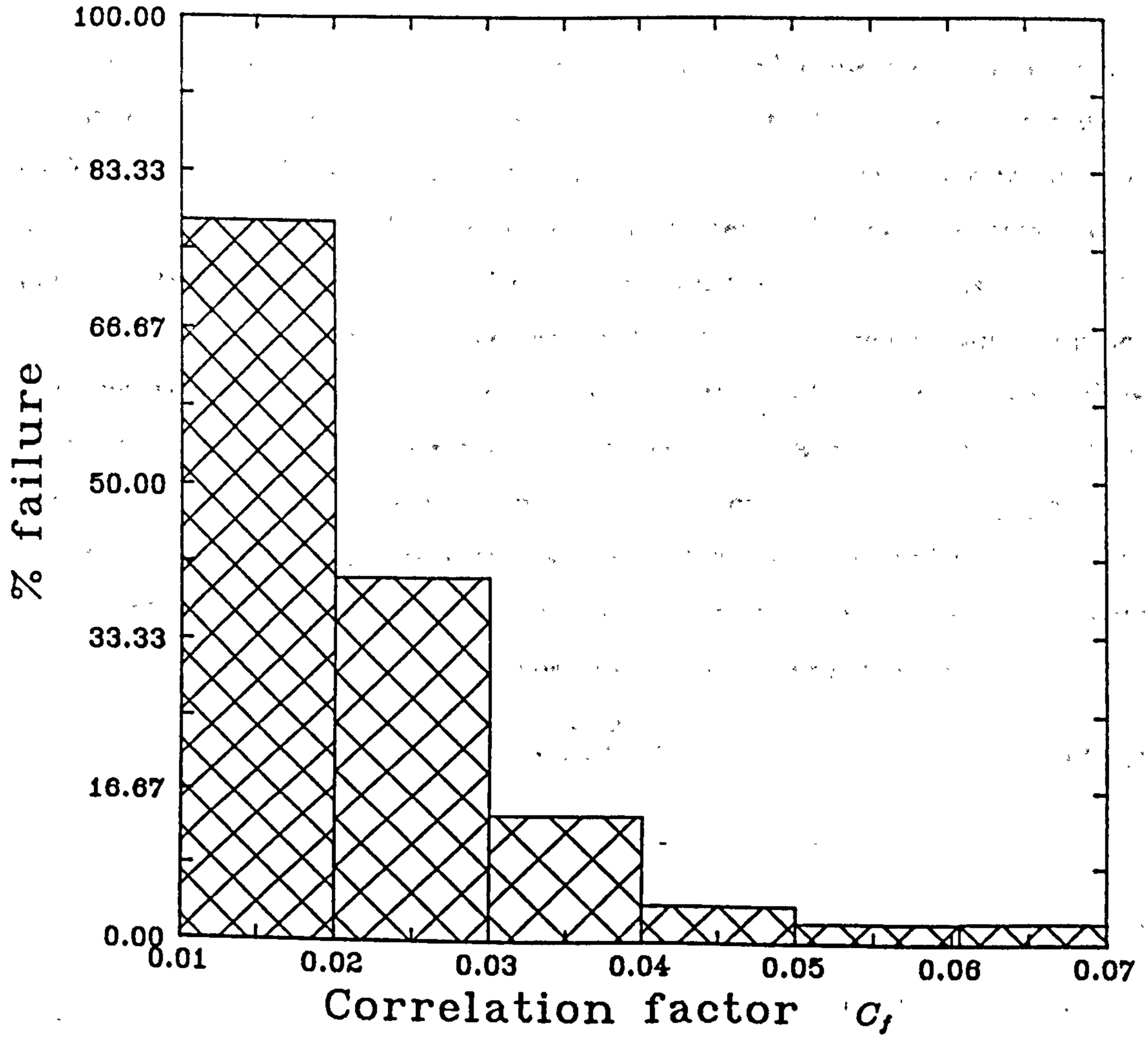

Figure 4.4: Percentage of detected spurious measurements versus C_f.

4.2.2 Velocity Gradient Uncertainty

It is shown in chapter 3 that the centroid of the displacement correlation peak R_{d+} gives, within the limits of uncertainty imposed by the random correlation peaks and the analysis hardware, the mean particle displacement η within the area of the probe beam. The probe beam diameter is chosen to be small compared to typical spatial scales of motion within the flow and it is commonly assumed that the particle displacements within this area are constant. In practice however, the probe beam area will cover a range of fluid velocity which is discretely and randomly represented by the particle image displacements within the interrogation area. For water waves up to breaking, the velocity profile is generally a non-turbulent velocity gradient and so the measured mean displacement η from each analysis point depends upon the particular particle displacements d_l that occur across the range of velocities within the probe region,

$$\eta = \frac{1}{N}\sum_{l=1}^{N} d_l \tag{4.74}$$

Consequently, η is a random variable with mean and variance given by,

$$\mu = E[\eta] \tag{4.75}$$

$$\sigma^2 = E[(\eta - \mu)^2] \tag{4.76}$$

where E represents an ensemble average over all possible values of the random variable η [17].

In order to evaluate μ and σ^2 analytically it would be necessary to calculate the probability density function $p(\eta)$, which itself will be a function of the particle image pair concentration and the range of velocities occurring within the interrogation region. For low seeding densities and large velocity gradients $p(\eta)$ will be wide. For higher seeding densities and smaller gradients of displacement across the probe spot $p(\eta)$ will become narrower with the variance σ^2 tending towards zero in the limits of very high seeding concentration and zero velocity gradient. Additionally, $p(\eta)$ will typically be assymetric due to the systematic bias against larger particle displacements (see Chapter 2, Section 2).

Using a computer simulation it is possible to model the effect of random sampling of a spatial velocity gradient across the probe region including the effect of finite particle image displacements. Thus, the mean and variance of PIV measurements made over varying velocity gradients and seeding densities can be estimated.

Numerical Model

NAG routines G05EBF and G05EYF [2] were used to generate a uniform random distribution of two-dimensional coordinates representing the initial positions of particle images within a $4mm^2$ area of a PIV negative (figure 3). The positions of the displaced particle images were calculated according to a spatial displacement gradient given by,

$$\underline{d}(x,y) = \underline{d}_0 + Fx + Gy \tag{4.77}$$

where $\underline{d}(x,y)$ gives the separation of a particle pair centred at x,y in the x and y directions, $\underline{d}_0$ is the particle displacement at $x = y = 0$ (the centre of the probe spot) and $F = \frac{\partial d}{\partial x}, G = \frac{\partial d}{\partial y}$, the rate at which the particle separation changes in the x and y directions respectively. This assumes that the displacement vector $\underline{d}$ varies linearly across the measurement area and is a reasonable assumption so long as the probe spot diameter is kept small. A circular probe region is defined in the centre of the seeded region and the positions of the particle image pairs checked to see if they fall within this area. If three or more complete particle image pairs are within the interrogation spot it is considered sufficient for a succesful measurement and the mean of the displacements calculated and stored. This procedure is repeated a large number of times (2000) to give a set of measurements of the same velocity field that is extensive enough to approximate the ensemble average required to calculate σ^2 and μ.

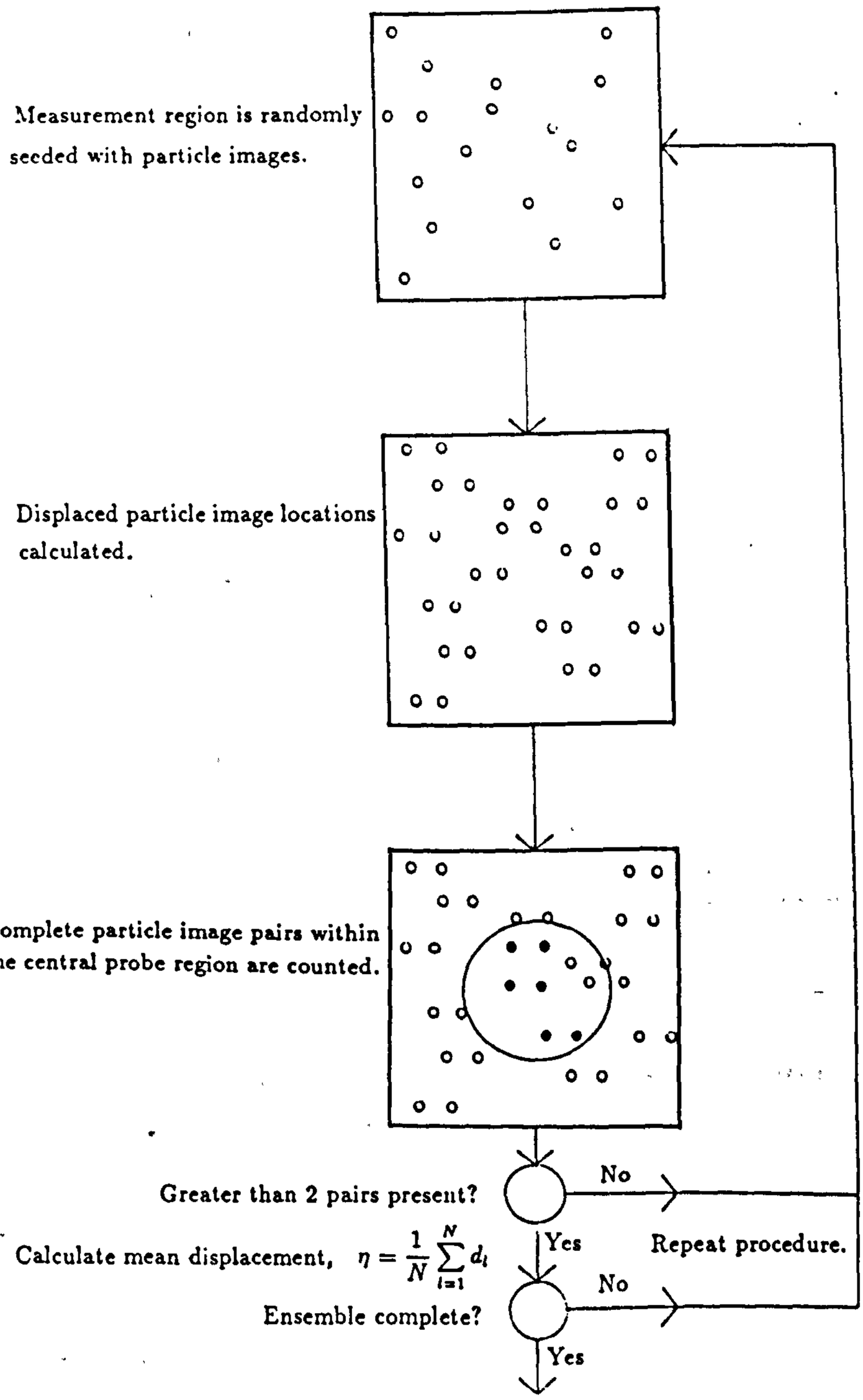

Figure 4.5: Numerical modelling of the measurement process

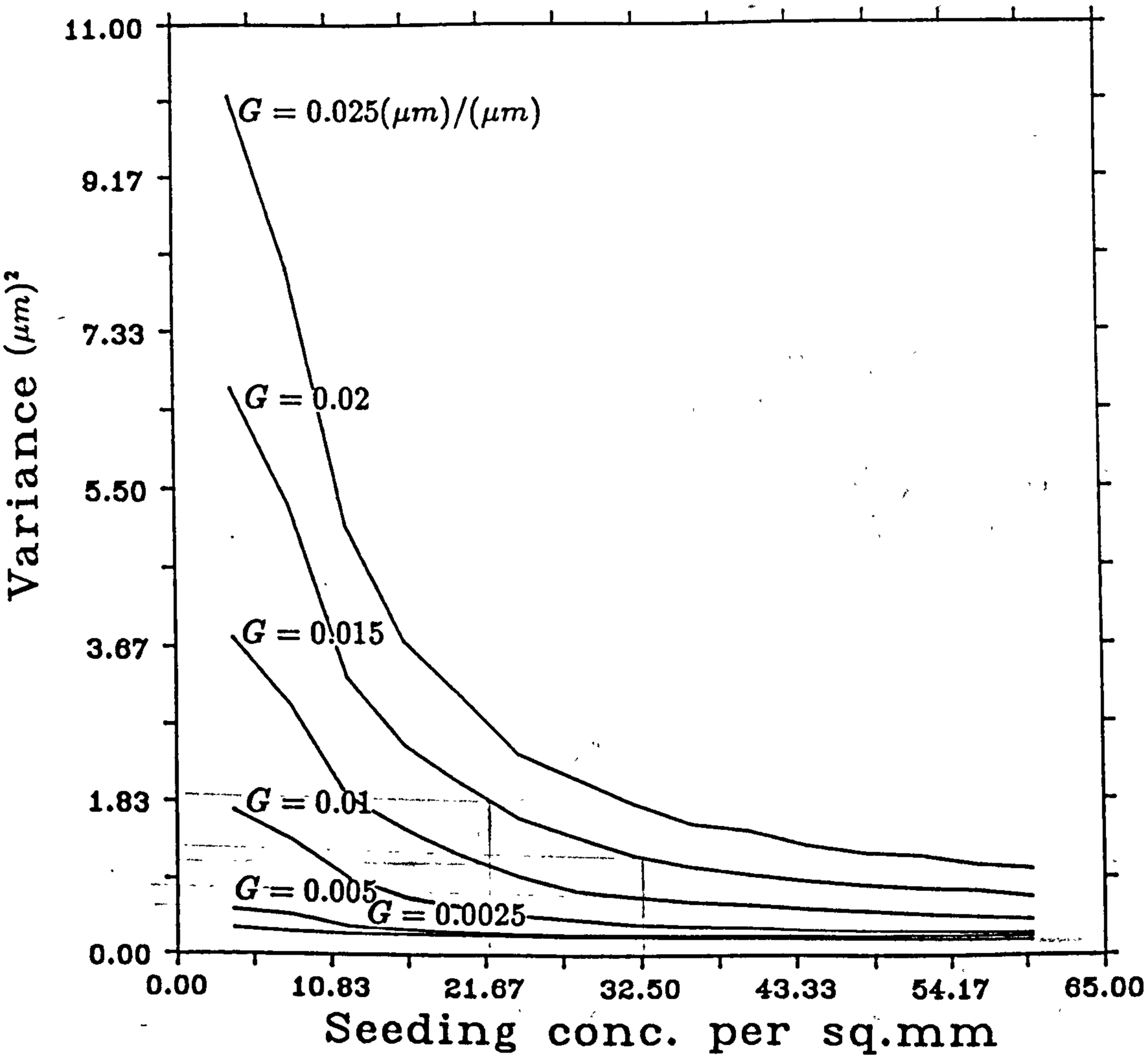

Figure 4.6: Measurement variance versus seeding concentration for a range of displacement gradients within probe spot.

Results

Figure 4.6 shows the dependance of the measurement variance on the seeding concentration and the gradient of displacement across the probe spot. These results are obtained for a probe spot diameter D of $1mm$ and a displacement gradient with $F = 0$, $d_0 = 150\mu m$ and G from $0.0025(\mu m)/(\mu m)$ to $0.025(\mu m)/(\mu m)$. The displacement vector $\underline{d}$ is chosen to have only one component perpendicular to the velocity gradient G. This is a simple case but illustrates the essential dependance of the measurement uncertainty upon the seeding density and the range of velocities within the probe spot. It can be seen from figure 4.6 that σ^2 decreases dramatically for increasing seeding density up to ≈ 20 particles/mm^2.

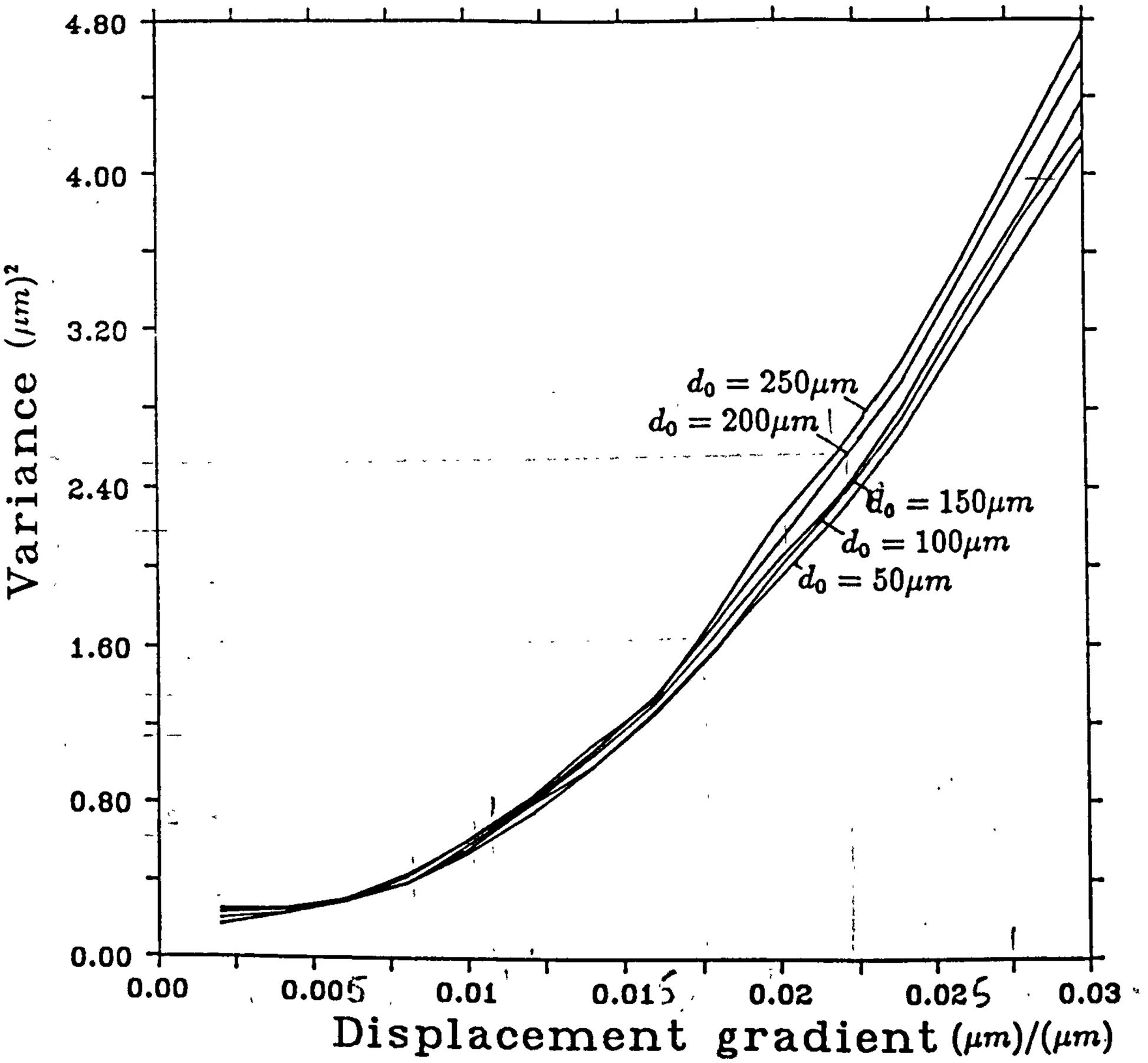

Figure 4.7: Measurement variance versus displacement gradient for a range of mean particle displacements d_0.

This suggests that seeding much past this level will not significantly reduce the measurement errors and from the discussion in Chapter 2 it is known that heavy seeding will result in a speckle pattern being recorded rather than resolved particle images with the measurement limitations that this entails. It is also seen that an increasing range of particle displacements within the probe spot will increase σ^2. The dependance upon the displacement gradient G is more clearly illustrated in figure 4.7 where it can be seen that σ^2 increases non-linearly with G. The absolute uncertainty will be given by σ the Standard Deviation and actually increases almost linearly with G. The variance σ^2 is kept here, however, as it allows the effect of increasing d_0 to be seen more clearly. Figure 4.7 shows the σ^2 versus displacement gradient curves for $d_0 = 50, 100, 150, 200, 250\mu m$ which represent $1/20, 1/10, 3/20, 1/5, 1/4$ of the probe diameter respectively. It can

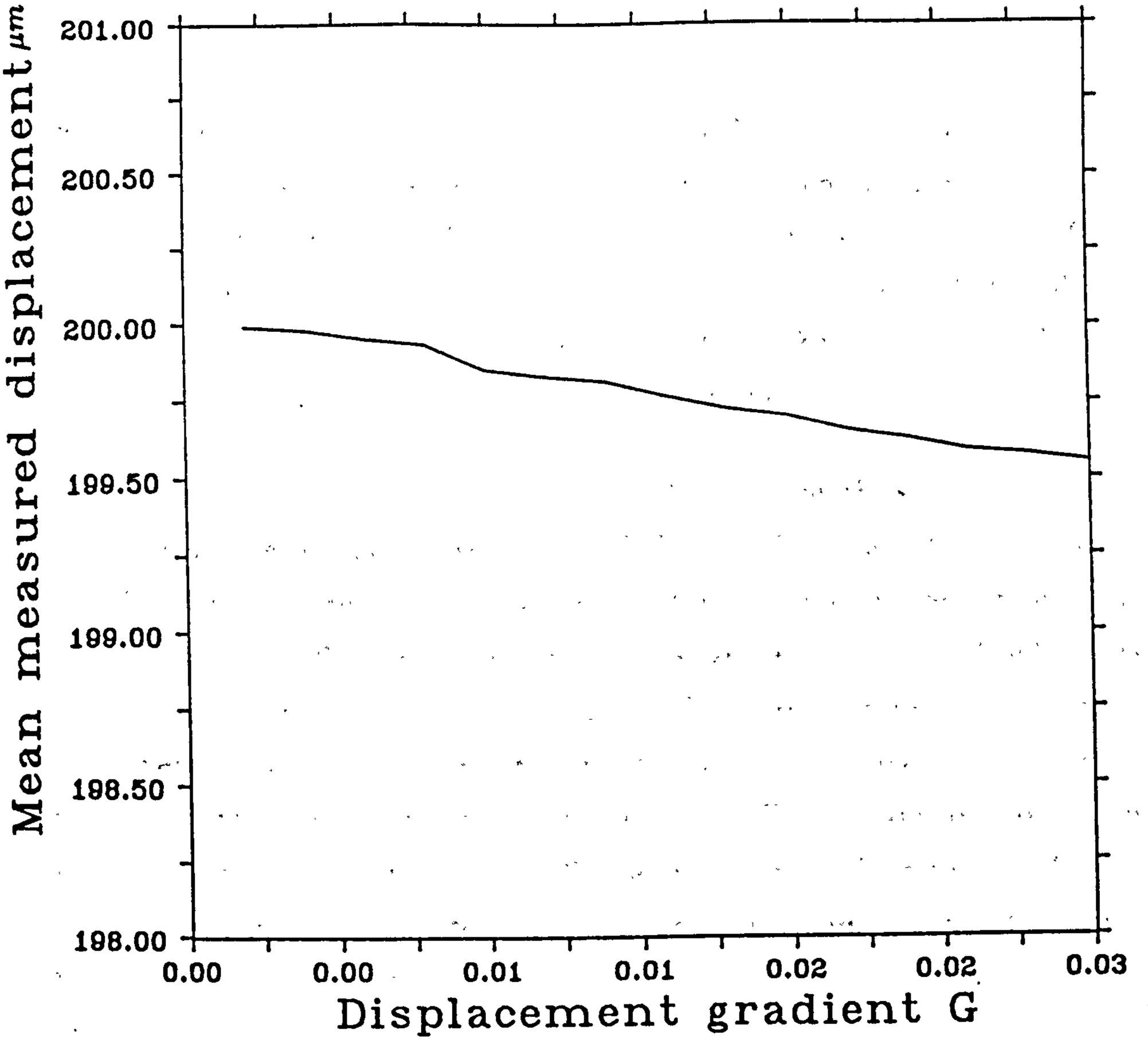

Figure 4.8: Mean measured displacement versus displacement gradient G for $d_0 = 200\mu m$.

be seen that as the mean particle displacement increases the variance also increases. This is a consequence of the reduced probability of a complete particle image pair falling within the probe spot as d_0 increases, producing an artificially lower seeding density and increasing uncertainty. This effect also influences the ensemble average of the measured μ.

The probability of obtaining a complete particle displacement within the probe spot decreases as the particle displacement increases. Thus, within an interrogation region that covers a range of particle displacements there will, on average, be less of the larger displacements included in the measured displacement. This effect is illustrated in figure 4.8 where the computer model is set up for a range of displacement gradients from 0.0 to 0.03$(\mu m)/(\mu m)$ about a displacement of

$200\mu m$ at the centre, $(x = y = 0)$, of the circular probe region. For small particle displacement gradients the measured displacement μ corresponds to the displacement at the centre of the probe i.e. $200\mu m$. However, as the value of G is increased the mean value of η drops below the central displacement value due to the inherent bias against larger displacements. This effect will typically be very small and only becomes significant $\approx 0.25\%$ for values of $G \approx 0.03(\mu m)/(\mu m)$.

An additional factor that will not be considered in depth is the influence of a velocity profile on the measurement reliability. The peak R_{d+} will become spread over a larger region of the autocorrelation plane as the velocity gradient represented on the PIV negative increases. Consequently, the amplitude of the displacement correlation peak is reduced and so, for measurements that are made over a strong displacement gradient and have other sources of decorrelation included, such as out-of- plane motion, the probability of a random correlation peak being located rather than the displacement peak will increase. This will introduce an upper limit to the velocity gradient that is measureable for a given probe diameter, seeding density etc.

It can be seen therefore, that velocity measurements made through a velocity gradient will be subject to a random error which will increase approximately linearly with the magnitude of the gradient. Additionally, there will be a small bias superimposed on the measurements due to the diminishing probability of measuring larger displacements.

4.2.3 Combined errors

From the estimated strength of the signal correlation C_f, the local velocity gradient and the concentration of particle image pairs on the negative it should be possible to estimate the measurement uncertainty. The local velocity gradient can be estimated from the values of neighbouring measurements and the local particle image concentration from a manual inspection of a photograph of the PIV transparency. The value of C_f is determined in the manner described in

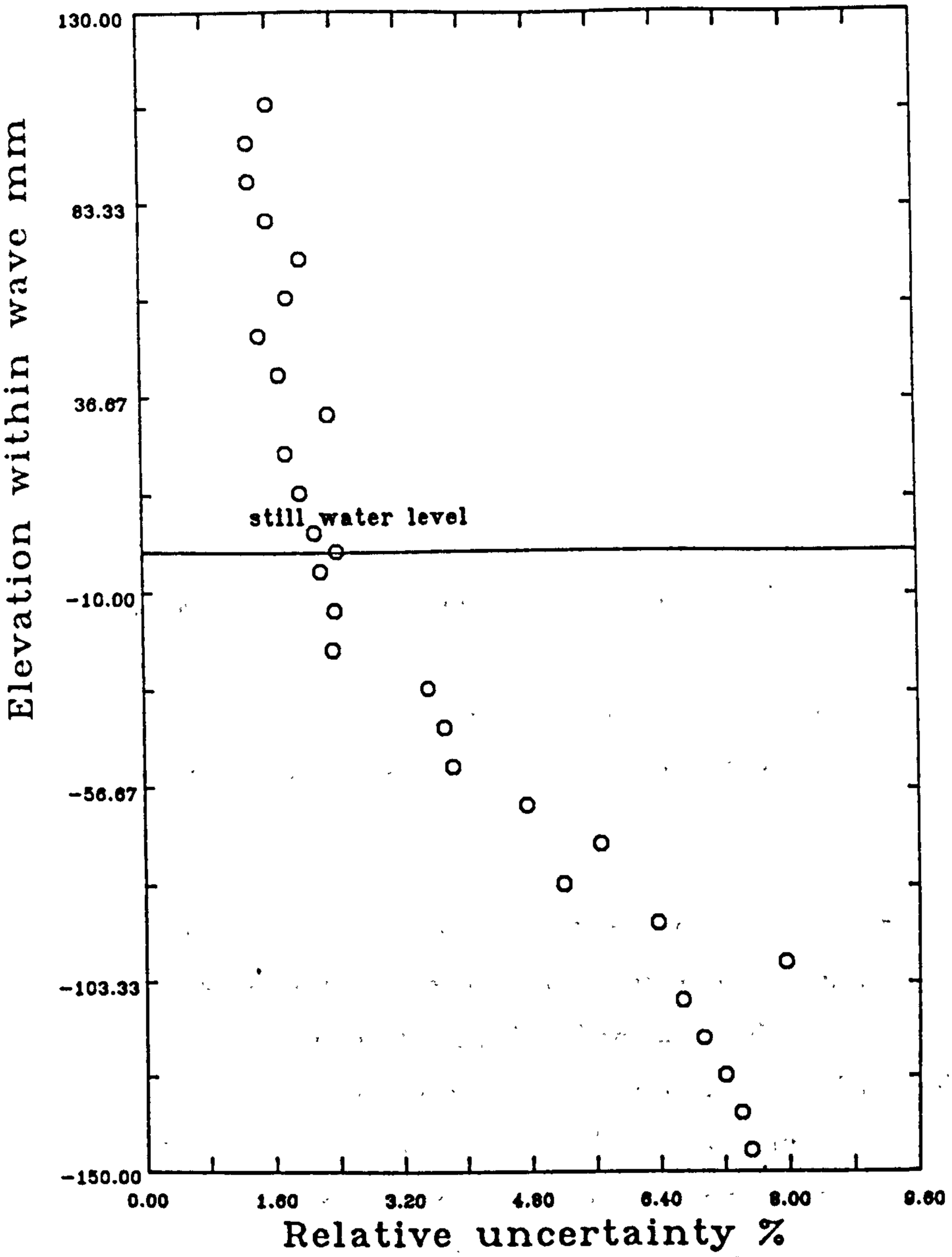

Figure 4.9: Estimated uncertainties associated with the horizontal component of velocity along a vertical line in a plunging breaker.

Chapter 3.

Figure 4.9 shows the relative uncertainty associated with velocity measurements made in a vertical line through a laboratory generated plunging wave[4]. The calculated uncertainties can be seen to range from $\approx$ 7% in the lower regions of the wave and decrease to $\approx$ 1.4% near the crest region. This estimate of the measurement errors assumes that the uncertainty associated with measurements made in a uniform flow is independent of the velocity gradient uncertainty.

[4]The details of the wave measurements are given in Chapter 6.

A similar computer model has been reported by Coupland et. al.,1988,[30] and used to investigate the statistical behaviour of the signal-to-noise ratio (based on the ratio of the height of the signal peak to the next highest peak) as a function of the seeding density. The procedure in the Coupland model is similar to the model used here in that a random number generator was used to "seed" the interrogation area and displacement coordinates added for a constant displacement. The autocorrelation of the random pairs is calculated and convolved with a particle image function to represent a correlation function similar to that derived from a PIV negative or positive. For each of these realisations of the simulated measurement process the ratio of the highest to the next highest peak is measured. A large number of such realisations then allowed the statistics of the SNR to be determined.

The model that is used here is similar in most respects in that it attempts to mimic the randomness with which the displacement information is represented on the PIV record by the particle image pairs. The main difference however is in the information derived from essentially the same starting point. The model used here represents the measurement process through a velocity gradient and allows the influence of seeding particle concentration on the measurement uncertainty to be estimated. However, it is interesting to note that both models result in similar conclusions being drawn concerning the optimum seeding density. Coupland concludes that up to a concentration of 7 particle image pairs per interrogation spot there will be an increase in the signal-to-noise ratio and thus a greater probability of successfully locating the signal peak. For the model used here to determine the statistical error in velocity measurements through a velocity gradient it is shown that a significant reduction in the random error can be achieved by increasing the seeding concentration up to approximately 8 pairs per interrogation spot. Beyond this value the reduction in the uncertainty becomes less pronounced.

Chapter 5

Post processing of velocity data

It is important to consider how large data sets, typically available from PIV measurements, can be presented to convey maximum information. Horizontal and vertical components of the measured velocity can be compared numerically with other experimental measurements or with theoretical calculations. Alternatively, the data may be presented on its own as an array of velocity vectors (see figure 5.1). This is a common method of presenting two dimensional velocity data and gives a useful quantitative visualisation of the measured flow. Regions of maximum and minimum velocity can be easily identified as well as the flow structure, from small scale turbulent regions to the large scale flow profile.

Another informative method of presenting the flow field is to calculate the vorticity distribution. Since vorticity is determined from the spatial derivative of velocity the vorticity field is not masked by a constant velocity reference frame, and therefore frequently reveals the flow structure more readily than the velocity field.

This Chapter considers the evaluation and presentation of PIV data and describes the procedure for presenting the data as a straight velocity distribution or as its derivative (vorticity).

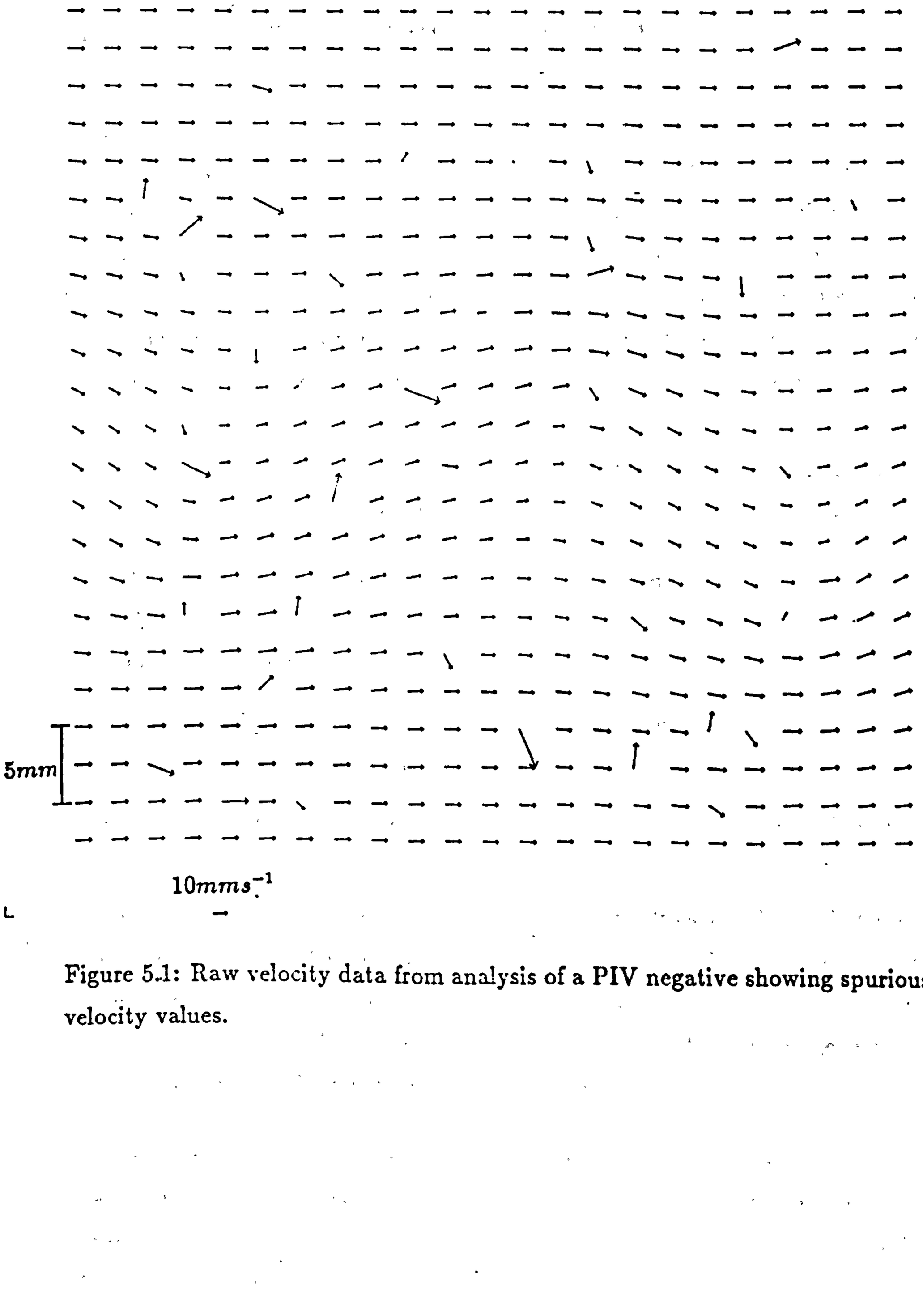

Figure 5.1: Raw velocity data from analysis of a PIV negative showing spurious velocity values.

5.1 Removal of anomalous data

Visual interpretation of the velocity field and calculation of vorticity is simplified if the velocity values are present on a regular grid. In the system described in Chapter 3 measurements are made over a regular grid on the flow record and to a good approximation (limited by the distortion of the image relative to the illuminated plane) will represent equally spaced measurements in the flow. However, further processing and display of the data is complicated by the presence of a number of spurious velocity values which occur because,

- The interrogation point falls outside the flow boundaries and consequently there is no displacement information present to give a measurement.
- The mean particle displacement within the interrogation spot is smaller than that resolvable by the seeding particles, ie. the second particle image partially or completely overlaps the first image.
- The particle displacement information within the probe area has become extremely decorrelated due to out-of-plane motion, etc.
- Insufficient or no particle image pairs exist within the interrogation area.

Observation of the "raw" velocity data from the analysis rig shows that these values are easily identifiable by eye (see figure 5.1). This is because the observer interperets the general motion of the flow from those vectors that seem to form a coherent structure. This allows the erroneous values, which will in general not be consistent with this structure, to be identified.

A filtering procedure described by Ochs, 1988[95] compares each vector with the mean of its nearest neighbours. If the difference between them is less than a user-specified limit the velocity measurement at that point is deemed valid. However, there are difficulties in implementing this approach which arise from,

- Correctly setting the bound outside which the majority of erroneous values will fall.
- Calculating an accurate local mean velocity from neighbouring values when there is no indication as to whether these values are themselves valid.

A more robust technique based on global evaluation of data would be required to identify the random spurious data values and is an area that requires further research.

For the measurements described in this thesis removal of spurious data was achieved using an interactive graphics program. This allows the whole or part of the measured velocity distribution to be viewed on the computer monitor as a vector arrow distribution (see figure 5.2). The C_f value of the velocity vector nearest to the mouse pointer is displayed on the right hand side of the screen and provides the user with an independent measure of the confidence that may be associated with that value. In this way erroneous data points can be easily identified and deleted by a subroutine activated via the mouse pointer.

For waterwave measurements typically only a small percentage of all measurements were spurious and so there was little difficulty in identifying and removing them. In other applications an automatic filtering routine may become necessary to cope with a higher percentage of erroneous measurements.

Flow boundaries

In regions of flow negatives that are outside the flow boundaries (e.g. above the wave profile) the lack of displacement information will result in spurious values being generated. These values are excluded from the final data by introducing the coordinates of such boundaries and then excluding the values that fall outside.

For the wave measurements described in Chapter 6 the surface profiles were

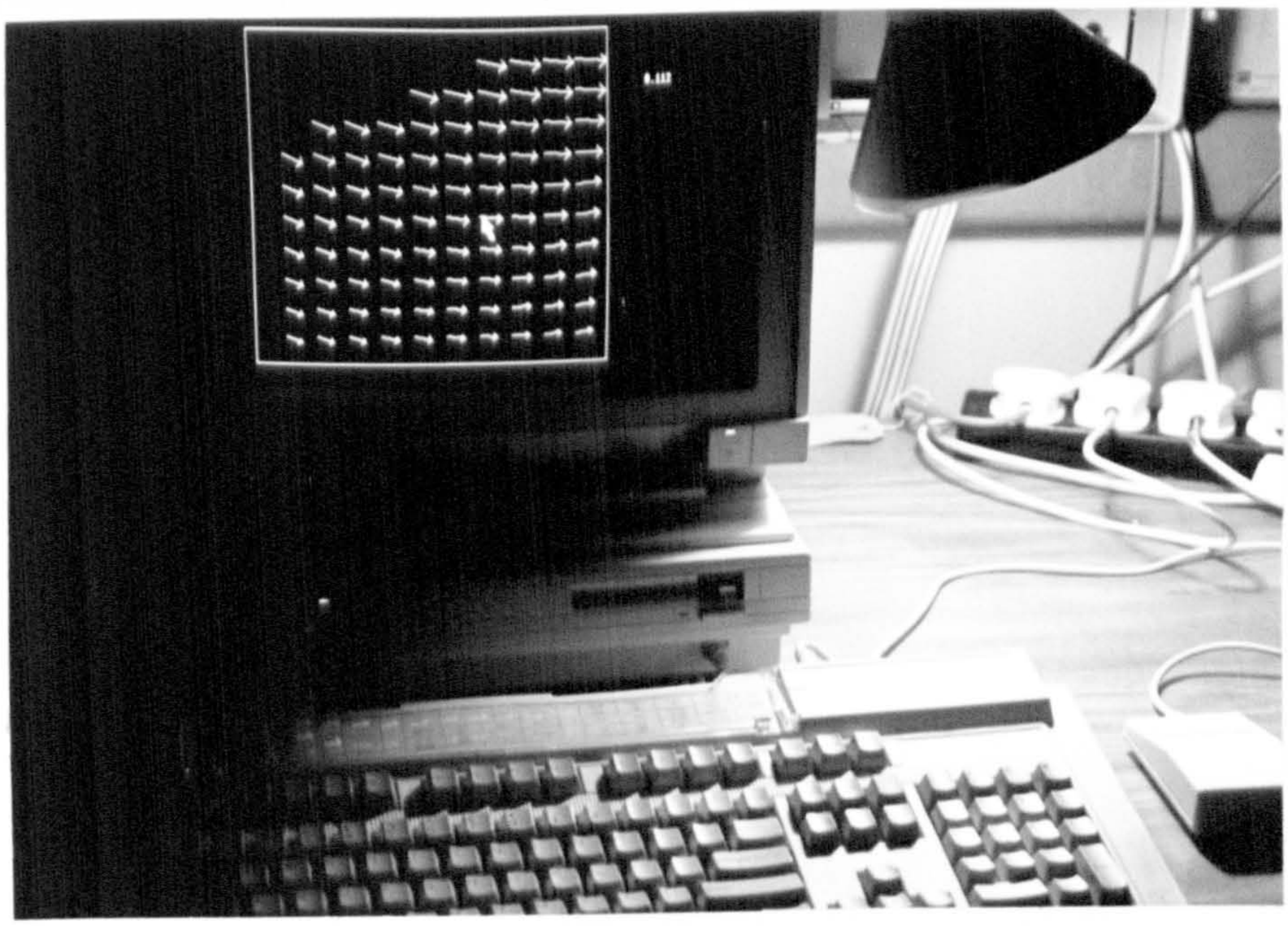

Figure 5.2: The interactive editing program allows the velocity data from the analysis of PIV negatives to be viewed and assessed visually. Magnification of smaller areas, removal of spurious vectors and interpolation are performed via the mouse, permitting rapid and precise processing of small data sets.

measured using a pupose built light table onto which the PIV negative is fixed with a flat transparent plate. The plate is scribed with a precise $1mm^2$ grid and the surface of the wave viewed through the grid using a travelling microscope. The approximate coordinates of the surface at a discrete number of points are determined from the scribed grid on the plate relative to a central datum mark[1]. The travelling microscope is then used to make precise measurements of the wave profile relative to the nearest grid point. The resulting set of coordinates are then input into the graphics plotting routine as a data file [2].

[1]The same datum used as a reference for the velocity measurements.

[2]Post processing of data as described in this chapter is performed on the Edinburgh Multi Access System Mainframe computer EMAS. The code is written in FORTRAN 77 and uses a number of basic graphics routines to create a graphics file which can be output to a plotter.

5.2 Interpolation

The use of an interpolation routine to fill those regions of the data set that were removed as spurious is useful for two reasons. Firstly, a continuous grid of velocity values provides the observer with a complete and therefore more easily visualised picture of the flow. Secondly, numerical differentiation of the velocity distribution to get vorticity will be seriously incomplete if even a few velocity values are missing. It must be appreciated that interpolation of data is only approximate and cannot be assigned the same accuracy as those velocities that have been succesfully measured from the negative. The closeness of a given interpolated point to the actual velocity will depend upon the accuracy of the neighbouring values and the interpolation scheme used.

The method described here is a very simple linear type interpolation where the horizontal and vertical components of velocity $u_x(x,y)$ and $u_y(x,y)$ are calculated from a "plane" that has been fitted to the nearest neighbouring velocity values (not including values that are themselves interpolated). ie,

$$u(x,y) = a_0 + a_1 x + a_2 y \tag{5.78}$$

$$v(x,y) = b_0 + b_1 x + b_2 y \tag{5.79}$$

The coefficients a and b are chosen to minimise the least squares error between the plane and the surrounding data values.

An example of this scheme is shown in figures 5.3 and 5.4. Measurements made from the surface flow system, described in Chapter 7 are shown before and after interpolation of the missing values. It can be seen that visually, a sensible representation of the flow is produced. More accurate interpolation may be possible with higher order schemes and this is an area that requires further research.

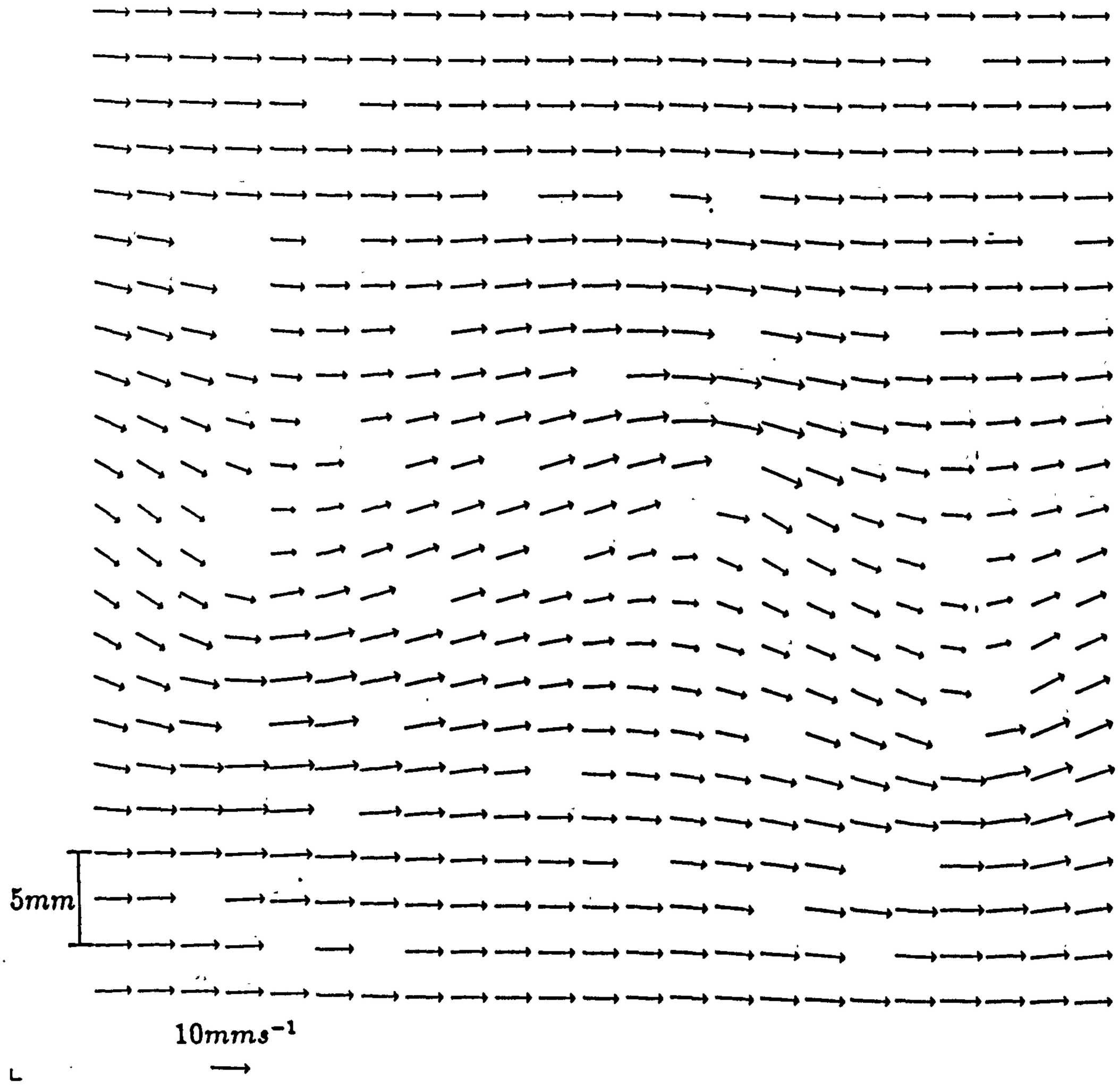

Figure 5.3: Velocity data set with the spurious values shown in fig. 5.1 removed.

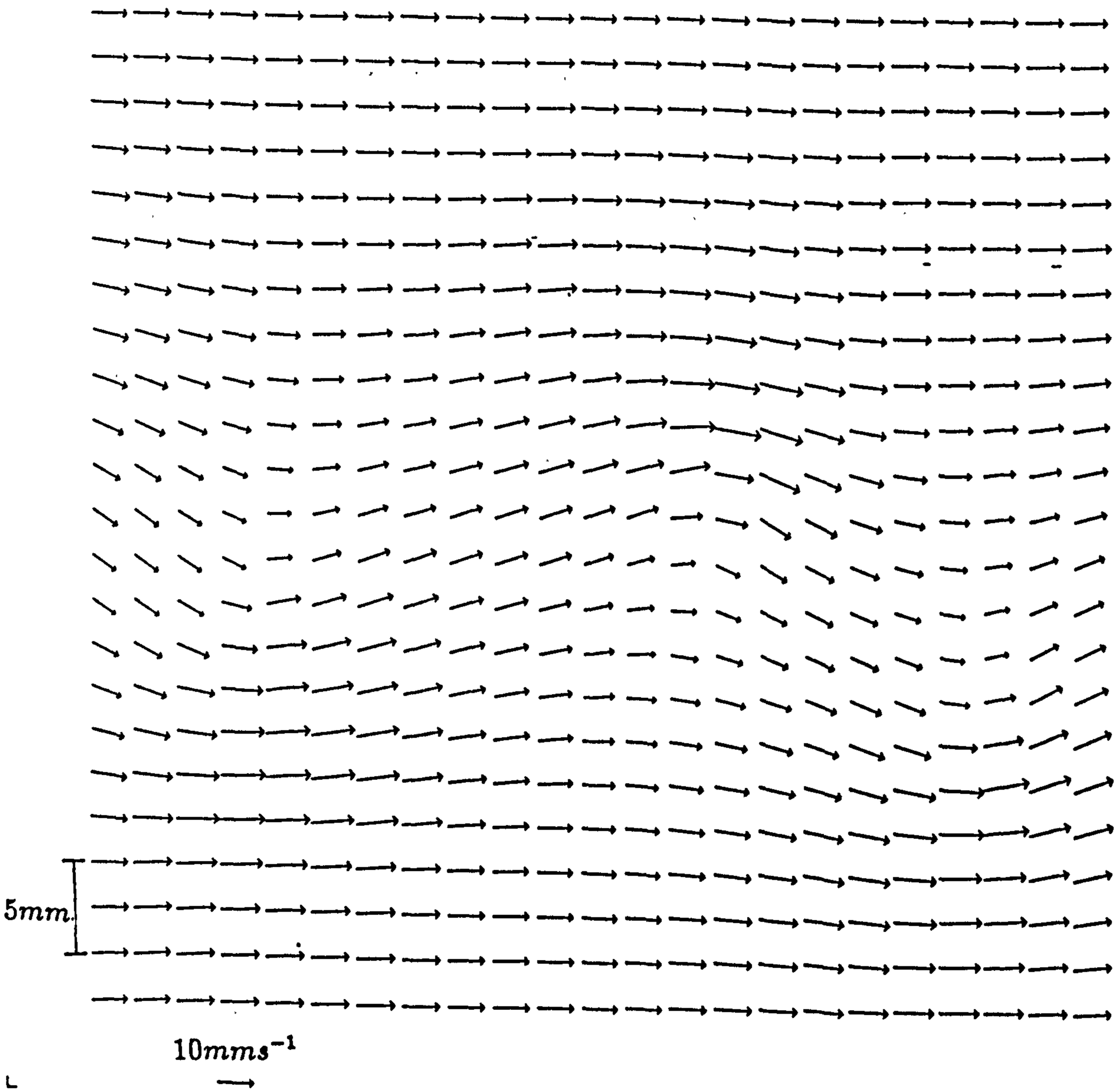

Figure 5.4: Velocity data set with interpolated values replacing those missing from fig. 5.3.

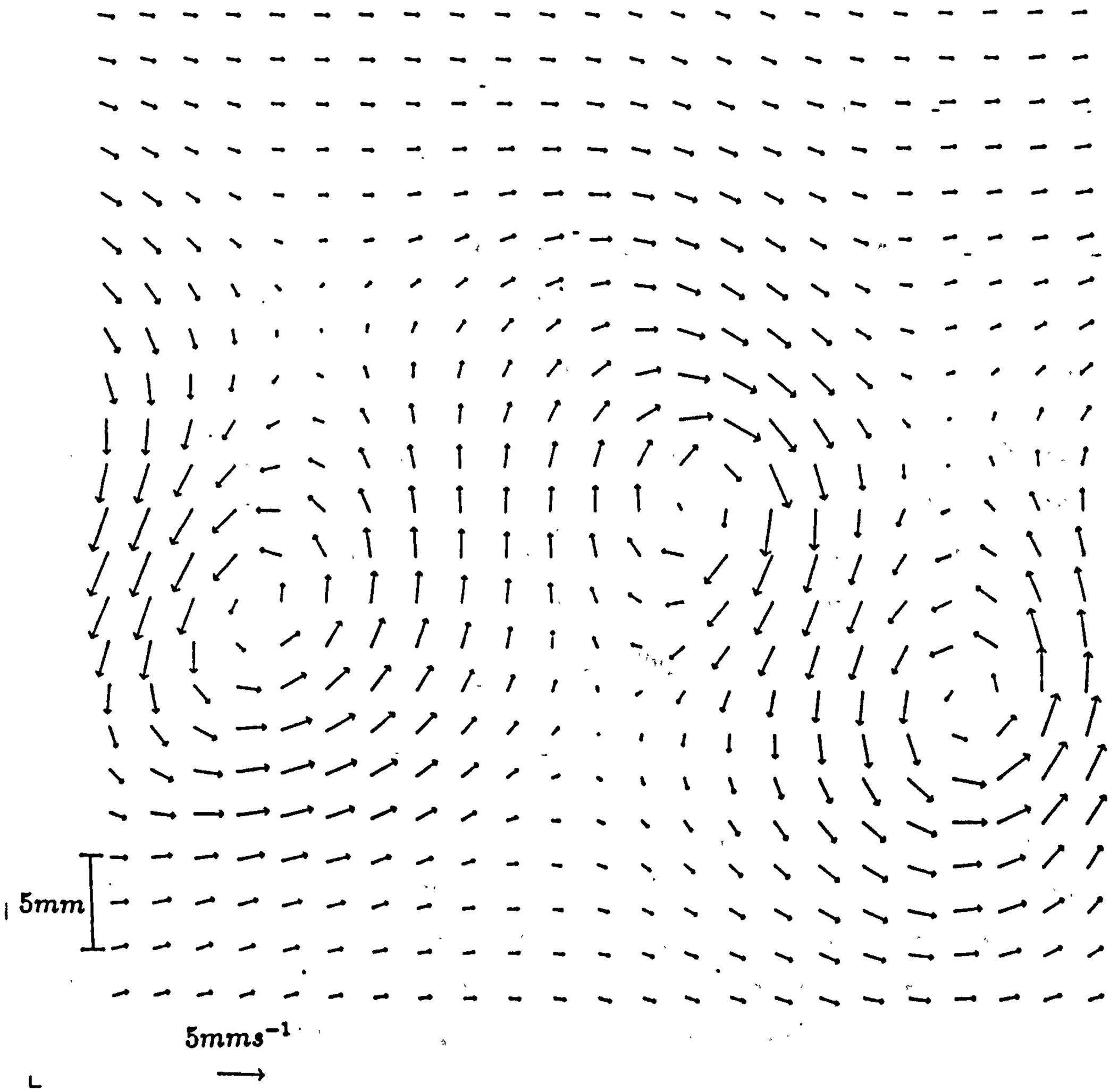

Figure 5.5: The velocity data shown here is the same as that in figures 5.1,3 and 4 but is represented from a frame of reference that is moving at approximately the same velocity as the vortices.

5.3 Vorticity Calculations

Having prepared the velocity data by identifying the spurious data points and replacing them with interpolated values the velocity distribution can now be differentiated to get the vorticity.

Vorticity is a measure of the rotation of an individual fluid element about its centre and, in vector notation, is given by,

$$\underline{\omega} = \nabla \times \underline{u} \tag{5.80}$$

where $\underline{\omega} = (\omega_x, \omega_y, \omega_z)$ represents the three components of vorticity in the x, y and z directions and $\underline{u} = (u_x, u_y, u_z)$ represents the velocity in the x, y and z directions. If the flow is two-dimensional in the plane imaged on the flow photograph the vorticity perpendicular to this plane is given by,

$$\omega_z = \frac{\partial u_y}{\partial x} - \frac{\partial u_x}{\partial y} \tag{5.81}$$

The vorticity at a point within a set of PIV velocity values can then be calculated by numerically differentiating the velocity using neighbouring velocity values[95]. Considering the velocity value (A_x, A_y) and its four nearest neighbours $(D_x, D_y), (C_x, C_y), (B_x, B_y)$ and (E_x, E_y) (see figure 5.6) the vorticity perpendicular to the plane of the measurements is given as

$$\omega_z = [(B_y - D_y)/2dx - (C_x - E_x)/2dy] \tag{5.82}$$

. Applying this calculation to the whole grid of velocity values allows the vorticity to be calculated over a similarly spaced grid minus the outside values for which there is insufficient information.

The calculated vorticity is most easily represented as a surface. This can be done using a relief plot similar to those used to represent the autocorrelation functions in Chapter 3 or alternatively as a contour plot. Figure 5.7 shows the

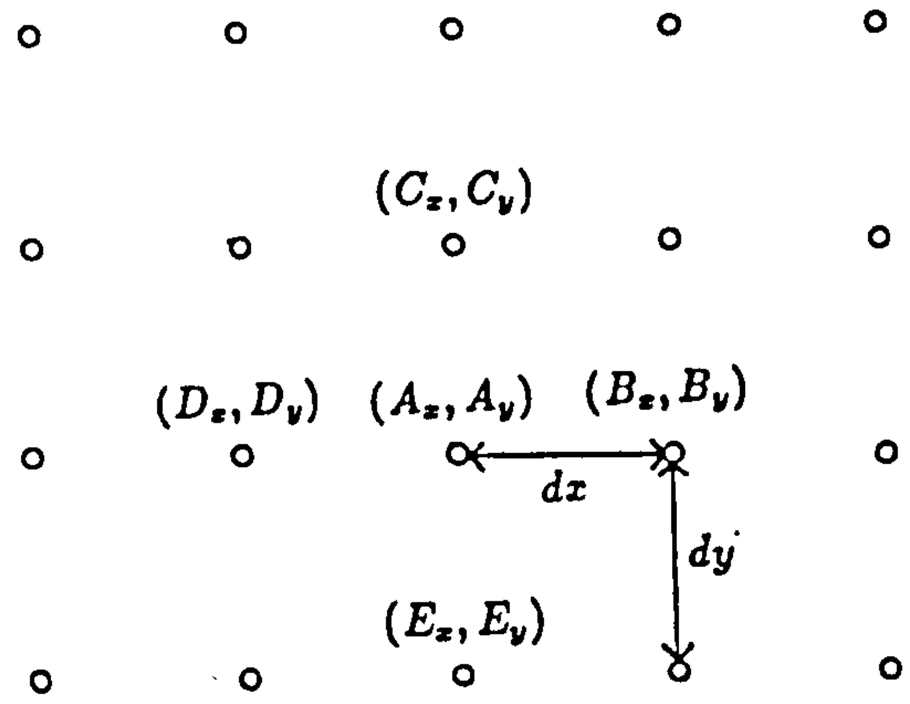

Figure 5.6: Small roundels indicate the positions of individual velocity measurements used in vorticity calculations.

vorticity distribution that has been calculated from the velocity measurements presented previously in figures 1,3,4 and 5.

The vorticity surface shown in figure 5.7 is not completely smooth. A certain amount of irregularity in the vorticity distribution will be due to the flow itself and is due to small variations in the towing speed of the cylinder, convective currents etc. However, further irregularity of the vorticity surface is due to random errors present in the velocity measurements. The errors associated with B_y, D_y, C_x and E_x are summed in the calulation of ω_z while the numerical differentiation in equation 5.82 produces a value that is generally much smaller than the individual velocity components from which it is calculated. Thus, the relative error associated with an individual vorticity value will be considerably larger than the errors in the raw velocity values.

For flows where the vorticity is large in magnitude it is likely that a reasonable representation of the vorticity distribution will be possible. However, when the vorticity levels are low the random errors associated with the velocity values will tend to swamp the calculated vorticity and produce an irregular surface. For the measurements in figure 5.7 the vortex structure can be seen quite clearly but the contours are fairly irregular because of the random component in the

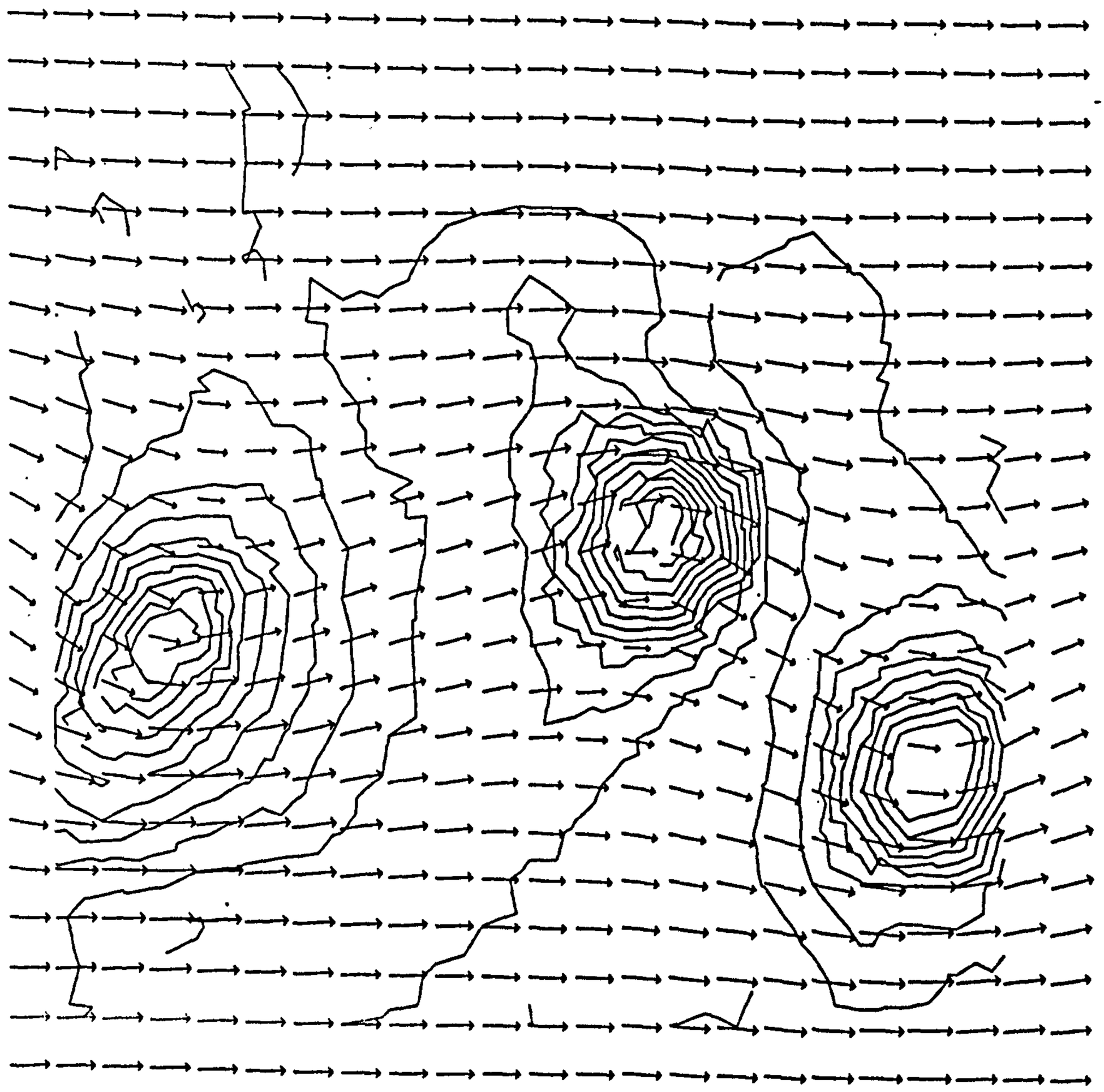

Figure 5.7: The vorticity contours are shown superimposed ontop of the velocity measurements and shows clearly the strong regions of vorticity that are centred on the vortices.

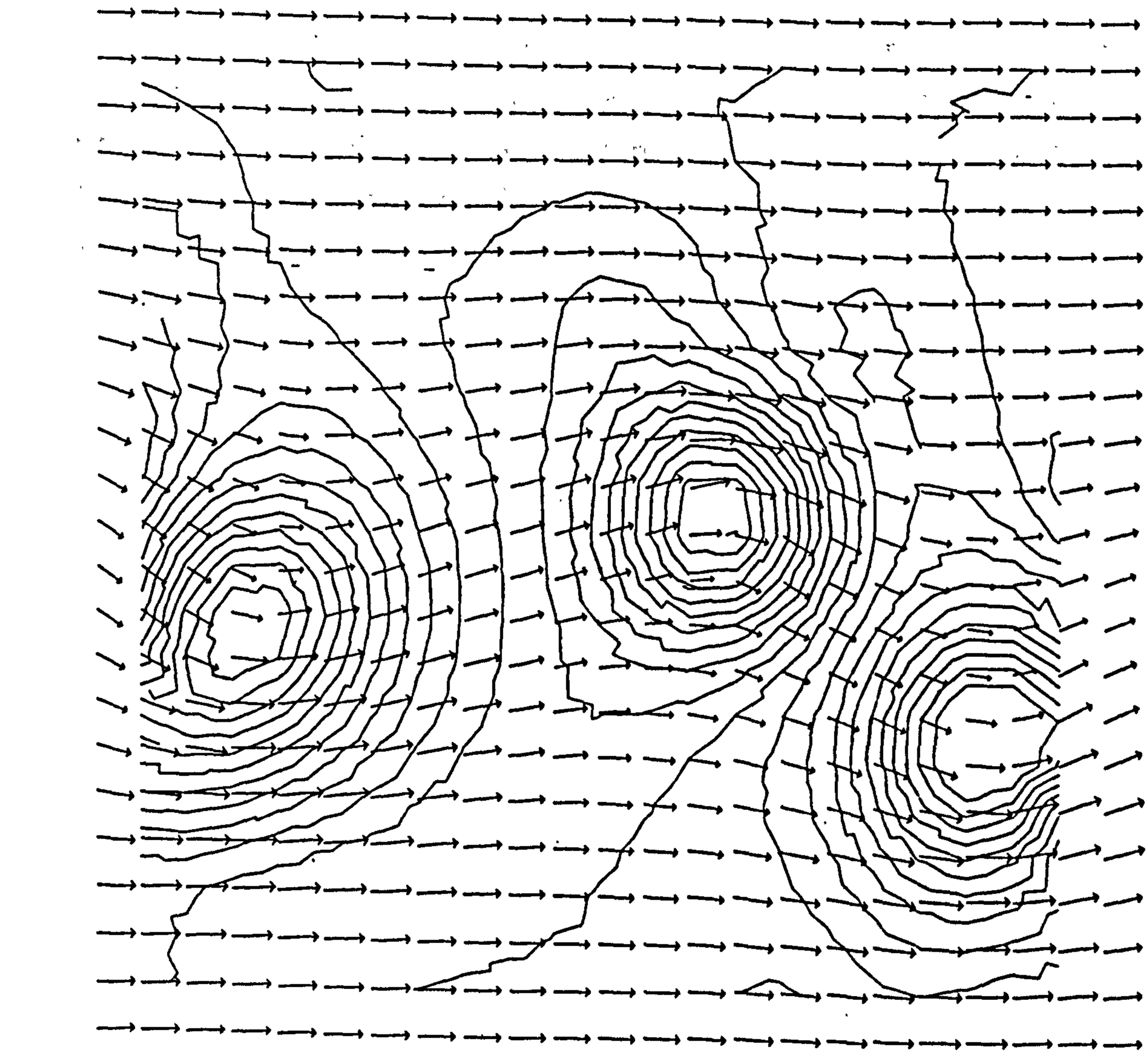

Figure 5.8: Contour representation of the vorticity surface after application of a median filter to remove small random irregularities.

vorticity values passed on from the random error associated with the velocity values. Application of a median filter to the vorticity surface before fitting the contours helps to smooth out the irregularities seen in figure 5.6 and clarifies the contour representation of the vorticity distribution (see figure 5.8).

Representing the PIV velocity data in this way provides a clear and visualisation of the measured flow. However, the calculated vorticity distribution will in general be most valuable for indicating, through its shape, the general vorticity. Absolute values of vorticity will be limited in accuracy and are likely to be further compromised in accuracy by the filtering procedure.

Chapter 6

Experimental measurement of a deep water breaking wave

Breaking waves represent one of the most extreme events in a marine environment and a knowledge of their internal kinematics is required for estimation of drag and inertial forces on offshore structures.

A number of robust, fully non-linear, time-stepping numerical models are now available for two-dimensional waves [84,38], but they can be difficult to apply to practical situations and are limited in their application to the early stages of breaking. Experimental studies have have also been undertaken using a range of velocity measuring techniques[39,119,78] but the results have frequently been of low accuracy, particularly in the crest region.

Laser Doppler Anemometry (LDA) has been succesfully used to make precise velocity measurements under water waves [45], but some problems are encountered in its application. Most of these complications have been solved by the use of established computer algorithms for the analysis of the Doppler signal and detailed studies of velocity distributions have been made and utilised for structural design purposes [44]. Nevertheless a fundamental limitation exists in the use of LDA and other point measuring devices used for water wave studies.

Generally, a whole vector plot of particle velocities under a specified wave is re-

quired for design purposes or as a sensitivity test for theoretical models. So, for point measurement techniques, complete vector plots can only be constructed in cases where the wavefield being studied can be repeated many times while moving the probe to a series of positions within the flow field. Exact repetition of waves up to and through breaking is difficult and even using sophisticated wave generation techniques crest velocities have been shown to vary significantly from one wave to the other[38]. This means that each point measurement is averaged over a number of realisations at the same point in successive waves. This allows a precise estimate of the mean and deviation of velocities but obscures the fine spatial velocity information particular to individual waves. For truly random events it becomes impossible to obtain full-field information from point measurement procedures.

The previous chapters have outlined the principles and techniques that have been employed in the development of a full field measurement system for wave studies. This chapter describes the application of this system to an example wave that may be experienced in an offshore environment. An in-depth Fluid Dynamical evaluation of the wave measurements is beyond the scope of this thesis. The main objective here is to show that it is possible to make detailed measurements of surface elevation and internal fluid velocities as functions of time and position so as to reasonably define the flow field within an extreme wave. It is particularily important that good quality measurements be possible above the still water level and up into the spout or crest region of the wave being studied.

The wave chosen to be measured is a plunging breaker and is the most extreme that may be encountered in a marine environment. Successful measurement of such a wave would indicate that the PIV wave measuring facility described here would be an invaluable tool for the extension and development of wave research.

6.1 Laboratory generation of waves

6.1.1 Waveflume

The wave flume used in this experiment is roughly based on a similar flume that has supported the development and implementation of LDA measurement of breaking waves [57]. The PIV flume is 6.0 meters long and 0.3 meters wide and has a still water depth of 0.53 meters (see figure 6.1). The scale of the tank allows waves of sufficient size to be generated that scaling laws can be used to reliably extrapolate velocity measurements up to real sea scale. Waves are generated by a hinged wave maker and propagate through a central 2 meter measuring region before being absorbed by a triangular cage packed with expanded aluminium beaching material. The central 2 meter section is constructed from 20mm thick glass and provides optical access through the side of the tank for photographing the flow and for introducing the light sheet to illuminate the plane of interest. Waveheight measuring gauges are positioned in front of the wave paddle so that the composition of the wavefield can be established and tank repeatability checked. The wave paddle itself is of the absorbing type [108], with its force on the the water dependent upon the drive signal and a filtered paddle velocity signal, leading to simultaneous generation of waves and absorbtion of reflections respectively. The drive signal is generated by a computer (Acorn Archimedes micro) which can sample the wavegauge and trigger the camera shutter while simultaneously generating the wavefield[1].

6.1.2 Wave generation

Water waves are dispersive in a finite depth of water and an extreme wave can be generated by choosing a wave-packet that will converge or self-focus. The

[1]Software used to generate the drive signal, sample the wave gauge and trigger camera written and operated by D.J. Skyner, Physics Department, Edinburgh University.

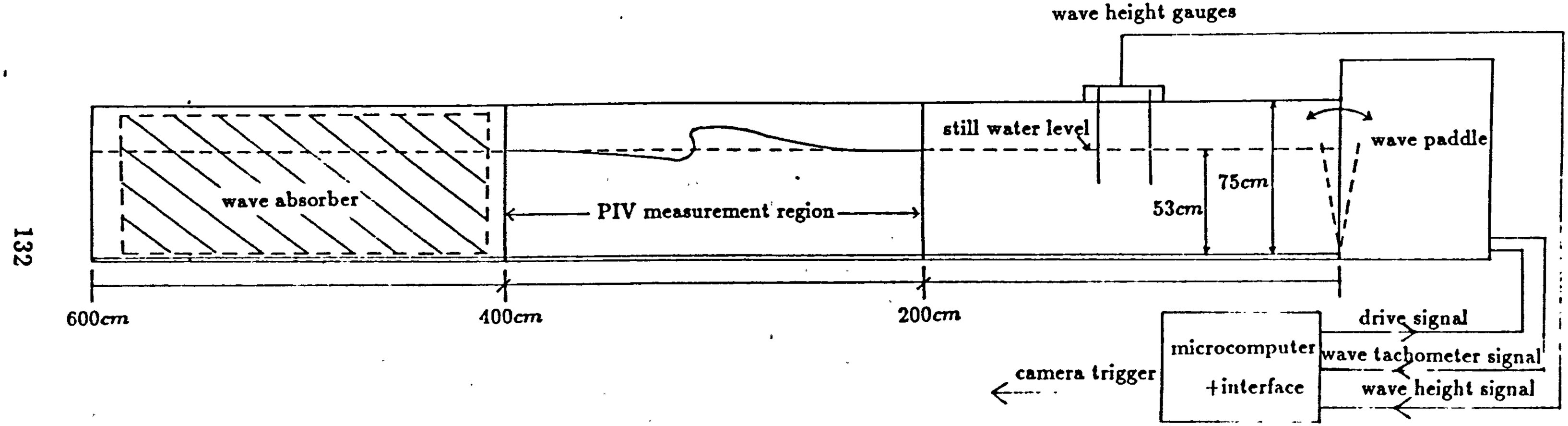

Figure 6.1: Side elevation of PIV wave flume.

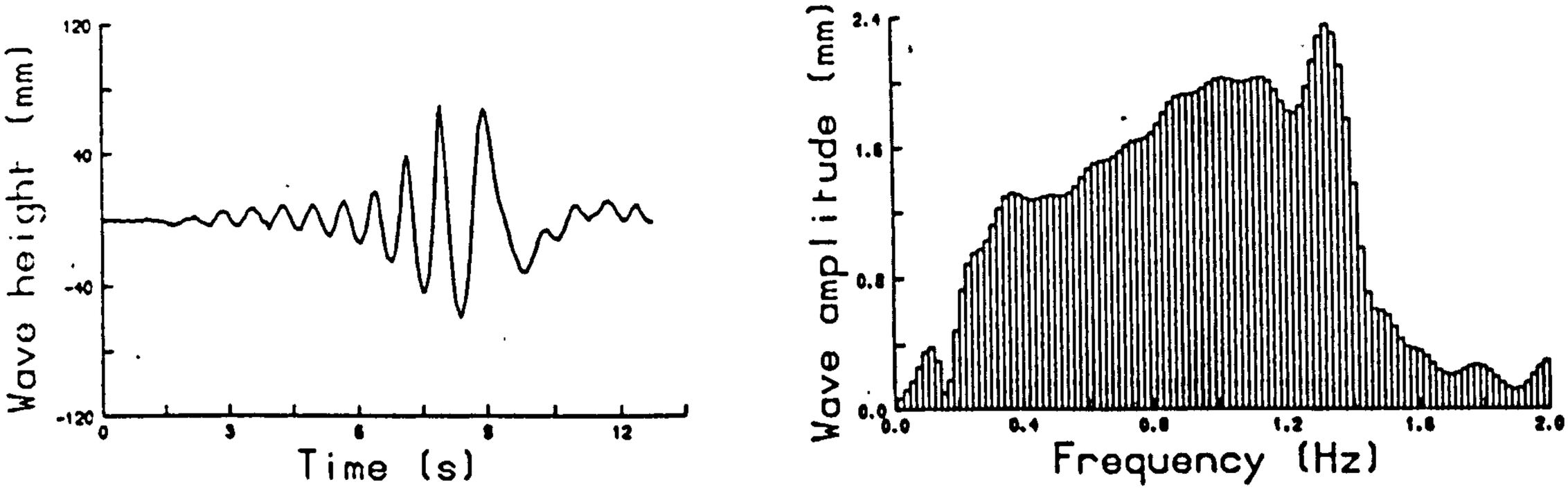

Figure 6.2: the composition of the wavefield ahead of the wave paddle is detected by the wave-gauge (see figure 6.1). The wave gauge record is shown on the left and its spectral content (calculated by FFT) on the right. Both diagrams courtesy of D.J.Skyner (see[114]).

choice of the starting wave packet usually assumes linear theory but since the propagation of the wave becomes non-linear as the wave approaches breaking the starting conditions are chosen arbitrarily and require the parameters to be adjusted until the required breaker is formed.

The breaking waves were generated by superposition of sinusoidal components with sufficient parameters in the final specification of the spectrum to allow fine adjustment of the form of the breaker. A description of the wavefield composed of discrete sinusoidal components at equally spaced frequencies is given by,

$$a(x,t) = \mathcal{R}\left\{ \sum_{n=N_0}^{N_1} A_n \exp^{ik_n x + i\omega_n t + i\phi_n} \right\} \tag{6.83}$$

where

$$\omega_n = 2\pi n \delta\omega \tag{6.84}$$

. The dispersion relationship for sinusoidal waves of frequency ω and wavenum-

ber k in a water depth of h is given by

$$\omega^2 = gk\text{tanh}kh \tag{6.85}$$

. The phases ϕ_n of the components of the wavefield were chosen so that, if linear theory applied, they would have a common phase at a point within the measurement region of the wave flume. Further fine adjustment of the phases and amplitudes was then used to obtain a clean plunging breaker within the central 2 meter section of the wave flume (see figure 6.2).

6.1.3 Two-dimensionality of waves

It was noted in Chapters 2 and 4 that considerable errors may be introduced into PIV measurements if there is a significant out-of-plane component of velocity in the flowfield being studied. It was not anticipated that this would be a problem due to the precise construction of the wave flume and the close fit of the wave paddle to the inside walls of the flume. However, as a test of the two-dimensionality of the waves generated and propagating within the tank a simple experiment was performed.

The laser illumination was set up as if to take a normal PIV photograph and the camera shutter set for an exposure of 1 second. A simple sine wave was generated in the tank and a photograph taken to record the motion over a time interval of approximately a whole wave period. The laser illumination sheet is approximately 2-3mm thick in the region shown in figure 6.3. The orbital motion of the particles is quite visible from the photograph and indicates that within the 1 second exposure time there was little fluid motion perpendicular to the plane of the illumination.

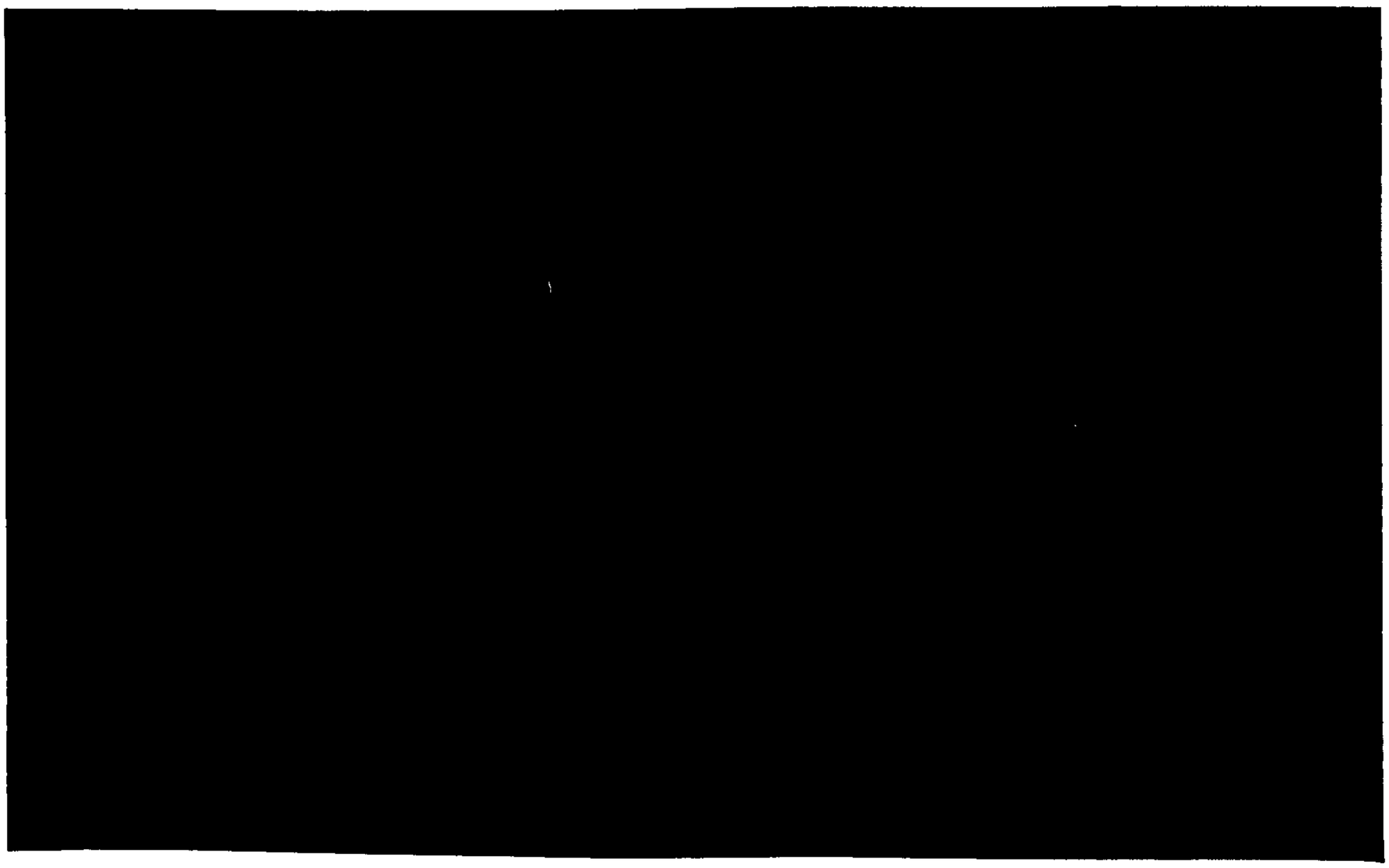

Figure 6.3: Multiple exposure photograph of particle motion within the wave flume over approximately one wavelength (pulse separation 4ms, shutter time $\approx$ 1 second).

6.2 Measurement procedure

Illumination system

The system used to illuminate the plane of interest within the tank is based on the scanning laser beam arrangement described in Chapter 2. Figure 6.4 illustrates the tank and laser system layout. The Spectra Physics 171 CW Argon Ion Laser providing illumination is cooled by purified water which is passed through a conditioner to remove heat and filter out impurties that may be deposited within the cooling pipes of the laser. The mirrors of the lasing cavity are kept clean with a Nitrogen purge. These components ensure that the power output from the laser does not fluctuate or drop within the time scales of an experiment and allow the laser to be operated at relatively high power $\approx$ 10W for longer periods of time. The external mirrors and lenses used in the illumination system are mounted on optical benches and where appropriate screwed to the wall or floor so that once set up, the beam will not become misaligned. The scanning rate of the beam is measured using a phototransistor arrangement positioned at the end of the parabolic mirror. This produces a small voltage pulse as the beam passes, allowing the scan period to be accurately measured using a digital storage oscilloscope. The system is typically operated with a scan period of 2-3ms which gives a pulse time of 6-10μs.

Camera positioning and triggering

The camera used to record the waves is a Hassleblad ELM with a 120 film back and a f2.8 T* Zeiss Tessar lens. The characteristics of the recording optics have been discussed in Chapter 2 and shown to give an extremely flat image field with almost negligible net distortion when the influence of the water and glass wall have been included.

The camera is mounted on a heavy duty tripod with the optical axis of the

PIV Breaking Wave Recording System

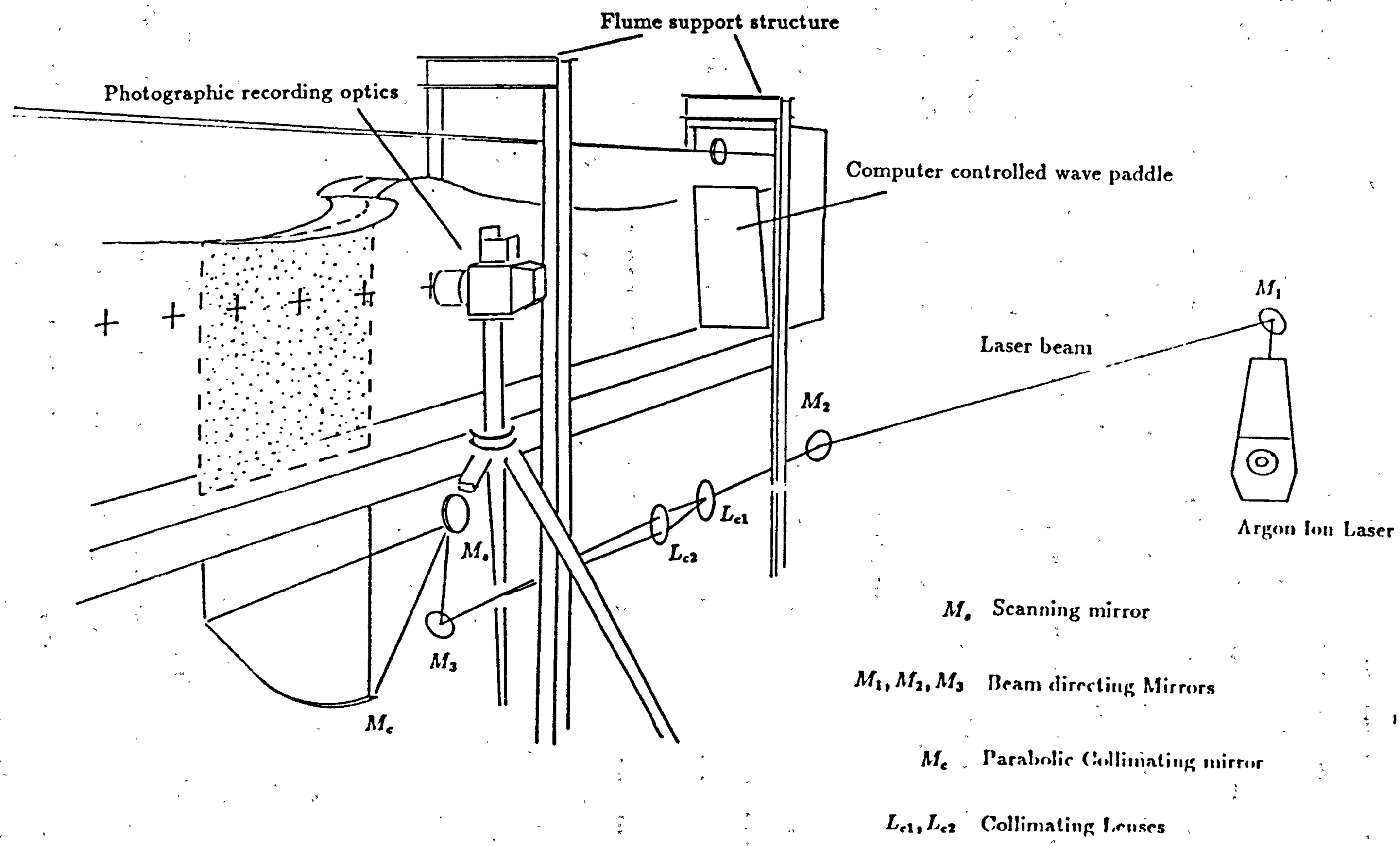

Figure 6.4: Tank and illumination system showing the directing and narrowing of the laser beam and then expansion into the measurement area using the scanning system described in Chapter 2.

camera lens perpendicular to the glass walls of the flume and centred on one of a number of datum marks along the length of the measurement section. Alignment of the camera with the tank wall and the datum mark is achieved by firstly levelling the tripod base using the tripod mounted spirit level and then focussing the lens on the image of the camera reflected from the glass wall of the flume. When the reflection of the camera from the tank wall is visible the camera orientation is adjusted to put the reflected image of the lens exactly in the centre of the viewfinder. The tripod position is then moved parrallel to the tank wall to bring the datum mark also to the centre of the field of view. This procedure is repeated until both the reflected image from the tank wall and the datum mark are precisely in the centre of the viewfinder. The lens is then carefully focussed on the particles within the plane of the illumination.

The photographs are taken with a datum mark at the centre of the image plane so that the position of the datum on the image and the tank can be related to a position within the illumination plane without any parallax error.

The highest velocities are within the crest of the wave and is the most important as far as wave forces are concerned. For the scale of waves generated in the PIV wave flume. measurements over an area of $\approx 50*50cm^2$ would need to be made in order to adequately cover this region. This implies a magnification of $\approx$ 0.1. The magnification is accurately measured by photographing the same grid used to estimate the net image distortion (see Chapter 2).

The computer used to generate the wavefield also triggers the camera, ensuring the trigger time is accurately known relative to the wave signal. A 1 Volt pulse is output via the user port of the computer and into a reed switch which then completes a circuit to trigger the camera. There is a small delay between the pulse and the camera shutter opening which is associated with mechanical inertia within the switch and shutter mechanisms. This delay was measured and tested for repeatability using the arrangement shown in figure 6.5 and show to be 74ms$\pm$0.5ms. This small delay is accounted for within the software that controls the experimental timing.

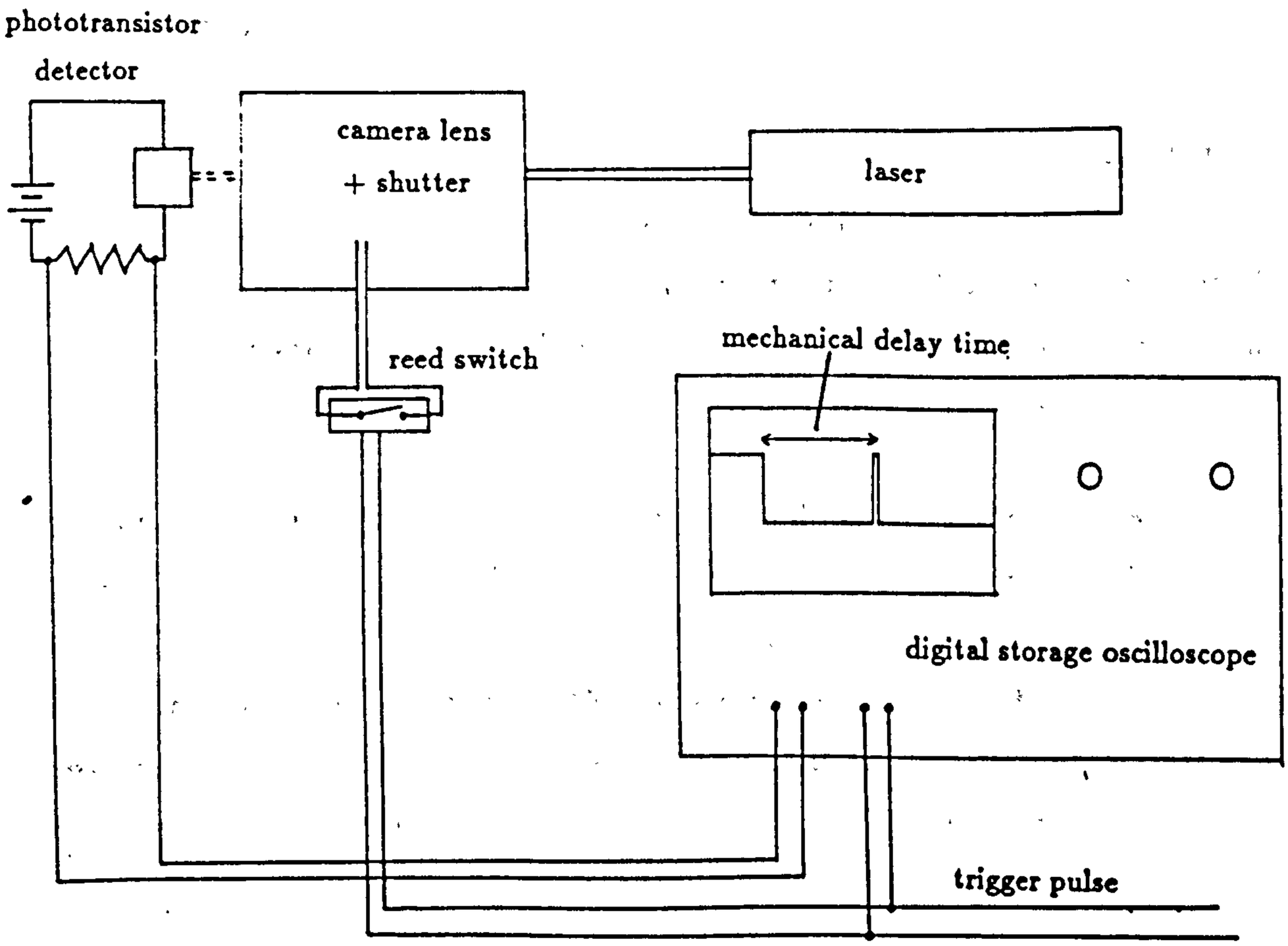

Figure 6.5: Measurement of the time delay between output of the trigger pulse and the opening of the camera shutter was achieved using the arrangement shown above. The opening of the shutter is detected by the phototransistor arrangement which is illuminated by the laser beam when the shutter opens. The trigger pulse and the signal from the computer are input into a digital storage oscilloscope where the pulse separation can be measured to within $0.5\mu s$. This was tested a number of times to check the repeatability and shown to give a mean and standard deviation of $74ms$ and $0.5ms$ respectively.

6.2.1 Seeding

The water within the wave tank is seeded with conifer pollen which has an average diameter of $\approx 70\mu m$. These particles are used because, when wet, their density is very close to that of water ensuring that, within the timescales of an experiment, there is no noticeable settling of the tracers as may be experienced with more traditional seeding material such as Aluminium powder.

The exact seeding concentration within the tank at any given time is difficult to determine and therefore difficult to regulate. In general a reasonable estimate can be obtained from a particle count within a small area and was maintained at a level that resulted in $\approx$ 10-15 particle images/mm^2 in the film plane This ensures that signal dropout is minimal and that the random errors associated with measuring through velocity gradients are reasonably small.

6.2.2 Exposure parameters

The most effective way of ensuring that the optimum light intensity is used to record the particle images is by experiment. No reliable methods exist for estimating the scattering efficiency of randomly sized, non-spherical particles and the amount of light loss due to the glass walls and propagation through the water would be difficult to account for.

A scan period of 2.5ms was set for the scanning mirror and a number of test exposures made of a simple non-breaking wave. The output power of the laser beam was varied from 2-20 Watts in 2 Watt stages. The resulting photographs were then developed in the manner described in Chapter 2 and subsequently inspected under a microscope. Negatives that had a dense background fog or ghostly particle images were considered over and underexposed respectively. The remaining few were examined by positioning them in the analysis rig and observing the fringes that resulted. Good visibility fringes were taken to indicate well recorded particle images and a laser power of $\approx$ 8 watts was taken to be

close to the correct exposure for the T-MAX 100 film being used. Wave fields that require a shorter pulse separation also get a shorter pulse time which then requires a higher illumination intensity. This is easily accounted for once the correct exposure at a given scan rate is known. No reciprocity effects were noticed.

The total exposure time used in the wave measurements was ≈ 8-10ms which, for a scanning period of 2ms ensures, that each particle within the measurement area results in 5-6 exposures per frame. Multiple exposures increase the degree of correlation for slower particles but the benefits are limited for more rapidly moving particles at the crest of the wave, due to the limited probe diameter.

6.3 Results

For the test wave 9 separate sets of measurements were made. Each separated by $\frac{1}{40}$second, starting 10.375 seconds after the initiation of the wave signal and ending 0.2 second later.

The limited film advance rate of the camera wind mechanism meant that the PIV negative obtained at each of the 9 phase positions had to taken from succes ive waves triggered at the appropriate time. Each photograph was taken at least 5 minutes after the previous one so that turbulence, generated by the previous wave, could be allowed settle.

Two spare frames on the test film were used to photograph the test grid, from which the magnification M is measured, and to record a single exposure negative of the particle images. The latter of these frames is used to estimate the mean particle size, or the halo function, which is used in the analyis of the PIV negatives. The scanning rate of the rotating mirror was noted immediately after recording each wave position.

The films were developed using T-Max developer at 20 degree centigrade with continuous agitation for 7 minutes, fixed and then washed for 20 minutes. The dried films were examined under a microscope to verify that the particles had been successfully recorded and were in-focus. Figures 6-10 show every other of the nine frames taken. The surface profile from each wave record was measured relative to the central datum mark in the manner described in Chapter 5, scaled according to the measured magnification M and then the position of the datum cross added to give the profiles of the wave relative to an origin at the foot of the wave paddle in its vertical position. These profiles are shown in figure 6.11 with the wave "0" approaching vertical frontedness and the rest progressing through breaking. The final wave "8" approaches the condition where the wave spout reenters the trough in front of it.

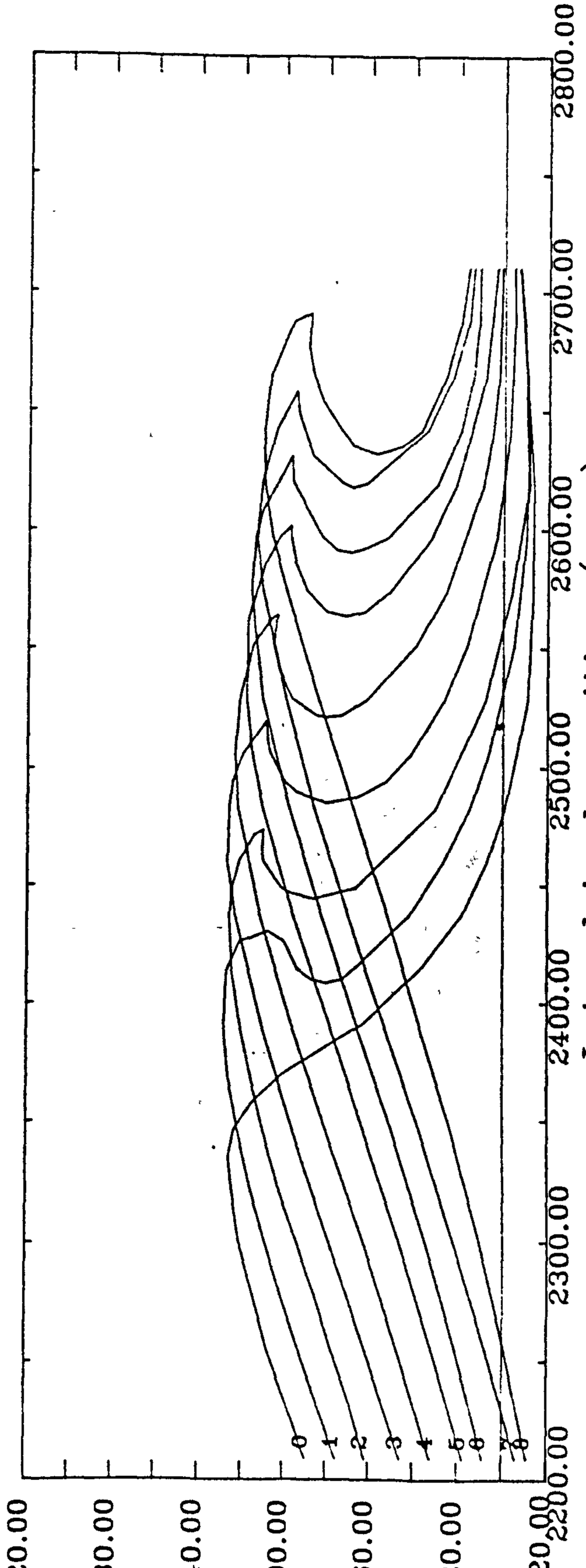

Figure 6.6: Surface profile measurements from PIV negatives from 10.375 seconds after initialisation of the wave signal to 10.575 seconds.

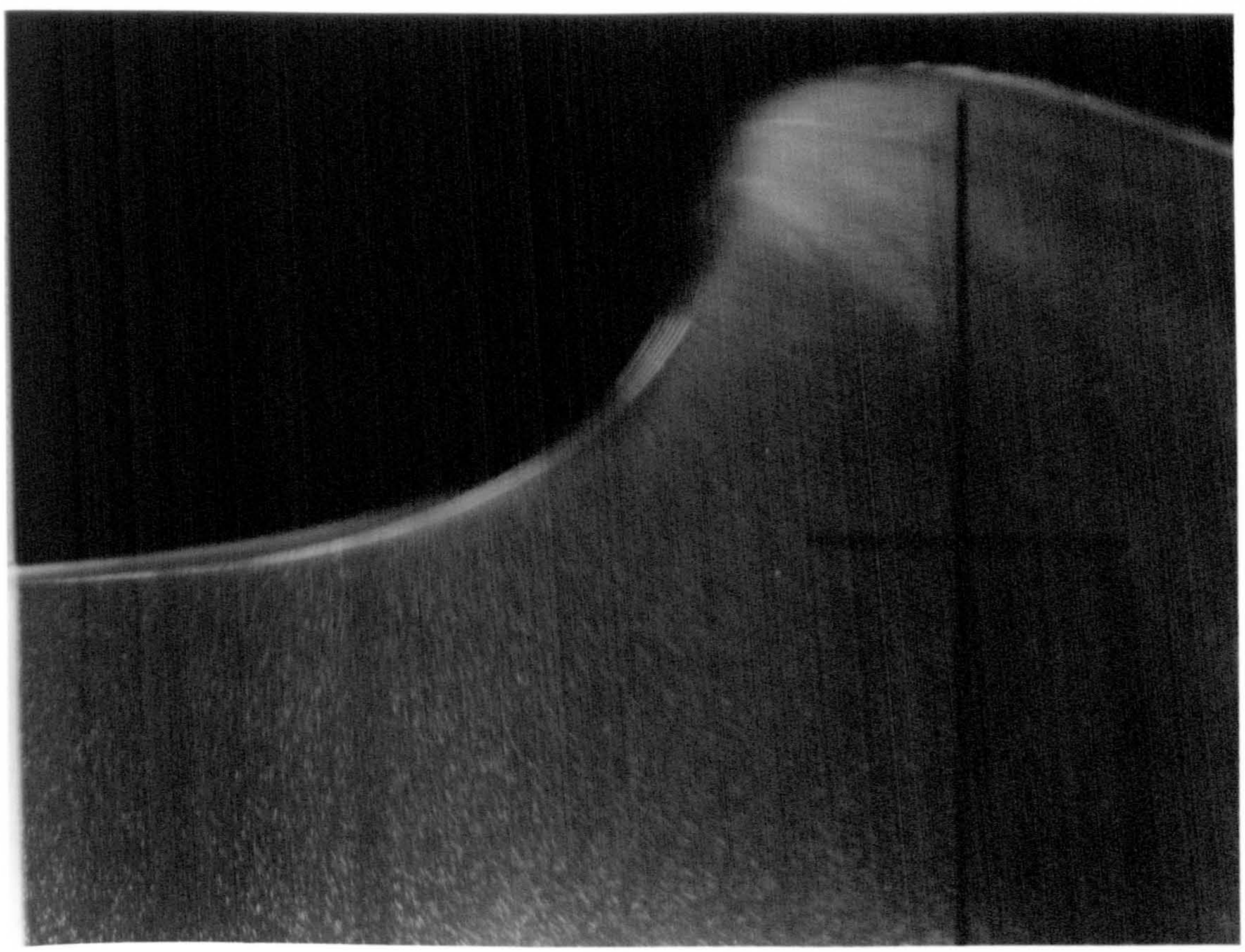

Figure 6.7: Frame "0", 10.375 seconds.

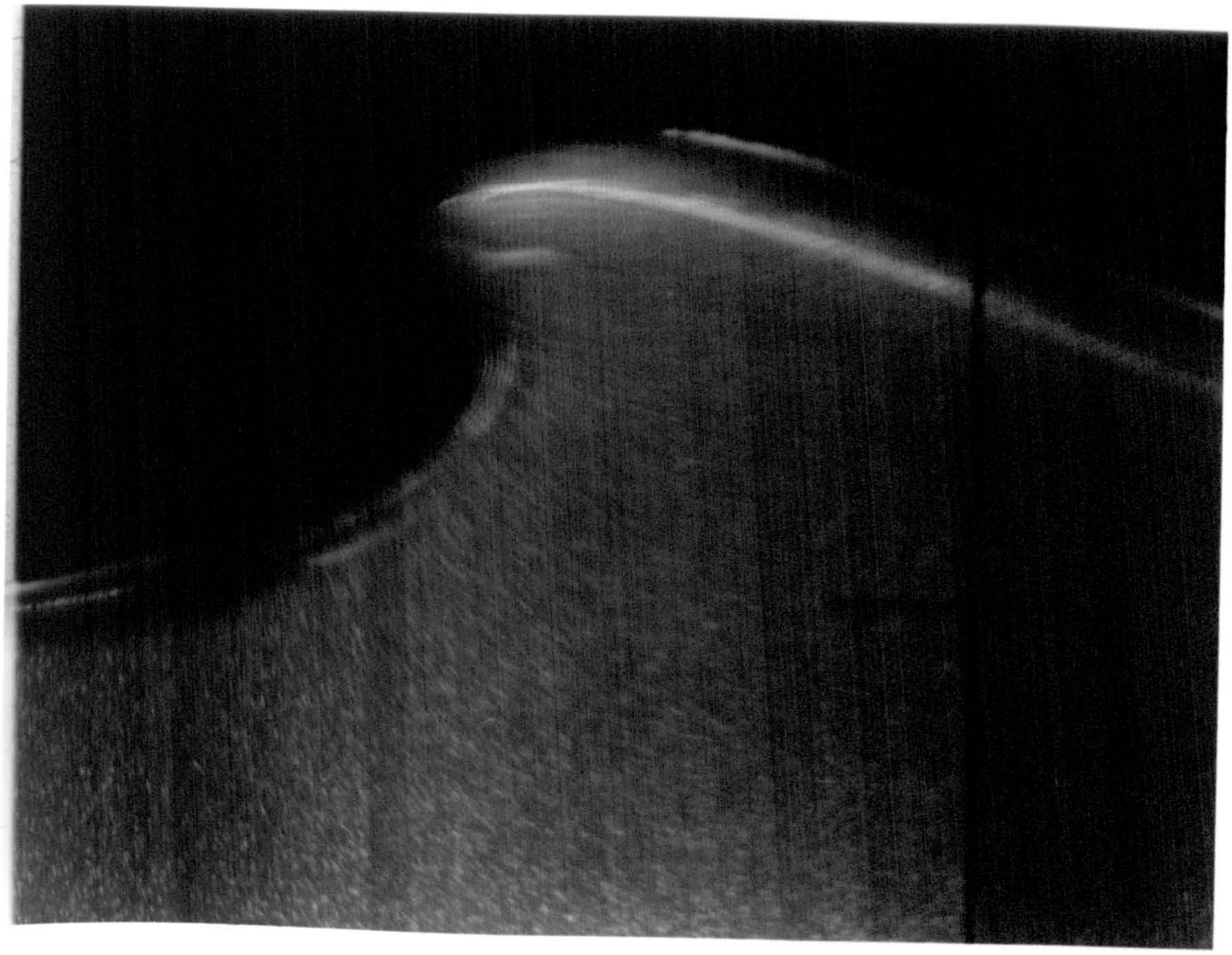

Figure 6.8: Frame "2", 10.425 seconds.

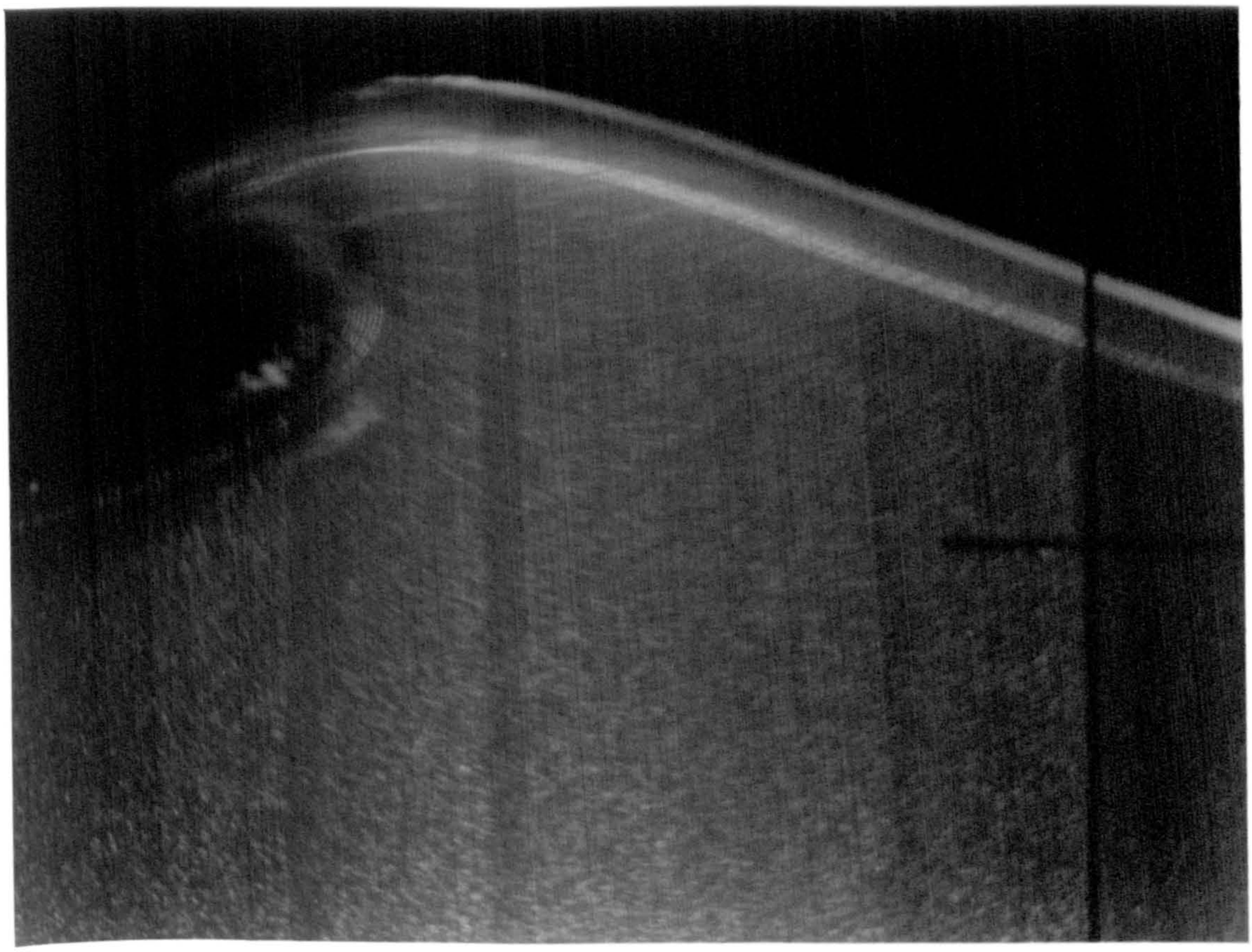

Figure 6.9: Frame "4", 10.475 seconds.

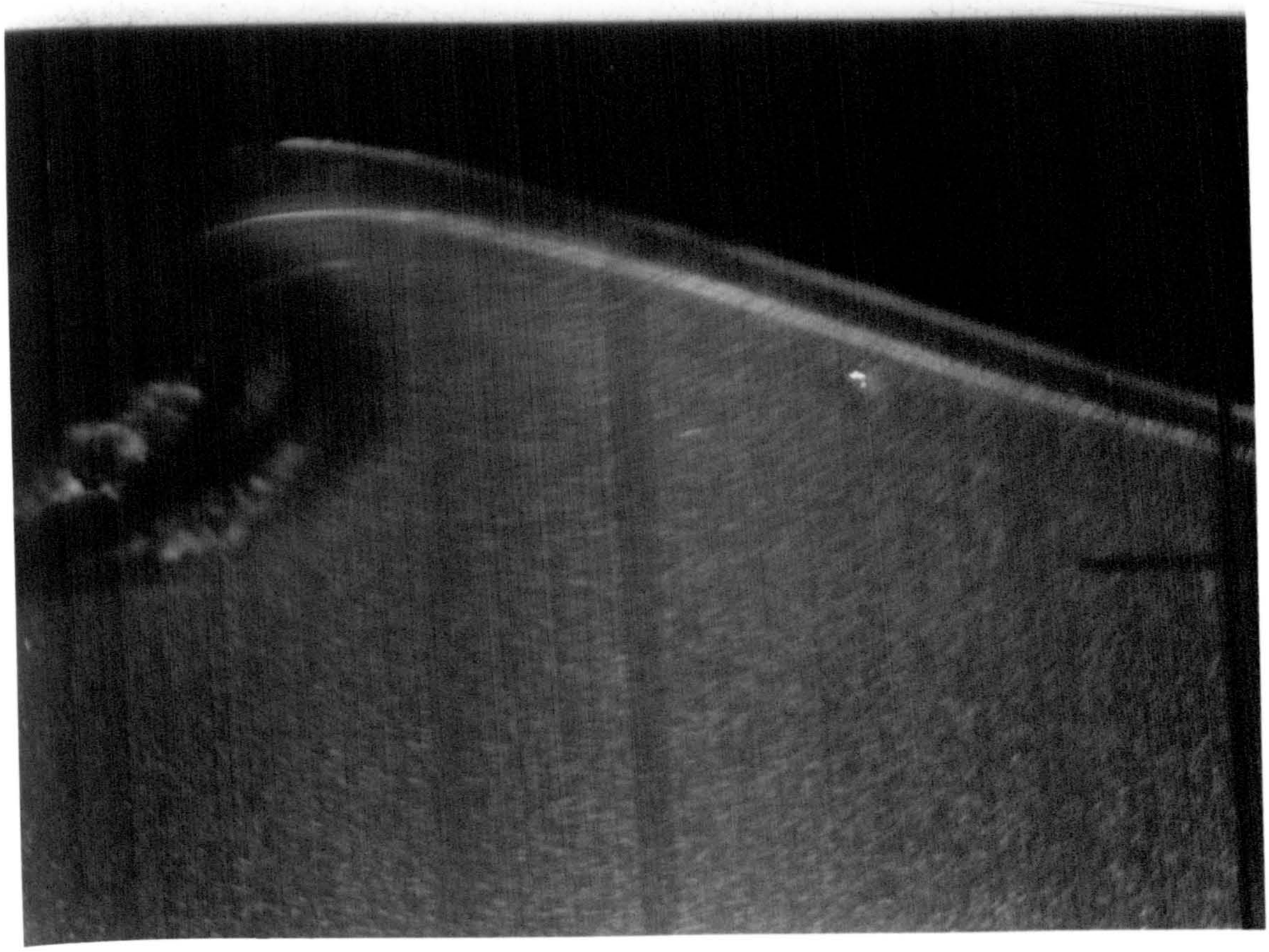

Figure 6.10: Frame "6", 10.525 seconds.

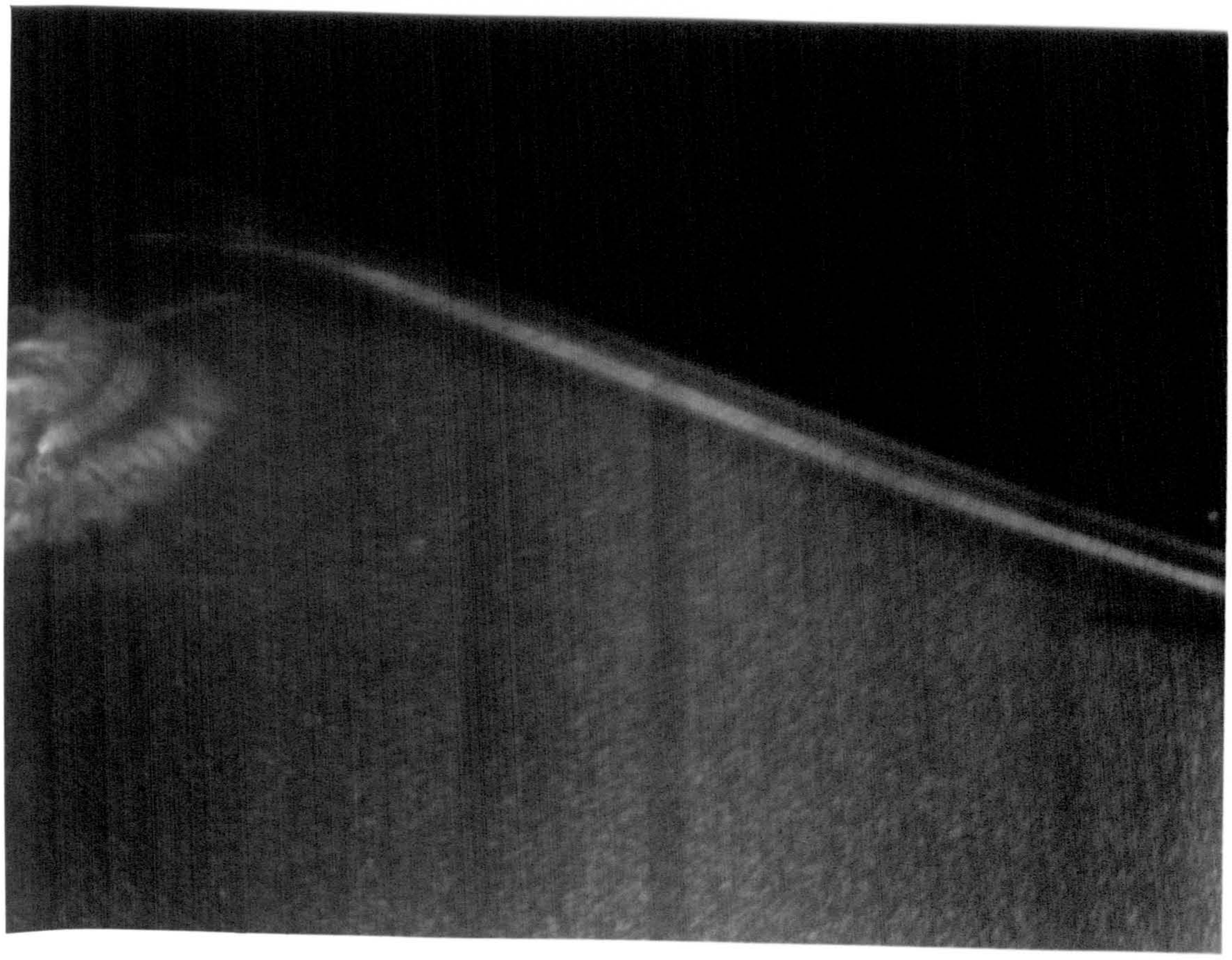

Figure 6.11: Frame "8", 10.575 seconds.

6.3.1 Velocity measurements

Each negative was analysed point-by-point over an area 49mm horizontally and 35mm vertically on a $1mm^2$ grid. The resulting values were scaled using M and T to give velocities from the measured displacements on the film and then edited, as in Chapter 5, to remove all the erroneous velocity values. Missing values were replaced with interpolated values where possible and then the data transfered to the mainframe to be plotted.

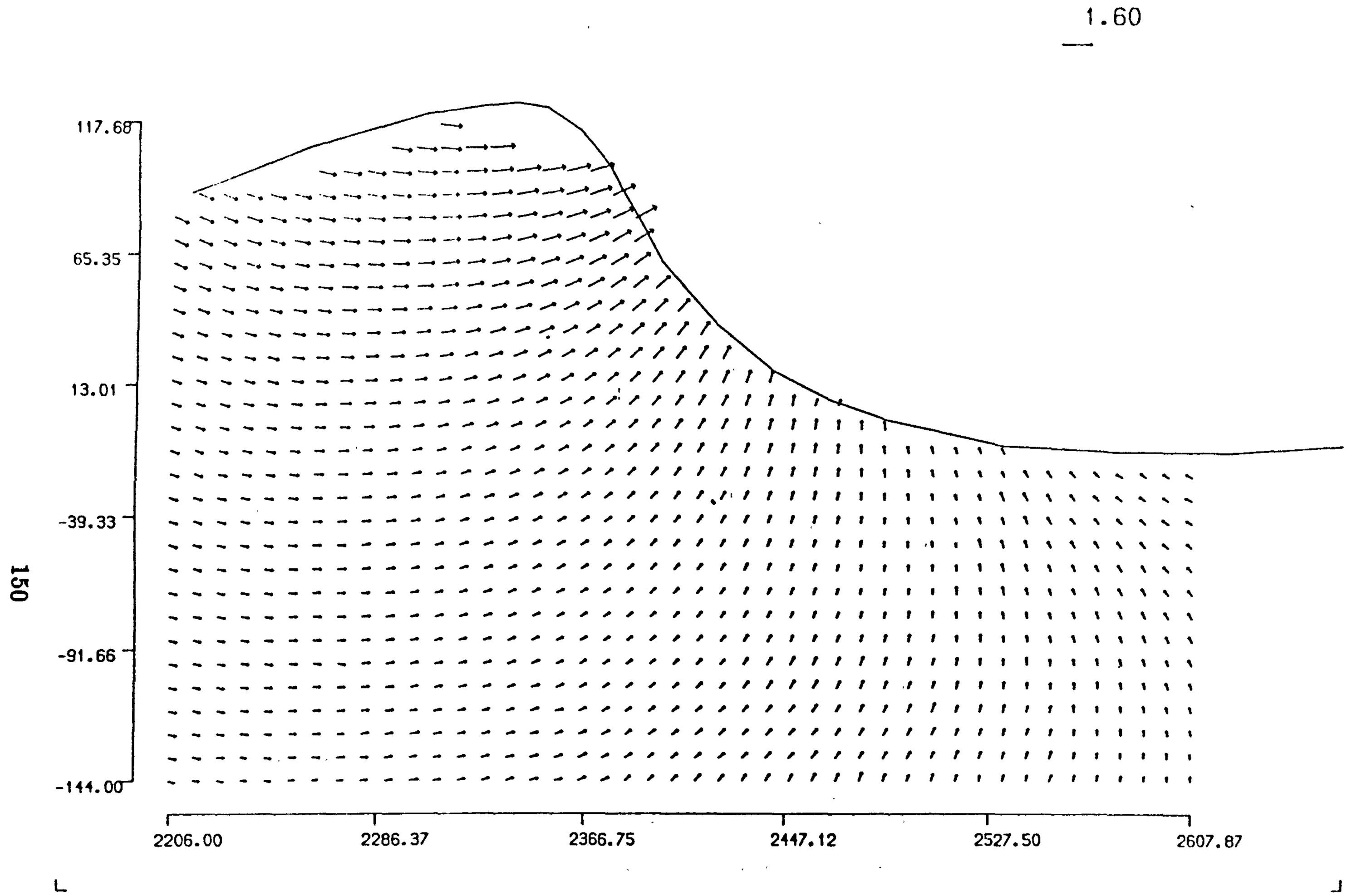

Figure 6.12: Frame 0. The numbers along the axes refer to the position of the wave in *mm* from the still water level vertically and from the wave paddle horizontally. An idea of the magnitude of the velocities can be gained from the reference length in the top right corner which represents 1.6 m/s.

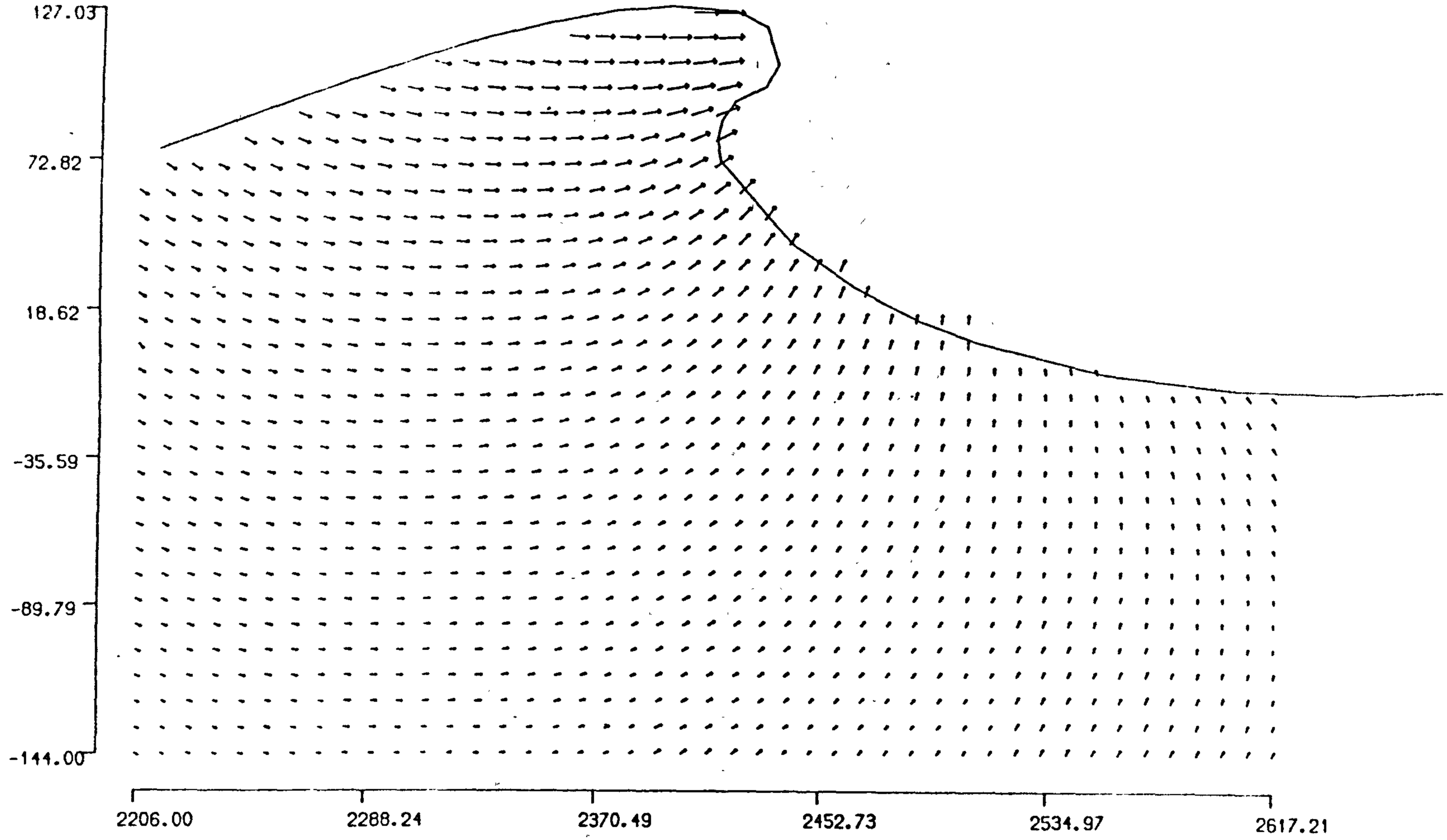

Figure 6.13: Frame 1.

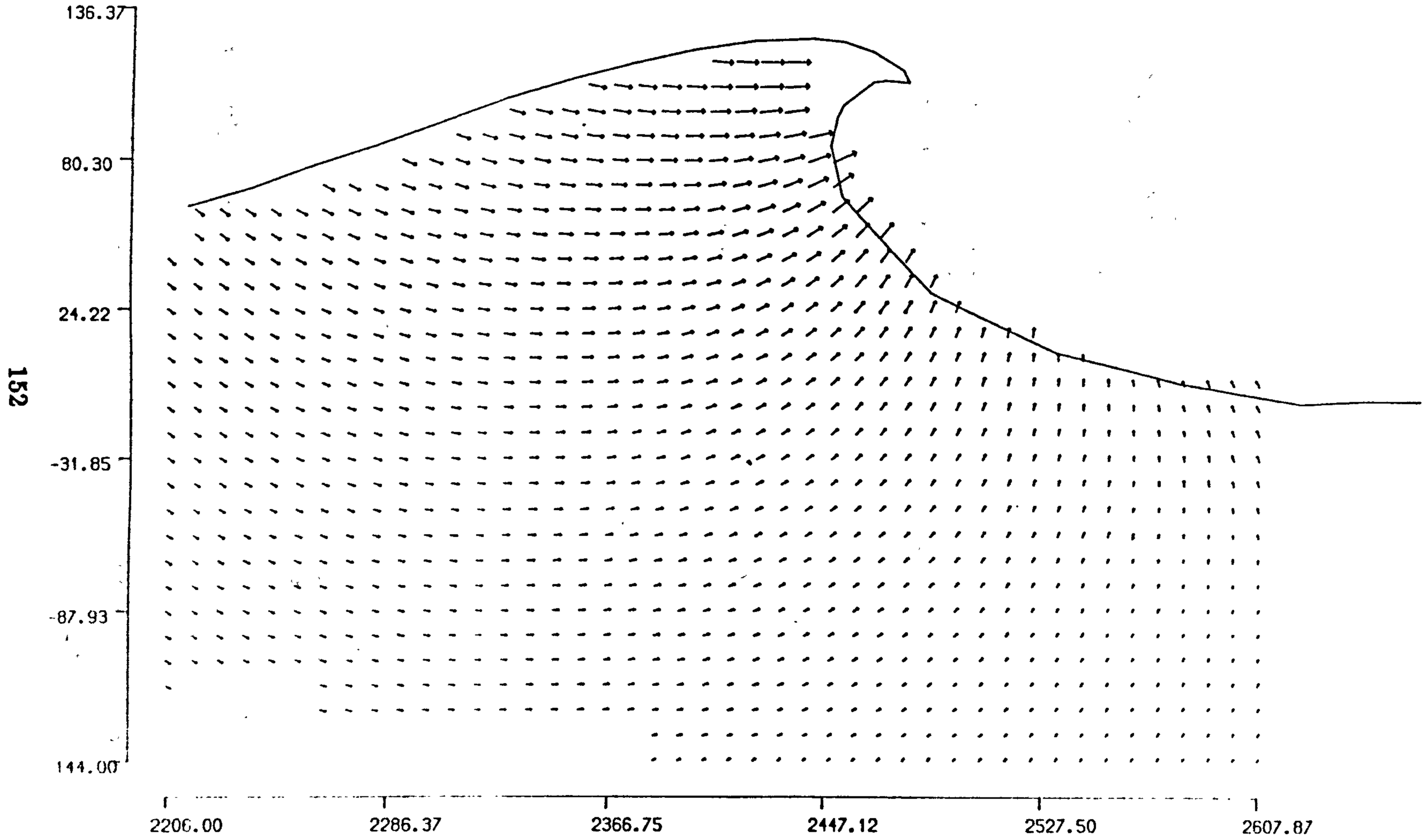

Figure 6.14: Frame 2.

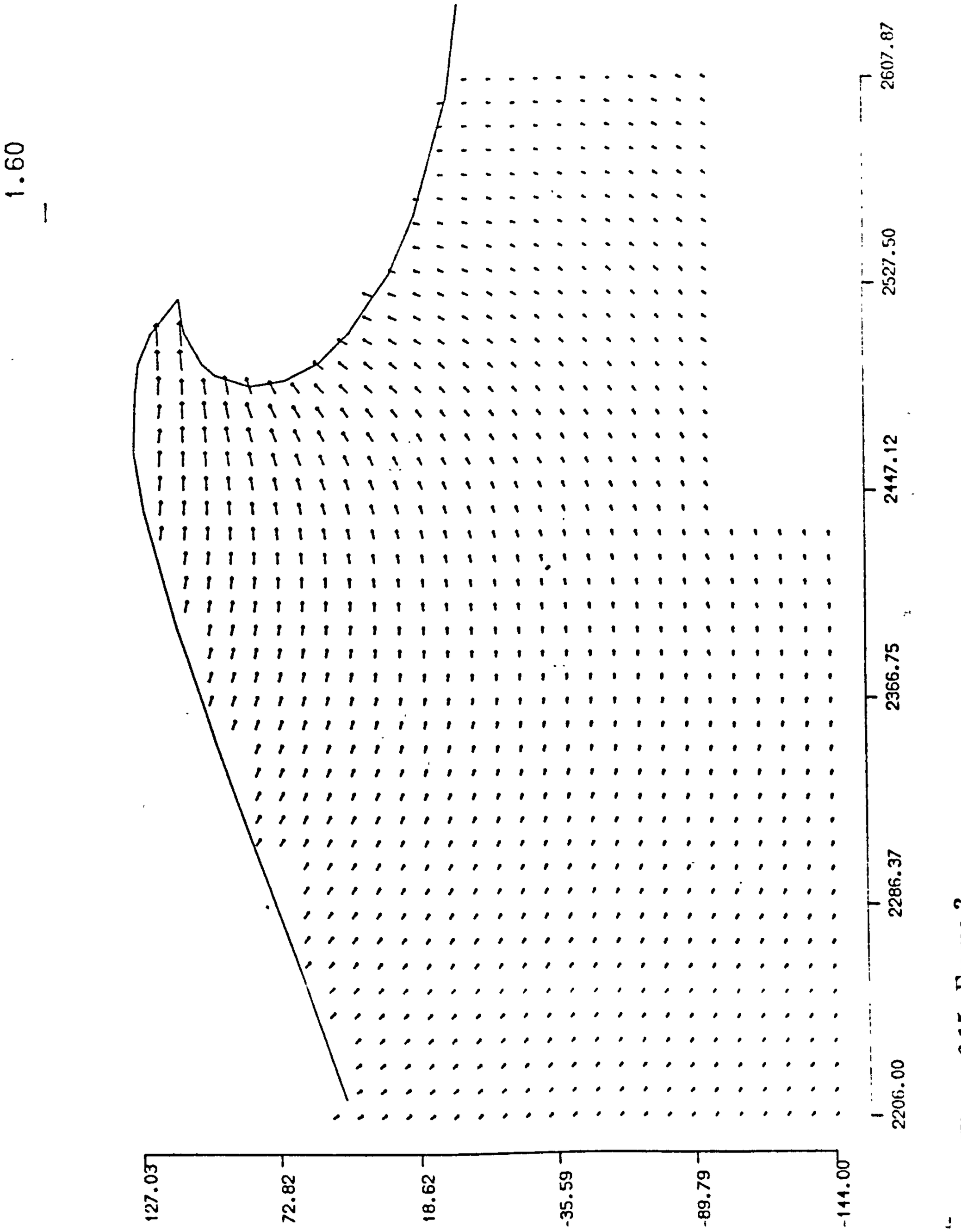

Figure 6.15: Frame 3.

Internal velocity fields

The evolution of the plunging breaker is clearly visible in considerable detail from the 9 sets of velocity measurements shown in figures 6.12-20. In the lower

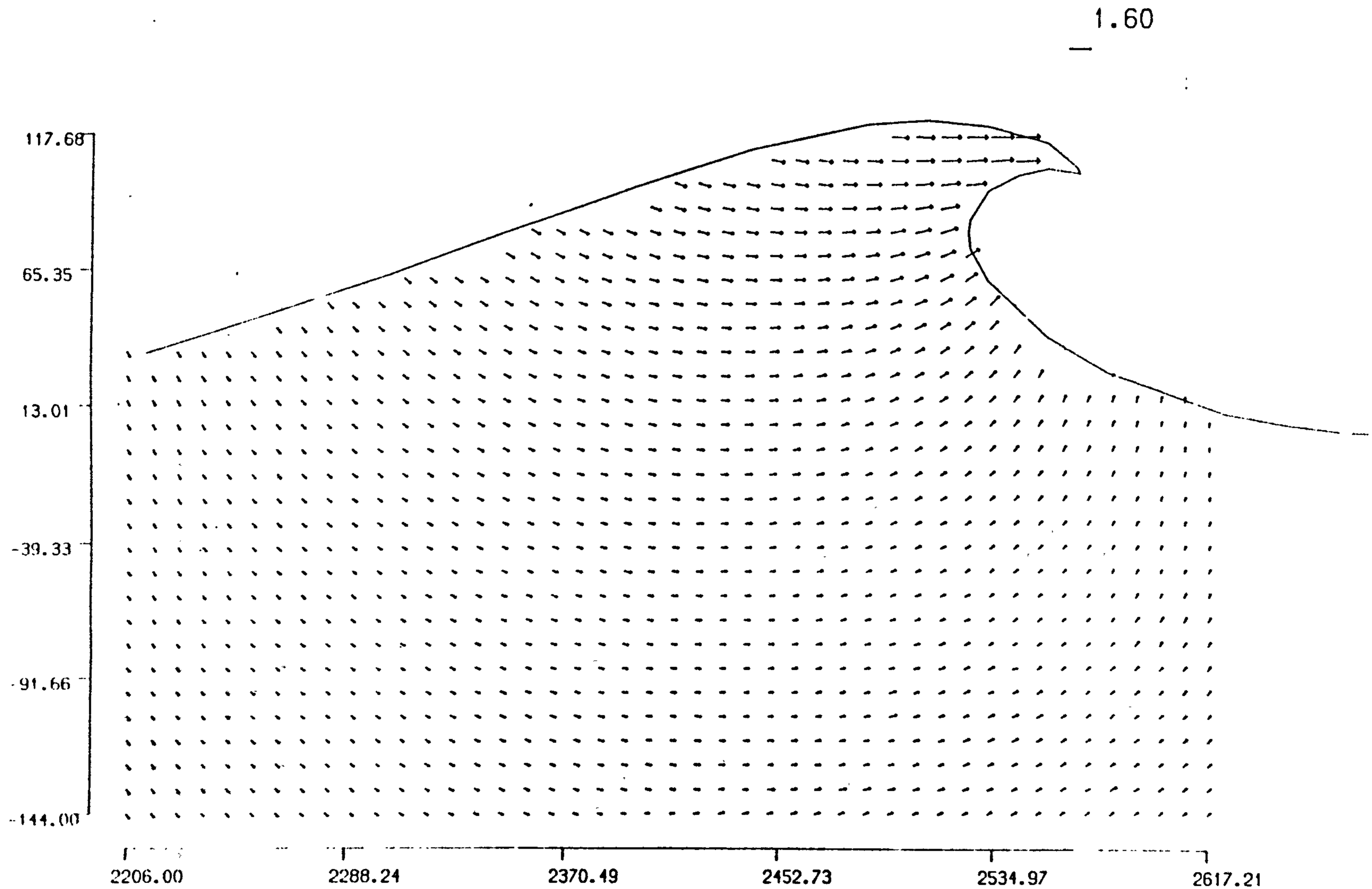

Figure 6.16: Frame 4.

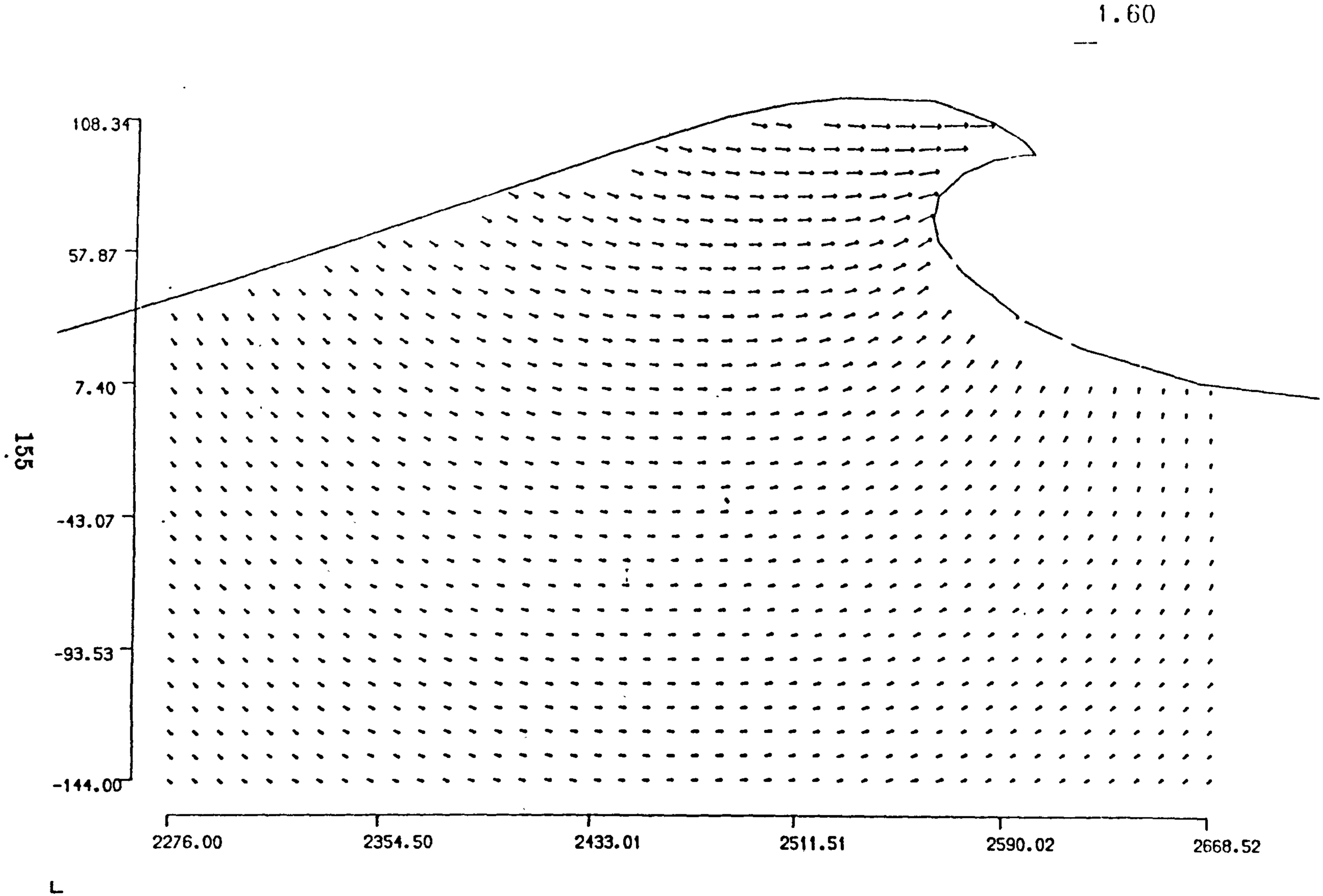

Figure 6.17: Frame 5.

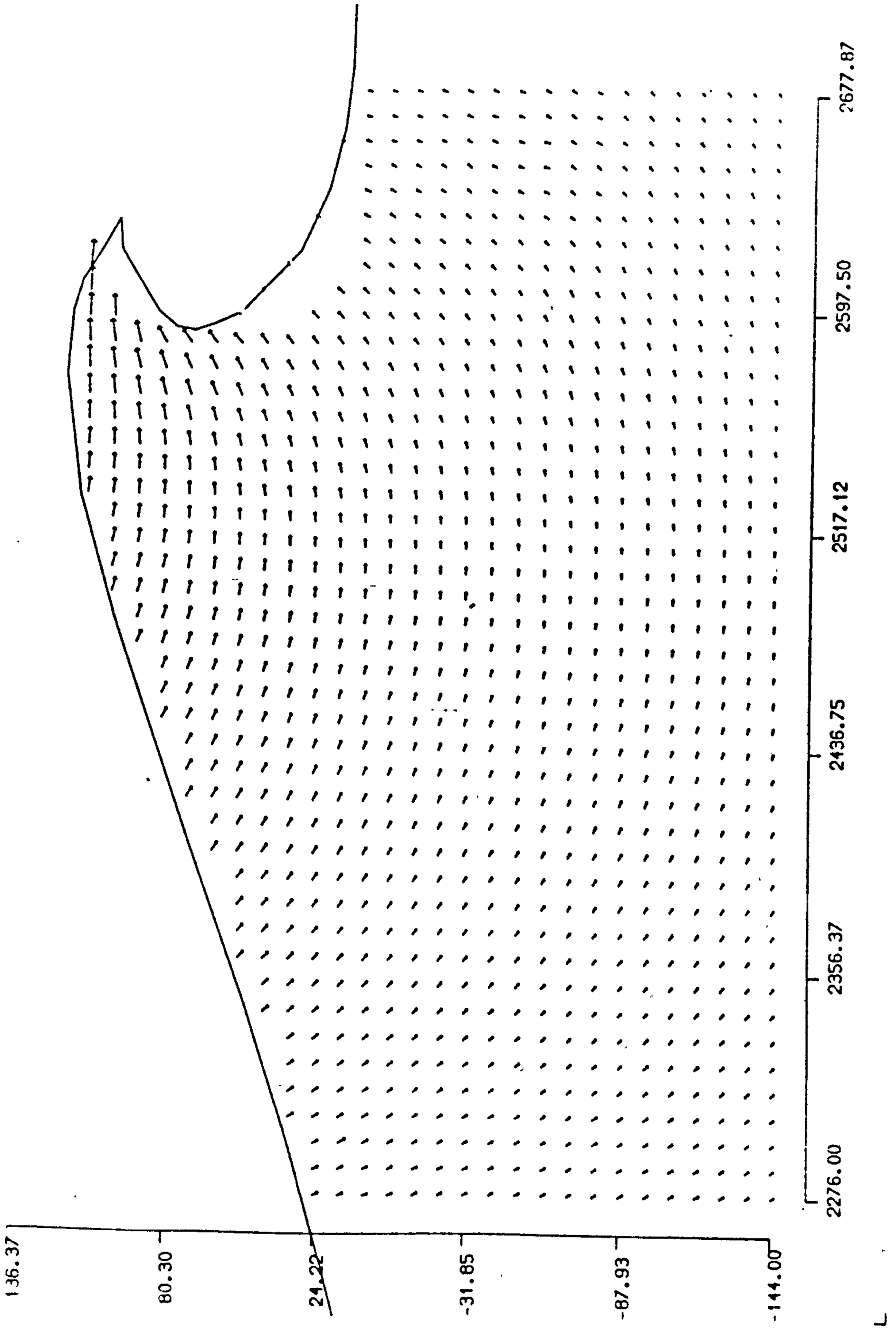

Figure 6.18: Frame 6.

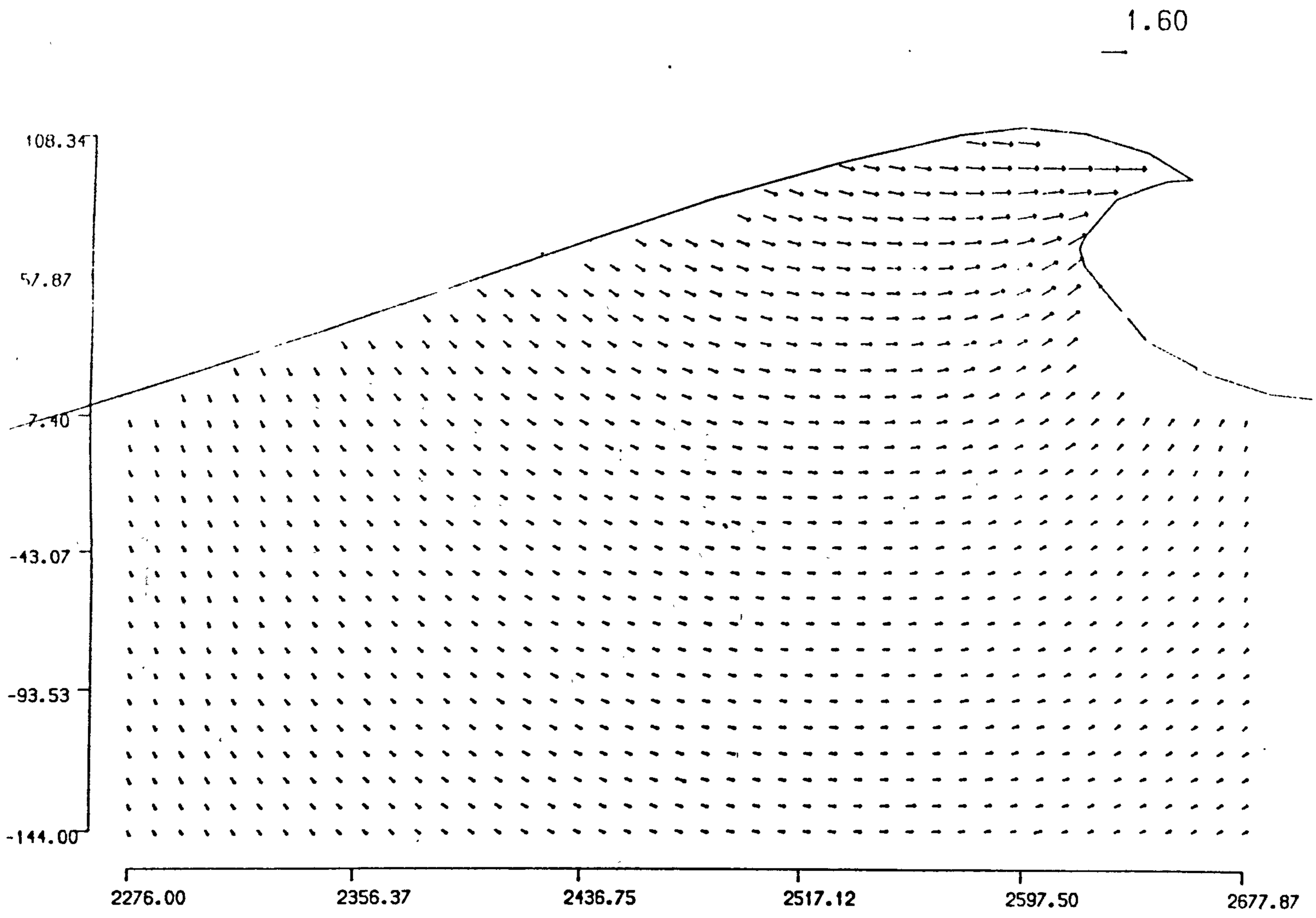

Figure 6.19: Frame 7.

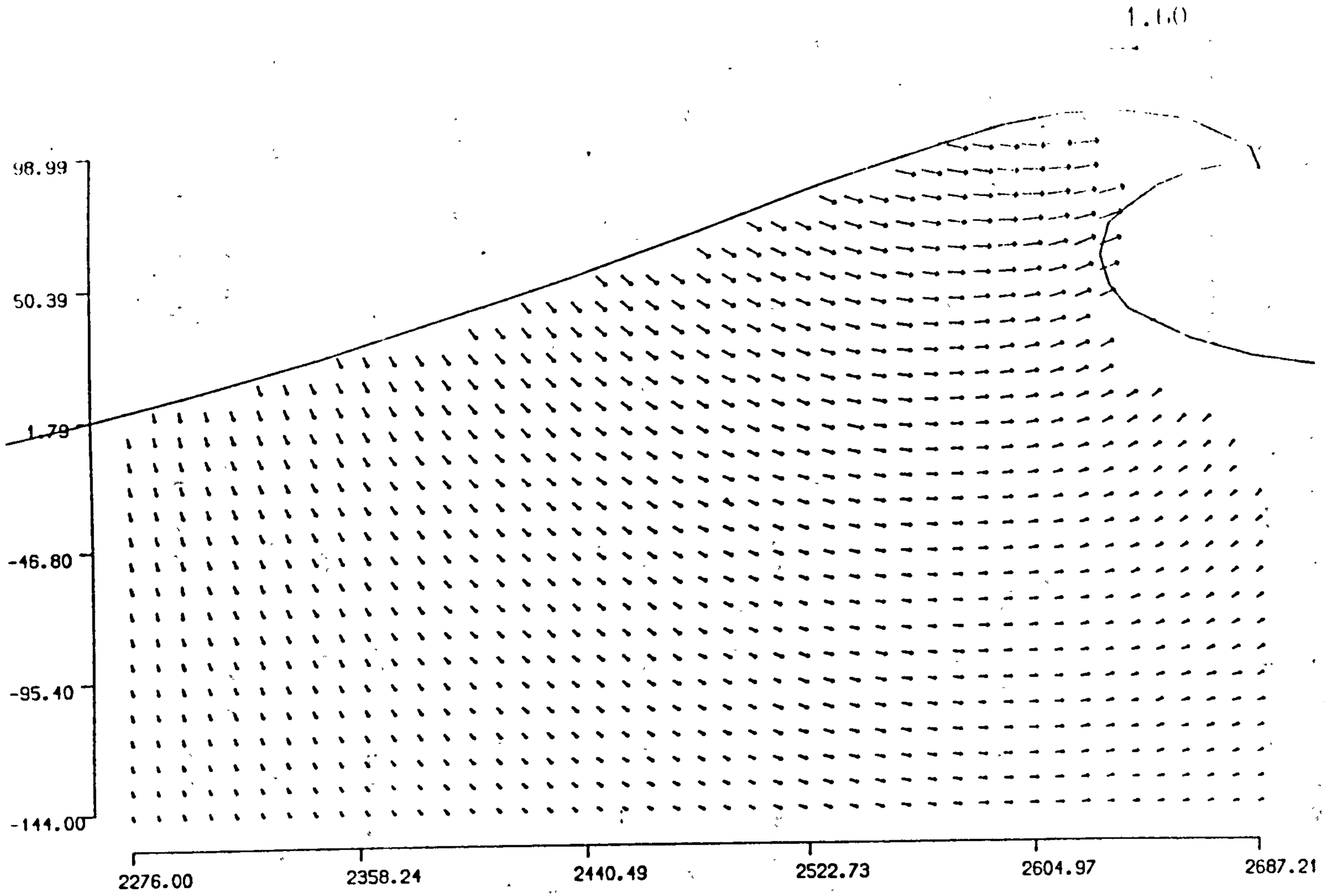

Figure 6.20: Frame 8.

regions of the wave the smallest particle displacements became more difficult to measure reliably. The pulse separation used to make the measurements was sufficiently small to ensure that velocities in the upper region of the wave were measureable. This means that in the lower regions of the wave the particle displacements will not be sufficiently large to allow the two particle images to be resolved from each other.

Above the still water level velocities were reliably measured right up to the upper surface of the water. A useful number of velocities were also measured within the spout of the wave. It is surprising that sufficient light was present within this region of the wave since the laser illumination had to exit the water just ahead of the wave and then re-enter the water within the spout without becoming diffused or refected in other directions.

In the later sets of measurements (frames 6,7,8, figures 6.18,19,20) it can be seen that the region just ahead of the wave crest is lacking in measurements. Inspection of the corresponding photographs of the negatives from which the measurements were made show this region to be obscured by reflected light. This may be due to reflection from the upper surface of the wave which is directly above this region. It is possible that repositioning of the camera so that the region of interest within the wave is in the centre of the frame may solve this problem. Alternatively, the use of a polarising filter may allow such extraneous reflections to be excluded from the film.

It is possible that greater detail may be obtained within the crest region of the wave by using a larger magnification. However, this would exclude most of the rest of the wave. For the measuring system in its present form it would be up to the user to decide, based on the nature of the velocity data required, what magnification and therfore area of the wave is to be recorded.

Comparison of results with numerical model

A numerical model of wave breaking was available for comparison with experimetal measurements. The numerical scheme is a fully non-linear, time-stepping model developed by Dold and Peregrine[38] at Bristol University and adapted to run on hardware at Edinburgh, Skyner et al, 1989[114]. Inviscid, incompressible and irrotational flow is assumed in the model and calculation of the fluid motion evaluated at discrete points along the water surface.

Comparing the results of the experiment with the numerical model is mainly intended to show that PIV can give sensible measurements through an extreme wave profile. The fundamental difficulty in such a comparison is achieving an accurate match between the numerical and laboratory wave through breaking. The numerical model requires the wave height and velocity potential to be defined in space at a particular time while the experimental wave is generated by a drive timeseries fed to the wavemaker which is 2 meters from the measurements region. Relating the two waves linearly is difficult as the wavefield is highly non-linear in its propagation upto and through breaking. The development of a scheme for accurate matching of numerical and physically generated waves is beyond the scope of this thesis but will form a large part of future work.

Here it will suffice to show that the velocities measured from the laboratory wave and calculated from a similar numerical wave are reasonably close in magnitude and form.

The numerical model was run in a simulated water depth of 53cm which is the same as the laboratory wave and given a starting surface profile derived from the wave gauge record shown in figure 6.2. The numerical wave was then allowed to propagate until it reached the limit beyond which the calculations break down. This was done several times, adjusting the components of the numerical wave field each time, so that the numerical wave would not break prematurely and would develop a wave profile that *looked* similar to the laboratory wave. The complex non-linearity of the breaking process meant that, using this rough

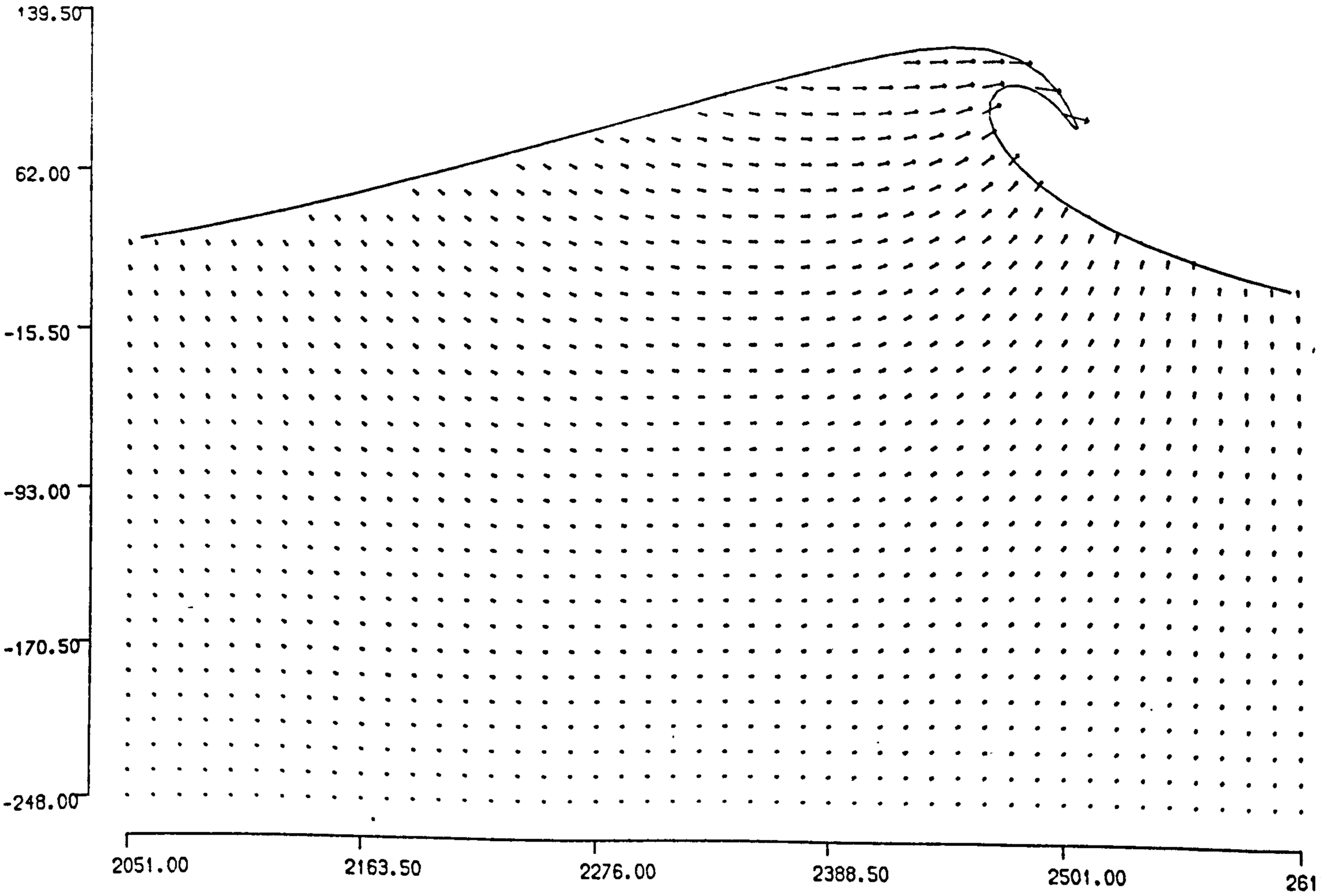

Figure 6.21: Surface profile and internal velocities generated from time stepping numerical model.

scheme, it was only possible to get a very approximate temporal and spatial match between the waves. Figure 6.21 shows the velocity distribution and surface profile of the numerical wave at the point at which it most closely resembles one of the measured frames (frame 7).

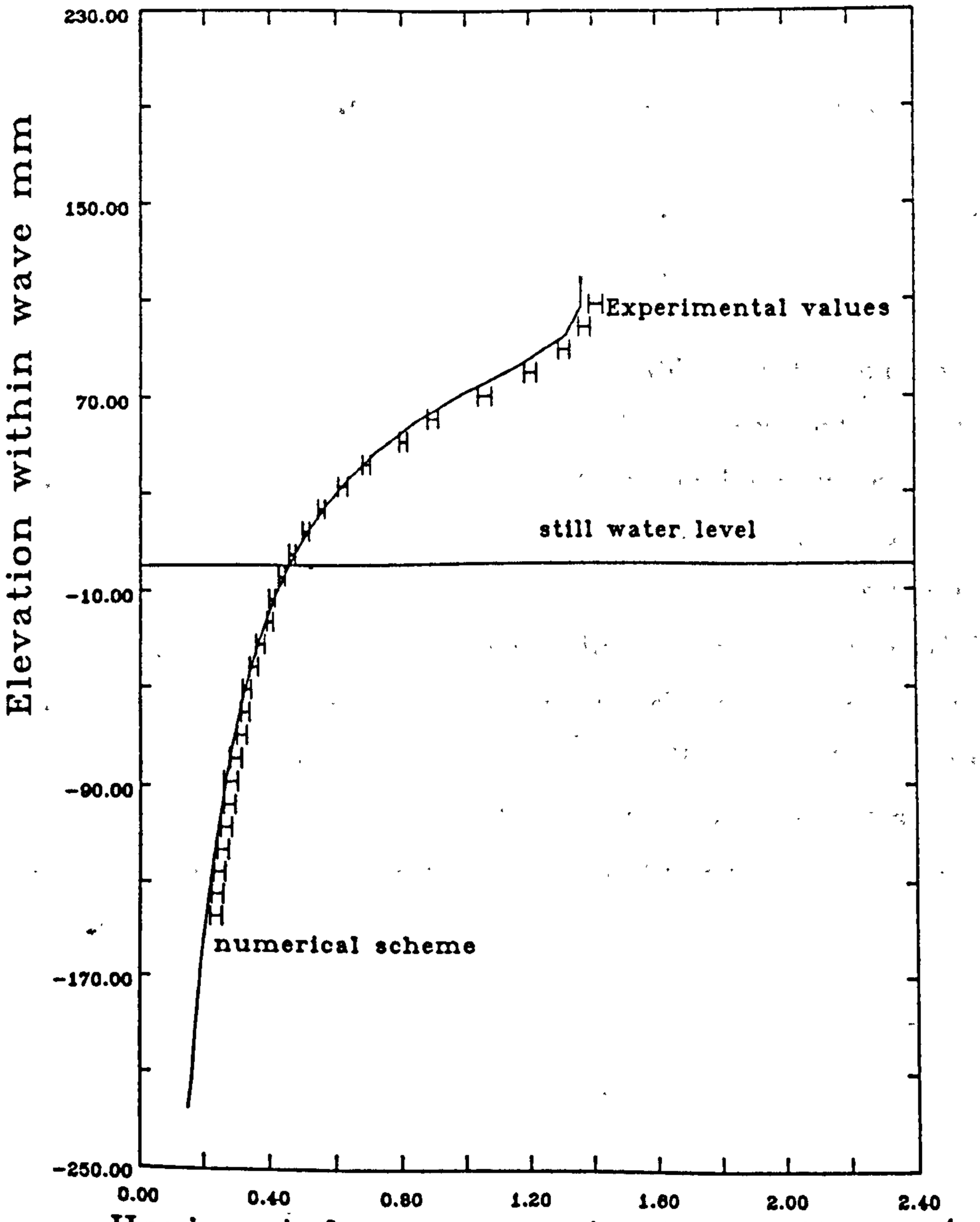

Figure 6.22: Horizontal components of velocity for laboratory wave (frame 7,) and numerical wave on a vertical line behind the wave spout.

Horizontal components of velocity vertically down through the wave just behind the spout were plotted for the laboratory and numerical waves and are shown in figure 6.22. The match between the two sets of data is surprisingly good, especially around the still water level. The magnitude of the velocities through the wave profiles is consistent with each other and the form of the velocity distributions are close but with a noticeable deviation in the upper regions of

the wave. Inspection of the laboratory wave measurements show a slight amount of randomness but the error bars, determined from the considerations discussed in Chapter 4, do not look unrealistic when compared. Further comment is hardly justified due to the loose criteria used to match the waves.

These initial results indicate that there is considerable potential in the use of PIV for water wave studies. The large area over which the velocity measurements were made will ensure that measurements that can be realistically scaled to offshore dimensions. The accuracy of the technique appears to be good, both from the estimated error bounds and the smooth progression of the measured velocities shown in figure 6.22. It is hoped that a more precise match between laboratory waves and numerical waves may be achieved so that the numerical scheme can be verified more fully. This would allow velocity measurements, obtained from laboratory waves beyond breaking, to be used as a starting point for extending theoretical schemes beyond the limit at which they presently break down and cease to give realistic results.

Chapter 7

Additional applications of PIV

The main interest in PIV, within this project, was its application to water waves. One of the major features of this technique however, is its versatility. The same equipment used to record the flow field under water waves can be easily adapted to record the motion of other flows. It is merely a matter of re-assessing the recording parameters such as illumination intensity, pulse separation, duration and the optical magnification so that they satisfy the required accuracy and resolution sought by the user. All PIV negatives can be evaluated in a similar manner on the analysis system described in Chapter 3.

This flexibility is illustrated in this chapter with brief descriptions of two other applications of PIV (Vortex shedding and Acoustic streaming). The work is preliminary in nature and therefore limited in experimental sophistication. However, the potential for development is illustrated by the results and lays the groundwork for more detailed work.

7.1 Surface flow measurements

One of the limitations associated with PIV is the need for a high intensity light source (usually a laser). The Argon Ion laser used in the wave studies is easily the most expensive component of the system. This section describes non-laser recording of two-dimensional vortex shedding from a cylinder being towed through a tank of stationary water.

The light source in this case is a pair of ordinary photographic flash lamps which are used to illuminate the surface of the water behind the cylinder. A clean, film free, water surface ensures that the surface motion of the water represents the 2-D motion through the water tank. Seeding of the surface then allows a PIV record of the flow to be taken without the need to form an intense laser sheet for illumination of a plane within the fluid. The arrangement used is shown in figure 7.1. The cylinder is supported from the trolley and mounted vertically in the water. The trolley itself runs on six sets of sealed precision bearings which carry it along two polished sets of rails mounted along either side of the tank. This ensures the trolley moves along the tank smoothly. The camera is mounted on the trolley and is fitted with a motor wind so that a number of frames can be taken on each run.

This whole approach assumes that the vortex wake behind the cylinder is two-dimensional in the plane perpendicular to the cylinder and that the surface motion is the same as the motion of the water within the body of the fluid further down the cylinder. Studies by Saouthi and Gerrard, 1981 [115] show that the vortex wake behind the cylinder can be rendered almost completely two-dimensional by minimising end effects at the lower end of the cylinder next to the base of the tank and where the cylinder emerges from the water. If the gap between the bottom of the cylinder and the base of the tank is not less than approximately 1/6 of the cylinder diameter the vortex wake becomes three dimensional and the vortices taper off towards that end. The dirt film that collects on still water after several hours also affects the vortex wake near the

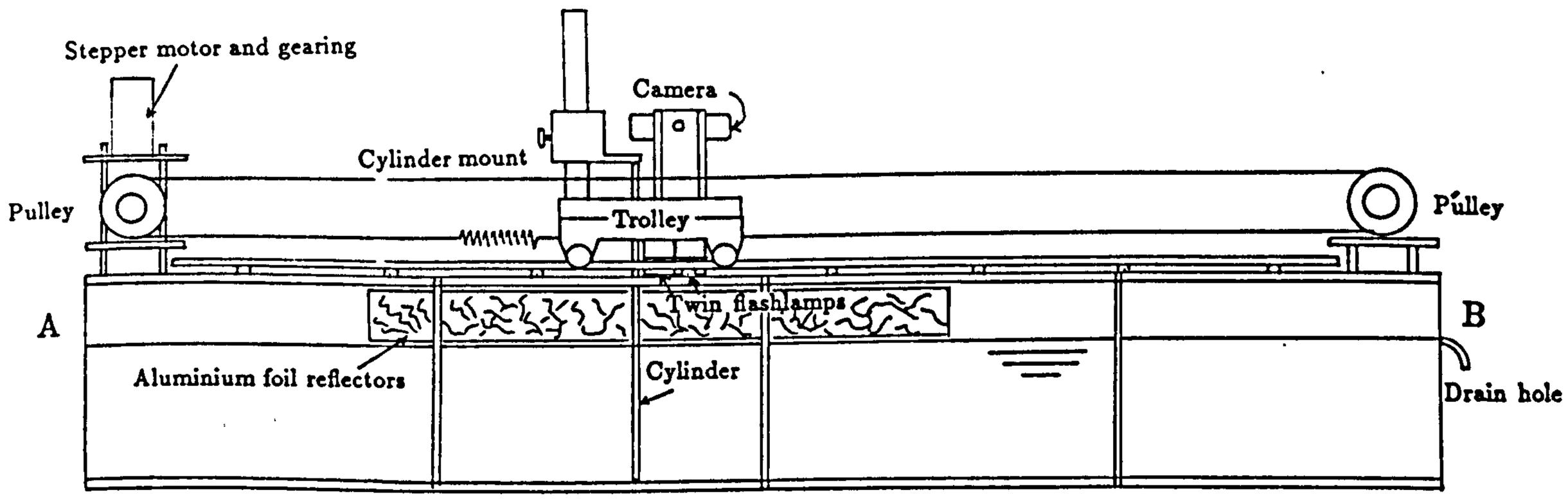

Figure 7.1: Towing tank with surface flow measuring arrangement mounted above on trolley. Flash lamps are mounted below and to one side. The light burst is reflected and diffused from the crumpled Aluminium foil along the sides of the tank. Cleaning of the water surface is achieved by introducing detergent at end A then floating off dirt and excess detergent at end B. Steady motion of the trolley is ensured by the spring damped stepper motor drive.

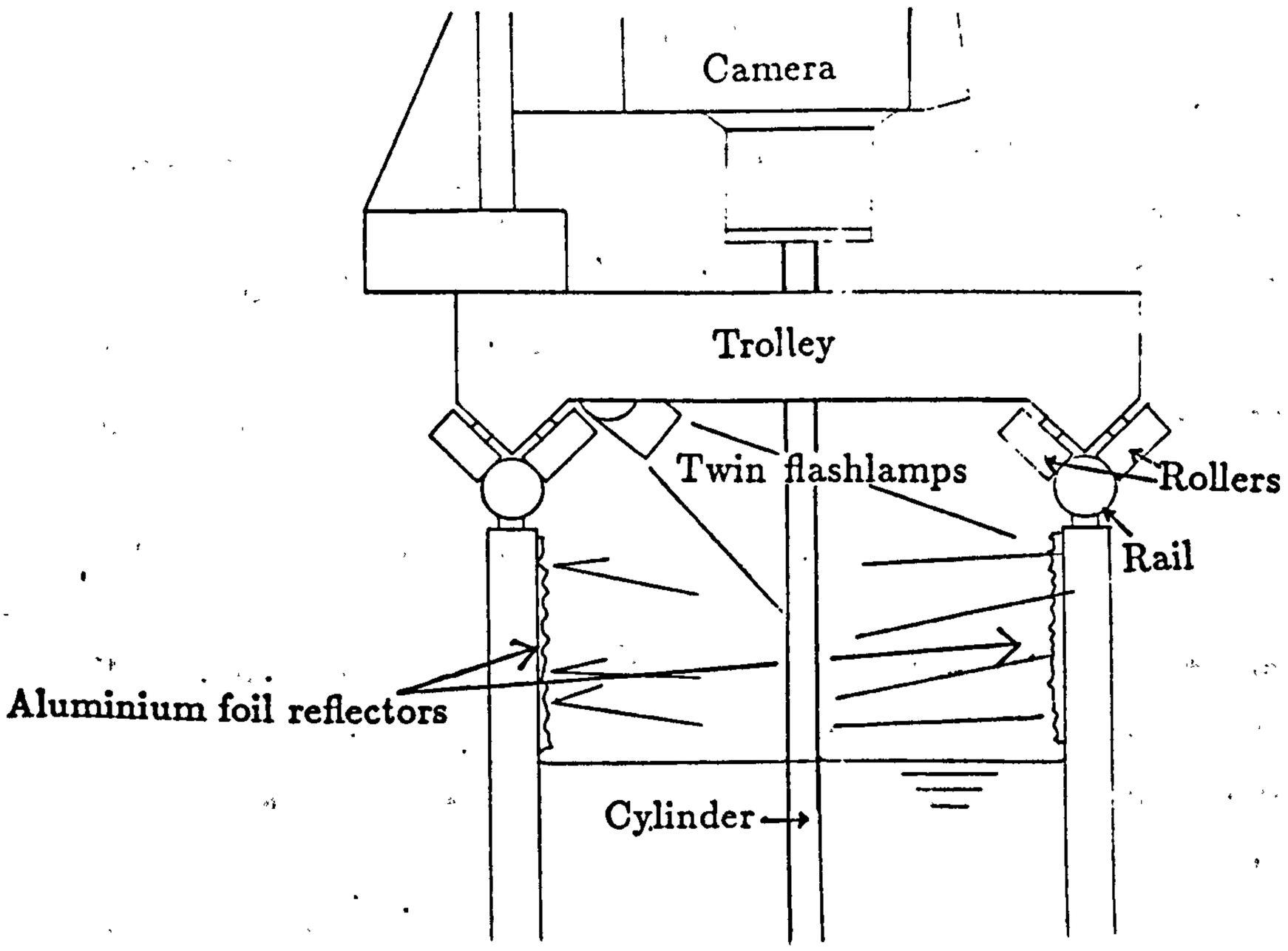

Figure 7.2: Configuration of towed cylinder, camera and flash guns. The cylinder is moving into the page.

water surface. This dirt film constrains the motion of the water at the surface and will ultimately damp all motion completely.

Both of these problems can be solved fairly easily. Precise positioning of the cylinder ensures the bottom gap is small and limits end effects near the bottom of the cylinder. Surface effects are minimised by introducing detergent onto the water at one end of the tank and floating the dirt off at the other end through overflow holes. This "clean surface state" will persist for several hours before a surface film forms and inhibits motion of the water at the surface of the tank.

The water surface is seeded with the same pollen grains used in the wave studies. Seeding is distributed evenly over the surface by sprinkling with a fine sieve to give a light and even distribution of particles on the water. The extent to which the seeding affects the surface motion is not known and remains an area for further research. The results presented below show that the measured surface motion is consistent with what is known and suggests that the influence of the pollen is extremely minor compared with the dirt film.

Background motion of the water is minimised before an experimental run by allowing the water to settle for an hour or so after cleaning the surface. There is always a certain amount of background motion in the tank due to convective currents. These currents can be reduced with the use of heating wires but it is a complicated procedure and was not felt necessary at this stage.

The illumination system, which is based on dual flashlamps, is triggered by the camera via an electronic delay box. The initial shutter contact is used to trigger the first flash with the second flash triggered by the timing electronics. The flash guns are mounted on the trolley and point across the water surface to the side of the tank where crumpled aluminium foil is used to diffuse the light burst to give a more even illumination of the seeded water surface, figure 7.2. In order maximise the contrast of the final image the base of the tank was painted matt black and the flashguns aimed at an acute angle to the water surface.

7.1.1 Results

The cylinder diameter used in the experiment was $9.5mm$ and towed at a speed of $8mms^{-1}$ gives a Reynolds number of 76. The double exposure photograph shown in figure 7.3 was taken with a magnification of 0.203 and a pulse separation of 120ms. The magnification was accurately estimated by photographing a piece of graph paper photocopied onto transparent acetate sheet and carefully floated on the water surface below the camera. The approximate pulse separation is indicated on the pulse delay box and a precise measure of the delay obtained using the phototransistor and digital storage oscilloscope arrangement used for the wave measurements.

The PIV negative was analysed on the analysis rig and the resulting velocities plotted as vector arrows shown in figure 7.4. The vortex structure is not evident from this representation as the flow was photographed from the trolley. The vortices that are shed behind the cylinder are travelling at a different velocity to the trolley and in order to reveal the vortex structure it is necessary to subtract the difference between the velocity of the trolley and the vortices. This is shown in figure 7.5 where the regions of positive and negative rotation can be seen quite clearly.

Calculating the vorticity distribution from the velocities shown above in figures 4 and 5 allows the vortex structure to be seen clearly.

7.1.2 Discussion

The completeness of the data shown in figure 7.4 above shows that extremely good quality flow photographs can be obtained from the surface flow arrangement. For the array ofvelocitiesshown here there were only 18 spurious values identified illustrating the extremely high quality of photographs that can be taken using this technique. As to the validity of the measurements however, it is less easy to say. The structure of the flow clearly shows the vortex street that

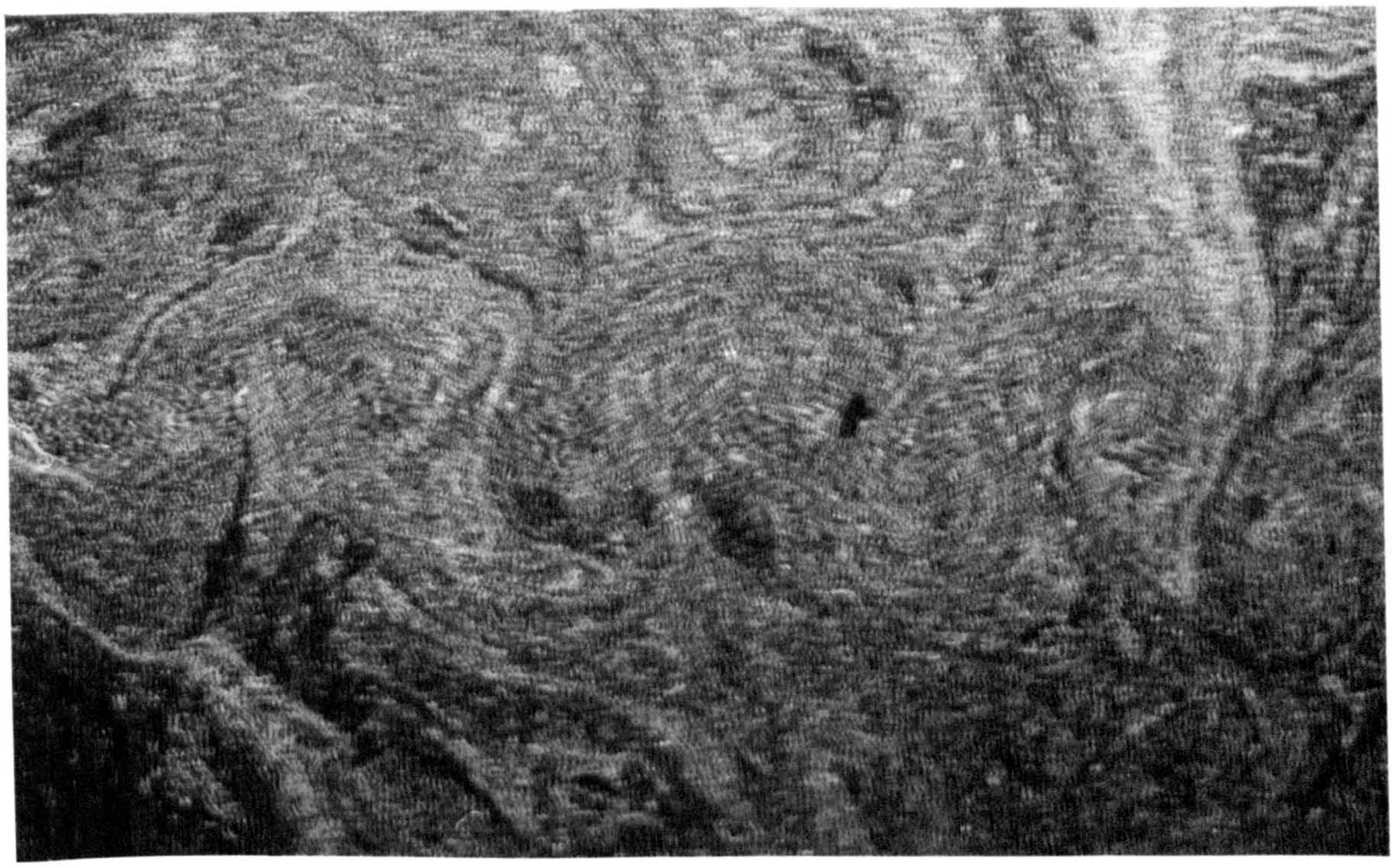

Figure 7.3: PIV negative of the flow behind the towed cylinder. The flow is from left to right and the cylinder is just outside the photograph on the left hand side.

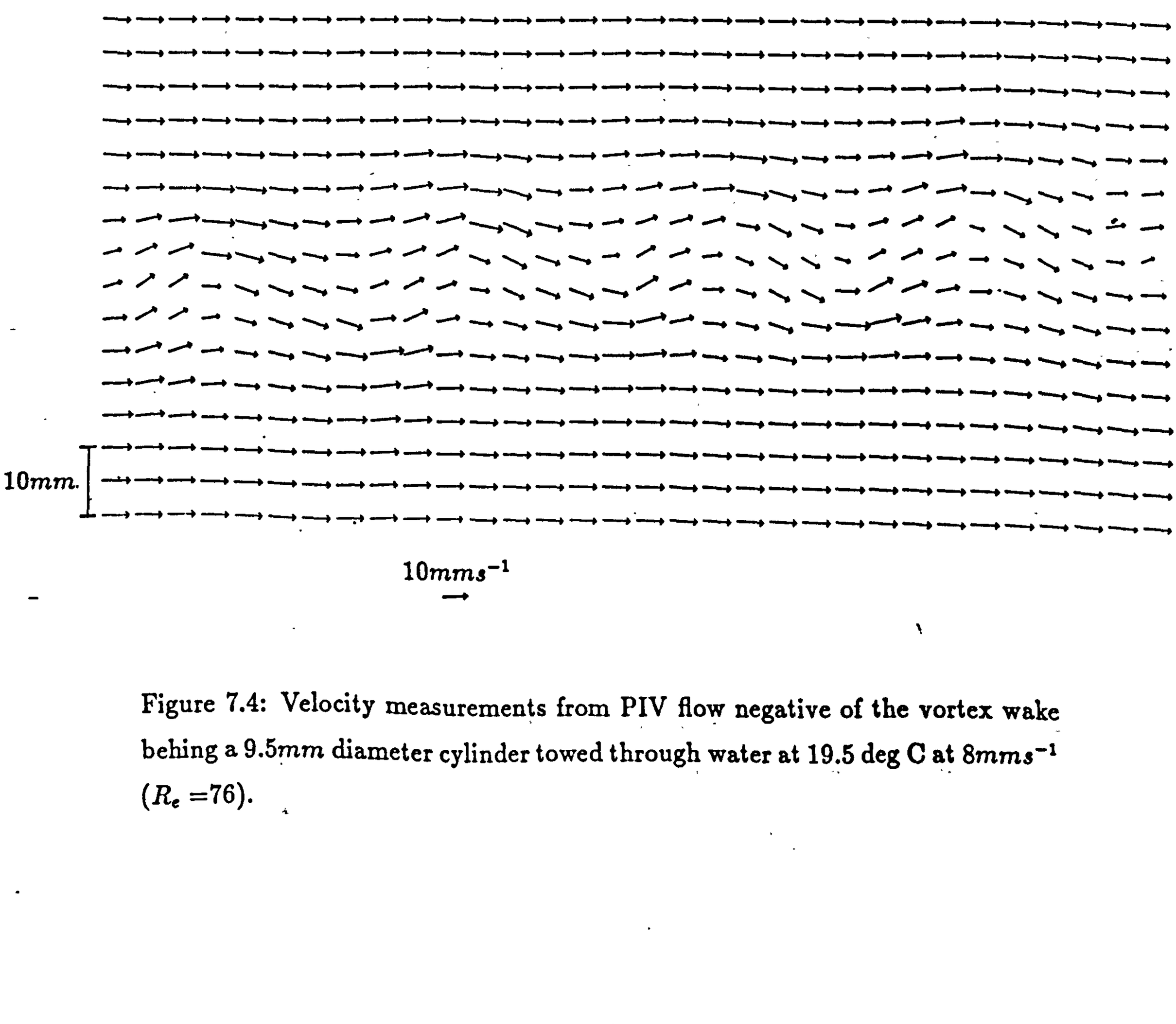

Figure 7.4: Velocity measurements from PIV flow negative of the vortex wake behing a 9.5mm diameter cylinder towed through water at 19.5 deg C at 8mms^{-1} (R_e =76).

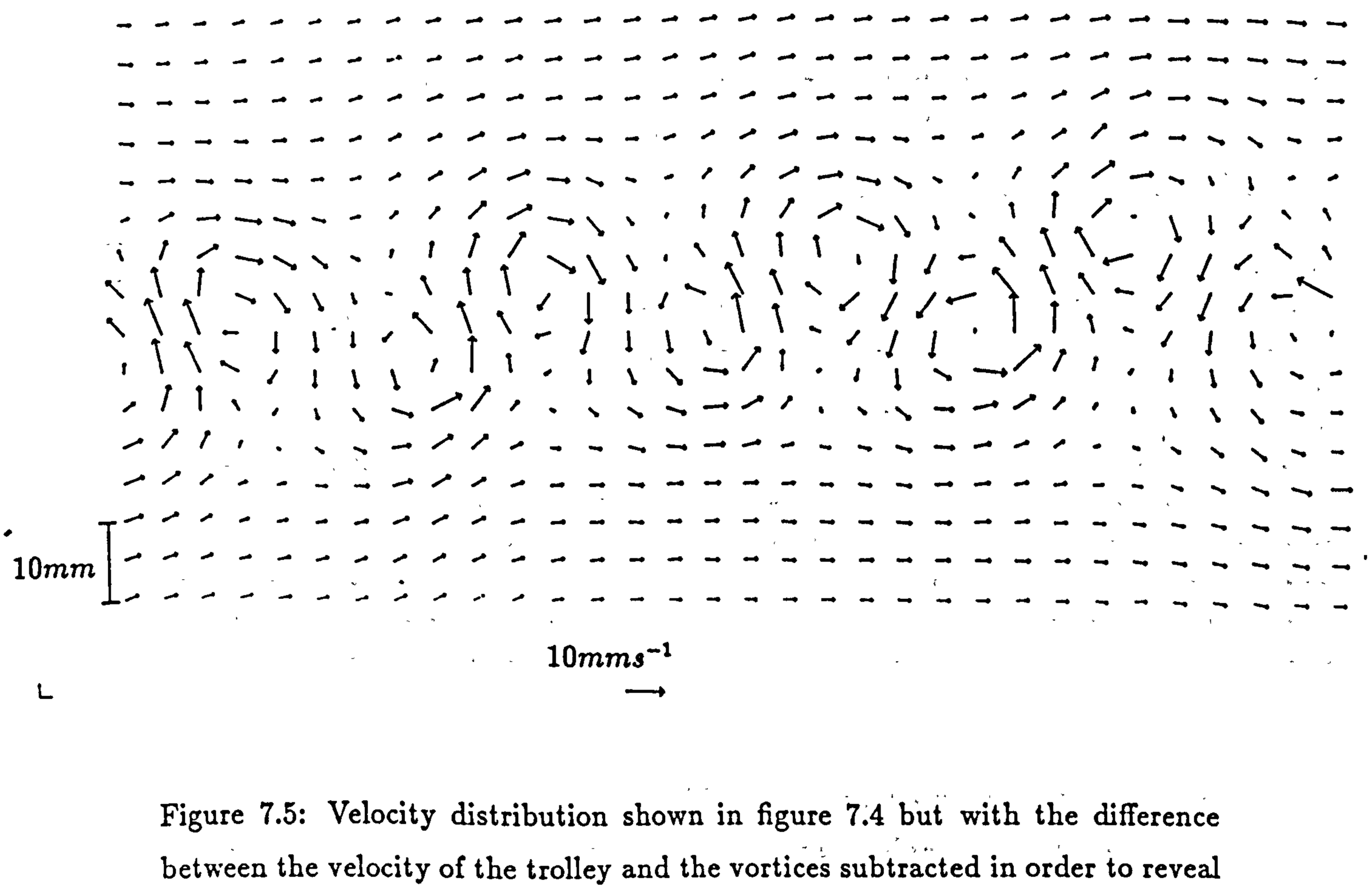

Figure 7.5: Velocity distribution shown in figure 7.4 but with the difference between the velocity of the trolley and the vortices subtracted in order to reveal the vortex wake.

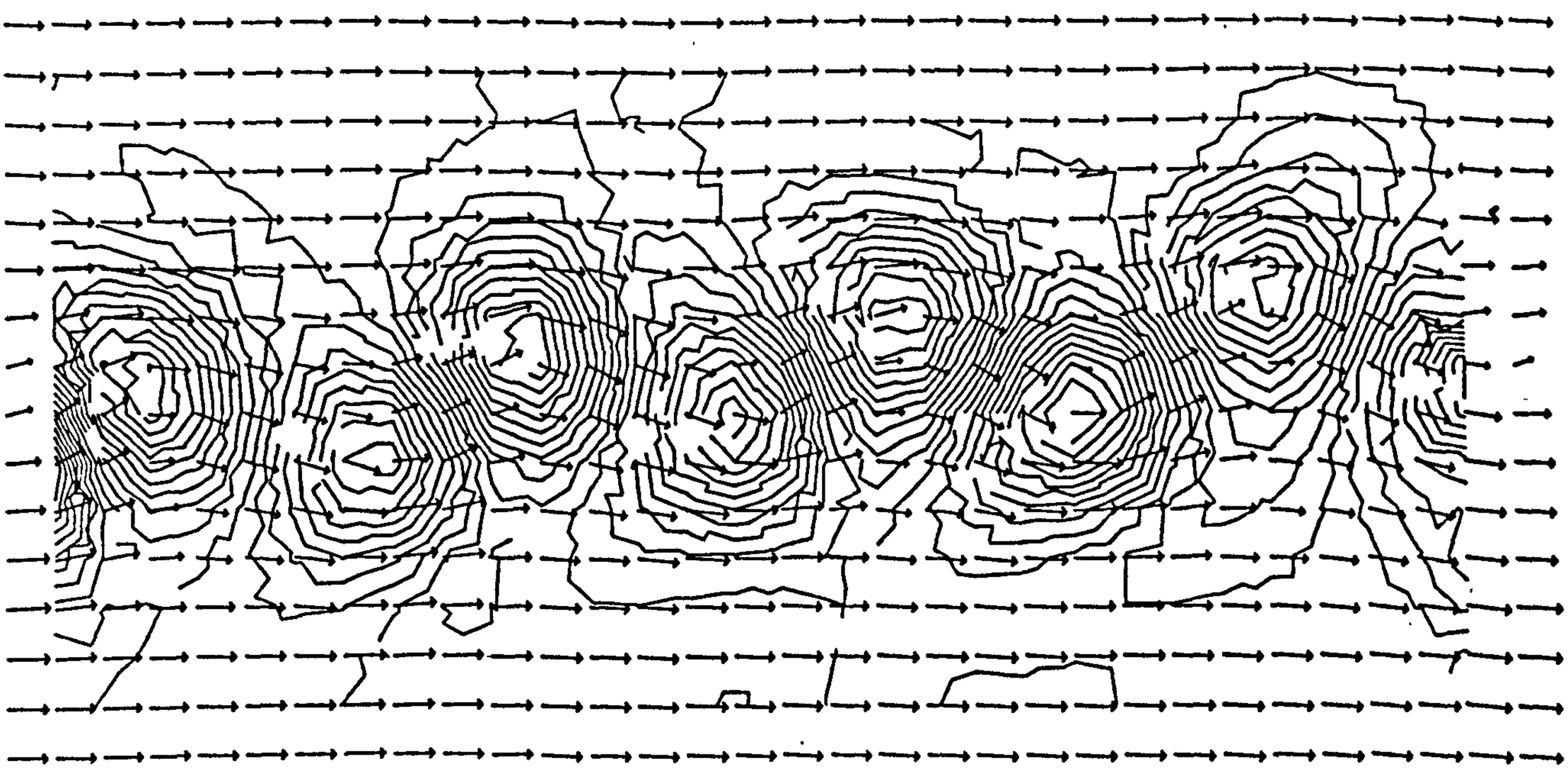

Figure 7.6: Vorticity distribution derived from the velocity measurements above. The vorticity distribution is independant of the frame of reference and would be the same if the velocities from figures 4 or 5 were used.

is well known for Reynolds numbers in this range. However, the relationship between these measurements and the vortex structure within the body of the fluid cannot be known at this stage. This is an area that will require further research if this method of recording a two-dimensional flow is to be taken any further.

If further research shows that the motion of the surface in such flows is representative of the flow within the body of the fluid this technique could provide a lot of valuable experimetal data. The high quality of the photographs that can be taken and the reduced cost of putting together a measuring system without a laser are good incentives for using PIV in this context.

7.2 PIV measurement of Acoustic Streaming

Acoustic streaming is the generation of non-zero mean flows by a sound field. The phenomenon typically arises due to attenuation or dissipation of a sound field in its medium of propagation or, when a solid wall is present, in the boundary layer [83]. The attenuation provides the mechanism for transferring momentum into the body of the fluid and thus generates the streaming.

Several articles consider streaming [?,20] but as a whole the subject has been neglected. This is possibly because high acoustic intensities are neccessary before streaming takes place. Additionally, it is particularily difficult to measure with probe type measuring instruments due to the measuring probe creating its own boundary layer and upsetting the flow under investigation. Consequently most experimental work is based on flow visualisation [20].

The work that is described in this section is the result of collaboration within the Fluid Dynamics group at Edinburgh and is more fully documented from a fluid dynamics point of view in the appropriate thesis Sharpe, 1988 [109]. The Streaming under investigation is known as Rayleigh streaming and was considered because it is relatively well understood, can be easily generated and the streaming velocities independently estimated by measuring the pressure of the sound field[109].

7.2.1 Rayleigh Streaming

This form of streaming was first explained by Rayleigh himself in his theory of Sound [103] and occurs due to the viscous attenuation of the sound field in the boundary layer when a solid wall is present. The most common configuration in which to observe this effect is when a standing wave is set up in a circular tube. The form of the streaming is evident from the PIV photograph in figure 7.7 with the direct current, along the walls, always pointing towards the velocity

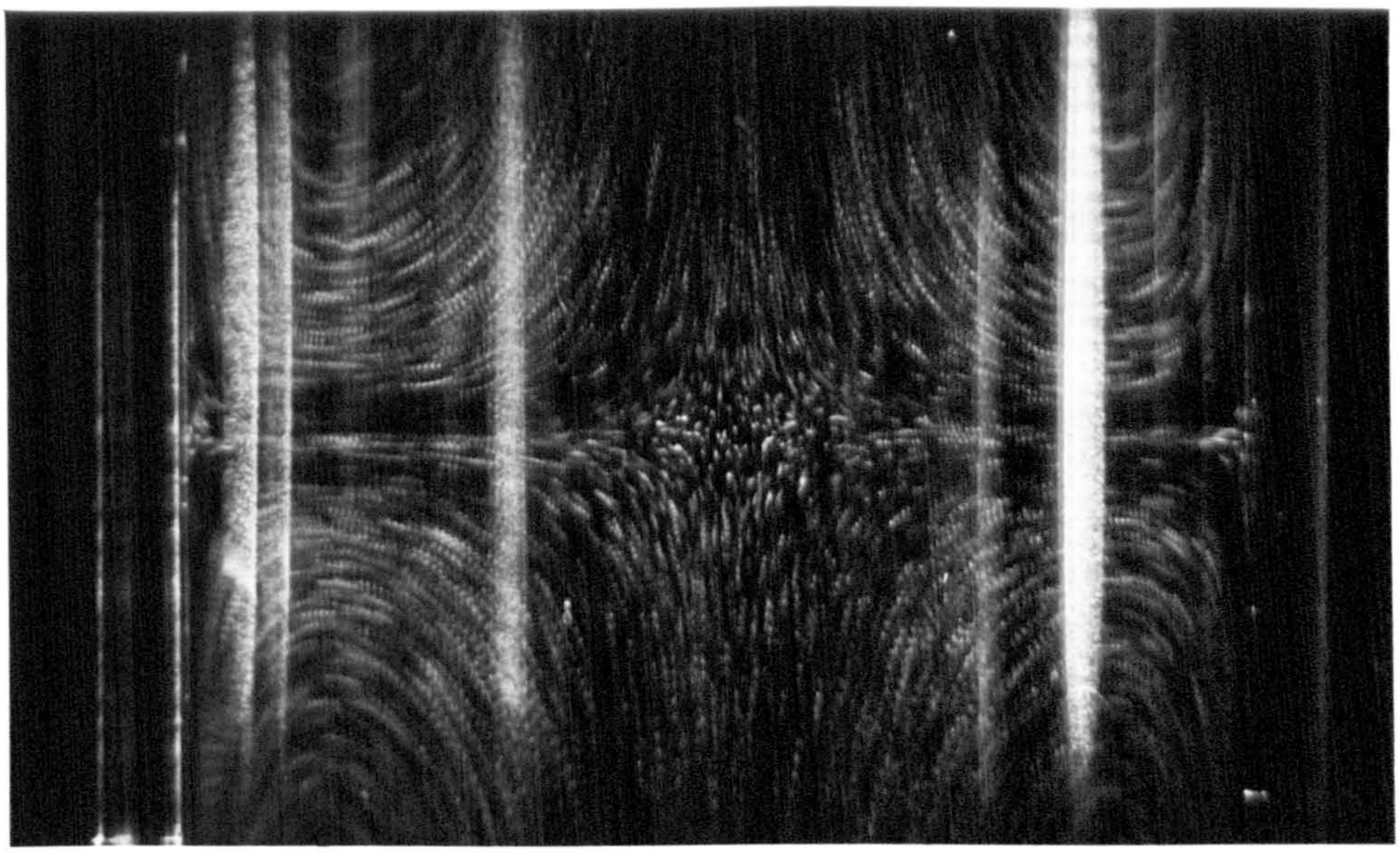

Figure 7.7: PIV negative of Rayleigh streaming within a glass tube

nodes and the return current, along the tube centre, towards the antinodes. For a standing wave of the form

$$U(x,t) = U(x)\sin\omega t \tag{7.86}$$

The velocity at the wall of the tube is given by Rayleigh's Law as,

$$U_w(x) = \frac{-3}{4}\omega^{-1}U(x)\frac{dU(x)}{dx} \tag{7.87}$$

It is then possible to calculate the velocity at any point of the tube perpendicular to the axis[1].

$$U_s = U_w(x)\left(1 - \frac{2s^2}{a^2}\right) \tag{7.88}$$

where a is the tube radius and s is the distance from the tube centre.

[1]This neglects the boundary layer.

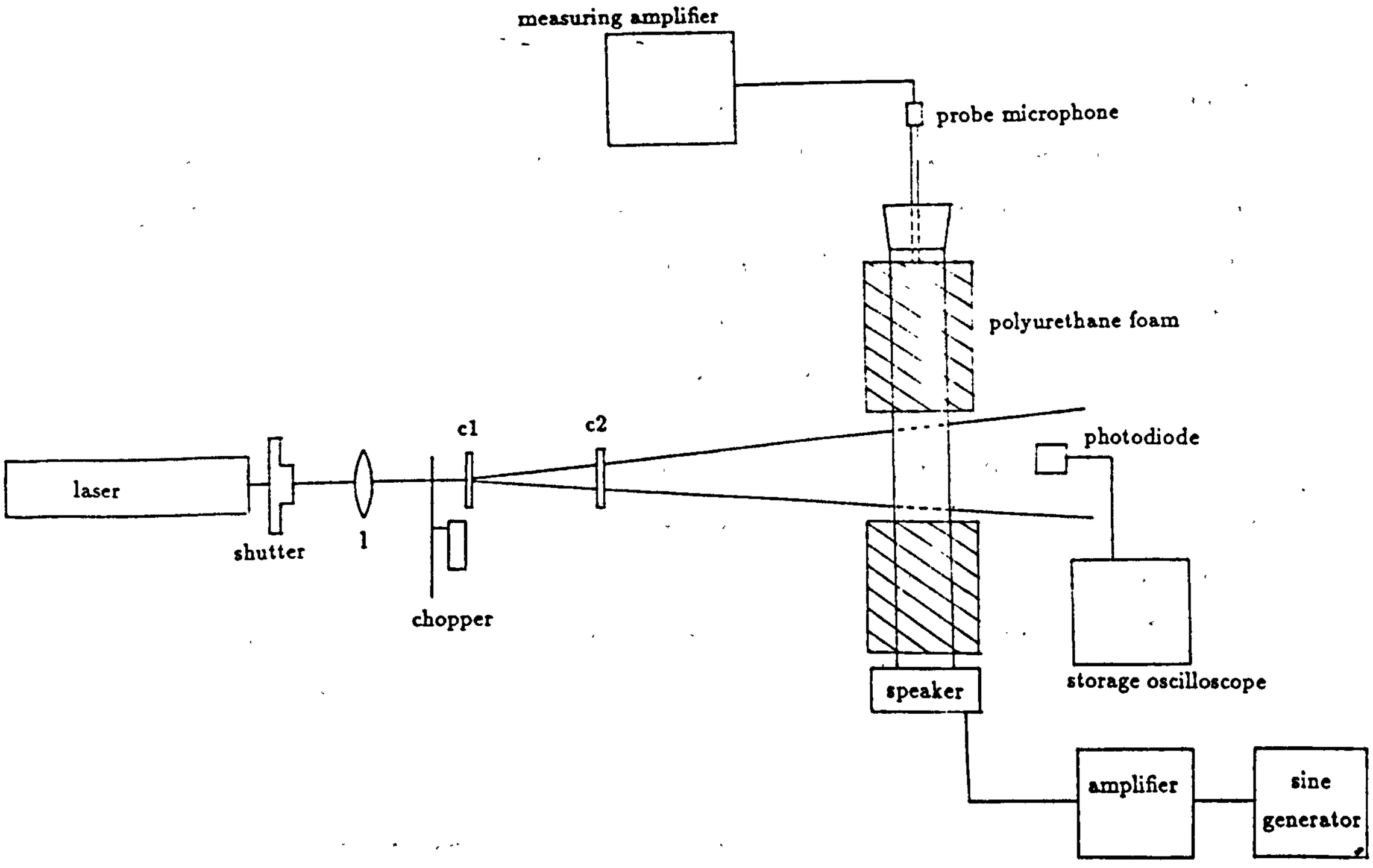

Figure 7.8: Arrangement used to record Acoustic streaming.

7.2.2 Experimental Apparatus

The experimental setup for recording the streaming is shown in figure 7.8. The very low velocities meant that very high laser power was not neccessary and a 32 mW He-Ne laser ($\lambda = 633nm$) was used to illuminate the flow. In this case the beam from the laser was expanded to form a sheet and then pulsed by chopping the beam with a rotating mechanical chopper positioned at the focus of l. A combination of spherical lens l and two cylindrical lenses C1 and C2 are used to form the light sheet which, when introduced into the tube was approximately 2cm high and 1/2 mm thick. An external shutter positioned behind l controlled the number of exposures on a given frame and was used rather than the camera shutter in order to minimise vibration at the film plane. The pulse period T was measured using the usual photodiode and storage scope arrangement.

The camera used to record the flow was a Nikon 35mm SLR with a 55mm flat

focus lens. Image distortion due to the lens was minimal comared to that due to the curved tube walls and this was estimated by photographing a regular grid which had been introduced into the tube. Subsequent measurement with a travelling microscope showed that distortion was negligible apart from aproximately 1mm from the tube wall. Flare from the wall precluded measurement in this region and so it was not neccessary to introduce any corrections.

The film used to make the measurements was T-MAX 400 which has adequate sensitivity for the laser power used and also exhibits good resolution ($\approx 100 lines/mm$ depending on contrast). Recording the flow field was always done in complete darkness to maximise the contrast and therefore resolution in the final image.

7.2.3 Measurements and Results

With the apparatus arranged as in figure 7.8 sound of frequency 2460 Hz was introduced into the tube (length 450 mm, internal diameter 23.3 mm) using a horn loudspeaker. The tube was terminated with a rubber bung having a metal plate firmly attatched to it. With this arrangement the sound field corresponded to the 7th normal mode of the air column.

An independant check of the streaming velocities was provided by means of pressure measurements which were made using a probe microphone inserted through the rigid end of the tube (Bruel & Kjaer type 4166).

Tobacco smoke was used as seeding and was introduced into the tube through the hole normally occupied by the probe microphone. The sound field was switched on and the streaming left to develop and mix the seeding. In this case It was possible to estimate the maximum velocity by eye which allowed the pulse separation and duration of the chopper to to be set to suitable values (0.114 and 0.0057 seconds respectively). The flow was photographed with four pulses near a velocity node. Individual smoke particles can be seen quite clearly and are not

recorded as point images but rather as streaks. This is because the vibrational amplitudes used to generate the streaming are quite large and in places are as large as the particle displacements themselves.

Certain dificulties were encountered in the analysis of the flow negative due to the large vibrational amplitudes mentioned above. Each particle image on the flow negative is recorded over 15 or so periods of the sound field and because the positional probability distribution of a particle in the sinusoidal sound wave is double peaked the particle images are dumbell shaped. The length of each dumbell image is proportional to the amplitude of the sound field which varies down the length of the tube ie. large at the antinodes and small at the nodes. This produces a non-circular diffraction halo in the Youngs fringe pattern, figure 7.9, whose ovality depends strongly upon the vertical position of the PIV negative being interrogated. Subtraction of an average halo shape from individual fringe patterns prior to transformation to the autocorrelation plane was found not to suppress the central correlation peak in the desired fashion. Instead, it was found that subtraction of the average halo actually introduced unwanted peaks into $R'(s)$, figure 7.10. This problem was solved in rather an ad hoc way.

The analysis program was instructed to aquire its "average halo" for a given row of measurements from that row of fringe patterns themselves. Each fringe pattern within a row, in general, had a different fringe frequency and orientation but a similar halo function and so by averaging all the halo's in one row it was possible to come up with a relatively *smooth* halo shape. Performing pedistal subtraction along that row with this function then allowed the displacement correlation peak to be detected at a high proportion of the measurement points[111].

Erroneous measurements were identified and removed and the missing values interpolated to form the smooth flow field shown in figure 7.11. The measurements look slightly asymmetric with the velocities in the upper left vortex seeming to sweep over to the right. It is possible that this was caused by outside air currents which were observed to have quite a profound effect on the stability of the

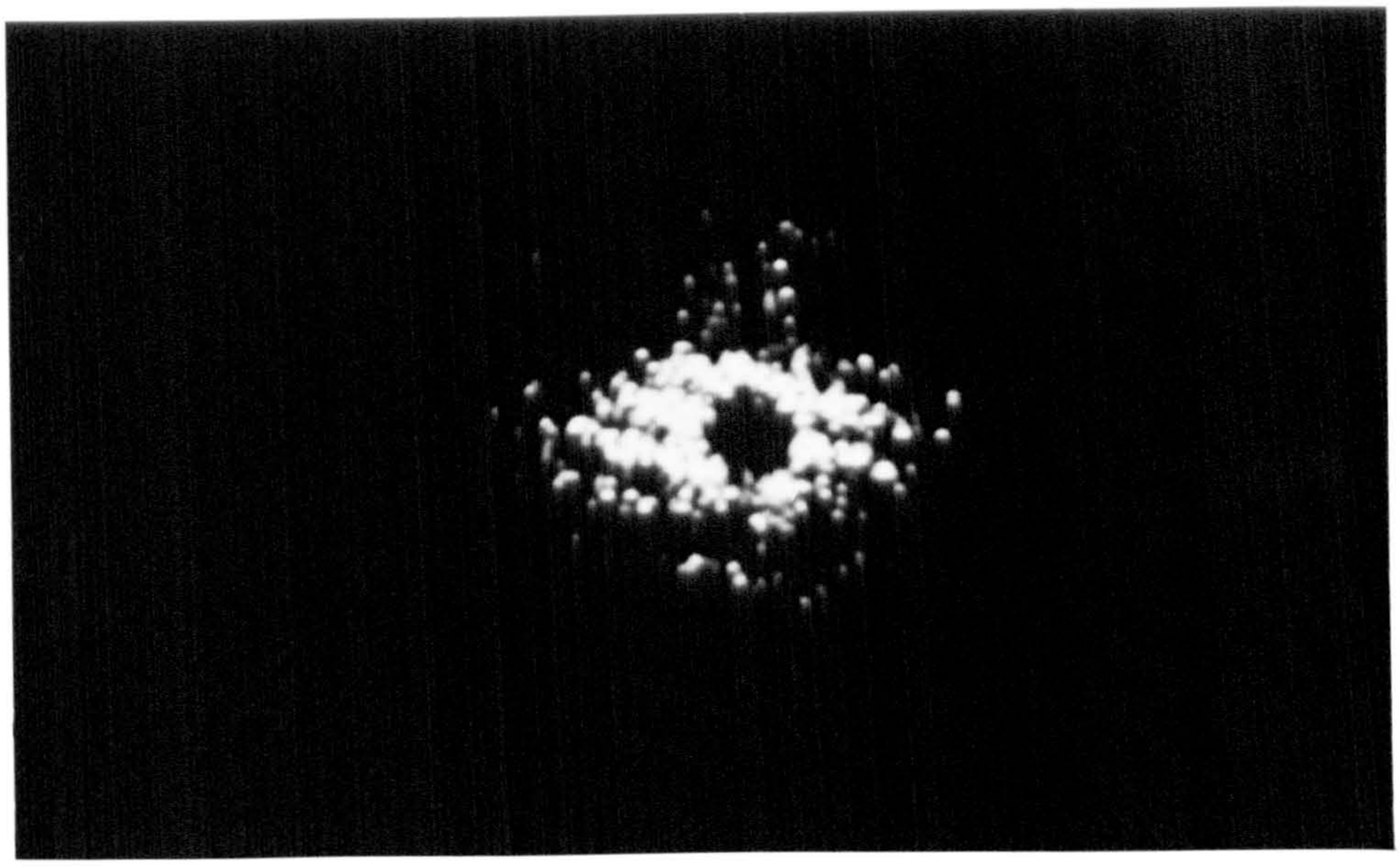

Figure 7.9: Typical fringe pattern from the flow negative in figure 7.

streaming. It was neccessary to lag the sound tube with insulating material so that warm or cold draughts would not upset the streaming. Even the warmth of a nearby hand had an observable effect. From equation 7.88 it can be seen that the axial velocity should be parabolic across any section of the tube with the maximum velocity given by equation 7.87 and zeroes at distances $0.707a$ from the axis of the tube. Axial velocities were taken from the data for three separate lines across the tube a few mm from the velocity node (see figure 7.12). The solid parabolae were fitted using the measured velocity maxima and the theoretical zero points. The fits are quite good though the velocities do show some deviation near the left crossover point, reflecting the assymetry mentioned earlier. The maximum slip velocity was calculated using equation 7.87 and a value of 151 dB for the maximum pressure to be $\approx 6.5mm/s$. This would make the maximum axial velocity a few mm from the velocity node 3-4mms^{-1} which is in aggreement with figure 7.12. The cross sectional velocity measurements agree with the theoretical curves to within about 10% in the region of the central return velocity but deteriorate in the outer regions.

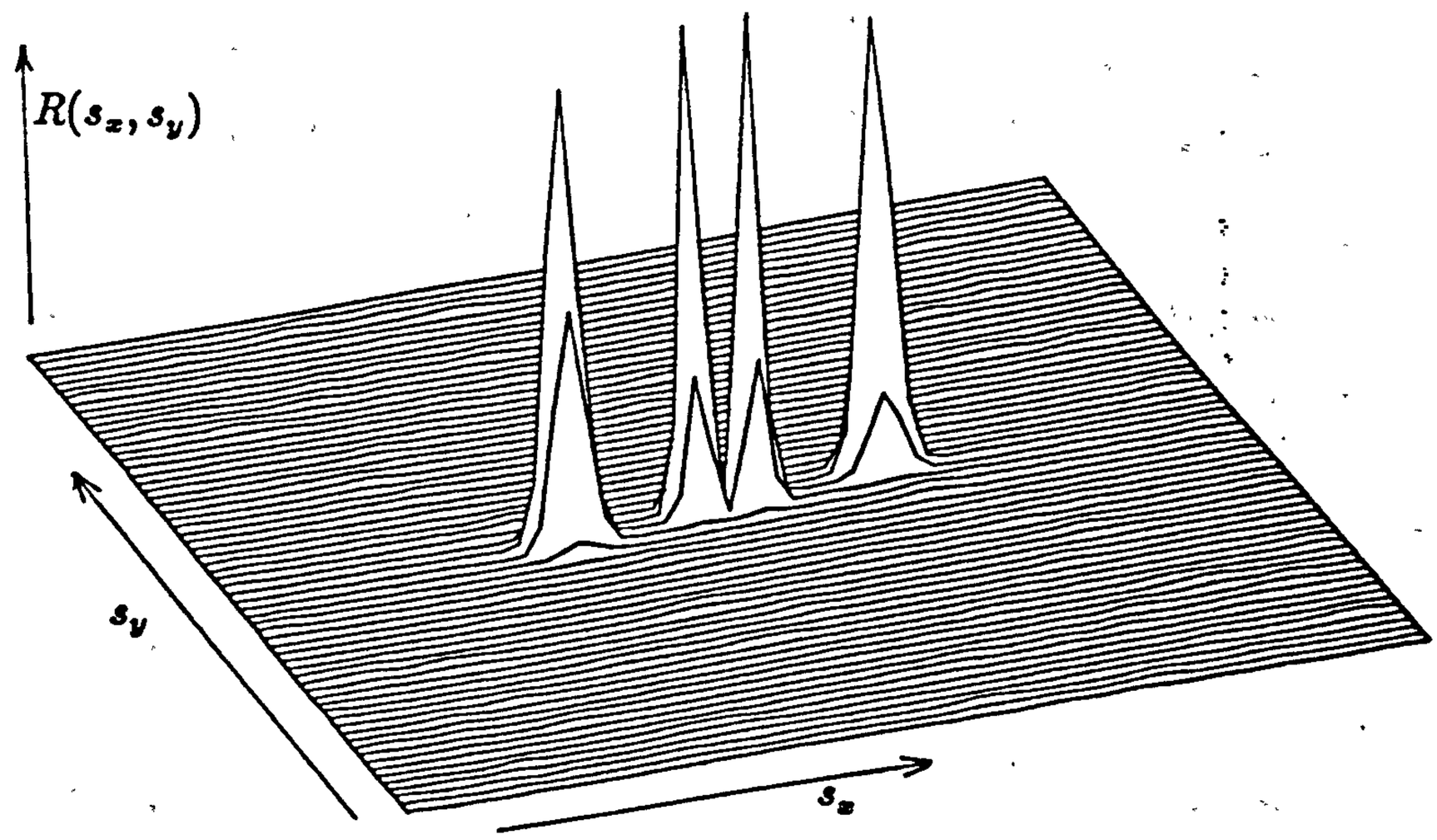

Figure 7.10: The two central peaks in the autocorrelation plane shown above resulted from the subtraction of an average diffraction halo from a fringe pattern whose halo was significantly different in shape.

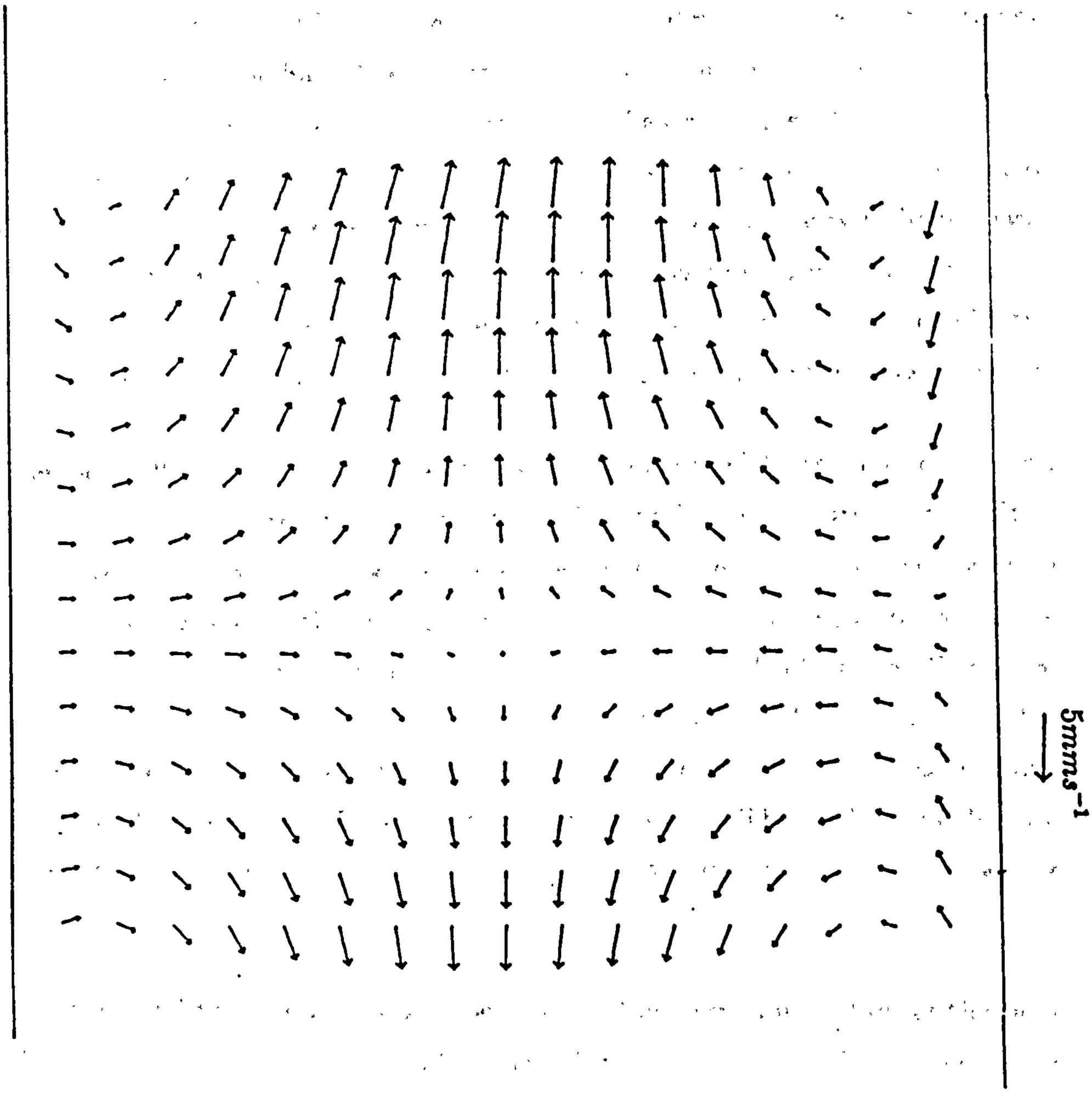

Figure 7.11: Velocity map of the streaming at standing wave node.

7.2.4 Discussion

It has been shown that PIV can be used to successfully measure acoustic streaming. This would not have been possible with conventional probe devices and unlike measurements that could be made with Laser Doppler Anemometry the PIV measurements were made "instantaneously" over a whole field. To obtain an equivalent set of measurements with LDA it would be neccessary to have a two-component LDA system with a precise traversing system to move it across the flow field and a carefully controlled environment to prevent external conditions from upsetting the streaming over the time required to make the measurements.

There are difficulties and limitations associated with the PIV technique however. A large out-of-plane component present in the flow being measured can result in significant errors being introduced into the measurements and in extreme cases causing such decorrelation in the final flow record that no measurements are possible. More importantly in this case though is the effect of the vibrational displacement on the velocity displacement measurements. The streaking of the particle images limit the smallest particle displacements that can be resolved and so reduce the range of velocies that can be measured. The analysis of the flow photograph was also complicated considerably by the elongation of the particle images.

A way around this problem would be to pulse the laser illumination at the same phase position of the sound field for a sufficiently short time to freeze the motion of the particle. For the frequency of the sound field used here this would require a pulse lasting only a fraction of a millisecond and would then require laser power of several watts. Successfull implementation of this idea would depend upon precise synchronisation of the illumination system with the sound field. This is not impractical and this research is likely to be pursued for sound fields at ultrasonic frequencies.

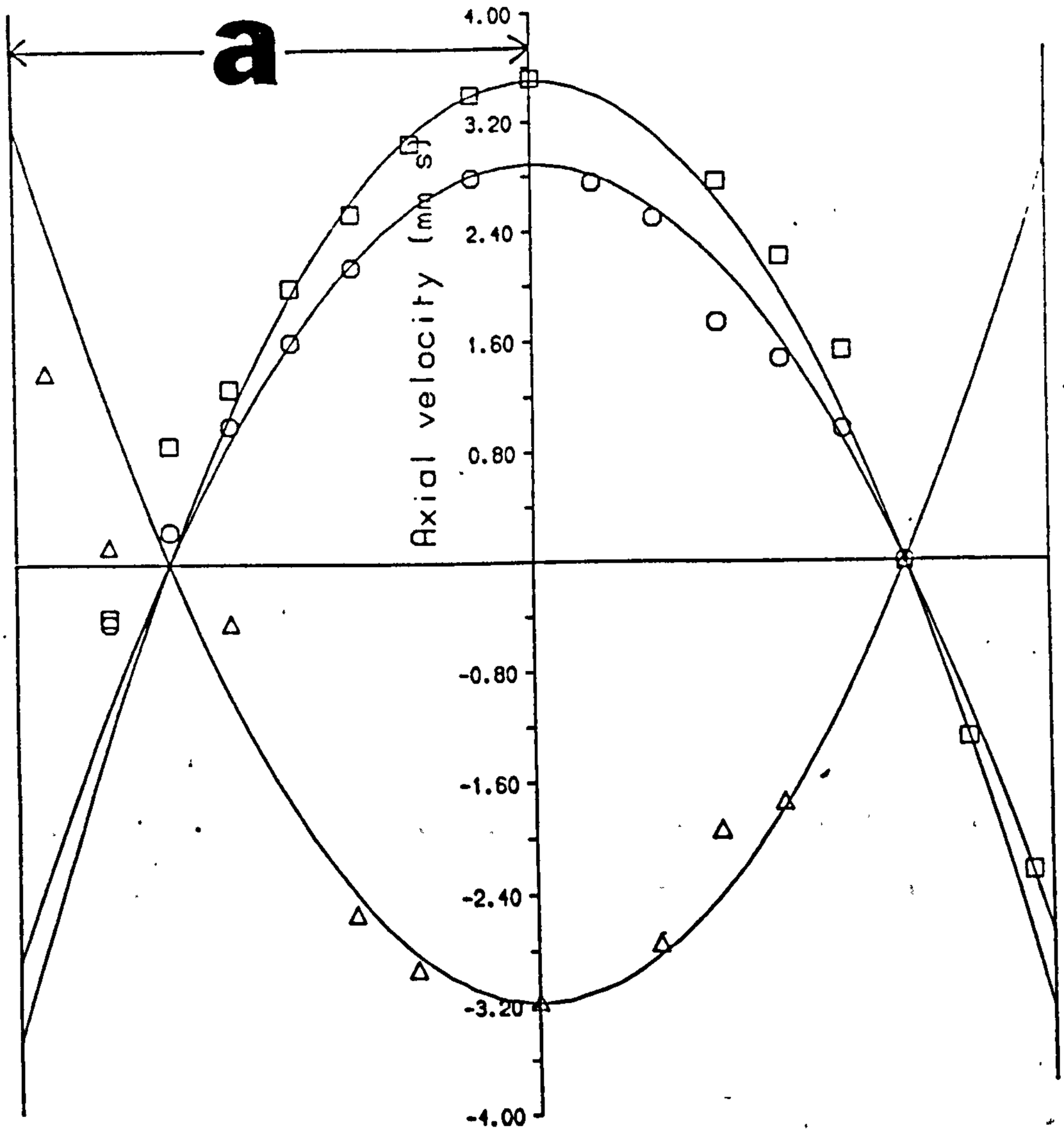

Figure 7.12: Experimentally measured axial velocities in the tube (symbols) and theoretical curves.

[2]

[2]Diagram 7.12 taken from Sharpe et al, 1988,[111].

Chapter 8

Discussion and Conclusions

The main aim of this project was to investigate the possibility of using the PIV technique to make full field velocity measurements under breaking waves. This has been done and the main components of this work are summarised below.

1. An initial literature search gave an indication of the extent to which particle image velocimetry has been developed and put into practice. A brief resume of the most important pieces of work is given in Chapter 1.

2. From background reading and experience based on initial experiments the photographic recording process is considered with regard to the flow characteristics, seeding, illumination, recording medium, optics and exposure parameters. A novel PIV illumination system based on a rapidly scanned laser beam is introduced and is shown to be significantly more efficient than the more conventional pulsed illumination arrangement based on expansion and modulation of a CW laser beam.

3. Evaluation of PIV negatives is discussed in Chapter 3. The automatic analysis of PIV negatives is achieved on a point by point basis over the area of the flow negative. It is shown that the mean velocity within each local analysis area can be accurately and reliably extracted from the autocorrelation function of the local image intensity distribution. The autocorrelation function is obtained efficiently using optical and digital techniques.

4. A preliminary investigation of the accuracy associated with the above methods of recording and evaluating the flow field is given in Chapter 4. The factors that limit this accuracy are identified and discussed. It is shown from an example wave record that individual velocity measurements can be made with accuracy approaching 1%.

5. The evaluation of the velocity data from the analysis rig is considered. The identification of spurious data values is discussed and the procedure for the filtering out of these values described. Interpolation and calculation of vorticity is also considered.

6. A wave measuring facility based on the foregoing techniques is described and shown to give sensible results when applied to a plunging deep water breaker. The versatility of PIV is illustrated with two further applications of the technique to surface flow and acoustic streaming.

From the results of the studies that are summarised above it is believed that PIV has been shown to have considerable potential for future studies of water wave breaking. The wave recording and analysis system that has been developed in the course of this project has the potential of providing the basis for an ongoing program of work that would concentrate on both the application of the measurement system to various wave types and the continuing development of the measuring technique itself. Additionally, it has been shown that as well as having significant potential for wave measurements PIV can be applied in a wider context. It is anticipated that further development and commercialisation of the particle imaging technique will lead to it being widely used in academic and industrial research. However, the need for good quality optical access to the flow being studied and high power laser light sources will necessarily confine PIV to being a research tool for use in a laboratory environment.

8.1 Limitations

It is apparent, from research described in this thesis and from the published work of other workers in this field, that there are certain limitations associated with PIV. One of the most fundamental limitations is the need for a certain amount of *a-priori* information about the flow before serious measurements can be made.

1. It is neccessary to know what the maximum velocity will be.

2. If no facility to resolve directional ambiguity is incorporated into the measurement system then the basic structure of the flow must be known so that the velocity vectors may be interpreted correctly.

3. The smallest scales of motion present within the flow must be known so that a suitable combination of photographic magnification and probe beam diameter can be used to resolve these small flow structures in the measurements.

Associated with the latter of these points is the limited spatial resolution of measurements made from a flow negative. It is neccessary that, for a successful measurement, the probe spot covers three or more complete particle pairs so that the flow particle displacements can be unambiguously identified among all the random connections between particle images. Increasing the seeding density and decreasing the particle displacement would allow a smaller probe beam diameter to be used leading to greater spatial resolution. However, the upper limit of particle concentration before speckle is formed in the image plane[1] and the smallest measureable particle separation are themselves limited by the diameter of the particle images. Smaller particles will form smaller images down to the resolution limit of the camera lens and the recording medium. These factors therefore represent the practical limit on the resolution and accuracy

[1] see Chapter 2

achievable with PIV. Large lens apertures can be used to lower the diffraction limit of the lens system but their effect is constrained by the limitations of lens design and manufacture. Higher resolution photographic emulsions are available (Holographic, 1250 lines/mm) but are of very low sensitivity (1 ASA). This then requires higher illumination intensities and although extremely high power lasers are not uncommon the associated cost and hazards begin to prohibit their use. Reducing the total measurement area and increasing the magnification of the imaging system will permit an increase in the measurement resolution and accuracy but neccessarily reduces the area over which measurements can be made. It can be seen therefore, that for a given configuration of lens/recording resolution, seeding size and illumination power there will be a range of measurement areas and scales of motion that will be measureable but which cannot be maximised simultaneously.

A further limitation that was mentioned earlier is the requirement that there be optical access to the flow for introducing the illumination sheet and imaging the measurement area. Thus, certain measurements will require the construction of special transparent models e.g. acoustic streaming in musical instruments.

Furthermore, the measurements described within this thesis are limited to two dimensions and although sterio-photography techniques have been used [36] the third component is limited in accuracy.

8.2 Future work

Particle image velocimetry is still at a relatively early stage in its development and it is likely that future research will cover all aspects of its operation. However, there are several areas in the research undertaken in this project that would benefit significantly from some further work.

The analysis rig described in Chapter 3 could be improved in several respects.

1. An improved method of removing the central peak in the autocorrelation plane of the image density at each probe position. At present, incomplete cancellation of this central peak limits the smallest measureable particle displacement and compromises the reliability of the search for the displacement correlation peak. It is possible that subtraction of the central correlation peak directly from the autocorrelation plane may lead to a more robust method of resolving small particle displacements.

2. The approach to identifying the displacement correlation peak could be improved. This peak is located with a simple maxima search but could be improved by a more sophisticated search algorithm that considers neighbouring values as well as the average background value.

3. An overall improvement in the efficiency of the software could lead to a significant decrease in computation time per measurement point. A floating point co-processor and translation of the present interpreted language into a compiled language could easily result in an order of magnitude reduction in analysis time.

4. Registration of individual frames is, at present, done manually and is relativly crude compared to the rest of the film interrogation process. An automatic film registration system which could level and position the negative at its origin could be developed which would form the basis for an analysis rig capable of analysing whole films without user intervention. Combined with an increase in the overall computation speed it would be

possible to compute ensemble averages of a flow or automatically make measurements at a number of phase positions of a flow.

In Chapter 5 it was shown how spurious data points are identified and removed by means of an interactive vector editing program. In order to remove the predjudicial influence of a user and to speed up the operation for very large data sets it will be neccessary to formalise the procedure for identifying anomalous data points. Local comparison routines are useless when there is a large proportion of erroneous values. It is felt that a more reliable approach based on the identification of the most probable coherent structure from the data present and then removal of those that are inconsistent with this structure would mimick the evaluation of the data by a human observer. Additionally, there is the correlation strength C_f which is shown to be related to the confidence attributable to a measurement and which could be used as a further indication of the reliability of a given measurement.

Two fundamental sources of random error were identified in Chapter 4.

- Errors due to random correlation noise.
- Errors due to the discrete and random manner in which the continuous flow field is represented by particle image pairs on the PIV negative.

A formal treatment of the uncertainty associated with random correlation noise is needed so that the random errors associated with the flow recording process can be evaluated. Additionally, the measurement errors due to the finite range of particle displacements within the probe area require further work. This treatment would relate the randomness of the measurements to the seeding density and size and the nature of the flow within the probe region. The simplest case of a one dimensional velocity gradient is considered at the end of Chapter 4 and it is proposed that more complex situations such as higher non-linear flow profiles and turbulence be treated in a similar manner.

.1 Appendix A: Youngs fringes

Consider a region of film with N particle image pairs recorded randomly over it where the particle images are assumed to be identical and circularly symmetrical. The photographic density distribution can be represented by,

$$g(r) = h(r) * \sum_{l=1}^{N} [\delta(r - r_l) + \delta(r - r_l - d_l)] \tag{.89}$$

where $h(r)$ represents a single particle image, δ is the Dirac delta function and $*$ is a convolution operator. The particles originally at r_l have been displaced by d_l where all the values of d_l for the N particles within the region have a small amount of scatter about a mean value due to random particle positions over a spatially varying flow field ie. turbulence or velocity gradient.

With the film positioned in front of a converging lens and illuminated over the region of interest with a beam of spatially coherent light (from a laser) the optical Fourier transform of $g(r)$ will be present in the back focal plane of the lens [51] (see figure 3.6). and is given by,

$$\mathcal{F}.\mathcal{T}.[g(r)] = \mathcal{F}.\mathcal{T}.[h(r)] \sum_{l=1}^{N} \left\{ \exp^{-j\frac{2\pi}{\lambda f}(r_f r_l)} + \exp^{-j\frac{2\pi}{\lambda f}(r_f (r_l + d_l))} \right\} \tag{.90}$$

where $\mathcal{F}.\mathcal{T}.$ denotes a Fourier transform, λ is the wavelength of the coherent illumination, and r_f the position in the Fourier plane of the lens. This expression neglects a phase factor, but is of no consequence when the intensity is detected. Thus if $k = \frac{2\pi}{\lambda f} r_f$, the intensity detected in the Fourier plane is given by,

$$I(k) = |\mathcal{F}.\mathcal{T}.[g(r)]|^2 \tag{.91}$$

giving

$$I(k) = S(k) \sum_{l=1}^{N} \left(\exp^{-jkr_l} + \exp^{-jk(r_l + d_l)} \right) \sum_{m=1}^{N} \left(\exp^{jkr_m} + \exp^{jk(r_m + d_m)} \right) \tag{.92}$$

where the first and second bracketed terms are also denoted by B_l and B_m^* respectively and $S(k) = |\mathcal{F}.\mathcal{T}.[h(r)]|^2$ which finally gives,

$$I(k) = S(k) \left(\sum_{l=1}^{N} (2 + 2\cos k d_l) + \sum_{l<m}^{N} (B_l B_m^* + B_l^* B_m) \right) \tag{.93}$$

If all the displacements d_i within the probe region are similar then the first term in the brackets will represent the speckle displacement fringes whose frequency is inversely proportional to the particle image displacement. The second term is a random interference term which is due to the random positions of the particle pairs and for a large N will constitute a random background speckle noise. However, if N is small ie $N \leq 3$ then this term will contribute a noise signal whose magnitude and frequency will be comparable to that of the first term and corresponds to the ambiguous situation discussed in Chapter 2. $S(k)$ is the diffraction halo that is representative of the individual particle images themselves and modulates the fringes and speckle noise. In practice there will be a high intensity spike at $k = 0$ that is associated with the mean transmittance of the photographic transparency and is usually removed with a small light stop at the origin. The above analysis neglects the finite extent of the probe area, which is usually a circular region centred on the optical axis of the transforming lens, and which will in practice widen the central spike discussed above and increase the significance of random noise due to the inclusion of single particle images whose corresponding displaced images fall outside the probe area.

.1 Appendix B: Publications

The following articles, published in journals and conference proceedings, were generated from the work undertaken in this project.

- C. Gray, C.A. Greated, W. Easson and N.E. Fancey, *The application of particle image velocimetry to measurement under waves*, Proc. 2nd Int. Conf. of Laser Anemometry, Strathclyde, 1987.

- C. Gray and C.A. Greated, The application of particle image velocimetry to the study of water waves, *Optics and Lasers in Engineering*, 19,pages 625-276, 1988.

- C. Gray and C.A. Greated, *A scanning laser beam system for the illumination of flow fields*, Von Karman Inst. for Fluid Mechanics lecture series 1988-06, selected papers, pages 53-62, 1988.

- C. Gray, D. Skyner and C.A. Greated, *The measurement of breaking waves using particle image velocimetry*, Proc. ICALEO, pages 166-177, 1988.

- D.J.S. Skyner, C. Gray and C.A. Greated, *A comparison of time-stepping numerical predictions with whole field flow measurements of breaking waves*, Proc. Water particle kinematics, Molde, Norway, 1989.

- J.P. Sharpe, C.A. Greated, C. Gray and D.M. Campbell, The measurement of acoustic streaming using particle image velocimetry, *Acustica*, pages 168-172, 1989.

- C. Gray and C.A. Greated, *Fringe analysis for PIV measurements in acoustic streaming*, Proc. Fringe Analysis 89, Loughborough, 1989.

PAGE NUMBERING AS ORIGINAL

Bibliography

[1] Kodak technical specifications for T-MAX films.

[2] *NAG function library.* May 1977. Random number generators,G05.

[3] *Zeiss technical specifications for Planar T*, f2.8, 80mm lens.*

[4] R. Adrian. Scattering particle characteristics and thier effect on pulsed laser measurements of fluid flow: Speckle velocimetry vs. Particle image velocimetry. *Applied Optics*, 23(11), 1984.

[5] R. Adrian and C.S. Yao. Application of pulsed laser technique to liquid and gaseous flows and the scattering power of seed material. In *Proc. second Int. Symp. on Applications of Laser Anemometry to Fluid Mech.*, Lisbon, Portugal, 1984.

[6] R. Adrian and C.S. Yao. Development of pulsed laser velocimetry PLV for measurement of turbulent flow. In X.B. Reed et al., editors, *Symposium on Turbulence*, pages 170–186, Univ. of Missouri, Rollo, 1984.

[7] R.J. Adrian. *Fluid Mechanics Measurement*, chapter 5. Hemisphere, Washington DC, 1983.

[8] R.J. Adrian. Image shifting technique to resolve directional ambiguity in double- pulsed velocimetry. *Applied Optics*, 25(21):3855–3858, 1986.

[9] R.J. Adrian. Optical methods for measuring velocity fields. In *Von Karman Institute Lecture series 1988-06*, 1988.

[10] E. Archbold, J.M. Burch, and A.E. Ennos. Recording of in-plane surface displacement by double exposure speckle photography. *Optica Acta*, 17:883–898, 1970.

[11] M. Arnold, K.D. Hinsch, and D. Mach. Turbulence level measurement by speckle velocimetry. *Applied Optics*, 25:330–331, 1986.

[12] W. Arnold and K. Hinch. Purely optical parallel processing in particle image velocimetry and the study of flow structures. In *Proc. ICALEO*, 1988.

[13] M.P. Arroyo, M. Quintanilla, and J.M. Saviron. Three dimensional study of the Rayleigh Bénard convection by particle image velocimetry measurements. In *Proc. ICALEO*, 1988.

[14] D.B. Barker and M.E. Fourney. Displacement measurements in the interior of 3-d bodies using scattered light speckle patterns. *Exp. Mech.*, 16(6):209–214, 1976.

[15] D.B. Barker and M.E. Fourney. Measuring fluid velocities with speckle patterns. *Applied Optics*, 1(4), 1977.

[16] D.B. Barker and M.E. Fourney. Three dimensional speckle interferometric investigation of the stress-intensity factor along a crack front. *Exp. Mech.*, 17(7):241–247, 1977.

[17] J.S. Bendat and A.G. Piersol. *Measurement and analysis of random data.* John Wiley and Sons, 1966.

[18] E. Berabeau, J.C. Amaré, and M.P. Arroyo. White light speckle method of flow velocity distribution. *Applied Optics*, 21(14):2583–2586, 1982.

[19] P. Bergè and M. Dubois. Study of unsteady convection through simulataneous velocity and interferometric measurements. *Journal de Physique-Lettres*, 19:506–509, 1979.

[20] R.T. Beyer. *Non Linear Acoustics.* U.S. Navy, 1974.

[21] A. Bicciolo, A. Cenedese, and A. Paglialmga. Tracking analysis of multi-exposed photographs. In *Proc. ICALEO*, 1988.

[22] R.N. Bracewell. *The Fourier Transform and its applications.* McGraw Hill, 1986.

[23] J.M. Burch and J.M.J Tokarski. Production of multiple beam fringes from photographic scatterers. *Optica Acta*, 15:101–111, 1968.

[24] L. Celaya, J.M. Jonathan, and S. Mallick. Velocity contours by speckle photography. *Opt. Comm.*, 18(4):496–498, 1976.

[25] F.D. Chiang and A. Asundi. Perspective effect in the white light speckle method. *Applied Optics*, 21(10):1708–1710, 1982.

[26] F.P. Chiang and R.P. Khetan. *Strain analysis by one beam laser speckle interferometry: Part 2 Multiaperture method.* Technical Report 253, College of Eng. and Appl. Sci., Stony Brook N.Y., 1974.

[27] G. Cloud, R. Falco, R. Radke, and J. Peiffer. Non-coherent light speckle photography for measurement of fluid velocity fields. *Proc. Soc. Photo-opt. Instrum. Eng.*, 243, 1980.

[28] S.H. Collicott and L. Hesselink. Anamorphic optical processing of multiple-exposure speckle photographs. *Opt. Lett.*, 11, 1986.

[29] S.H. Collicott and L. Hesselink. Real time photorefractive recording and optical processing for speckle velocimetry. *Optics Letters*, 13:348, 1988.

[30] J.M. Coupland and C.J.D. Pickering. Particle image velocimetry: Estimation of measurement confidence at low seeding densities. *Optics and Laser in Engineering*, 1988.

[31] J.M. Coupland, C.J.D. Pickering, and N.A. Halliwell. Particle image velocimetry: The ambiguity problem. *Optical Engineering*, 27(3):193–196, 1988.

[32] J.M. Coupland, C.J.D. Pickering, and N.A. Halliwell. Particle image velocimetry: Theory of directional ambiguity removal using holographic image separation. *Applied Optics*, 26(9):1576–1578, 1987.

[33] M. Coutanceau and R. Bouard. Experimental determination of the main features of the viscous flow in the wake of a circular cylinder in uniform translation. *JFM*, 79(2):231–256, 1977.

[34] J.C. Dainty. *Image Science: Principles, analysis and evaluation–*. Academic press, 1974.

[35] T.W. Darling, A.G. Klein, G.I. Opat, and S.N. Tovey. Direct measurement of rotation by a laser speckle method. *Optica Acta*, 31(7):813–821, 1984.

[36] J.F. De Almeida Dias Delgado. *Laser Speckle Velocimetry three dimensional measurements.* VKI project report 1986-13, Von Karman Institute for Fluid Dynamics, 1986.

[37] P.E. Dimotakis, F.D. Debussy, and M.M. Koochesfahani. Particle streak velocity field measurements in a two-dimensional mixing layer. *Physics of Fluids*, 24(6):995–999, 1981.

[38] J.W. Dold and D.P. Peregrine. *Numerical Methods for Fluid Dynamics II.*, pages 671,679. Oxford University Press, 1986.

[39] D.G. Dommermuth, D.K.P. Yue, W.M. Lin, R.J. Rapp, E.S. Chan, and W.K. Melville. Deep-water plunging breakers: a comparison between potential theory and experiments. *J. Fluid Mech.*, 189:423,442, 1988.

[40] T.D. Dudderar and P.G. Simpkins. The development of scattered light speckle metrology. *Opt. Eng.*, 21:396, 1982.

[41] T.D. Dudderar and P.G. Simpkins. Laser speckle photography in a fluid medium. *Nature*, 270, 1977.

[42] T.S. Durrani and C.A. Greated. *Laser Systems in Flow Measurement.* New York:Plenum, 1977.

[43] F. Durst, A. Melling, and J.H. Whitelaw. *Principles and Practice of Laser-Doppler-Anemometry.* London:Academic, 1976.

[44] W.J. Easson. Velocity and force measurements in the splash zone. *J. of Strain*, 15,18, Feb. 1987.

[45] W.J. Easson and C.A. Greated. Breaking wave forces and velocity fields. *Coastal Engineering*, 8:233–41, 1984.

[46] A.E. Ennos. Speckle interferometry. *Progress in Optics*, 16:233–288, 1978.

[47] R. Erbeck. Fast image processing with microcomputer applied to speckle photography. *Applied Optics*, 24(22), 1985.

[48] B.C.R. Ewan. Particle velocity distribution measurement by holography. *Applied Optics*, 18(18), 1979.

[49] U. Gärther, U. Wernekinch, and W. Merzkirch. Velocity measurements in the field of an internal gravity wave by means of speckle photography. *Experiments in Fluids*, 4:283–287, 1986.

[50] M. Gharib, M.A. Hernan, A.H. Yavrounian, and V. Sarohia. Flow velocity measurement by image processing of optically activated tracers. *AIAA*, 85-0172, 1985.

[51] J.W. Goodman. *Introduction to Fourier Optics.* McGraw-Hill, 1968.

[52] J.W. Goodman. A random walk through the field of speckle. *Optical Engineering*, 25, 1986.

[53] I. Grant, G.H. Smith, and C.A. Greated. Velocity and vorticity measurements using speckle interferometry. In *Conf. Ser. No. 77 Photon corellation and other techniques in Fluid Mechanics*, 1985.

[54] C. Gray and C.A. Greated. A scanning laser beam system for two dimensional illumination of flow fields. In *Von Karman Inst. of Fluid Mechanics Lectuer series 1988-06*, pages 53–62, 1988.

[55] C. Gray and C.A. Greated. The application of particle image velocimetry to the study of water waves. *Optics and Lasers in Engineering*, 9:265–276, 1988.

[56] C. Gray, C.A. Greated, W.J. Easson, and N.E. Fancey. The application of particle image velocimetry to measurement under waves. In *Proc. 2nd Int. Conf. of Laser Anemometry*, pages 281–287, Strathclyde, Sept. 1987.

[57] M.W.P. Griffiths. *Breaking Waves.* PhD thesis, Physics Dept., Edinburgh University, 1989.

[58] R. Grousson and S. Mallick. Study of flow pattern in a fluid by scattered light. *Applied Optics*, 16:2334–2336, 1977.

[59] N.A. Halliwell. Particle image velocimetry: Automatic data processing. In *Proc.ICALEO*, 1988.

[60] Hesselink. Digital image processing in flow visualisation. *Annual Review of Fluid Mechanics*, 20:421, 1988.

[61] K. Hinch, D. Mach, and W. Schipper. Air flow analysis with double exposure speckle photography. In *Proc. third Int. Symp. on Flow Visualisation*, pages 789–793, 1983.

[62] K. Hinsch, W. Schipper, and D. Mach. Fringe visibility in speckle velocimetry and the resolution of random flow components. *Applied Optics*, 23(24), 1984.

[63] J.M. Huntley. Comarison of speckle photography fringe analysis algorithms. In *Fringe Analysis 89*, 1989.

[64] J.M. Huntley. An image processing system for the analysis of speckle photographs. *J. Physics E: Scientific Instum.*, 19:43–49, 1986.

[65] K. Imaichi and K. Ohmi. Quantitative flow analysis aided by image processing of flow visualisation photographs. In Hemisphere Publishing Co. New York, editor, *Proc. Third Int. Conf. on Flow Visualisation*, page 301, 1985.

[66] B. Ineichen, P. Eglin, and R. Dandliker. Hybrid optical and electronic image processing for strain measurement by speckle photography. *Applied Optics*, 19(13), 1980.

[67] K. Iwata, T. Hakoshima, and R Nagata. Measurement of flow velocity distribution by means of double exposure holographic interferometry. *J. Opt. Soc. Am.*, 67(8), 1977.

[68] K. Iwata, T. Hakoshima, and R. Nagata. Measurement of flow velocity distribution by multiple exposure speckle photography. *Opt. Comm.*, 25:311–314, 1978.

[69] R. Jones and C. Wykes. Decorrellation effects in speckle pattern interferometry ii. *Optica Acta*, 24, 1977.

[70] G.H. Kaufmann. Digital analysis of speckle photography fringes: processing of experimental data. *Applied optics*, 21:3411, 1982.

[71] G.H. Kaufmann. Numerical processing of speckle photography data by Fourier transform. *Applied optics*, 20(24):4277–4280, 1981.

[72] G.H. Kaufmann. On the numerical processing of speckle photograph fringes. *Optics and Laser Technology*, 12:207, 1980.

[73] G.H. Kaufmann, A.E. Ennos, B. Gale, and D.J. Pugh. An electro-optical read-out system for analysis of speckle photographs. *J. Phys. E: Sci. Insruments*, 13:579–584, 1980.

[74] J.C. Kent and A.R. Eaton. Stereo photography of neutral density He-filled bubbles for 3-D fluid motion studies in an engine cylinder. *Applied Optics*, 21(5), 1985.

[75] M. Kerker. *The scattering of light.* Academic press, 1969.

[76] R Kingsklake. *Applied optics and Optical Engineering.* Volume 3, Academic Press, 1965.

[77] A. Kirita, C.J.D. Pickering, and N.A. Halliwell. Particle image velocimetry: Automatic fringe analysis by cross correllation. *Optical Engineering*, 27(3):188–192, 1988.

[78] S.P. Kjelsen, R. Vinge, and P. Brevig. Kinematics of deep water breaking waves. In *Proc. 12th Annual Offshore Technology Conference.*, pages 317,325, 1980.

[79] J. Kompenhaus and R. Hocker. Application of PIV to high speed flows. In *Von Karman Institute Lecture series 1988-06:Selected papers*, 1988.

[80] H. Kreitlow and T.M. Kreis. Automatic evaluation–deformation by speckle technique. In M. Grosmann and other, editors, *Eur. Congr. Opt. Appl. Metrol. METROP*, pages 18–24, 1980.

[81] C.C. Landreth, R.J. Adrian, and C.S. Yao. Double pulsed velocimeter with directional resolution for complex flows. In *Tenth Symposium on Turbulence*, September 1986.

[82] J.A. Leendertz. Interferometric displacement–utilising speckle effect. *Journal of Physics E*, 3:214–218, 1970.

[83] M.J. Lighthill. Acoustic streaming. *J. Sound Vib.*, 61:391–418, 1978.

[84] M.S. Longuet-Higgins and E.D. Cokelet. The deformation of steep surface waves in water. a numerical method of computation. *Proc. Royal Soc.*, 350, 1976.

[85] L. Lourenco. Some comments on PIV. *Von Karman Institute Lecture series 06*, 1988.

[86] L. Lourenco, A. Krothapalli, J.M. Buchlin, and M.L. Reithmuller. Noninvasive experimental technique for the measurement of unsteady flow fields. *AIAA*, 24(10):1715, 1986.

[87] G.E. Maddux, S.L. Moorman, and R.R. Corwin. *A Programmable Data Retrieval system for in-plane displacements from Speckle Photographs.* technical report AFFDL-TM-78-109-FBE, U.S. Air Force, 1978.

[88] K.A. Marko and L. Rimai. Video recording and quantitative analysis of seed particle track images in unsteady flows. *Applied Optics*, 24(21), 1985.

[89] R. Meynart. Convective flow field measurement by speckle velocimetry. *Revue de Physique Applique*, 17:301–305, 1982.

[90] R. Meynart. Digital image processing for speckle flow velocimetry. *Rev. Sci. Instrum.*, 53(1):110–111, 1982.

[91] R. Meynart. Digital image processing for speckle flow velocimetry. *Rev. Sci. Instrum.*, 53, 1980.

[92] R. Meynart. Equal velocity fringes in a Rayleigh-Benard flow by a speckle method. *Applied Optics*, 19:1385–1386, 1980.

[93] R. Meynart. Speckle velocimetry study of vortex pairing in a low-Re unexcited jet. *Phys. Fluids*, 26(8):2074, 1983.

[94] R. Meynart and L.M. Lourenco. Digital image processing in fluid dynamics. Von Karman Institute for Fluid Dynamics lecture series 1984-03, 1984.

[95] J. Ochs. *The generation of vorticity contour maps from two dimensional randomly located velocity fields with random errors.* Senior research report, Dept. of Theor. and Appl. Mech., Univ. of Illinois, 1987.

[96] The Japan Society of Mechanical Engineers, editor. *Visualized Flow: Fluid motion in basic and engineering situations revealed by flow visualisation.* Pergamon Press, 1988.

[97] C.J.D. Pickering and N.A. Halliwell. Laser speckle photography and particle image velocimetry: Photographic film noise. *Applied Optics*, 23(17), 1984.

[98] C.J.D. Pickering and N.A. Halliwell. Laser speckle photography: Preprocessing of fringe pattern data to improve dynamic range. *Journal of Photographic Science*, 33(5), 1985.

[99] C.J.D. Pickering and N.A. Halliwell. Particle image velocimetry: Fringe visibility and pedestal removal. *Applied Optics*, 24(16):2474–2476, 1985.

[100] C.J.D. Pickering and N.A. Halliwell. Particle image velocimetry: Improving fringe signal-to-noise ratio with a two step photographic process, Part 2. *J. Optical Soc. of America*, 2(10), 1985.

[101] C.J.D. Pickering and N.A. Halliwell. Particle image velocimetry: Improving fringe signal-to-noise ratio with a two-step photographic process. *J. Optical Soc. of America*, 2(4):610, 1985.

[102] C.J.D. Pickering and N.A. Halliwell. Speckle photography in fluid flows: signal recovery with two step processing. *Applied Optics*, 23(8), 1984.

[103] Lord Rayleigh. *Theory of sound.* Volume 2, Dover Publications, 1945.

[104] G.A. Reynolds, M. Short, and M.C. Whiffen. Automated reduction of instantaneous flow field images. *Optical Engineering*, 24(3), 1985.

[105] D.W. Robinson. Automatic fringe analysis with a computer image processing system. *Applied Optics*, 22(14):2169–2176, 1983.

[106] D.W. Robinson. Role for automatic fringe analysis in optical metrology. *SPIE : Optical sensing techniques*, 376, 1983.

[107] H. Royer.. Full 3-d measurements: the holographic approach. In *VKI Lecture series 1988-06*, 1988.

[108] S.H. Salter. Absorbing wave makers and wide tanks. In *Proc. Conf. Directional Wave Spectra Applications*, pages 185,200, 1982.

[109] J.P. Sharpe. *The Optical Measurement of Acoustic Velocity Fields.* PhD thesis, Physics Dept., Edinburgh University, 1988.

[110] J.P. Sharpe and C.A. Greated. The measurement of periodic acoustic fields using photon correlation spectroscopy. *J. Physics D (Applied Physics)*, 20:418–423, 1987.

[111] J.P. Sharpe, C.A. Greated, C. Gray, and D.M. Campbell. The measurement of acoustic streaming using particle image velocimetry. *Acustica*, 1989.

[112] M. Short and M.C. Whiffen. The relationship between seeding density and analysis methodology in particle image velocimetry. In *Proc. 3rd Int. Symp. on applications of laser anemometry to fluid mechanics*, Lisbon, Portugal, 1986.

[113] P.G. Simpkins and T.D. Dudderar. Laser speckle measurement of transient Benàrd convection. *J.F.M.*, 89(4):665–671, 1978.

[114] D.J.S. Skyner, C. Gray, and C.A. Greated. A comparison of time-stepping numerical predictions with whole field flow measurements in breaking waves. In *Proc. Water Wave Kinematics, Molde, Norway*, 1989.

[115] A. Slaouti and J.H. Gerrard. An experimental investigation of the end effects on the wake of a circular cylinder towed through water at low reynolds numbers. *J. Fluid Mech.*, 12:297,314, 1981.

[116] C.A. Smith, L. Lourenco, and A. Krothapalli. The development of laser speckle velocimetry for the measurement of vortical flow fields. In *Proc. AIAA, 14th Aerodynamic Testing conference*, 1986.

[117] K.A. Stetson. Vulnerability of speckle photography to lens aberations. *J. Opt. Soc. Am.*, 67, 1977.

[118] N. Takai and T. Asakura. Displacement measurement of speckles using a 2-D level crossing technique. *Applied Optics*, 22(22):3514–3519, 1983.

[119] W.G. Van Dorn and S.E. Pazan. *Laboratory Investigation of Wave Breaking, Part 2, Deep Water Waves.* S10 Ref. No. 75-21, Research Report, Advanced Ocean Engineering Laboratory, Scripps Institute of Oceanography, University of California., 1975.

[120] M. VanDyke. *An Album of Fluid Motion.* Parabolic Press, Stanford, California, 1982.

[121] C.S. Vikram and K. Vedam. Selective counting path of Youngs fringes in speckle photography for eliminating diffraction halo effects. *Applied Optics*, 22(15), 1983.

[122] O.S. Vikram. Error in speckle photography of lateral sinusoidal vibrations: a simple analytical solution. *Applied Optics*, 21:1710, 1982.

[123] C.S. Yao and R.J. Adrian. Orthogonal compression and 1-D analysis technique for measurement of 2-D particle displacements in pulsed laser velocimetry. *Applied Optics*, 23(11):1687, 1984.

[124] H. Yeh and H.Z. Cummins. Localised fluid flow measurements with a He-Ne laser spectrometer. *Appl. Phys. Lett.*, 4:176–178, 1964.

[125] J.M. Coupland and N.A. Halliwell. Particle image velocimetry: rapid transparency analysis using optical correlation. *Applied Optics*, 27(10), 1988.

[126] M.P. Wernet and R.V. Edwards. Real time optical correlator using a magnetoptic device applied to particle imaging velocimetry. *Applied Optics*, 27(5), 1988.

THE APPLICATION OF P.I.V. TO MEASUREMENTS UNDER WATER WAVES.

C. Gray, C.A. Greated, W.J. Easson and W.E. Fancey.
Department of Physics, Edinburgh University.

Abstract

Application of Particle Image Velocimetry (PIV) to water waves is described. The major advantage of the method is its ability to record a 2-D velocity distribution at an instant. Here it is applied to measuring fluid velocity distribution under small amplitude water waves which are travelling in a miniature wave flume. The experimental set up is outlined and a comparison of measured velocities with theoretical values using linear wave theory is given.

1. INTRODUCTION

Particle Image Velocimetry is a relatively recent application of the Laser Speckle Photography principle to fluid flow. Two or more successive images of an illuminated plane within a seeded flow are recorded photographically on film allowing subsequent measurement of the displacement field. Pointwise analysis by coherent illumination of small regions of the film produces interference fringes in the far field from which the particle image displacement vector, and thus flow velocity, can be calculated[1].

In contrast to conventional methods of fluid velocity measurement such as L.D.A., hot wire anemometry etc., P.I.V. makes recording of a 2-D velocity distribution at an "instant" possible rather than a time history of a single component of velocity at one location in the flow. Thus in the study of water particle kinematics in waves P.I.V. offers a convenient means of making velocity measurements. This is conventionally done using L.D.A. on successive similar waves assuming that such waves are repeatable. The repeatability assumption, however, is not always valid, especially when waves are breaking or close to breaking. P.I.V. offers a convenient solution to the problem of studying breaking and other unique wave phenomena.

Presented in this paper is an account of preliminary work in applying P.I.V. to water waves to record and measure their spatial velocity distribution. Although the scale of the waves studied is small they are large enough for Froude's similarity relationships to be applied, making measurements applicable to larger scale waves.

2. EXPERIMENTAL ARRANGEMENT

The miniature wave flume in which measurements were taken is shown in Figure 1. It is constructed from Perspex with dimensions 1.7m x .075m x 0.15m. Small amplitude waves were generated by an electric motor driving a flat paddle and were beached on a gently sloping absorbent beaching material.

Seeding of the water was by addition of ~ 25 μm diameter latex spheres to a concentration of 10E11 per cubic meter of water. Illumination of the plane of interest within the flume was by a 60 mW Helium Neon Laser expanded to a thin collimated sheet using an arrangment of biconvex and cylindrical lenses. The laser used was of insufficient power to illuminate a whole wave length within the flume, and so was set up with the beam quite narrow. This meant that only a thin strip of measurements could be made at one time and therefore as in other measurement systems, a repeating wave measurement arrangment had to be employed. This seems to negate the advantages of using P.I.V. but the measurements made in 1-D strips highlight the applicability of the method for further work when a higher powered laser is available.

A disadvantage of using HeNe laser light is that red light is strongly absorbed in water. However the water depth in the wave flume is typically only 8.5 cm. Total absorbtion due to water plus seeding over this length was measured to be less than 12%.

Exposures were made using a 35 mm S.L.R. camera with a 55 mm, f 2.8 flat focussing lens in order to allow a nondistorted image of the illuminating plane to be made. The lens aperture was kept fully open in order to maximise light arriving at the film and to minimise diffraction effects in the Particle Images. Double exposure of the film was achieved by pulsing the illuminating laser beam with a rotating mechanical chopper which incorporated a light sensor to accurately measure the rate of rotation and thus the time between pulses.

The exposure time is a function of the fluid velocity when a CW laser is used to illuminate the flow. It should be short enough to accurately record the particle image but long enough to deliver sufficient light to expose the film. The optimum time between exposures is a function of the particle image size, the diameter of the "probe" laser beam, and the velocity of the flow. The paper by Lourenco et.al. (1984) [2] provides a good account of the inter-relation of these parameters.

Approximate maximum and minimum velocities expected in the waves were estimated using linear water wave theory giving ~ 9 cms^{-1} maximum and ~ 3 cms^{-1} minimum. From these estimates and the other known parameters of the system, exposure time and time between exposures of 1×10^{-3} and 5×10^{-3} seconds respectively were chosen.

Photographic film used was Ilford HP5 ASA 400 push processed to 1600ASA. [See Fig. 1 diagram of optical System for recording particle images].

3. OPTICAL ANALYSIS OF FILM

Particle image pair separation and orientation provide the information required to calculate the velocity vector at that point on the film. Coherent illumination of the film generates fringes [see Fig. 2], from which these quantities can be calculated, and point by point analysis of the film in this manner enables the velocity distribution to be constructed.

Measurement of Fringe Separation is accurately and quickly performed using an image capture and computer analysis system [see Fig. 3]. The fringe intensity distribution is measured by imaging the diffraction pattern onto the optical sensing matrix of a video camera. The image is then digitised and stored using a 256 x 256 pixel framestore with an eight bit grey level i.e. 254 grey levels between black and white. The fringes have previously been aligned parallel to the columns on the video monitor and the fringe orientation recorded at the same time. Averaging of the pixel intensities along the columns is then performed to reduce the data to a 1-D intensity distribution and also to average out speckle noise which is present due to random scattering of the coherent laser light from the film.

It is important at this point that a pedestal subtraction routine is performed ref. 3) and 4). This is necessary so that the operation of 1-D Fourier Transformation of the fringe intensity is not swamped by large D.C. and low frequently components. Such low frequency components tend to obscure the fringe periodicity peak when there are only a few fringes within the diffraction halo [see Fig. 4].

The rather simple system of fringe analysis described allows processing of many sets of fringes within a short time.

4. RESULTS

About 30 velocity measurements are shown over three consecutive waves. Each individual film was triggered at the passing of a different part of the wave allowing velocity information from beneath the crest, the trough, and the zero crossing to be collected.

The velocity map [Fig. 5] snows that the measured velocities agree qualitatively with what is known about the kinematics of water particles under waves. However the velocity vectors present in this velocity map contain directional information that was not obtained from analysis of diffraction fringes. Analysis of fringes yields quantitative information about particle image separation and orientation but cannot show which direction the flow was going when the exposures were made i.e. cannot detect which is the forward or reverse direction of flow. In this measurement situation it was possible to include directional information, but in other flow situations e.g. very turbulent flows it may not be possible to do so. This is a major failing of P.I.V. and is likely to limit its possible applications.

A quantitative comparison of measured velocity magnitudes with those predicted by linear water wave theory is shown [Fig. 6]. It can be seen that there is a general agreement between the two sets of data, but individual measured points tend to vary randomly about the calculated values.

Two possibilities are considered to account for this discrepancy
1) The linear theory for water waves may not be accurately applicable to the waves generated in the wave channel. The linear theory is based upon the assumptions that the waves are small in amplitude so that second order terms can be neglected and also, the surface profile of the wave is sinusoidal. The first approximation is satisfied, but the second may not be, due to the simplistic nature of the wave generator, which tends to distort the wave profile.
2) The technique has the fundamental limitation that velocity measurement is made over an area and not at a point. Therefore, in general a number of particle image pair separations are being measured at the same time. The particle pairs are randomly distributed about the probe area and so the resulting velocity measurement has only a limited probability of indicating the precise velocity of the field at the centre of the measuring area.

5. SUMMARY

Flow velocity measurements have been performed on small scale water waves using a non-intrusive optical measuring technique. Comparison with theory has shown the accuracy attainable using P.I.V. in general to be good. The method does, however, exhibit a fundamental inability to resolve forward and reverse flow. This is not a major problem when the flow situation under examination is well enough known to incorporate directional information but could prevent use of the technique in more complicated flows.

The flow velocity measurements made also show slight random deviations when compared with the theoretical results. This may be a consequence of measurement over a finite area, the non-linear behaviour of the waves generated, or a combination of the two.

REFERENCES

1. J.M. Burch and J.M.J. Tokarski, 1968 "Production of multiple beam fringes from photographic scatterers". Optica Acta Vol. 15, No.2, Pp 101-111.
2. L.M.M. Lourenco and M.C. Whiffen, 1984 "Laser Speckle in Fluid Dynamics Applications". Proc. 2nd Int. Symp. on Applications of Laser Anemometry to Fluid Mechanics.
3. G.H. Kaufmann, A.E. Ennos, B. Gale, D.J. Pugh, 1980 "An electro-optical readout system for analysis of speckle photographs". The Institute of Physics Vol. 13, Pp. 579-584.
4. C.J.D. Pickering and N.A. Halliwell, 1985 "Laser speckle photography: reprocessing of fringe pattern data to improve dynamic range". Journal of Photographic Science. Vol. 33, No. 5, Pp 183-186.

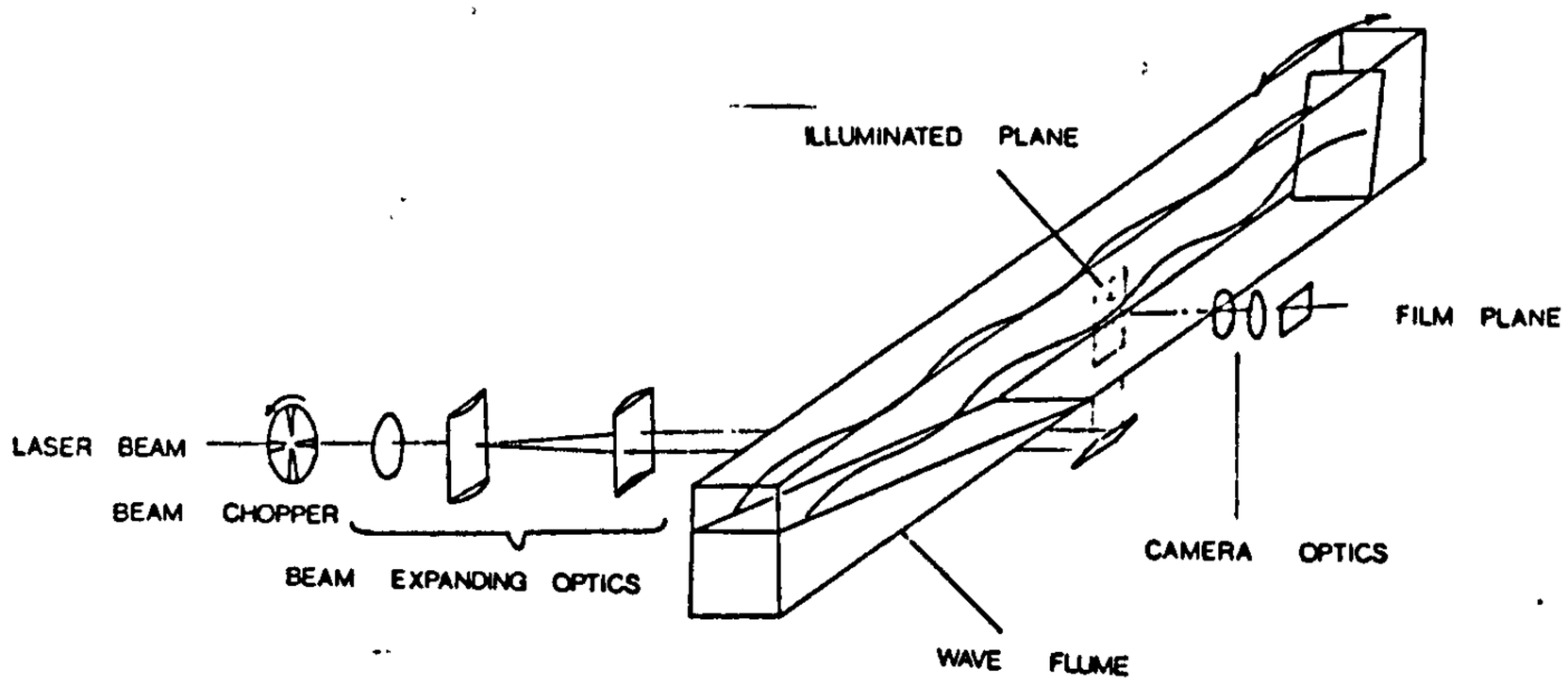

Fig. 1. Wave flume and imaging system.

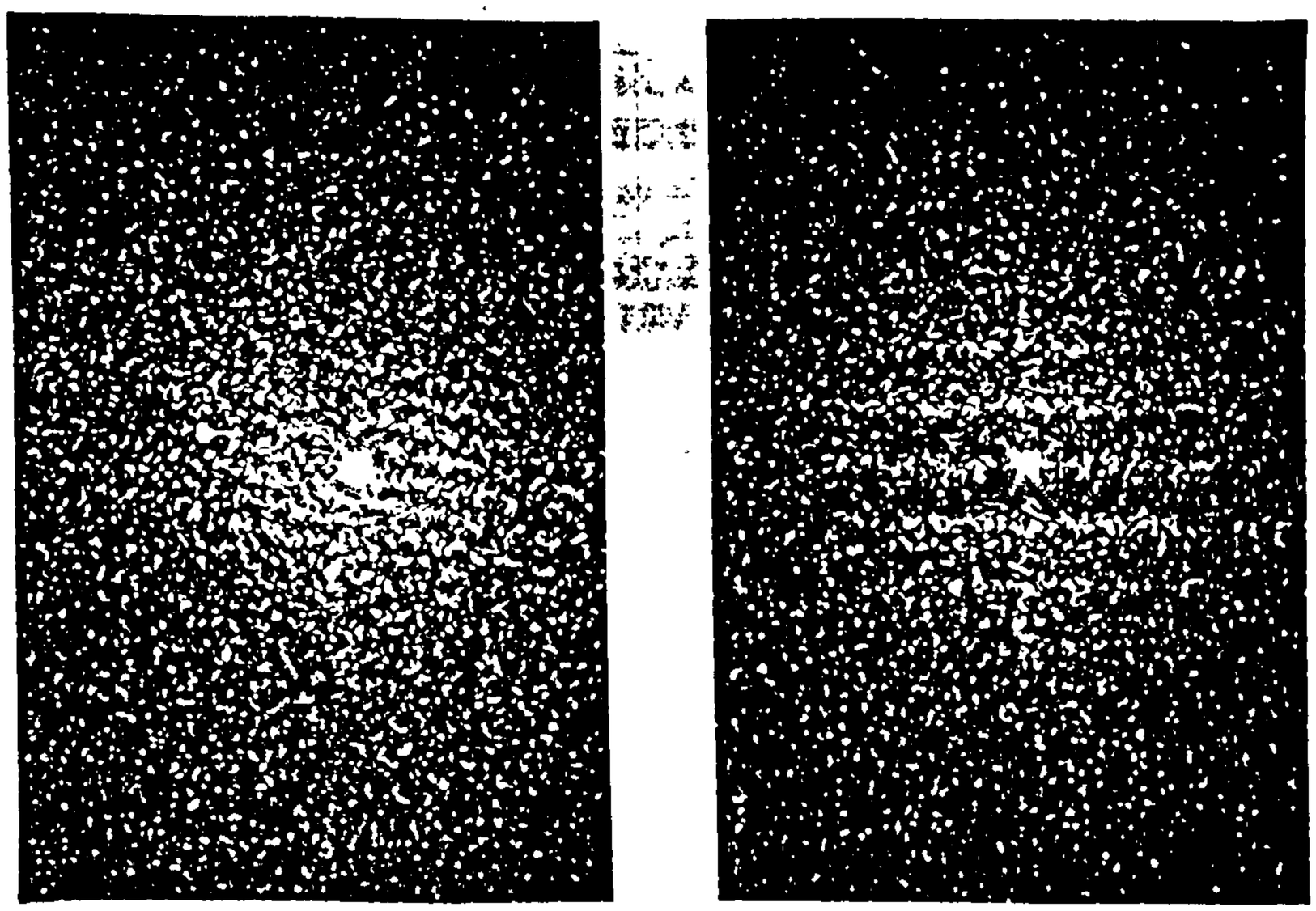

Fig. 2. Photographs of typical Young's fringes diffraction pattern generated from double exposure particle images.

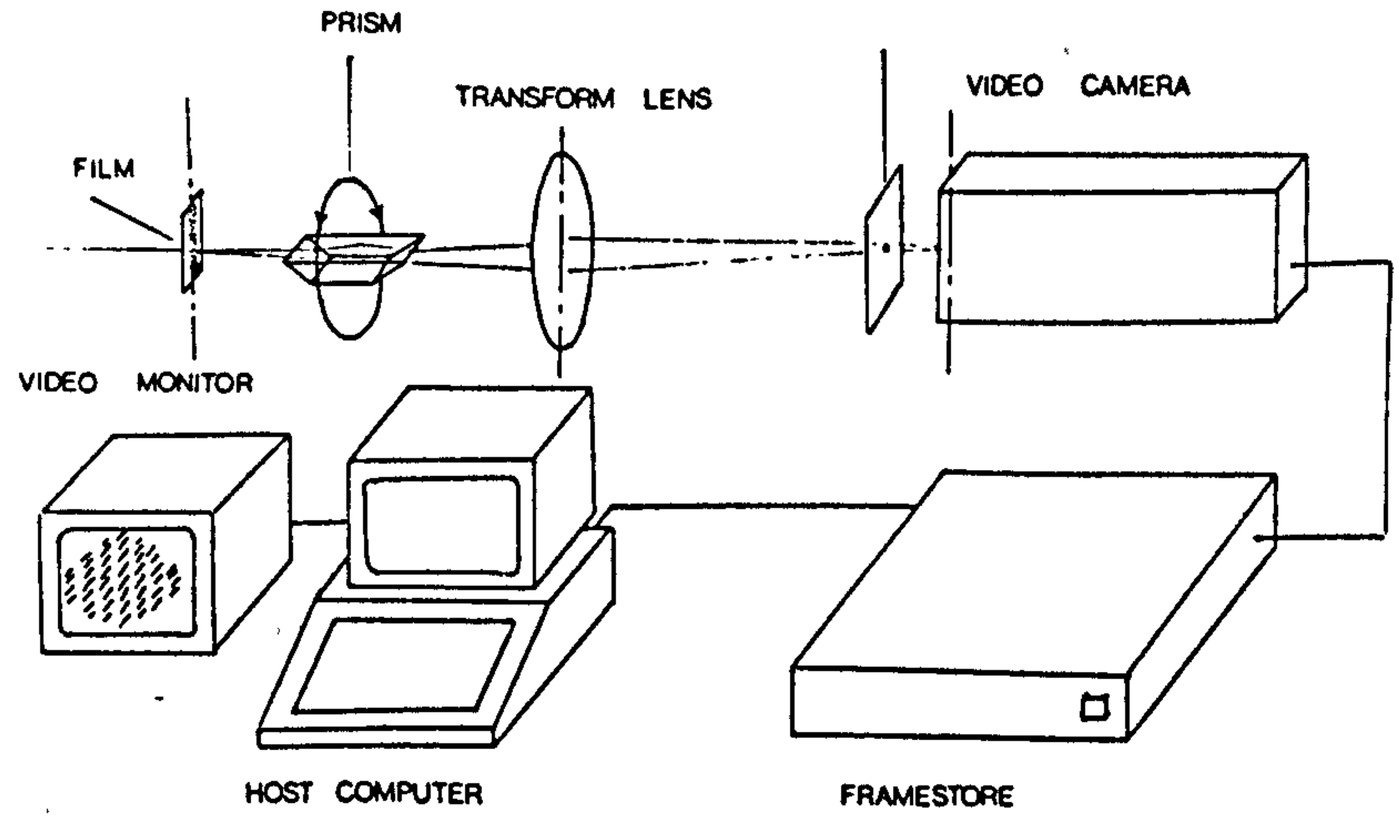

Fig. 3. Fringe analysis system.

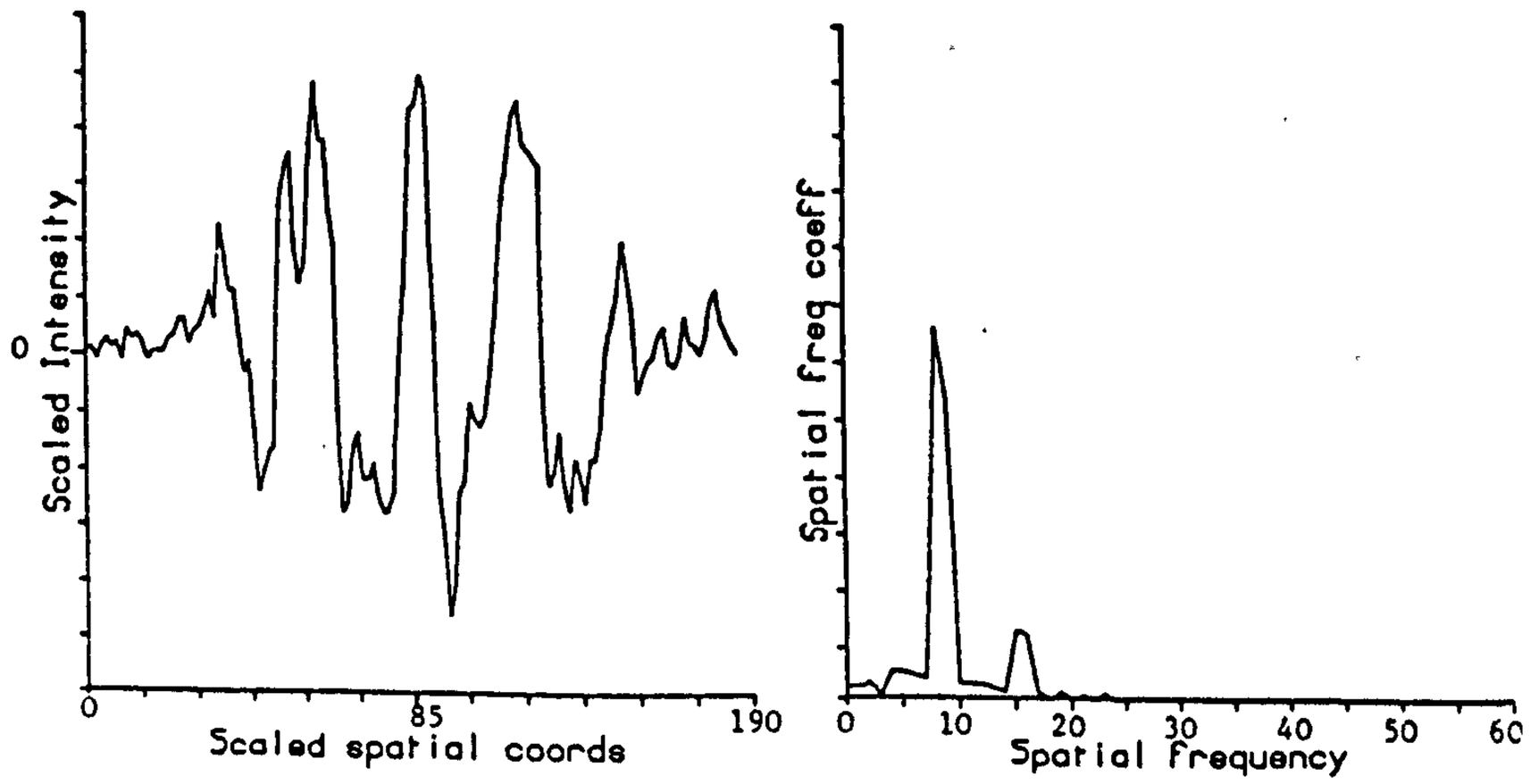

Fig. 4. a) Fringe Intensity distribution after pedistal removal
b) F.F.T. of a) showing maximum peak corresponding to fringe frequency.

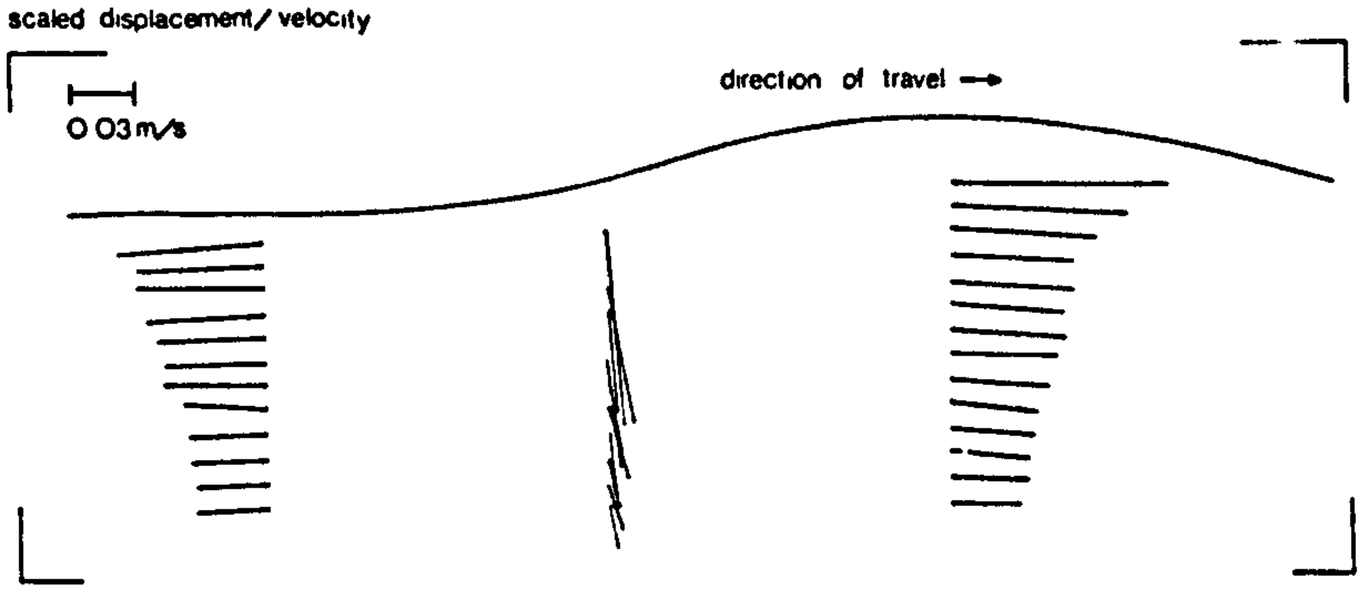

Fig. 5. Representation of flow field under 320 mm wavelength, 9 mm Amplitude water wave.

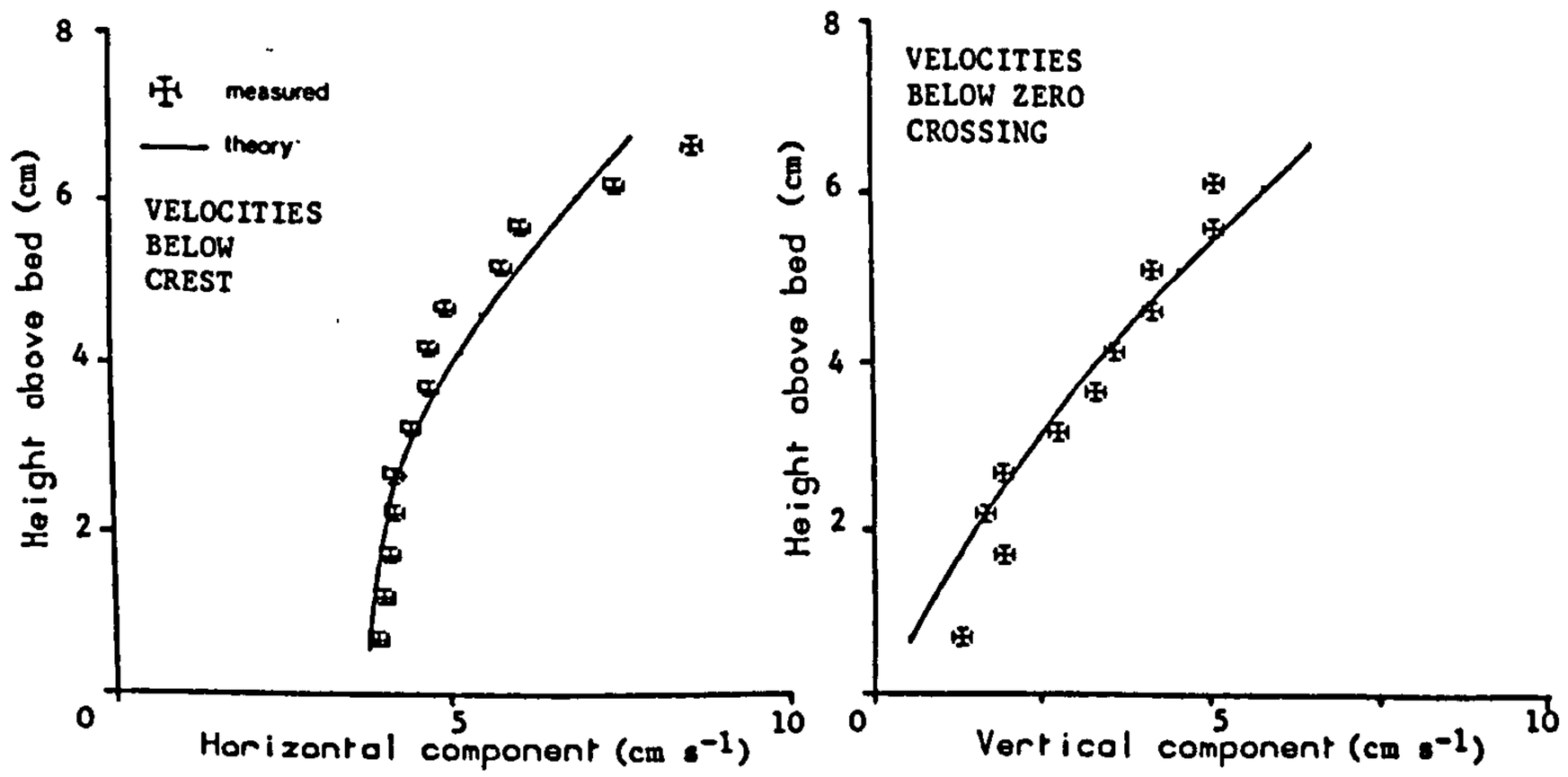

Fig. 6. Major velocity components under crest, zero-crossing point, and trough. The full lines are calculated from linear water wave theory.

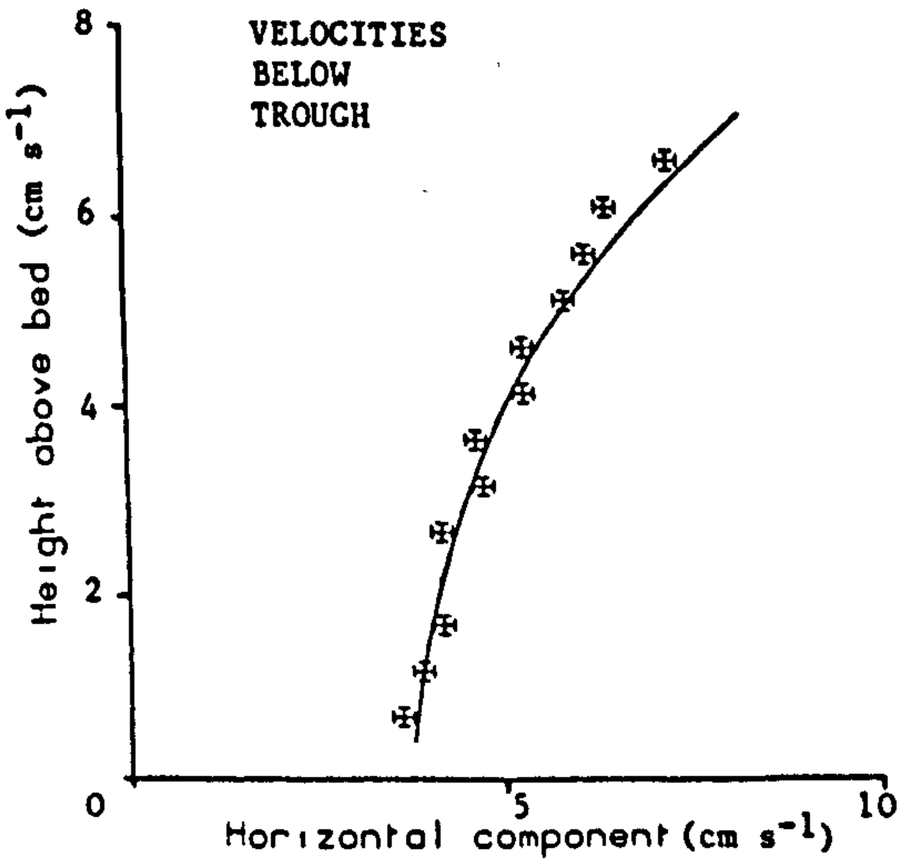

Optics and Lasers in Engineering **9** (1988) 265–276

The Application of Particle Image Velocimetry to the Study of Water Waves

C. Gray & C. A. Greated

Department of Physics, Edinburgh University, James Clerk Maxwell Buildings, The Kings Buildings, Mayfield Road, Edinburgh EH9 3JZ, UK

(Received 1 September 1987; accepted 21 December 1987)

ABSTRACT

The application of Particle Image Velocimetry (PIV) to the measurement of velocity distributions under water waves is described. Two-dimensional water waves are generated in a laboratory wave flume with the measurement area illuminated by a powerful CW Argon ion laser. Photographic recording and subsequent electro-optical analysis of the film provides the displacement and hence velocity field for passing waves. The accuracy and reliability of the technique is illustrated by typical experimental results and a comparison with Linear wave theory.

INTRODUCTION

The study of velocity distributions under water waves is a subject of great practical importance since a knowledge of these is essential for the prediction of forces on ocean structures. In many situations, particularly when the waves are breaking or reaching a point of instability, there are no analytical or computational techniques available which will give reliable results. In these cases the designer must resort to modelling the waves in the laboratory and making use of well tested scaling laws.

A major difficulty with experimental measurement is that traditional velocity probes, such as miniature propeller meters or hot wire anemometers, either do not respond accurately in the wave environment or suffer severe calibration problems. Laser Doppler anemometry (LDA) has been successfully applied to measuring velocities under water waves[1] but many problems are encountered in its application. The major difficulties are associated with the fact that the laser beams

Optics and Lasers in Engineering 0143-8166/88/$03·50

are only submerged for a part of the wave period when measurements are being recorded above the level of the wave troughs.

With sophisticated computer techniques for analysing the Doppler signal it has been possible to overcome many of these difficulties, and detailed studies of velocity distributions have now been made which have been utilised for structural design purposes.[2] Despite these advances, a fundamental limitation of this type of measuring device remains. For water wave studies the designer is generally interested in vector plots of the velocities under a specified surface profile. The laser Doppler technique, however, measures at only one fixed point in space at any given instant. Complete vector plots can then only be constructed in situations where the wave profile in question can be accurately repeated many times, the probe being moved to a succession of points across the flow field as the train of waves is generated. This necessitates the use of elaborate wave generation technique to ensure the requisite repeatability. For random waves and single event situations the procedure becomes impossible.

Particle Image Velocimetry (PIV)[3] is a non-intrusive technique which allows the complete two-dimensional flow field in a wave tank to be captured at a single instant. It also has the advantage of being experimentally uncomplicated. The water is seeded with small neutrally buoyant particles and illuminated with a plane sheet of pulsed laser light. Using a conventional camera operating with an exposure time exceeding the pulse period, photographic film is exposed to double (or sometimes multiple) images of the moving particles. The displacement of the particle pairs, which determines the velocity at any particular point, is found by illuminating the appropriate point on the developed film with light from a low power laser. Young's fringes are formed in the diffraction pattern, whose separation and orientation are related directly to those of the particles.[4]

The results presented in this paper have been recorded in a wave tank purpose-built for PIV analysis. The optical system incorporates a 20 W CW laser. Fringes are captured using a video camera and framestore linked to a microcomputer and are analysed using a two-dimensional Fast Fourier transform routine.

EXPERIMENTAL SET-UP

Wave tank and photographic system

In order to use PIV to study the flow field in water waves a special glass based wave flume had to be built (Fig. 1). The tank is 6 m × 0·33 m with

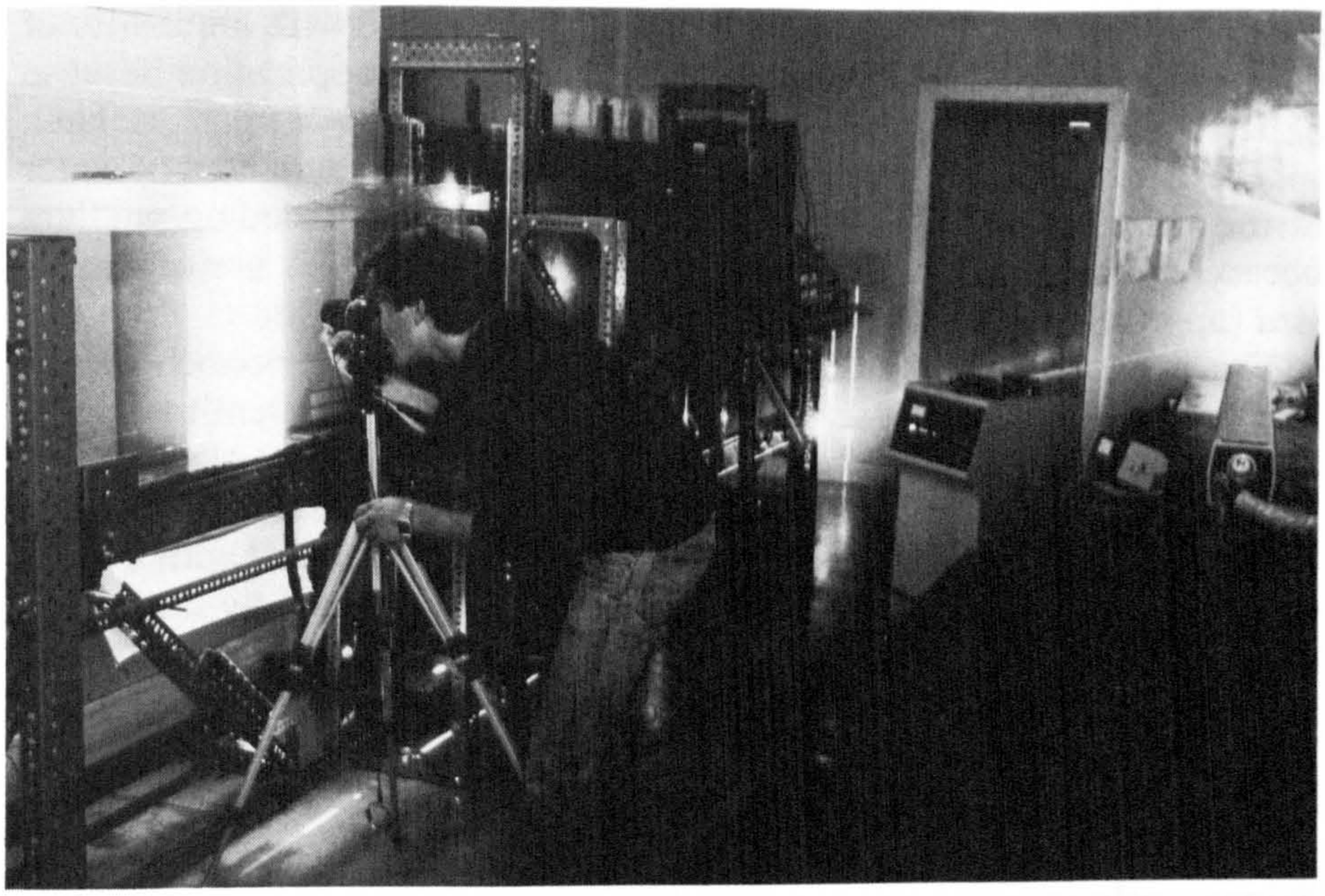

Fig. 1. Laboratory wave tank and beam expansion system.

a water depth of 0·53 m. Waves are generated by a hinged paddle and beached on folded layers of expanded aluminium mesh. The narrowness of the tank and close fit of the wavemaker to the tank sides ensures the waves generated are 2-dimensional and that there is no significant fluid motion perpendicular to the sides of the tank. A 0·32 m wide 3 mm thick sheet of Argon ion laser light is used to illuminate the plane of interest within the tank, entering the tank through the glass base and passing up through the wave, perpendicular to the base and parallel to the glass sides. Expansion of the light from the laser into a sheet is achieved using a short focal length cylindrical lens. A front silvered mirror reflects the expanding sheet of laser light up through the base of the tank. The mirror is tensioned from behind, midway down its length in order to bow it slightly, which has the effect of recollimating the light sheet. Since the light is incident perpendicular to the glass base, unwanted reflection is reduced to a minimum. The light lost through reflection can be considerable when using a high power laser and steps taken to reduce the effect (including multicoating of the expanding lens) help to maximise the light reaching the measurement surface as well as reducing the risk of eye damage from strong reflection. Control over the expansion of the light sheet in the tank also helps maintain a constant light intensity vertically through the measurement area which otherwise would become less intense further up the tank as the light

continued to expand. The water in the tank is seeded with a quantity of Conifer pollen. This form of seeding is ideal for this application because of its cheapness compared to other seeding materials such as latex spheres which would be prohibitively expensive for the volume of water in the wave flume (1000 litres). Pollen is also a good seeding medium because it is neutrally buoyant in water, all the particles are of similar size (approx. 50–100 micron), and it scatters a lot of light.

The exposures are made with a sensitive 400 ASA monochromatic film so that the short pulse times used (0·002 s) are sufficient to actuate the emulsion. Photographs of the flow are taken with a standard 35 mm Nikon f2 SLR camera with motor film advance and a f2·8 55 mm flat focus macro lens. Levelling of the camera base is achieved with a spirit level so that the exposed and developed film automatically has a true horizontal from which to base the subsequent analysis points. Finally the width of the illumination plane is measured so that measurement of the width of its image on film can be used to calculate M the object/image magnification necessary for the final velocity calculation.

Fringe analysis

The displacement field captured on the double exposure film of the flow is determined point-by-point by measurement of the spacing and

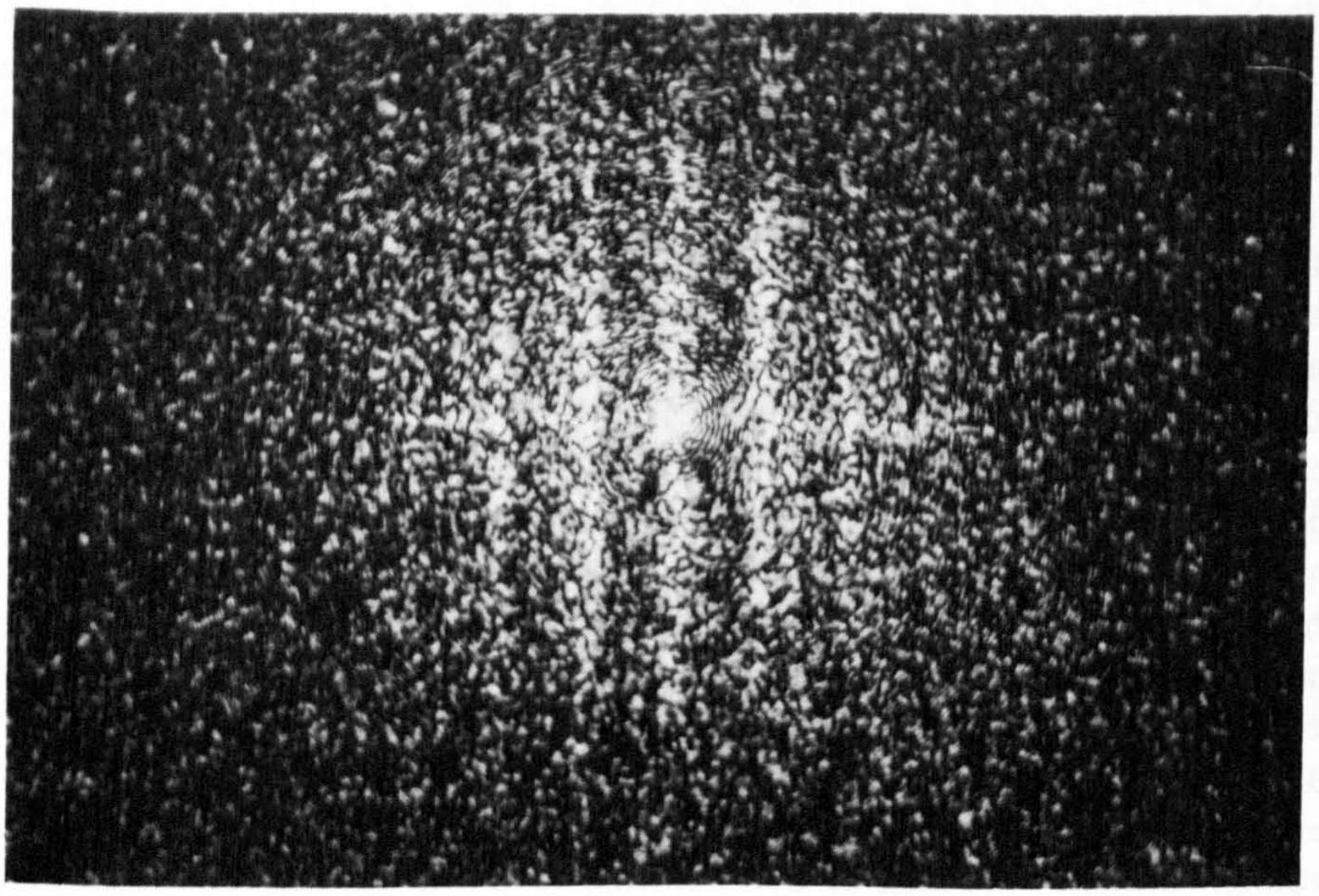

Fig. 2. Typical PIV fringes obtained from double exposure photographs under water wave.

orientation of the diffraction fringes produced in the far field by the intersecting probe laser beam. Because of the considerable noise present in typical PIV fringes (Fig. 2) and due to the typically large number of measurement points required (50–500) it is necessary to automate the analysis of fringes. A low power (1 mW) Helium Neon laser is used to illuminate the exposed and developed negative film which is mounted on a manual X, Z stage allowing the probe laser beam to intersect the film at any point. A 50 mm f2 Nikon camera lens projects the power spectrum of the small illuminated region of film onto the Vidicon tube of a Phillips LDH 402 Indoor video camera where the fringes are digitised to an array of 64×64 intensity values with an 8 bit grey scale. The digitised fringes can be represented by I_F (Fig. 3).

$$I_F(i, j) = I_H(i, j)\left\{1 + \cos\left(2\pi \frac{k_X i + k_Z j + C)}{N}\right)\right\}$$

$$0 \leqq i \leqq 63$$

$$0 \leqq j \leqq 63$$

$$N = 64$$

where (i, j) represents the co-ordinates of a pixel location in the digitised intensity field. k_X and k_Z are fringe spatial frequency components in the i and j direction respectively. I_H is the intensity distribution resulting from diffraction through a single exposure photograph and C is a constant.

Crossed polarisers are used to control the intensity of light reaching the camera. All components are mounted on a triangular optical bench for rigidity (Fig. 4). The digitised fringes are transferred to a Seescan video framestore where they can be read onto a floppy disc. A single

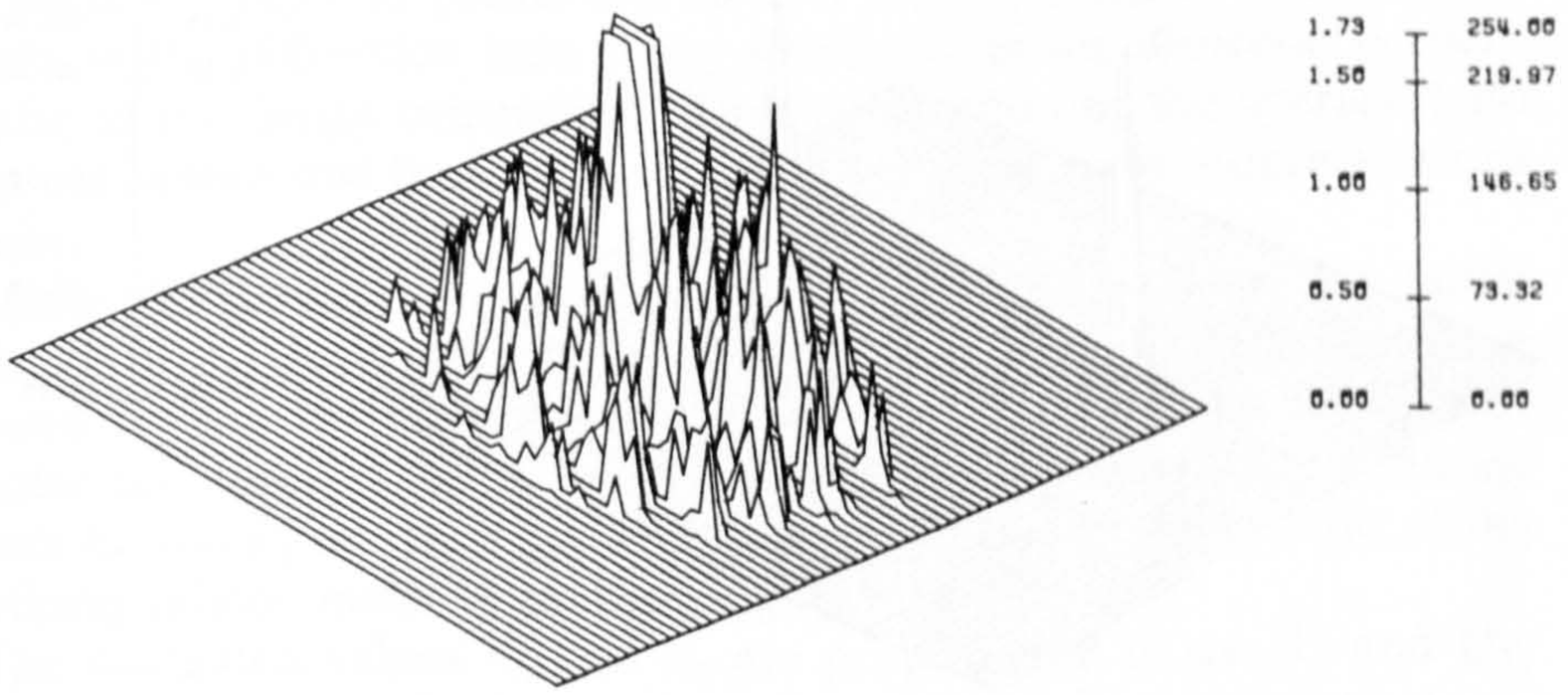

Fig. 3. Uncorrected fringe I_F.

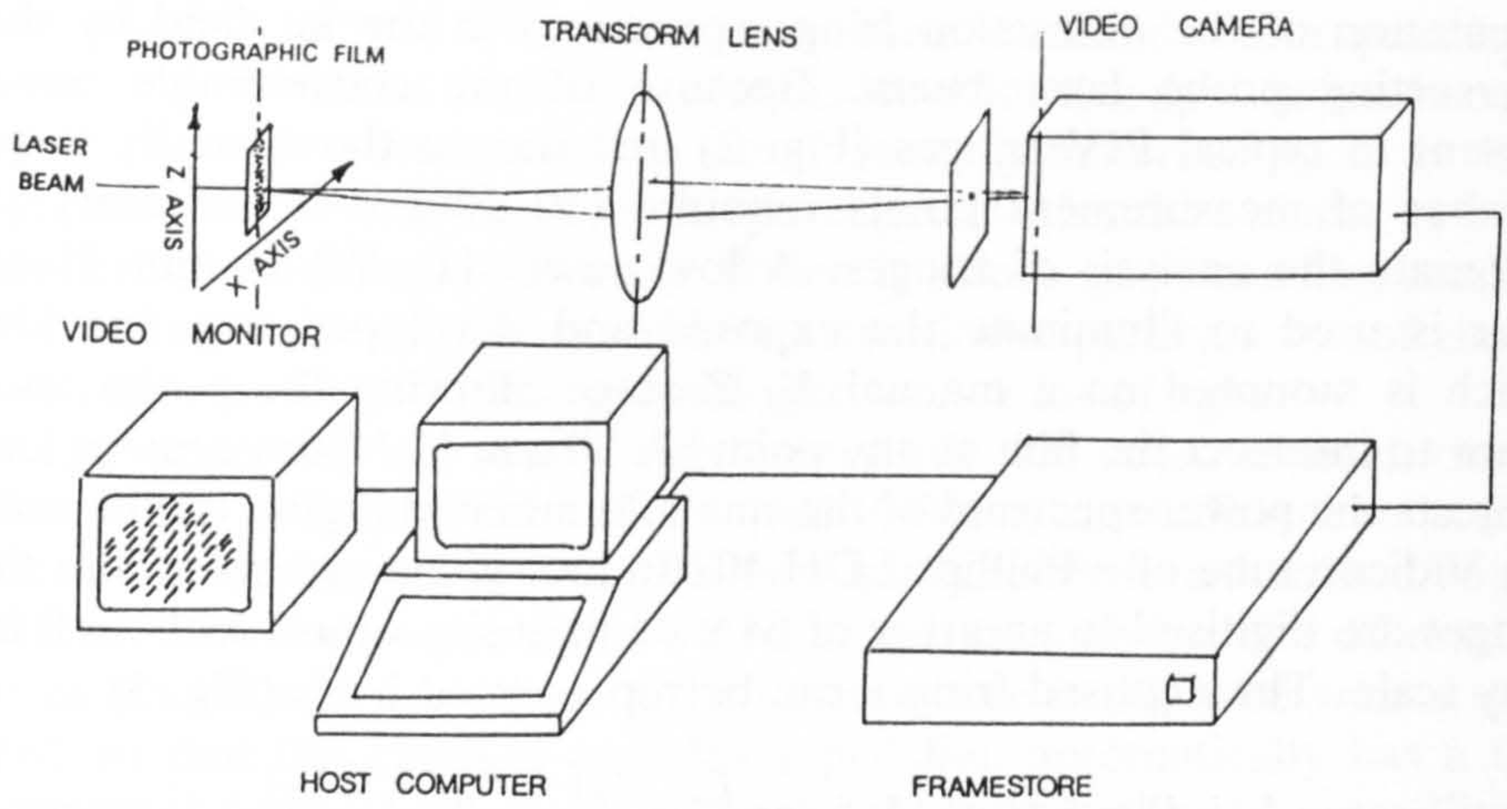

Fig. 4. Optical arrangment used to produce fringes.

disc stores 60 fringes and is subsequently read by the analysing computer a frame at a time calculating the fringe frequencies in the X and Z directions.

The analysis procedure used to determine the two frequency components of the fringes is based upon two-dimensional Fourier transformation of the digitised fringe intensity distribution.[5] This procedure puts the fringe information into a form from which it is easy to deduce the fringe frequencies (Fig. 5). The fringe spatial frequency components k_X and k_Z are proportional to the displacements dx and dz respectively and are present in the 2-dimensional frequency domain of the fringes as two peaks either side of a large zero order peak. Subtraction of the function I_H from the fringe intensity distribution I_F before transforming

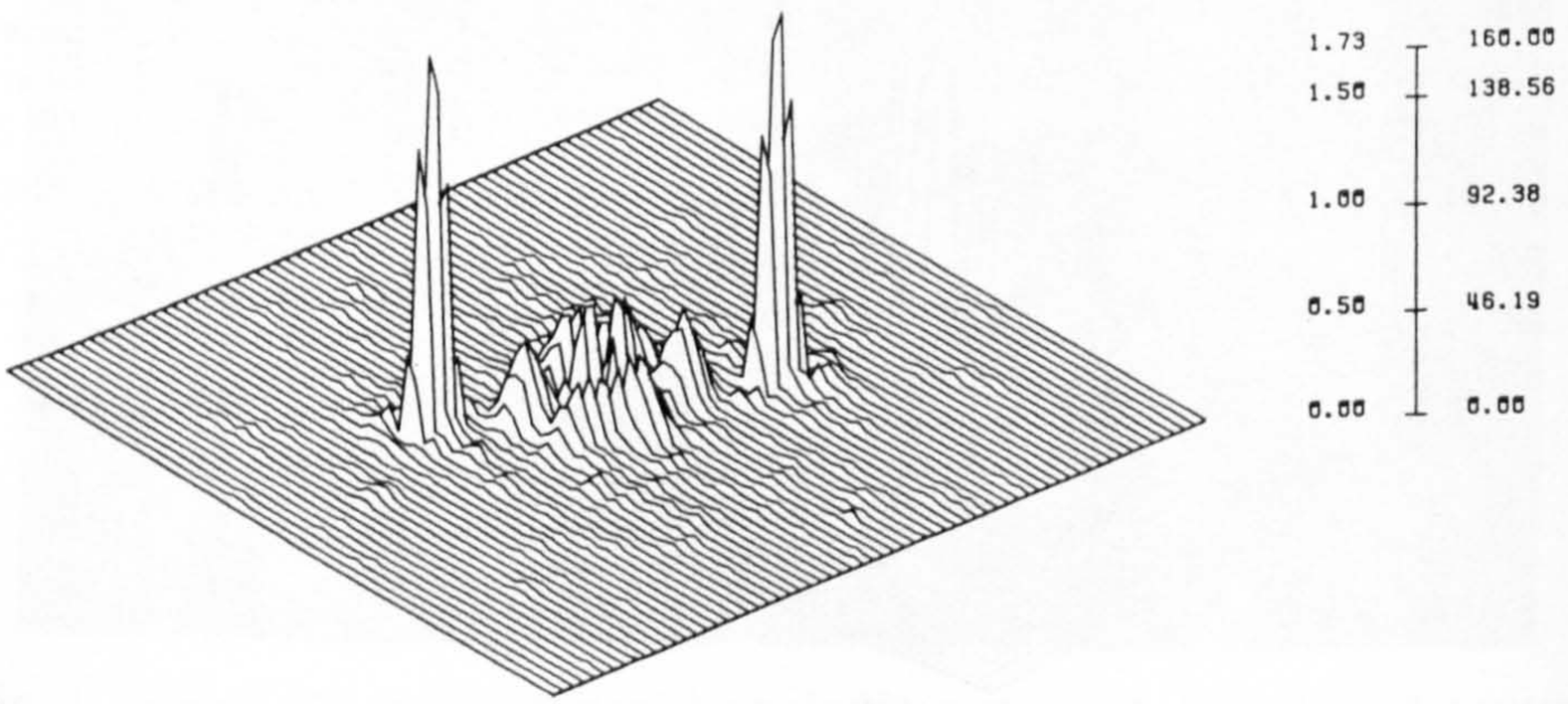

Fig. 5. Modulus of Fourier transform of corrected fringe.

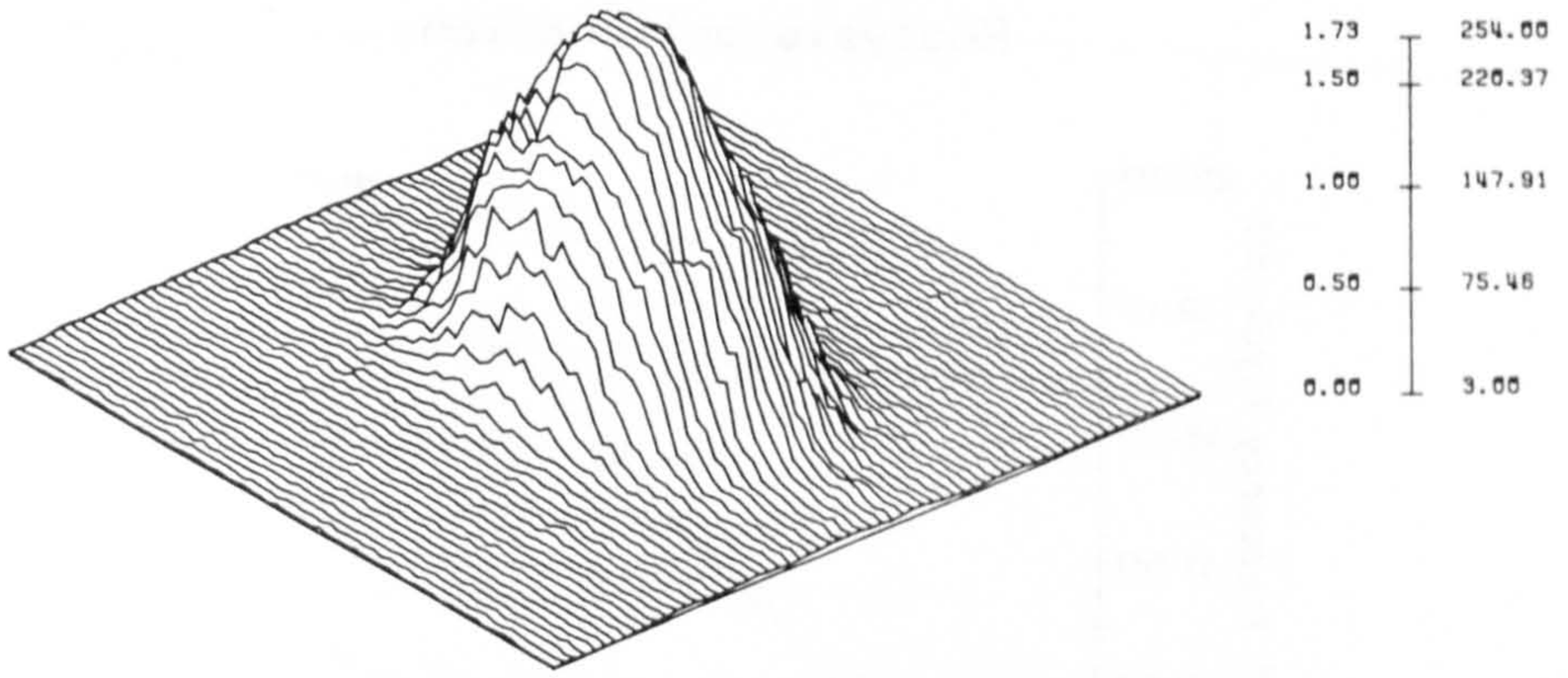

Fig. 6. Average diffraction halo I_H.

the fringes, reduces the size of the zero order peak[5,6] so that a simple search for the maximum spatial frequency component locates the nearest data point to the fringe frequency. The function I_H is approximated by averaging 20 diffraction halos produced from a single exposure film (Fig. 6).

The ratio of the volume under the fringes I_F to the volume under the halo I_H is the proportion of I_H to be subtracted in order to reduce the central peak to zero.

In practice there is never complete cancellation of low frequency components about zero and in certain cases their amplitude is greater than the fringe peak so causing the analysis to fail. Subtraction of I_H should reduce the amplitude of these low frequencies but in some cases does not because the shape of the fringe diffraction halo is different to I_H the average halo. This situation is most common when the illumination pulse recording the flow field is not short enough to record the particle images as points but instead records them as streaks. This results in the diffraction halo being shortened in the direction perpendicular to the fringe orientation. Thus subtraction of the average halo does not reduce low frequencies but instead tends to introduce some of its own.

Using the position of the largest Fourier coefficient as an initial estimate of the position of the true peak, a Newton–Raphson iteration is used to find the position of the zero gradient on the continuous Fourier spectrum in the X and Z directions separately. The resulting values k_X and k_Z are then corrected for the non-unit aspect ratio of the digitising vidicon mesh by multiplying k_Z by 1·455.

The calculated values k_X and k_Z are proportional to dx, dz and Ux, Uz, the particle pair displacement and particle velocity, respectively, in

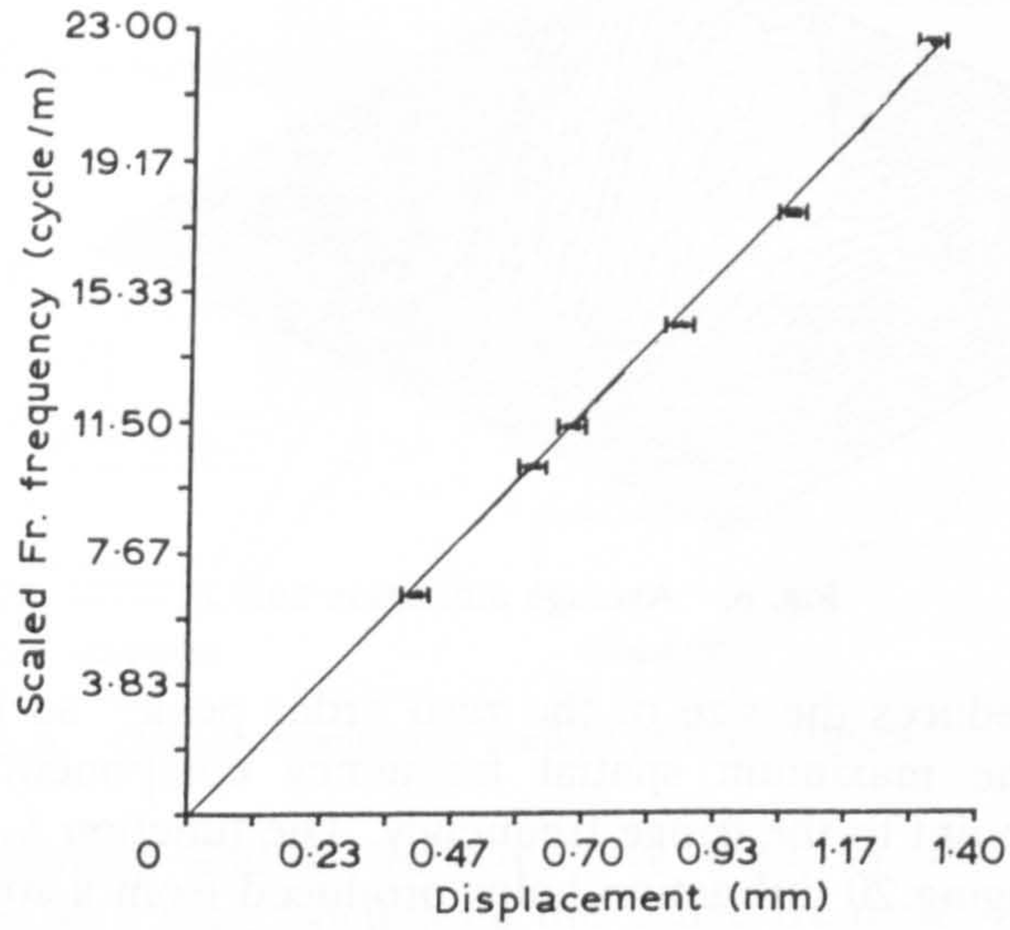

Fig. 7. Calibration plot of measured against known displacements.

the X and Z directions. Calibration of the system is necessary to determine the constant of proportionality required to convert from the arbitrary spatial frequency units to components of displacement and hence velocity. A glass slide sprayed with tiny droplets of liquid latex was mounted on a manual translation stage and illuminated with an expanded Helium Neon laser. Six double exposure photographs were taken of the plate with displacements between 0·36 mm and 1·32 mm and an image/object magnification of 0·26. For each of these calibration films 30 measurements were made at various positions and orientations. The mean and standard deviation for each film was calculated and then plotted against the known displacement (Fig. 7). A least squares fit yielded a constant of $0{\cdot}01586 \pm 0{\cdot}00007$ mm/unit.

EXPERIMENTAL RESULTS

The camera was set-up and levelled in front of the wave tank and several exposures taken of waves of different wavelength at different positions as they passed the observation point. The developed films were then analysed on a grid 2 mm between horizontal measurements and 2·5 mm between vertical measurements. This corresponds to a grid size of (20 mm × 25 mm) beneath the real wave for an image/object

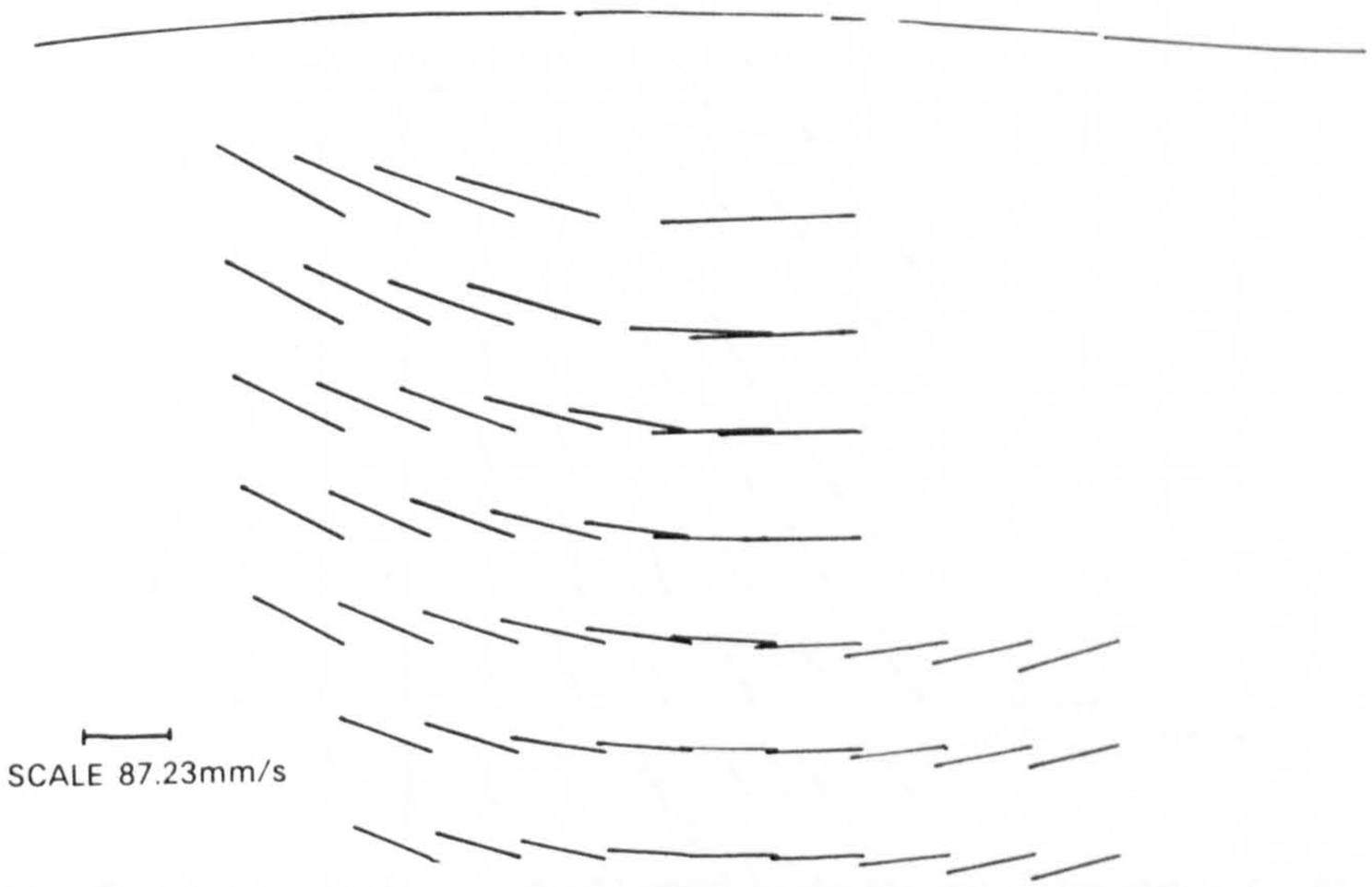

Fig. 8. Velocity map under crest of water wave (1·01 Hz, 1·464 m wavelength, 29 mm amplitude.

ratio of 0·1. The fringes obtained from these exposures were generally of high visibility (Fig. 2) enabling accurate measurement of the image pair displacement vectors.

The velocity maps in Figs 8, 9 and 10 were plotted using *a priori* knowledge of the flow sense as this information cannot be determined

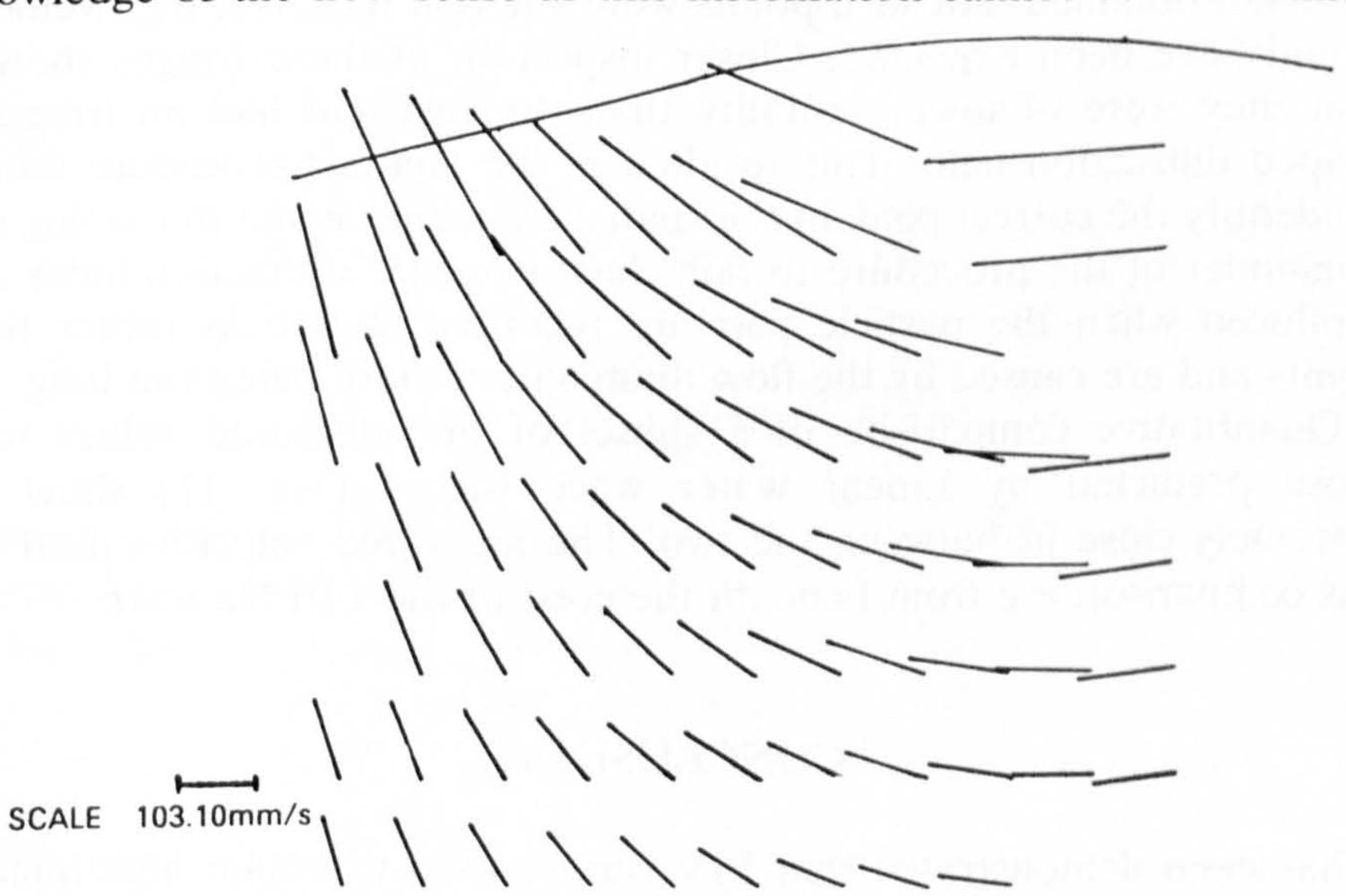

Fig. 9. Velocity map before crest of water wave (1·316 Hz, 1·559 m wavelength, 33 mm amplitude).

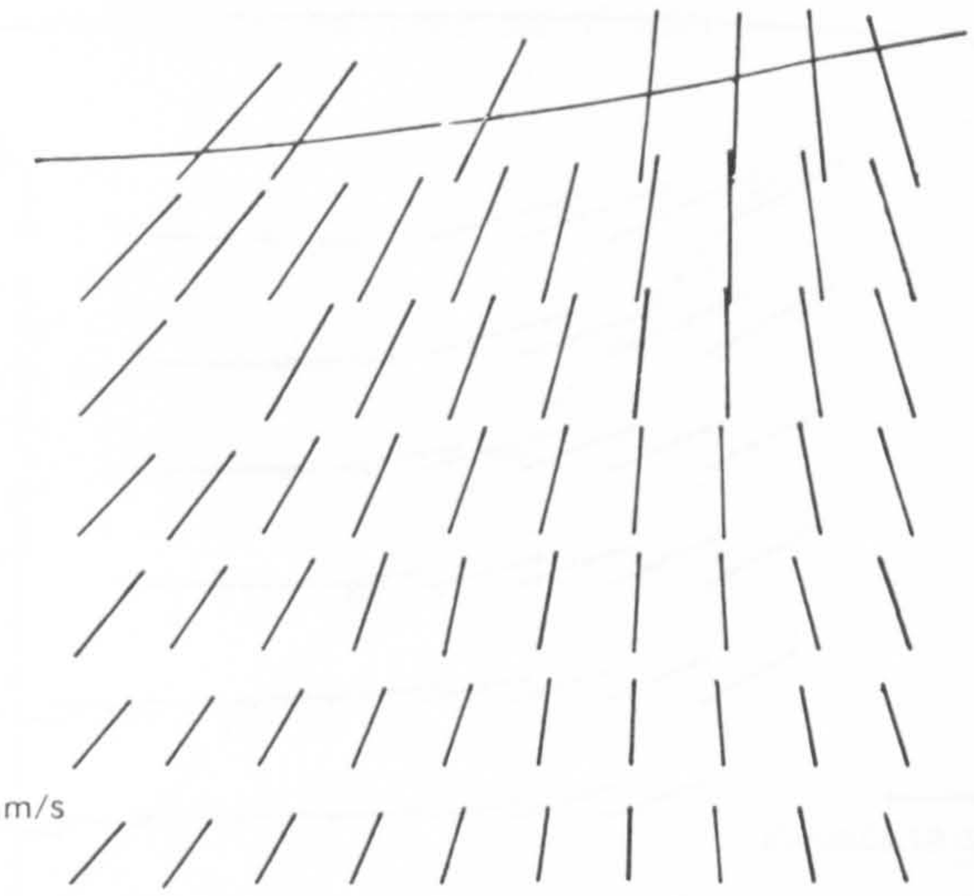

Fig. 10. Velocity map after trough of wave (1·208 Hz, 1·510 m wavelength, 31 mm amplitude).

from PIV photographs. The change in direction and magnitude of the plotted velocities is smooth and they are consistent with what is known of small amplitude sinusoidal profile water waves. However there are positions on the measurement grid for which realistic measurements were not obtained. All such points were where a relatively high velocity would have been expected. Closer inspection of these fringes showed that they were of lower visibility than the rest and had an irregular shaped diffraction halo. This resulted in the analysis procedure failing to identify the correct peak in the spatial frequency plane so causing the remainder of the procedure to fail. Such irregular diffraction halos are produced when the particle pair are recorded as streaks rather than points and are caused by the flow illumination pulse being too long.

Quantitative comparison of a subset of the measured values with those predicted by Linear water wave theory (Fig. 11) show an extremely close fit between the two. The measured velocities used for this comparison are from beneath the crest of the 1·01 Hz wave.

CONCLUSIONS

It has been demonstrated that PIV can be used to obtain high quality velocity distributions under water waves in a full size laboratory flume. The technique is to be seen as complementary to LDA, each approach

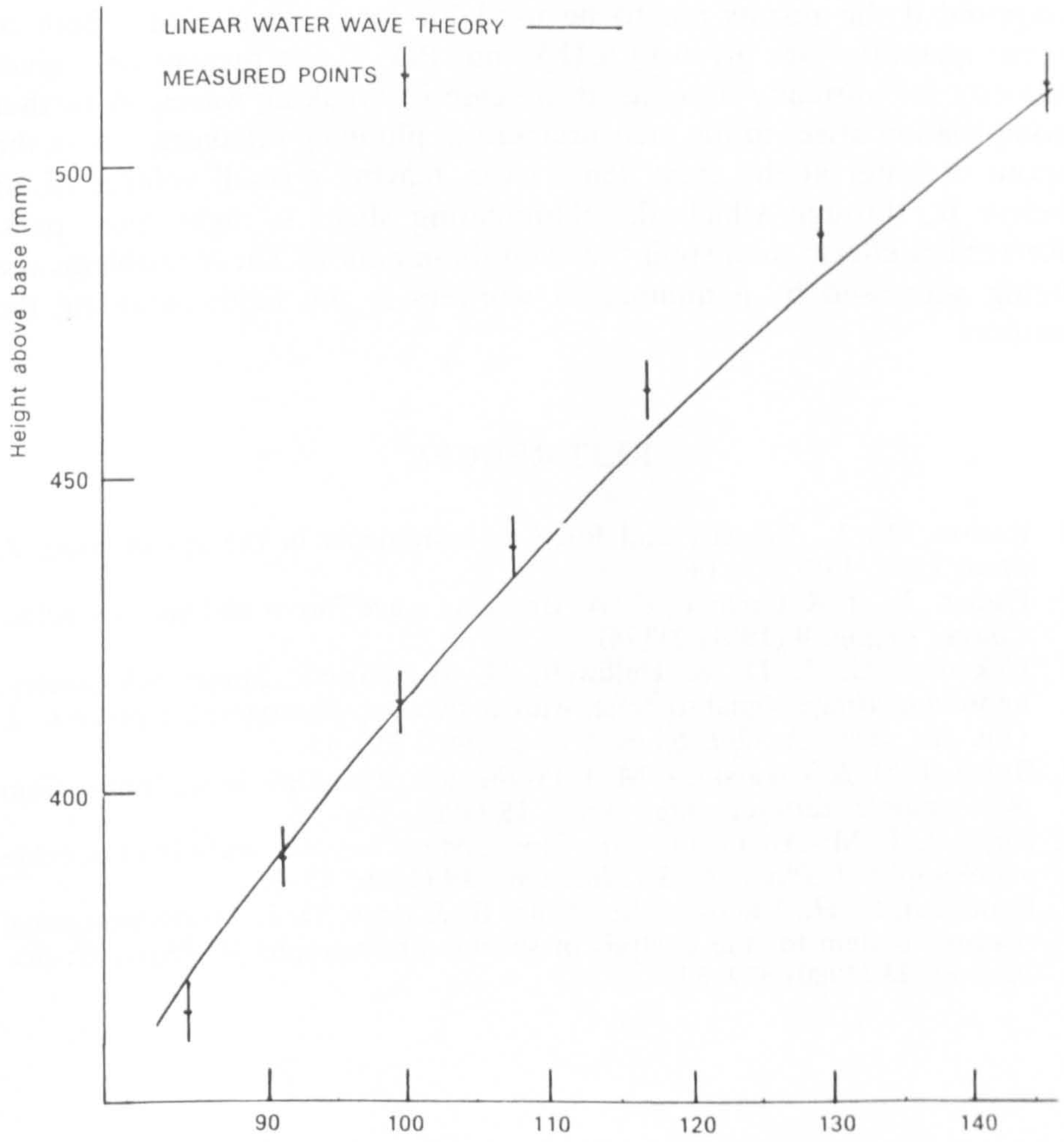

Fig. 11. Comparison of measured velocities with Linear water wave theory for velocities under crest in Fig. 8.

having merits in particular situations. PIV has the great advantage that a complete velocity field can be captured at a single instant which reduces the tank testing time to a minimum. It also allows random and single event waves to be studied. There are however, limitations which have not yet been fully overcome. In particular, PIV does not give the sense of the flow direction. Nor does it give temporal acceleration.

Under water waves the flow sense is usually obvious at any particular point, although this is not necessarily the case if obstacles are introduced. The acceleration, in addition to the velocity is generally

required if the results are to be used for force calculations. Both of these quantities are given by LDA, but PIV at the present only gives velocity for unsteady flows as in the case of breaking waves. A further complication arises in the measurement of plunging breakers, where the spout of water at the crest bends over, leaving a small volume of air below it, through which the illuminating sheet of light must pass. Refraction effects then spoil the even illumination. These problems are being addressed by a number of workers in the field, including the authors.

REFERENCES

1. Easson, W. J., Velocity and force measurements in the splash zone. *J. Strain* (Feb. 1987) 15–18.
2. Easson, W. J. & Greated, C. A. Breaking wave forces and velocity fields. *Coastal Engng*, **8** (1984) 233–41.
3. Pickering, C. J. D. & Halliwell, N. A. Particle image velocimetry: improving fringe signal-to-noise with a two-step-photographic process. *J. Opt. Soc. Am., A: Opt. Image Sci.*, **2** (1985) 610–15.
4. Burch, J. M. & Tokarski, J. M. J. Production of multiple beam fringes from photographic scatterers. *Opt. Acta.*, **15** (1968) 101–11.
5. Huntley, J. M. An image processing system for the analysis of speckle photographs. *J. Phys., E: Sci. Instrum.*, **19** (1986) 43–9.
6. Kauffman, G. H., Ennos, A. E., Gale, B. & Pugh, D. J. An electro-optical read-out system for the analysis of speckle photographs. *J. Phys., E: Sci. Instrum.* **13** (1980) 579–84.

A SCANNING LASER BEAM SYSTEM FOR TWO DIMENSIONAL ILLUMINATION OF FLOW FIELDS

C. GRAY AND C.A. GREATED

ABSTRACT

Introduction

Succesfull exposure of photographic film used in the recording of flow fields as in Particle Image Displacement Velocimetry relies upon intense illumination of a planar region within the flow. Much contemporary work in this field utilises an optical system which spreads the beam from a powerfull CW or pulsed laser into a sheet before introducing it into the flow[1]. Pulsing of a continuous light sheet is generally achieved by mechanical chopping of the laser beam before, or at an early stage in the expanding optics (fig.1). This approach has certain limitations however when high velocities or large areas are to be examined.

It is fundamentally important that the time between exposures is as short as is practically possible with the given flow and photographic parameters such as Image/Object magnification, film resolution, tracer particle diameters,maximum expected velocity, and available light power. Shortening the time between illuminating pulses enables the velocity measurement being made to more closely approximate an instantaneous velocity for any given measurement point. However, a short pulse separation requires a correspondingly short pulse time so that individual particles are precisely recorded with very little movement of the particle in the time of the exposure. Meynart and Lourenco[2] quote a ratio of 1:20 for the exposure time to the time between exposures. This means that for a chopped expanded mode of flow illumination only 1/20 of the available laser power is used and as such the maximum area and velocities measureable are severely restricted.

The system that is presented here for the pulsed illumination of a large planar region

from a CW Argon Ion laser source is currently in use at Edinburgh University for the study and measurement of velocity distributions under water waves. Pulsed illumination of the area of interest is acheived by successive passes of a vertically aligned unexpanded laser beam. Thus, any particle within the plane of interest will be illuminated by a very intense beam of light for the very short time that the beam takes to pass that point (fig.2). The period of scan from 1 to 2 on fig.2 is the same as the time between pulses for a chopped system.

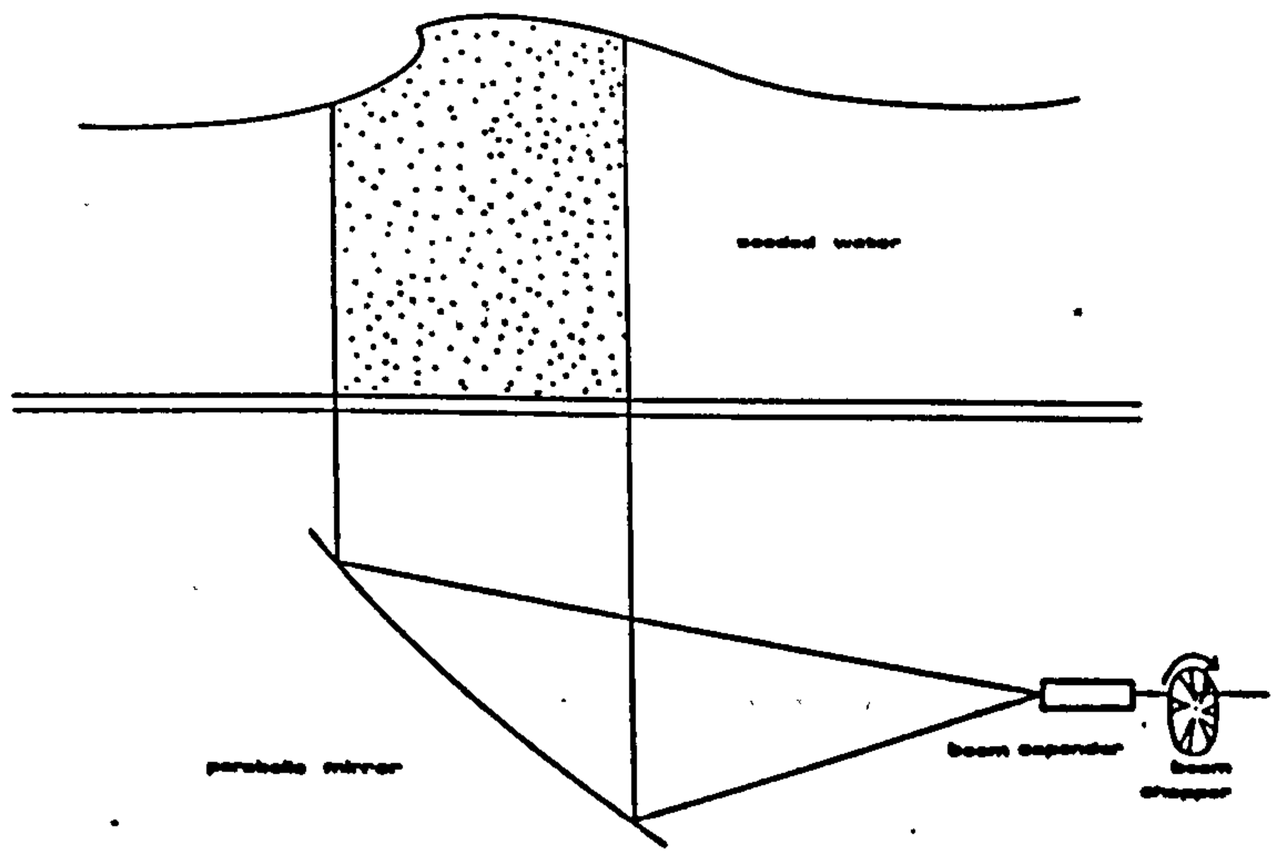

Fig.1 Configuration of chopped illumination system.

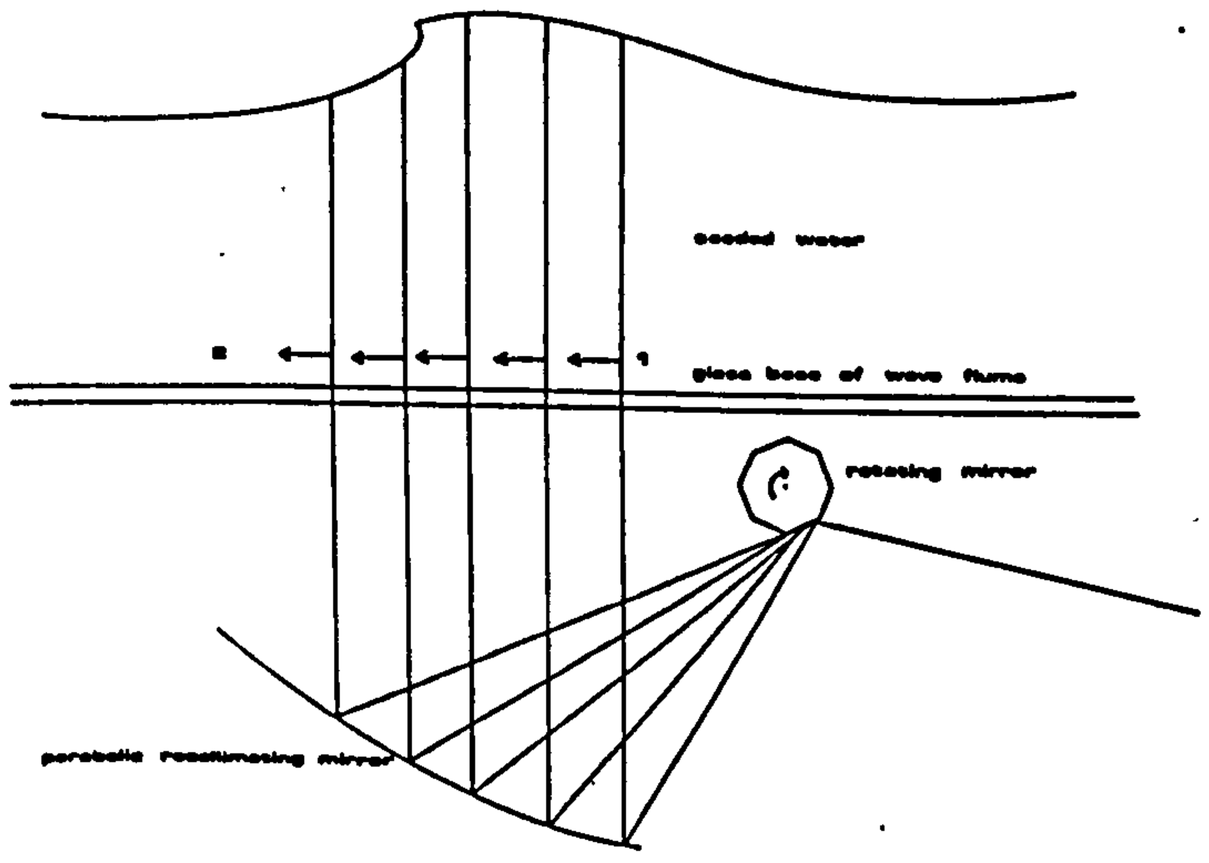

Fig.2 Configuration of scanning illumination system.

Comparing the exposure value for chopped and scanning systems with the same

illumination area.

(1) $E = C * I * t$

Where I is the intensity of the expanded sheet of laser light in the chopped system and t is the time of exposure. C is a constant and assumes that the exposure on the recording photographic film is proportional to the light intensity incident upon the scattering particles.

(2) $E^1 = C * I^1 * t^1$

Where I^1 is the intensity of the unexpanded beam and will be approximately equal to I*L/d where L is the horizontal length of the illuminated region for the chopped case and d is the diameter of the laser beam.

t^1 is the time that the scanning laser beam takes to pass any particular point i.e. $t^1 = d$ / horizontal velocity of beam .Thus eqn.(2) can be expressed as.

(3) $E^1 = C * I*L/d * d/L * t * R$

Assuming that the scanning system is arranged to cover the same horizontal distance as the chopped system L. R is the aforementioned ratio of pulse separation to pulse time t for (1) i.e. R*t represents the period of scanning for (2).

(4) $E^1 = C * I * t * R$

Thus, for the same laser power and the same area of illumination the exposure value is increased by R (approx. 20). this enables the user the choice of using finer and so generally less sensitive photographic film to record greater detail within the flow of interest, illuminating a larger area at a similar exposure, or the capability of measuring higher velocities.

Apparatus

This technique is implemented by a dynamic reflection system incorporating a rotating octagonal mirror and a parabolic recollimation and beam directing mirror (fig.3,4). The laser beam is directed onto the rotating mirror arrangement which diverts the beam through a 90 degree arc. This angular sweep of the beam is then converted to a constant speed repeating scan by a parabolic[3] shaped mirror. The rotating mirror system can be seen in fig.3. Each mirrored face is independently adjustable so that successive beam reflections traverse precisely the same path, neccessary if the same particles within the flow are to be repeatedly illuminated. The octagonal block on which the mirrors are mounted has been milled from a solid piece of Aluminium its weight smoothing out any inconsistencies in the speed of the 12 V. d.c. motor which drives the mirrors through a 12:1 gearbox. The parabolic mirror used to recollimate and direct the reflected beam is manufactured from 2mm thick, front silvered rectangular mirrors which have been stressed into a section of a parabola with a focal length of 100 cm fig.4.

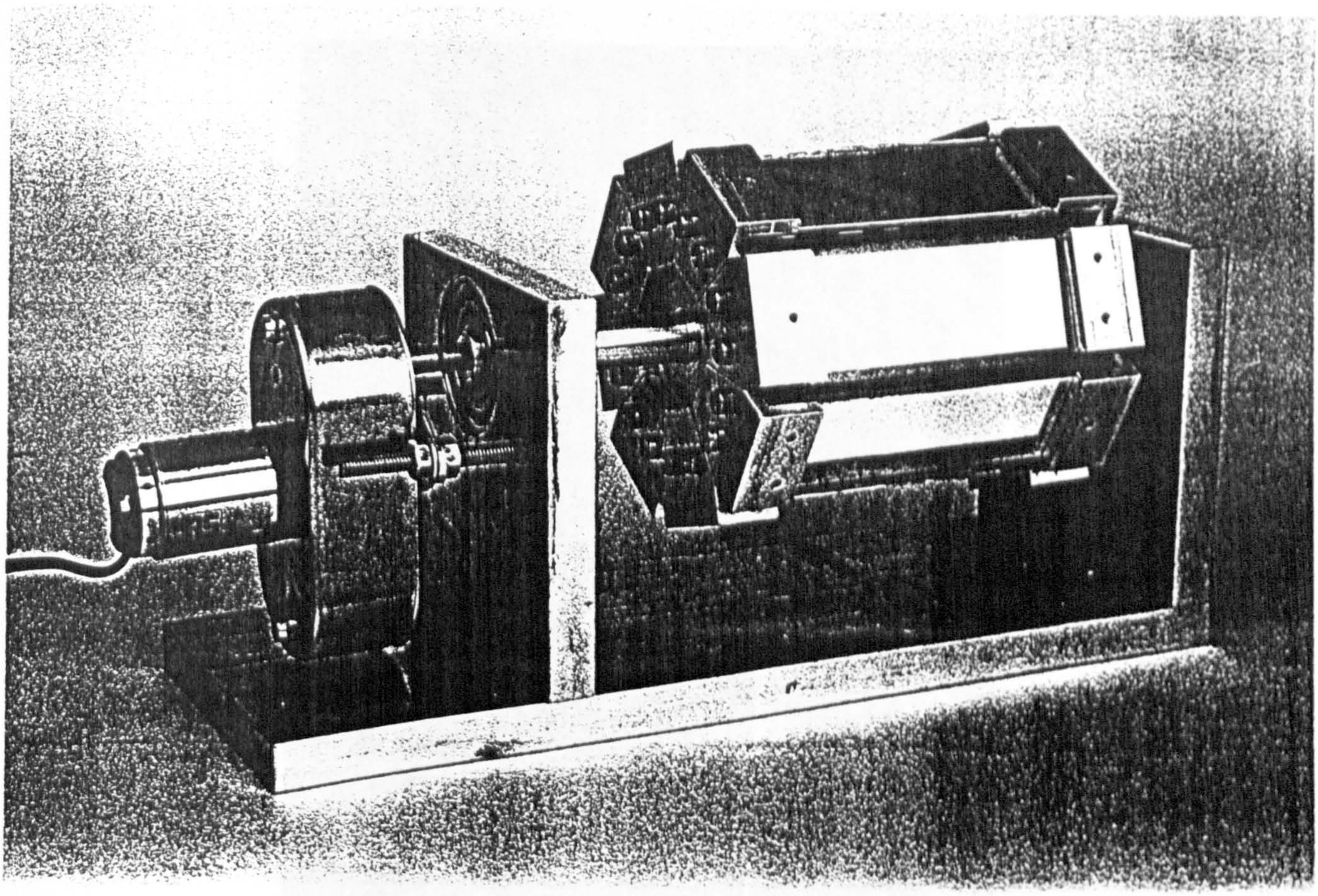

Fig.3 Octagonal mirror assembly.

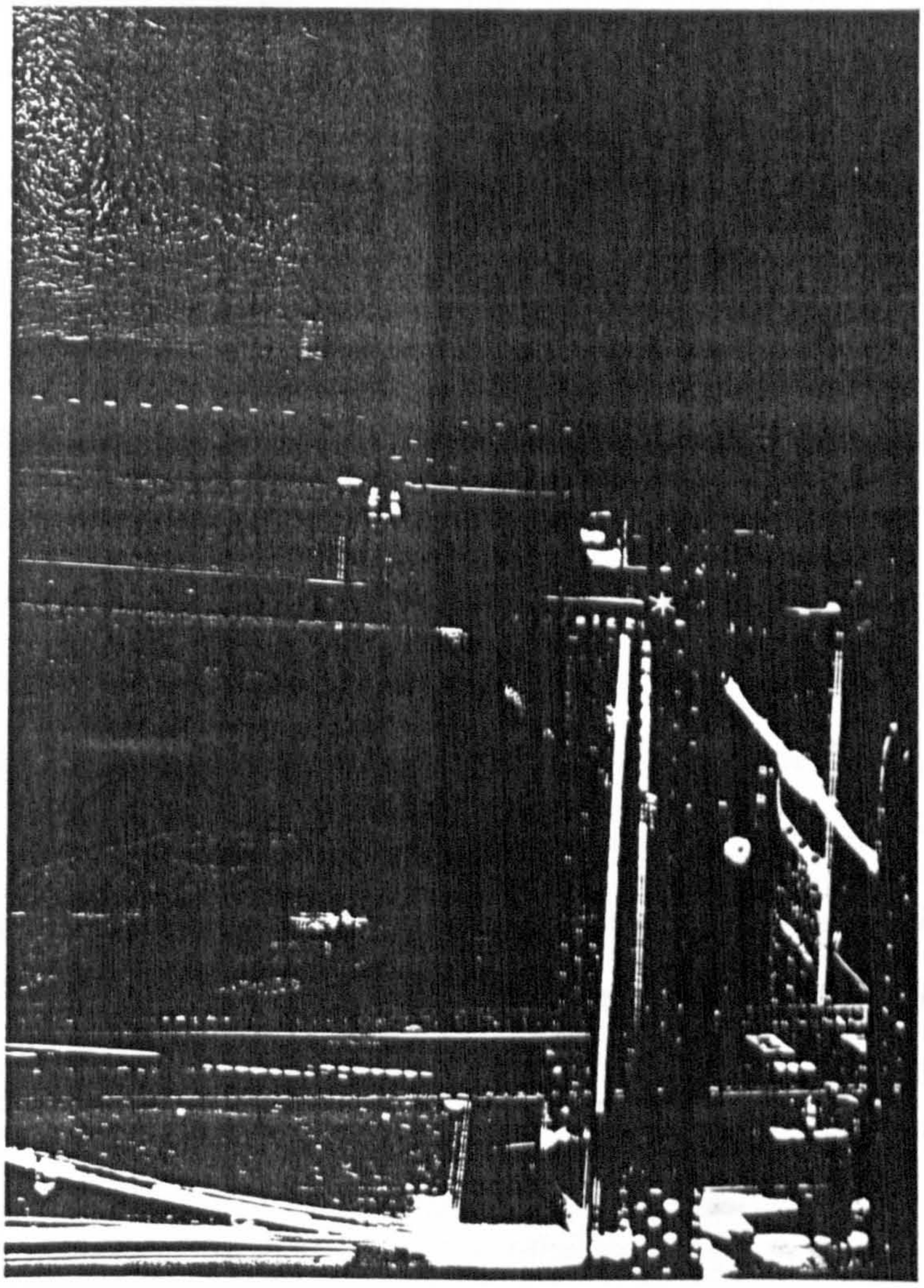

Fig.4 Rotating mirror and parabolic reflector installed beneath wave flume.

Discussion

It can be seen that the use of the scanning illumination system described above will result in a photographic record of the velocity field of the flow, where the velocity measured from a particular point corresponds to the average velocity in an instant in time. However the time that that particular velocity was measured differs from the time that the velocities to the left and right of it was measured by a known amount determined by the horizontal position of the measurement point in the measurement area. The maximum difference in the effective measurement time for any photograph will be equal to the time between pulses, in which case the effect will be insignificant

as the time between pulses is chosen such that in this short period of time a particle will not change its velocity significantly.

As well as making very efficient use of the available light power from a CW laser the scanning beam method of flow illumination provides significant advantages over an expansion system. Because the effective pulse time from the rapidly moving beam is very short illuminated particles within the flow will be properly recorded as points and not streaks as tends to happen if the pulse time is not sufficiently short in a chopped system. This maximises the dynamic range of velocity measurement from the photographic record. A more even illumination of the flow is also acheived with this technique compared with illumination from an expanded laser beam. A laser beam with a circular Gaussian intensity distribution is difficult to expand to a sheet with a constant intensity over its length and so beam expansion tends to provide illumination which is significantly reduced in intensity near the edges of the measurement area.

References

(1) Lourenco, L., Krothapalli, A., Buchlin, J.M., Riethmuller, M.L.,"Noninvasive Experimental Technique For The Measurement of Unsteady Velocity Fields",A.I.A.A. Journal, Vol 24, No 10, 1986, pp1715-1717

(2) Meynart, R. and Lourenco, L.M.,"Laser Speckle Velocimetry in Fluid Dynamics Applications",Von Karman Institute for Fluid Dynamics, Lecture Series 1984-03,pp10-16

(3) Hecht, E. and Zajac, A., "Optics", Addison-Wesley, 1974 ,p335

The Measurement of Breaking Waves using Particle Image Velocimetry

C. Gray, D. Skyner & C. A. Greated

Physics Dept., Edinburgh University, Edinburgh, Scotland.

ABSTRACT.

Instantaneous, full field velocity measurements have been achieved under the crest of a laboratory generated breaking wave. Measurements are made to within a few millimeters of the surface and covering an area of several hundred cm^2. The generation of the waves is achieved by means of a computer controlled wave paddle and measurements are made using a full field photographic technique(PIV). The photographic records of the flow are analysed by a fully automatic rig and the measurements shown to compare well with calculated velocities from a time stepping numerical model of a similar wave.

1. INTRODUCTION.

Breaking Waves represent one of the most extreme events in a marine environment, and a knowledge of thier internal kinmatics is neccessary for the estimation of drag and inertial forces on offshore structures.

Various numerical and analytical techniques have been developed to model the internal flow field of breaking waves [1,2] but these are difficult to apply to practical situations and are limited in their application to the early stages of breaking. Experimental studies have been undertaken, for comparison with results from numerical schemes, and for waves that cannot be realistically modelled numerically[3,4]. Major difficulties have been experienced when measuring waves with traditional probes, such as minature propeller meters and hot wire anemometers, due to their limited response accuracy in the extreme wave environment, severe calibration problems, and their physical effect upon the flow they are measuring.

Laser Doppler Anemometry (LDA) has been successfully used to make precise , high resolution velocity measurements under water waves[5] but many problems are experienced in its application. Most of these complications have been solved by the use of sophisticated computer techniques for analysing the Doppler signal and detailed studies of velocity distributions have been made and utilised for structural design purposes[6]. Despite these advances a fundamental limitation exists in the use of LDA and other point measurement devices for water wave studies.

Generally, a whole vector plot of particle velocities under a specified wave profile is required for design purposes and as a sensitive test of theoretical models. So, for point measurement techniques, complete vector plots can only be constructed in cases where the wave profile being studied can be faithfully repeated many times while moving the probe to a series of points across the flow field. Accurate repetition of a wave profile requires the

use of sophisticated wave generation techniques and for random waves and single event situations point measurement procedures become impossible. Genuine instantaneous velocity measurements over a whole wave profile would reveal the fine structure of a breaker so allowing detailed insight into the breaking process.

Recently Particle Image Velocimetry (PIV)[7,8] has been successfully applied to the study of water wave motions. This is a non-intrusive velocity measuring technique which allows a complete two-dimensional flow field to be captured at a single instant. The water is seeded with small neutrally buoyant particles and illuminated with a plane sheet of pulsed laser light. Using a conventional camera operating with a shutter time exceeding the pulse period, photographic film is exposed to two (or more) images of the moving particles. The displacement of the particle pairs determines the flow velocity at any particular point, and is measured by means of optical and digital processing of the developed film.

The application of the PIV technique to breaking waves is described. Waves are generated in a flume that has been purpose built for PIV analysis with an illumination system based upon a 20 W CW Argon Ion laser. Interpretation of the photographic flow records is by means of a fully automated analysis rig controlled by a microcomputer. A sample of typical full field velocity measurements is presented and compared with a recent numerical model.

THE WAVE TANK

The measurements of breaking waves were made in a 6m long flume, shown in figure 1. Waves are generated by a hinged wavemaker, and propagate through the PIV measuring region before being absorbed by an expanded metal beach. The experimental arrangement includes a wave gauge so that the exact composition of the wavefield can be established and tank repeatability checked. The wavemaker is of the absorbing type[9], with its force on the water made equal to the sum of a drive and filtered velocity signal, leading to the simulateous generation of waves and absorption of reflections respectively. The wave drive signal is produced by a microcomputer which can sample the wavegauge and trigger the camera while generating the wavefield.

BREAKING WAVE GENERATION

Water waves are dispersive in deep water, so that a solitary wave will spread into a group of waves as time passes. By considering the reversal of time it is apparent that a group of waves can contract into a single wave as it propagates. If the group is chosen correctly the final wave can be made to be too steep to be stable, resulting in breaking. Most methods of calculating the initial wavefield assume linear theory in its evolution (Kjeldsen 1983)[10] even though its final form is clearly non-linear. As a result, the linear methods often need fine adjustment of their parameters in order to produce breaking waves of a particular form.

We generate extreme waves by choosing a spectrum, then setting the phases of the spectral components so that they will all be in phase at the same time and place in the tank. The timeseries for the driving of the wavemaker is then calculated by transformation to the time domain. For the purpose of these tests the spectrum was chosen by trial and error to give a clean, plunging breaker, and this was achived by using a drive signal with 61 sinusoidal components in the range 0.2Hz to 1.4Hz each with equal amplitude. The breaking position parameter was adjusted to suit the PIV apparatus.

The breaking event was timed to occur 10 seconds after the start of the wave generation,

and each PIV picture was taken by allowing the tank to settle, starting the wavefield and triggering the camera after a known time. In a series of such measurements, the triggering time was incremented in 1/80 second intervals to obtain a sequence of pictures at different phases of the breaking wave.

Figure 2 shows wavegauge record + spectrum.

RECORDING OF PIV PHOTOGRAPHS

Photographic recording of the flow beneath laboratory generated waves requires optical access into the flume, consequently the central 2 meter section of the wave tank used for PIV analysis is built with 20mm thick glass sides and a glass base to allow passage of a plane sheet of light into the region of interest beneath the wave. In order that the PIV photograph represents a sufficiently instantaneous record of the flow within the wave the shutter time of the recording camera and the time duration between illuminating pulses of light into the tank must be as short as possible. This also imposes the requirement that the pulse time is very short. Lourenco[11], quotes a minimum pulse separation to pulse time ratio of 20, and although in practice smaller ratios than this can be used, generally the larger the ratio the better the quality of the flow records. The measurements described in this paper were made using a CW laser as greater control is afforded over pulse separations than with conventional pulsed lasers, so permitting this same light source to be used for PIV measurements on a variety of other flows[12,13]. However, for a sheet illumination system that is pulsed by mechanical or electrooptical means there will be a severe constraint upon the light power in each pulse if the pulse time is very short. In the system used at Edinburgh this difficulty is avoided by employing a 'Scanning Beam' system of flow illumination whereby the beam from the laser is narrowed to approx. 1.5mm using a telescope arrangement, and then reflected through a multi-faced rotating mirror and parabolic recollimating dish to scan through the area of interest[14] . This manner of illumination ensures that the light power from the laser actually entering the flow is maximised and that a very short but intense pulse of light is imparted to the tracer particles within the flow. For the system in operation each illuminating pulse is approximately 200 times shorter than the time between pulses, which for a pulse seperation of 1ms gives a pulse time of 5×10^{-6}s ensuring that streaking of the particle images is negligible ; this avoids the associated problems with analysis of streaked photographs[12]

The water within the wave tank was seeded with Conifer Pollen which has an average diameter of 70 microns. These particles are used because, when wet, their density is very close to that of water ensuring that within the typical timescale of an experiment there is no noticeable settling of the tracers as may be experienced with more traditional seeding materials such as Aluminium powder. This is important as any settling will result in an inadequate density of tracers in the upper measurement region of a passing wave ultimately resulting in signal dropout where a good record of the flow is particularily important. The closeness of the seeding density to that of water also ensures that the tracer particles faithfully follow the flow even under high flow accelerations.

Seeding concentrations are maintained at a level that will ensure a high density of non-overlapping particles on the resulting film record. This is important so that within the small region within which a point measurement of the particle separation is calculated there are three or more particle pairs allowing an unambiguous determination of the flow direction and magnitude. For a light sheet of thickness 1.5 mm, an Image/ Object magnification of 0.102, and a circular probe diameter of 0.75mm, a minimum seeding density of 2×10^7 particles per cubic meter of water is required.

In order to record the whole crest region of the breaking wave in a single exposure it is neccessary to have a large illuminated measurement region. Consequently a large film format is required so that image/object magnification is maximised to allow good

resolution of the velocity measurements from the final flow record. A Hassleblad ELM camera body with a 120 film back was used giving 28.25 cm^2 of exposable film for each flow photograph. The illuminated tracer particles are imaged onto the film plane by a planar T 80mm focal length f2.8 lens system. The high quality of the lens ensures that the imaged particles are not excessively enlarged over the diffraction limit of the lens by optical aberrations.

Sinha[15], points out that the refraction effects of a water/glass/air boundary will lead to distortion of the image plane when photographing a planar region within a glass tank of fluid with a different refractive index to air. This effect is more pronounced the greater the angle of incidence of light from the optical axis of the imaging optics. In order to account for such disortions, which would lead to significant positional errors on analysis of the flow record, a perspex grid of known dimensions was photographed while in the same position as the illuminated region of the flow. Precise measurement of the positions of the intersection points of the grid on the developed film were made using a travelling microscope with the film positioned on a light table. Relating these measurements back to the precisely known dimensions of the real grid gave a map of the geometric distortion due to refractive index differences, the limited optical quality of the tank walls, and any small distortions from the lens . The photographic emulsion used was T-Max 100 ASA which has good spectral sensitivity between 4700 nm and 5500 nm which covers all the lasing lines of the Argon Ion laser used. Each film is developed for 7 minutes at 20 deg. C with agitation by multiple inversion every 30 seconds to reduce particle image migration due to developer starvation. The film is washed by dilution and then fixed for 3.5 minutes, again at 20 deg. C to avoid reticulation. The resolution achieved with this film is good (200 lines/mm) even though it has considerable sensitivity over the wavelengths used to illuminate the flow allowing good image definition and little effect upon particle image shape or size.

ANALYSIS OF PIV PHOTOGRAPHS

Typical PIV photographs contain an enormous amount of precise velocity information relating to the recorded flow; this is visible by inspection of the film under magnification, as the physical separation of particle images recorded from successive illuminations. The separation of 'related images' must be measured without confusion from other nearby images and combined with the parameters M (the Image/Object magnification) and Δt (the time between illuminating pulses) to determine the particle and thus flow velocity at that point . Manual analysis of flow records has been achieved with apparently good accuracy[16] but for the large quantity of data contained in the wave records presented here precise automatic analysis is required.

The system used at Edinburgh is based on a 32 bit microcomputer and interprets the film point by point over a dense grid using methods of optical and digital analysis. The film is mounted on a two-dimensional microtranslation stage allowing motion vertically and horizontally in the plane of the photograph. At points generally separated by 0.5-2.0mm the film is coherently illuminated over a small circular region (0.75mm diameter) and the diffracted light passing through the photograph is collected and observed at the front focal plane of a biconvex lens as displacement speckle fringes or Youngs Fringes[16]. The orientation and separation of such fringes is related to the separation and orientation of the particle images within the probed region of film. If three or more particle image pairs exist within this region then the most common particle separation is that induced by the flow and so the fringes generated will unambiguously represent the flow velocity. The automatic analysis of displacement fringes has recieved much attention in order to determine a fast, reliable, and accurate method of resolving their orientation and frequency.

Semi-automatic techniques have been used based upon one-dimensional Fourier

transformation of the intensity distribution after they have been averaged in the direction of the fringes. This of course requires an operator to align the diffraction pattern. Fully automatic methods have been developed[17,18] utilising one-dimensional autocorrelations in several directions to determine both fringe frequency and orientation but for fringes that are particularily noisy the failure rate may be high. The fringes generated from most PIV photographs are typically of very low visibility due a number of factors including,

- Refractive index and thickness variations across the film backing
- Film grain noise
- Noticeable cross interference due to small numbers of particle pairs
- Small variations in particle velocity across measurement area due to turbulence and/or large velocity gradient.
- Reduction in particle image contrast due to air entrainment etc.

This neccessitates the use of a fringe analysis algorithm that utilises all the information present in the fringe intensity distribution. Huntley[19]), describes a system of fringe evaluation based on two-dimensional Fourier transformation of the digitised fringes which achieves 100% success for fringes of visibility greater than 7%. Even though the calculation of the 2-D transform is time consuming this scheme is adopted due to its ability to successfully process exremely noisy fringes.

Digitisation of the fringes is achieved using a Panasonic CCD camera. . The digitised intensity pattern is transferred to the computers hard disc until all the fringe data from the whole film is saved. This allows the CCD camera and the probe laser (2mW HeNe) to be switched off while the more time-consuming fringe analysis is being performed, prolonging the life of the camera and preserving the fringe data for visual inspection should a particularily important point measurement fail. The 2-D Fourier transform is calculated by performing a Fast Hartley transform [20] on the rows and then the columns of the digitised data. This gives a significant reduction in the computation time over an FFT as the data has no imaginary part on starting the calculation. Subtraction of the fringe pedestal prior to transformation zeroes the d.c. component and significantly aids the resolution of low fringe frequencies[21]. Location of the discrete signal peak is then a simple search for the maximum data point in the transform plane. The peak of the continuous Fourier Spectrum of the fringes is located by means of a trigonometric interpolation and a Newton Raphson iteration using the maximum from the discrete spectrum as the starting point. The position of the peak kx,ky calculated as above gives the spatial frequency components in the horizontal and vertical directions which when multiplied by a calibration factor is converted to horizontal and vertical components of velocity. The visibility of the fringes is also calculated from the height of the signal over the area under the fringe intensity data allowing an estimate of the measured velocities reliability.

Figures 3 and 4 illustrates the fringe aquisition system and the complete analysis rig respectively.

Within each set of data generated from a flow photograph there is a subset of measurement points which are not consistent with those velocity values about them. Their orientation and/or magnitude may differ significantly from neighbouring values due to the fact that the fringe frequency values are anomalous and generated by detection of a peak other than the peak due to the flow separated particle images. The reasons for such failures are noted above and occur more frequently the poorer the quality of the fringes. The success rate quoted above from Huntley[19] is consistent with measurements made with

the system described above but a significant fraction of fringes measured from wave records have visibilities well below 7%. By considering the measured fringe visibility and the fringe frequency and orientation together it is possible to identify most of the spurious vectors. These values are removed and in places where sufficient numbers of valid neighbours exist an interpolated value substituted.

NUMERICAL COMPARISON

In order to judge the form of the PIV velocity plots we attempted the generation of breaking waves in a numerical model The model used was a time-stepping scheme developed at Bristol University, by Peregrine et al[2] and assumes the fluid is undergoing inviscid, incompressible irrotational motion. With these assumptions it is possible to reduce the calculations of the fluid motion to the evaluation of the motion of discrete points along the surface, resulting in a computationally efficient scheme. The model requires the coordinates of points along an initial surface along with their velocity potentials, and will time-step the surface motion until breaking occurs, after which the algorithm fails.

We have not attempted an exact comparison, only a comparison of breaking events resulting from similar experimental and numerical wavefields. The starting profile for the mathematical model was in fact obtained from the wavegauge record measured in one of the experiments. From the wave spectrum the waveheight and velocity potential were calculated for a particular time (t=1s) using linear theory at a series of 200 points concentrated near the expected breaking position. In order to accomodate the whole wavefield it was necesssary to consider points not only in the region of the tank, but also up to 20m behind the wavemaker. Because the waves are always quite steep linear theory cannot be expected to predict starting conditions which will yield the same wavepacket as used experimentally, and this became apparent when the numerical wave 'broke' at the leading crest just before the main event. In order to produce a wave which would break in approximately the right place the overall height of the starting profile was reduced by 13% and the resulting numerical breaker is plotted in figure 5.

EXPERIMENTAL RESULTS/DISCUSSION

Figure 6 shows the velocity measurements derived from one of a number of records taken of the wave chosen for comparison with the numerical model. It can be seen that, qualitatively, the measurements are very similar to the calculated velocities shown in figure 5. The smoothness of the results shows the PIV technique to be capable of making precise and noise-free velocity measurements over considerable areas demonstrating its considerable potential for flow studies of this kind where traditional measuring techniques fail.

The typical accuracy possible from such measurements would appear to be good, but future work by the authors will concentrate on theoretical and experimental analysis of the factors which limit this accuracy.

ACKNOWLEDGEMENT

The Authors gratefully acknowledge the funding provided by the Marine Technology Directorate U.K. for this project. They also wish to thank Prof. D.H. Peregrine of the Mathematics Dept., Bristol University who developed the time-stepping computer program and allowed the authors to run this in Edinburgh.

REFERENCES

1. Longuet-Higgins, M.S. and Cokelet, E.D.:"The Deformation of Steep Surface Waves in Water. 1. A Numerical Method of Computation". Proc. Royal Soc. London, 1976. A. 350, 1-26.

2. New, A.L., McIver, P. and Peregrine, D.H.:"Computations of Overturning Waves" , J. Fluid Mech..150. 233-251, 1985.

3. Van Dorn, W.G. and Pazan S.E.:"Laboratory Investigation of Wave Breaking, Part 2, Deep Water Waves".Research Report, Advanced Ocean Engineering Laboratory, Scripps Inst. of Oceanography, University of California, San Diego, S10 Ref. No. 75-21. AOFL Report£71, 1975.

4. Kjelsen, S.P., Vinge, T. and Brevig, P.:"Kinematics of Deep Water Breaking Waves" , Proc. 12th Annual Offshore Technology Conference, Texas, 317-325, 1980.

5. Easson, W.J. and Greated, C.A.:"Breaking Wave Forces and Velocity Fields", Coastal Engineering. 8. 233-41.1984

6. Easson, W.J.:"Velocity and Force Measurements In the Splash Zone"', J. of Strain, 15-18, Feb.1987.

7. Gray, C., Greated, C.A. and Fancey, N.A.:"The Application of PIV to Measurements Under Water Waves", 2nd Int. Conf. on Laser Anemometry, Strathclyde, 1987.

8. Gray, C. and Greated, C.A.:"The Application of Particle Image Velocimetry to the Study of Water Waves",Optics and Lasers In Engineering, 9, 1988.

9. Salter, S.H.:"Absorbing Wave Makers and Widetanks",Proc. Conf. Dirctional Wave Spectra Applications, ASCE, 1982, 185-200.

10. Kjeldsen, S.P.:"2 and 3 Dimensional Deterministic Freak Waves", Norwegian Hydrodynamic Laboratories Report, 1983.

11. Lourenco, L.:"Theory and Application of Particle Image Displacement Velocimetry", in Lecture Series 1986-09, Von Karman Inst. of Fluid Dynamics, Brussels 1986.

12. Sharpe, J.P., Gray, C., Greated, C.A. and Campbell, M.:"Measurement of Acoustic Streaming using PIV", to be published, Acoustica, 1989.

13. McCluskey, D.R., Easson, W.J., Greated, C.A. and Glass, D.:"The Use of Particle Image Velocimetry to Study Roping in Pneumatic Conveyence",4th European Symposium in Particle Characterisation, Nuremberg, W.Germany, Apr.1989.

14. Gray, C. and Greated, C.A.:"A Scanning Laser Beam System for Two Dimensional Illumination of Flow Fields",Lecture Series, Von Karman Inst. of Fluid Dynamics, Belgium, March 1988.

15. Sinha, S.K.:"Improving the Accuracy and Resolution of Particle Image or Laser Speckle Velocimetry",Experiments in Fluids, 6, 67-68, 1988.

16. Burch, J.M. and Tokarski, J.M.J.:"Production of Multiple Beam Fringes from Photographic Scatterers",Optica Acta, Vol15, No.2, 101-111, 1968.

17. Robinson, D.W.:"Automatic Fringe Analysis with a Computer Image Processing System", Appl. Optics, 22, 1983, 2169-2176.

18. Moraitis, C.S., Buchlin, J.M. and Reithmuller, M.L.:"Improved Autocorrellation Analysis of Fringe Images for Laser Speckle Velocimetry", ICIASF June 22-25, 1987.

19. Huntley, J.M.:"An Image Processing System for the Anlysis of Speckle Photographs", J.Physics. E. Sci. Instrum.,19, 1986.

20. Bracewell, R.N.:"The Fourier Transform and its Applications",McGraw-Hill, 1986.

21. Pickering, C.J.D. and Halliwell, N.A.:"Particle Image Velocimetry: Fringe Visibility and Pedestal Removal", Appl. Optics, Vol 24, No.6. 2474-2476, 1985.

Callum Gray

Callum Gray graduated in Physics at Edinburgh University with a first class honours degree and is now a Research Student in the Fluid Dynamics Unit. He has developed a fully automated PIV system at Edinburgh which has been used in flow studies ranging from acoustic streaming to the kinematics of water waves. He has a number of publications in this area.

David Skyner

David Skyner graduated in Physics at Cambridge University with a first class honours degree and is now a Research Fellow in the Fluid Dynamics Unit at Edinburgh. Previously he worked on the development of wave energy devices but is now researching into the mechanics of breaking waves. He has published in this area and also been engaged in industrial consultancy.

Clive Greated

Clive Greated is Director of the Fluid Dynamics Unit at Edinburgh. Previously he was an engineer at the Danish Institute of Applied Hydraulics. Whitworth Scholar at Cambridge University and Lecturer in mathemetics at Southampton University. His primary research interests are in wave mechanics and laser measuring systems. He has published extensively in these areas and is becoming increasingly involved in industrial consultancy.

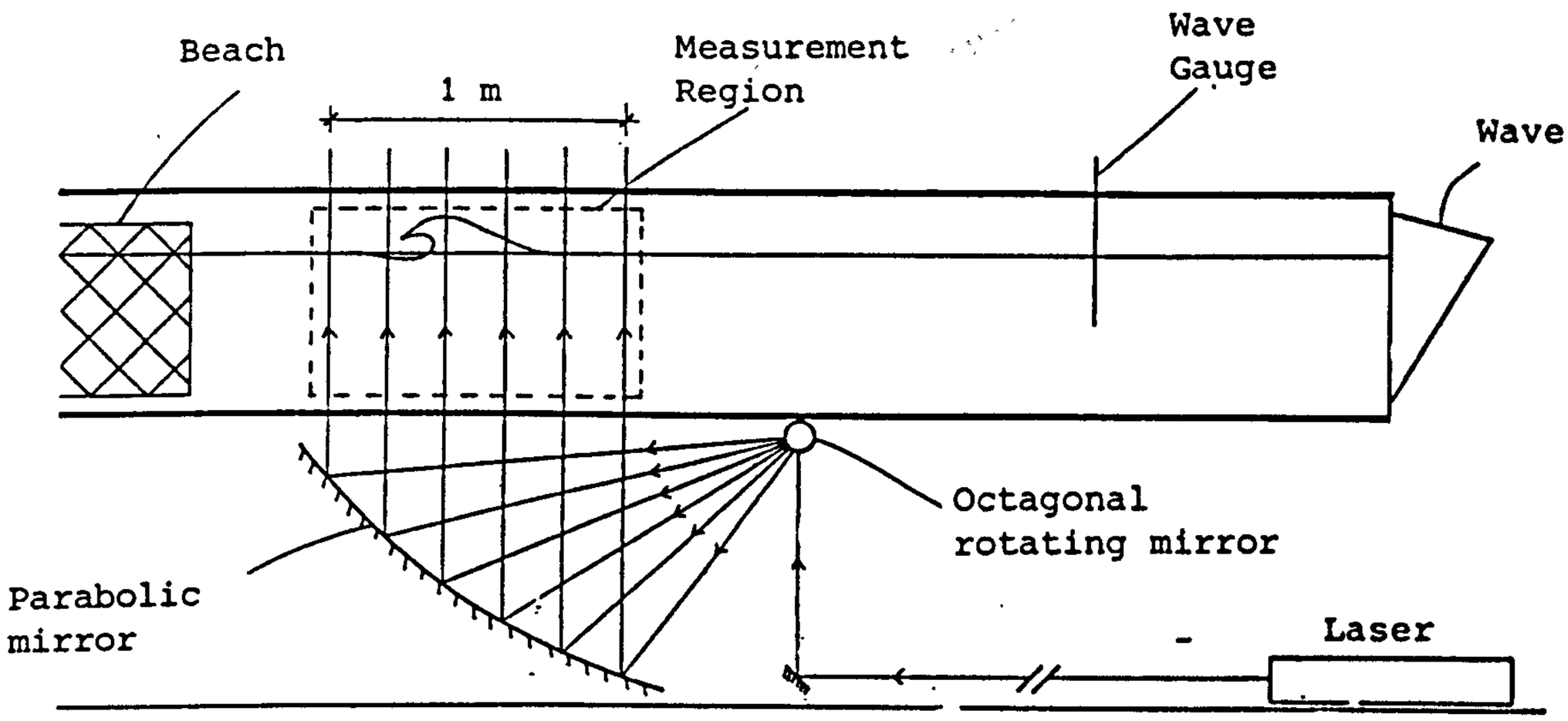

Figure 1. Wave flume used for PIV analysis of breaking waves.

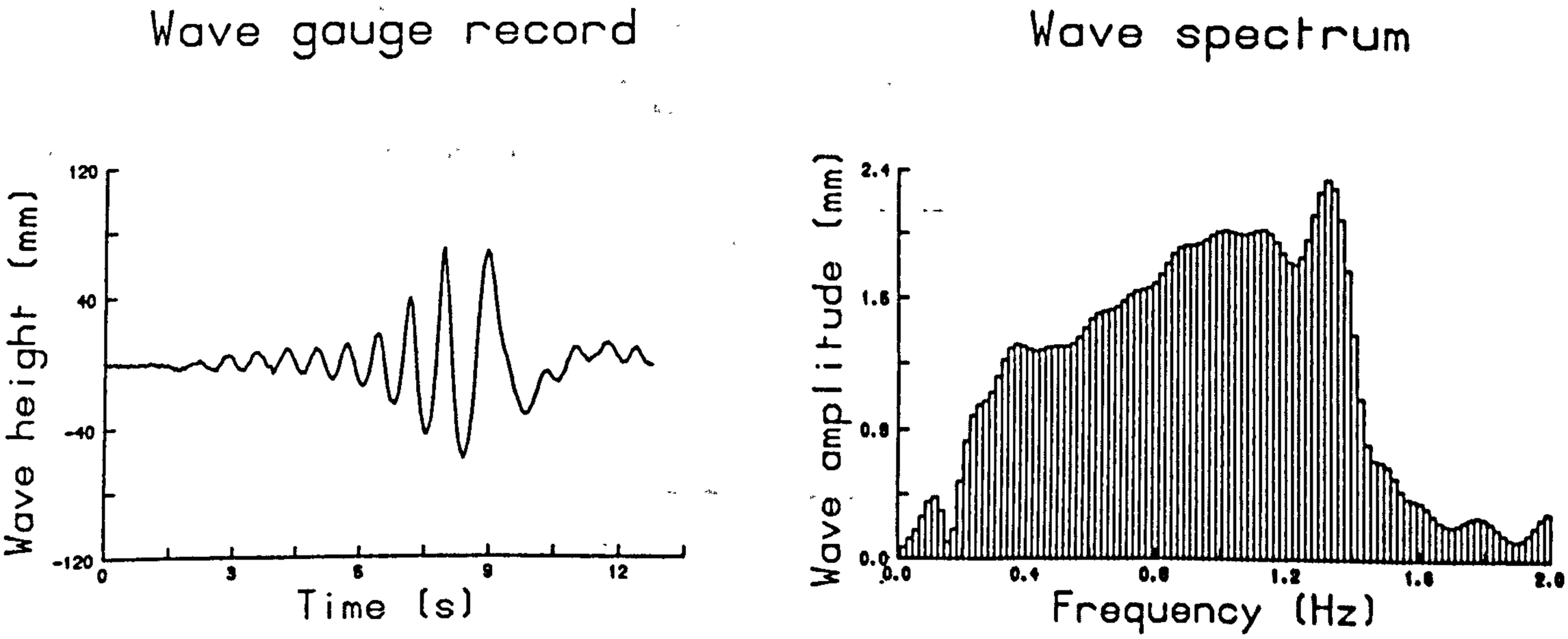

Figure 2. Wavegauge record from a single test with its spectral content calculated by FFT.

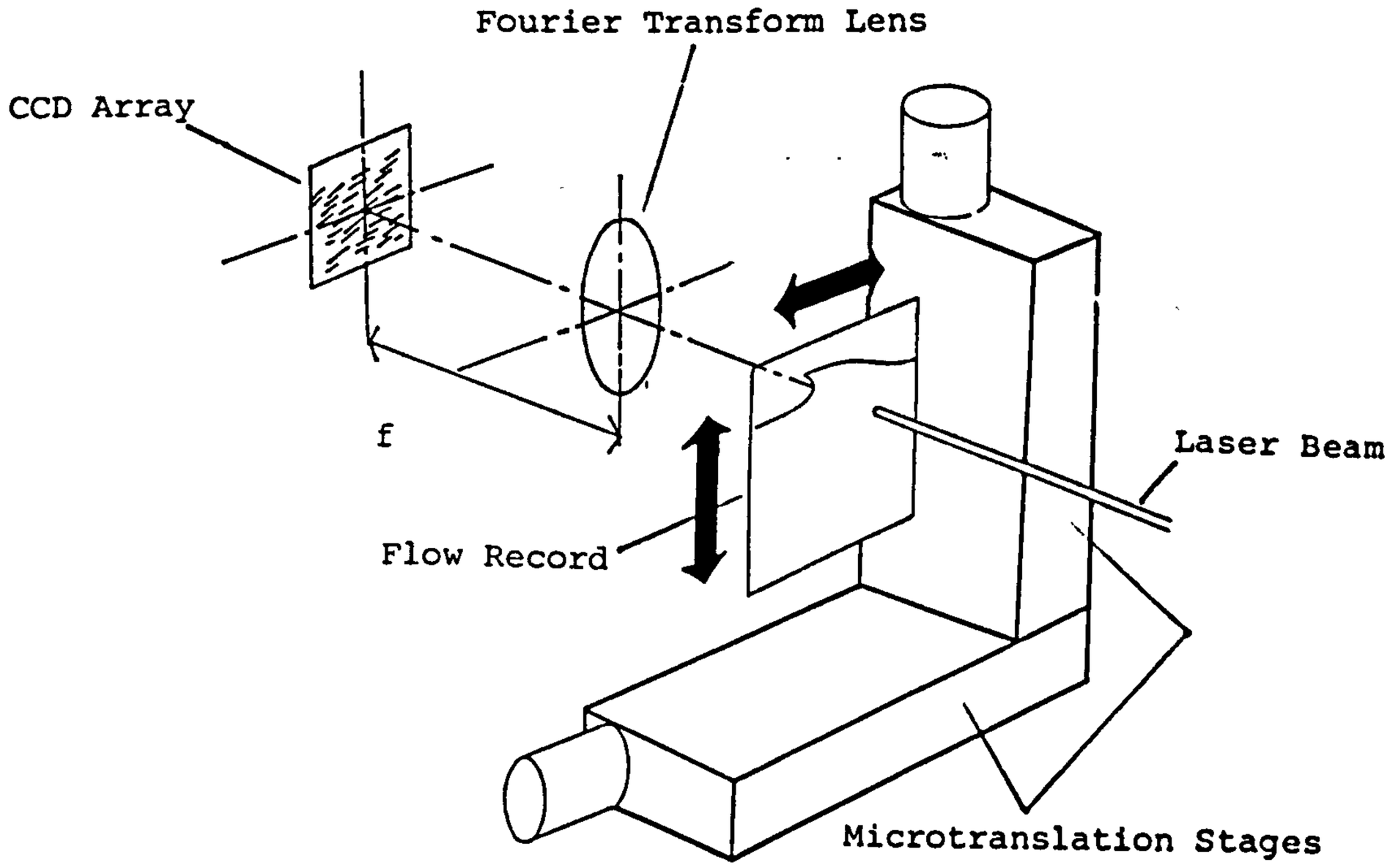

Figure 3. Generation of Speckle displacement fringes and digitisation in Fourier plane of lens.

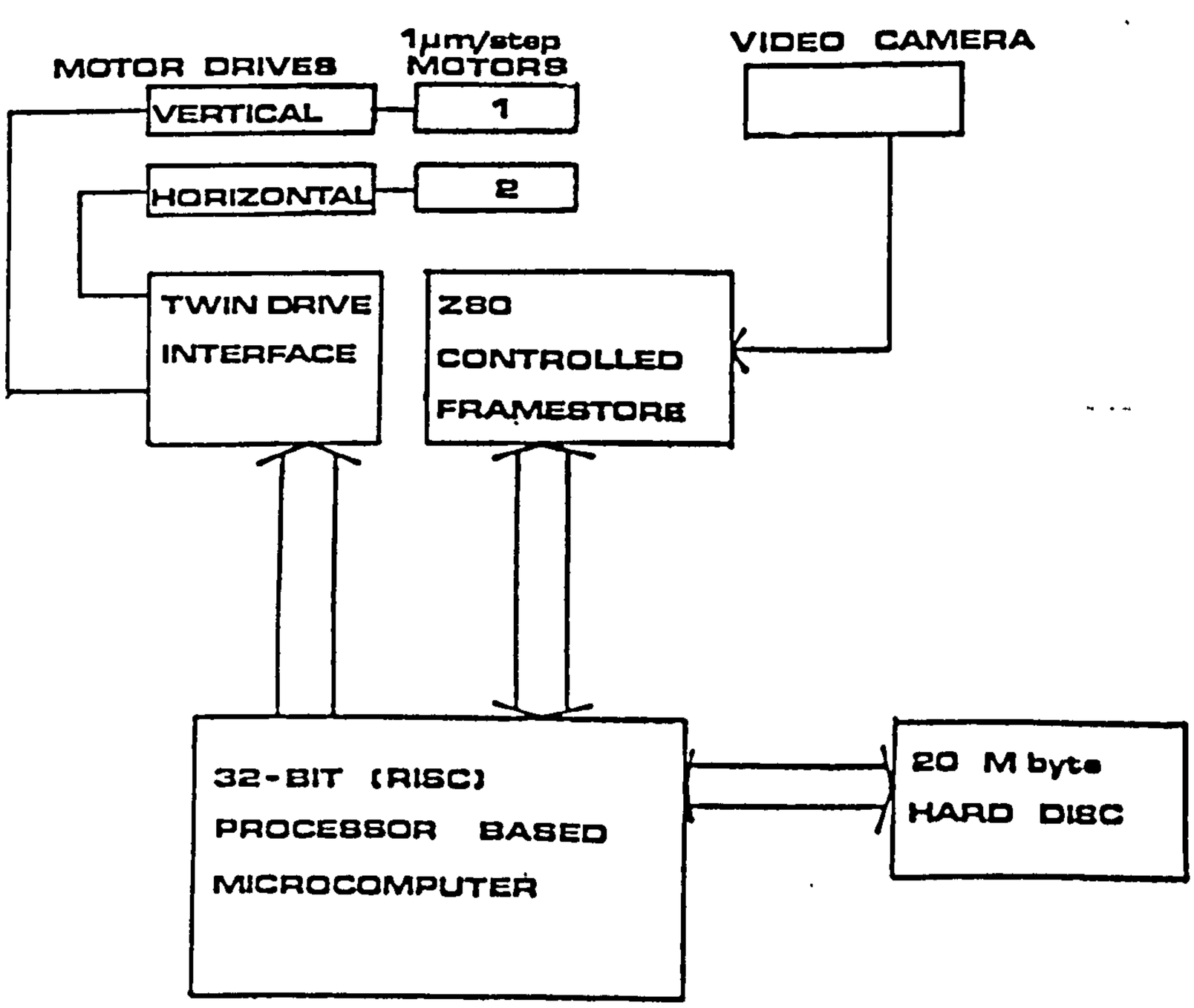

Figure 4. PIV film analysis hardware.

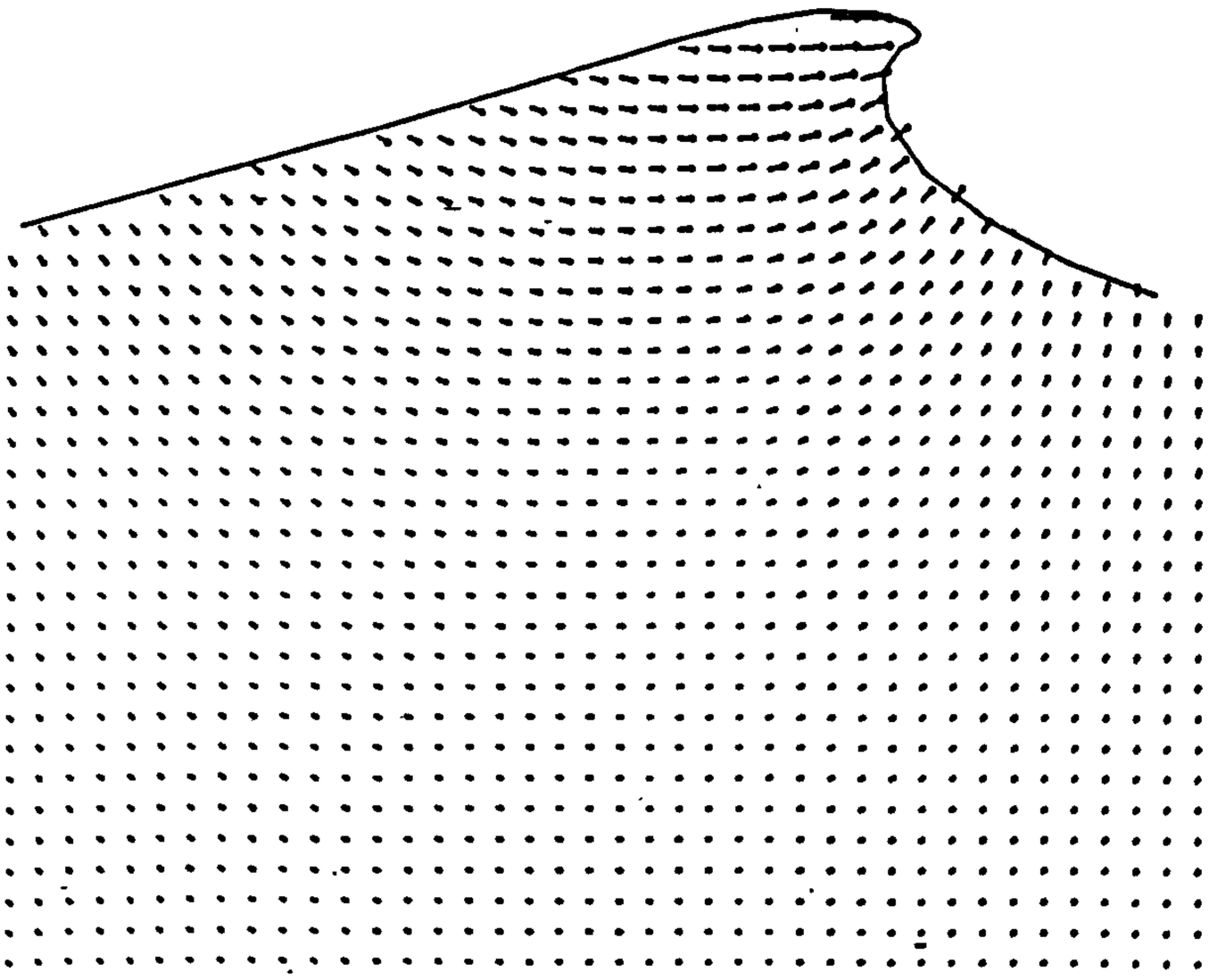

Figure 5 Velocity distribution generated from numerical model.

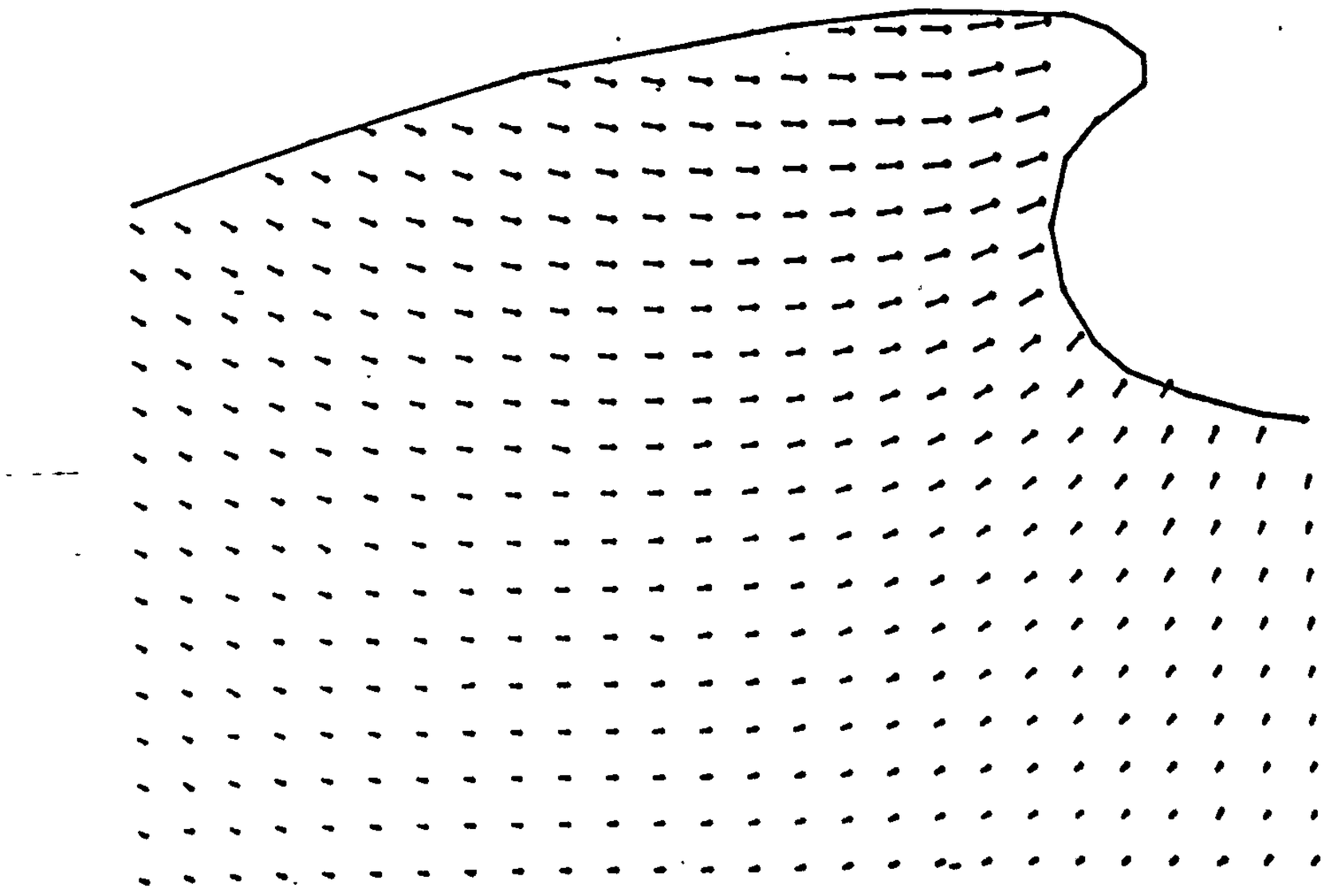

Figure 6. Velocity distribution measured from Laboratory generated wave.

A COMPARISON OF TIME-STEPPING NUMERICAL PREDICTIONS WITH WHOLE-FIELD FLOW MEASUREMENT IN BREAKING WAVES

D.J. SKYNER, C. GRAY AND C.A. GREATED
Physics Department
Edinburgh University
Edinburgh
EH9 3JZ
SCOTLAND

ABSTRACT. Instantaneous, full-field velocity measurements under the crest of a laboratory generated breaking wave are presented and compared with a fully non-linear time-stepping numerical model. A plunging breaker is generated, on constant water depth, using the numerical model, then reproduced in a wave flume by matching wave amplitude timeseries at a position just before the breaking. The generation of the waves is achieved by means of a computer controlled wave paddle and measurements of the flow made with a full-field photographic technique (PIV). The photographic records of the flow are analysed on an automatic rig and the measurements are shown to compare well with the numerical calculations.

1 Introduction

Breaking waves represent one of the most extreme events in a marine environment and a knowledge of their internal kinematics is necessary for the estimation of drag and inertial forces on offshore structures.

A number of robust, fully non-linear time-stepping numerical models are now available for two dimensional waves [1] [2], but they can be difficult to apply to practical situations and are limited in their application to the early stages of breaking. Experimental studies have been undertaken, for comparison with results from numerical schemes [3] and for waves that cannot be realistically modelled numerically [4] [5]. A potentially fruitful area of research is the comparison of numerical predictions with experimental measurements, along with an assessment of the relative merits of the two approaches.

1.1 COMPARISON OF NUMERICAL AND EXPERIMENTAL WAVES

If the fluid flow is inviscid, irrotational and incompressible, and the numerical model accurately time-steps the boundaries, then similar waves would propagate identically in an experiment as numerically. By trying to achieve a comparison our first intention is to show that the full-field measurement technique (PIV) can give sensible measurements in the inaccessible parts of extreme waves. If the match is good then the numerical method is also validated. Furthermore, experimental measurements can continue past breaking, where the current numerical schemes stop, so that a good match up to this point would provide a useful starting point for future numerical modellers.

The main difficulty encountered in trying to compare waves propagated numerically and experimentally was that the available numerical model required the wave height and velocity potential to be defined in space at a particular time, whereas experimentally a driving timeseries is supplied to the wavemaker at a particular position.

Our first attempt at a comparison was to generate, by trial and error, a plunging breaker in the laboratory, then to try to replicate it numerically by calculating the starting profile and velocity potential from a wavegauge record. However, linear theory proved to be inadequate for the task as the wavefield is too non-linear in its propagation towards breaking.

A more successful scheme was found to be the iterative selection of a starting profile which would propagate numerically into a plunging breaker and then to attempt its reproduction in the wave tank. This method has the advantage that a timeseries can be obtained from the computations for a particular place, which then should not be too difficult to reproduce experimentally. The main difficulty is that the wave height is related to the paddle motion via a transfer function, which is only easily determined if the motion is sufficiently linear.

1.2 FULL-FIELD VELOCITY MEASUREMENT

Laser Doppler Anemometry (LDA) has been successfully used to make precise velocity measurements under water waves [6], but some problems are encountered in its application. Most of these complications have been solved by the appropriate implementation of established computer algorithms for analysing the Doppler signal and detailed studies of velocity distributions have been made and utilised for structural design purposes [7]. Nevertheless a fundamental limit exists in the use of LDA and other point measurement devices used in water wave studies.

Generally, a whole vector plot of particle velocities under a specified wave is required for design purposes and as a sensitivity test of theoretical models. So, for point measurement techniques, complete vector plots can only be constructed in cases where the wavefield being studied can be faithfully repeated many times while moving the probe to a series of positions within the flow field. Accurate repetition of a wave profile relies on the quality of the wave generator and for truly random waves it is impossible to obtain full-field information from point measurement procedures.

Recently Particle Image Velocimetry (PIV) [8] [9] has been successfully applied to the study of water wave motions. This is a non-intrusive velocity measurement technique which allows a complete two-dimensional flow fields to be captured at a single instant. The water is seeded with small neutrally buoyant particles and illuminated with a plane sheet of pulsed laser light. Using a conventional camera operating with a shutter time exceeding the pulse period, photographic film is exposed to two or more images of the moving particles. The displacement of the particle pairs determines the flow velocity at any particular point, and is measured by means of optical and digital processing of the developed film.

The application of the PIV technique to breaking waves is described. Waves are generated in a flume that has been purpose built for PIV analysis with an illumination system based on a 20 W CW Argon Ion laser. Interpretation of the photographic flow records is by means of an automatic analysis rig controlled by a microcomputer.

2 The Generation of Breaking Waves

Because water waves are dispersive on finite depth, extreme waves can be generated by choosing a wave-packet which will self-focus. Most methods for choosing the starting wave-group assume linear theory, possibly augmented by the inclusion of a non-linear phase

speed [11]. However, since the wave-propagation becomes increasingly non-linear as breaking approaches the starting conditions are somewhat arbitrary and normally require their parameters to be adjusted until the required breaker is formed.

We decided to attempt the generation of breaking waves by the superposition of sinusoidal components, with enough parameters in the specification of the spectrum to allow some fine adjustment of the breaker's form. Equation 1 describes a wavefield composed of discrete sinusoidal components at equally spaced frequencies.

$$a(x,t) = \Re\left\{\sum_{n=N_0}^{N_1} A_n e^{ik_n x + i\omega_n t + i\phi_n}\right\} \tag{1}$$

where

$$\omega_n = 2\pi n\,\delta\omega \tag{2}$$

and

$$\omega^2 = gk\tanh kh \tag{3}$$

In order to limit the number of parameters the spectral shape was selected such that the components had amplitudes given by

$$A_n = (a_0 + a_1\omega)\exp\left(-\left|\frac{\omega-\omega_1}{\omega_0}\right|^s\right) \tag{4}$$

And phases ϕ_n chosen so that, if linear theory applied, the components would have some common phase Φ at $x = 0, t = 0$.

The spectral form (4) was selected as covering the 'flat top' spectral shape often used in the generation of freak waves [3][12], while allowing the spectrum to tail off smoothly at the extremes.

3 Numerical Model

The numerical model available for comparison with experimental measurements was the fully non-linear time-stepping scheme developed by Dold and Peregrine [2] at Bristol University. The model assumes the flow to be inviscid, incompressible and irrotational. With these assumptions the calculation of the fluid motion is reduced to the evaluation of discrete points along the surface, resulting in a computational efficient scheme. The implementation available to us assumes periodic boundary conditions and requires the coordinates of points along an initial surface along with their velocity potentials, and will time-step the surface motion until breaking occurs.

Having decided on a spectral form and chosen initial parameters making use of experience in generating demonstration 'freak' waves in the laboratory, starting profiles and velocity potentials were calculated with linear theory for the numerical model.

In the model the computational points move with the surface. The resulting flexibility in the distribution of the computational points can be used to advantage as resources can be concentrated on regions of the wavefield where the most rapid changes are expected. The point distribution was made proportional to the local wavenumber, with enhancement in the region where breaking was expected.

The model requires periodic boundary conditions and for the horizontal extent to be rescaled to 2π, and other quantities by the appropriate Froude scaling. Care was taken that all the the wavepackets considered tailed off naturally before the boundaries. The point

distribution function was also forced to be continuous across the boundaries by employing a smoothing algorithm.

Each numerical wavegroup tested was allowed to propagate until it 'broke' or passed the place where breaking was expected. The spectral parameters, mainly overall size, were then altered until a plunging breaker was produced which just avoided breaking at the penultimate crest. With 200 computational points it was possible to try another iteration every few hours, and after couple of dozen iterations a suitable breaker was arrived upon. The chosen wave was then rerun with 400 computational points. The profile of the wave as it nears breaking, used to judge its suitability, is plotted in figure 2.

The spectral shape finally selected is shown in figure 1 and the resulting starting profile and velocity potential plotted in figure 3 along with the distribution function used to obtain the computational co-ordinates.

From the program output a wave amplitude timeseries was extracted by interpolation at x = -1.0 m. This is about 1.5 m before the breaking position and was chosen to be a suitable place to attempt the experimental match, given the limited length of the wave flume. In order to obtain a record which contained most of the passage of the wavepacket the timeseries was extented both before and after the time period covered by the numerical model, using linear theory. This extension was found to be necessary if Fourier analysis was to be used in the experimental reproduction, although the linear theory only applies correctly at the start of the record. The composite timeseries is shown in figure 4.

4 Experimental Measurements

4.1 WAVE TANK

The experimental measurements of breaking waves were made in a 6 m long wave flume, sketched in figure 5. Waves are generated by a hinged wavemaker, and propagate through the PIV measuring region before being absorbed by an expanded metal beach. The experimental arrangement includes a wavegauge so that the composition of the wavefield can be established and tank repeatability checked. The wavemaker is of the absorbing type [10], with its force on the water made equal to the sum of a drive signal and filtered velocity signal, leading to the simultaneous generation of waves and absorption of reflections respectively. The wave drive signal is produced by a microcomputer which can sample the wavegauge and trigger the camera while generating the wavefield.

Photographic recording of the flow beneath the waves requires optical access into the flume, so the central 2 metre section of the tank has 20mm thick glass walls and a glass base to allow passage of the illuminating laser sheet.

4.2 REPLICATION OF NUMERICAL WAVE

The wave height timeseries obtain from the numerical model provided the point at which the experimental wavefield was required to match the numerical. With a knowledge of the expected breaking position and taking into account the restriction of the PIV measuring region a wire wavegauge was placed 1.300m in front of the wavemaker. This position is about $2\frac{1}{2}$ times the hinge depth away from the wavemaker which was judged to be sufficiently far to avoid transient wave effects [13].

The replication of the timeseries is most easily undertaken by calculating wavemaker drive signals in the frequency domain, so the composite numerical timeseries was Fourier transformed, and the resulting spectrum is shown in figure 6. The transfer function of the

wavemaker, the wave amplitude and phase of the travelling wave generated by a unit sinusoidal drive signal, is experimentally measured and is only valid if the waves are linear. As the waves are markedly non-linear at the position where the timeseries was to be replicated, an iterative scheme was attempted for the generation of the required record.

The initial wavemaker drive spectrum was calculated from the linear transfer function and tried in the tank. The frequency limits for this spectrum are somewhat arbitrary as it is always likely that some spurious components will be generated outside the chosen bounds, and it was found that the form of the breaker was quite sensitive to the top frequency limit. The wavegauge was sampled as the wavegroup passed and the effect of the anti-aliasing filter in the sampling system removed computationally. The later portion of the wave record, after the breaking, contains reflections and spurious high frequencies from the wavemaker's final large motion which are difficult to disentangle in a non-linear wavefield. Therefore, the experimental wave record was patched with the linearly expected timeseries used to extend the numerical record. One advantage of this scheme is that the same operations are done to both numerical and experimental wave timeseries before Fourier Transformation. In the frequency domain the required and obtained spectra were compared. If the match was judged inadequate, then each component in the drive spectrum was modified in both amplitude and phase by multiplication by the complex quantity $R(\omega)$ given by

$$R(\omega) = \sqrt{\frac{A(\omega)_{required}}{A(\omega)_{obtained}}} \tag{5}$$

This modifier has the effect of stepping halfway to that required in both amplitude and phase and was used because the simple ratio was found to overshoot.

Iterations were continued until the obtained spectrum was judged to match that required sufficiently closely. In the iterations the lower frequencies were found to converge first, which is expected because the higher frequencies are partially composed of their harmonics. The final spectrum in shown in figure 6 and associated timeseries in figure 8, while the spectra obtain during the six steps of the iterative process are plotted in figure 7.

4.3 BREAKING WAVE EXPERIMENTS

Having established a wavemaker drive signal which would replicate the numerical wave at one position the wave was generated in the flume and photographs of the internal kinematics taken at number of phases of the wave through breaking. Because the camera took a couple of seconds to wind on, the different phases were recorded by allowing the tank to settle, then repeating the wavefield and triggering the camera at the appropriate time.

The photographs were taken at a series of times from the start of the wavefield incremented by 1/40 s on each occasion. The time that the camera takes to open its shutter having been triggered was measured to be 74 ms. Because the real time control of the tank is based around a 160 Hz interrupt rate this was rounded to 75 ms and subtracted from the required measurement time to give the trigger time.

Repeatability of the wavefield is illustrated in figure 9 and the experimentally measured profile of the wave as it approaches breaking in figure 10.

4.4 PIV PHOTOGRAPHY

The region of interest beneath the waves is illuminated by a sheet of light and photographed from the side. In order that the PIV photograph represents a sufficiently instantaneous record of the flow within the wave the shutter time of the recording camera and the time duration between illuminating pulses must be as short as possible. This also imposes the

requirement that the pulse time be very short. Lourenco [14] quotes a minimum pulse separation to pulse time ratio of 20, and although in practice smaller ratios than this can be used, generally the larger the ratio the better the quality of the flow records. The measurements described in this paper were made using a CW laser as greater control is afforded over pulse separation than with conventional pulsed lasers, permitting this same light source to be used for PIV measurements on a variety of other flows [15] [16]. However, for a sheet illumination system that is pulsed by mechanical or electrooptical means there will be a severe constraint upon the light power in each pulse if the pulse time is very short. In the Edinburgh system this difficulty is avoided by employing a *Scanning Beam* system of flow illumination whereby the beam from the laser is narrowed to approximately 1.5 mm using a telescope arrangement, and then reflected off a multi-faced rotating mirror and a parabolic recollimating dish to scan through the area of interest [17]. This manner of illumination ensures that the light power from the laser entering the flow is maximised and that a very short but intense pulse of light is imparted to the tracer particles within the flow. In our current system each illuminating pulse is approximately 200 times shorter than the time between pulses, which for a pulse separation of 1 ms gives a pulse time of 5 μs ensuring that streaking of the particle images is negligible; this avoids the associated problems of streaked photographs [15].

The water within the wave tank was seeded with Conifer Pollen which has an average diameter of 70 μm. These particles are used because, when wet, their density is very close to that of water ensuring that within the timescale of an experiment there is no noticeable settling of the tracers as may be experienced with more traditional seeding materials such as Aluminium powder. This is important as any settling time will result in an inadequate density of tracers in the upper measurement region of a passing wave, eventually resulting in signal dropout where a good record of the flow is particularly important. The closeness of the seeding density to that of the water also ensures that the tracer particles faithfully follow the flow even under high flow accelerations.

Seeding concentrations are maintained at a level that will ensure a high density of non-overlapping particles on the film record. This is important so that within the small region in which a point measurement of the particle separation is calculated there are three or more particle pairs allowing unambiguous determination of the flow direction and magnitude. For a light sheet of thickness 1.5 mm, an image / object magnification of 0.102, and a circular probe diameter of 0.75 mm, a minimum seeding density of 2×10^7 is required.

In order to record the whole crest region of the breaking wave in a single exposure it is necessary to have a large illuminated measurement region. Consequently, a large film format is required so that the image / object magnification is maximised to allow good resolution of the velocity measurements from the final flow record. A Hasselblad ELM camera body with a 120 film back was used giving 28.25 cm^2 of exposable film for each flow photograph. The illuminated tracer particles are imaged onto the film plane by a planar T 80 mm focal length f2.8 lens system. The high quality of the lens ensures that the imaged particles are not excessively enlarged over the diffraction limit of the lens by optical abberrations.

Sinha [18], points out that the refraction of a water/glass/air boundary will lead to distortion of the image plane when photographing a planar region within a glass tank of fluid with a different refactive index to air. This effect is more pronounced the greater the angle of incidence of light from the optical axis of the imaging optics. In order to account for such distortions, which would lead to significant positional errors on analysis of the flow record, a grid scribed on perspex was photographed in the same position as the illuminated region of the flow. Precise measurement of the positions of the intersection points of the grid on the developed film were made using a travelling microscope with the film positioned on a light table. Relating these measurements back to the known dimensions of the perspex grid gave a map of the geometric distortion due to refactive index differences, the limited

of the two-dimensional transform is time-consuming the scheme is adopted because of its ability to successfully process extremely noisy fringes.

Digitisation of the fringes is achieved using a Panasonic CCD camera. The digitised intensity pattern is transferred to the computer's hard disc until all the fringe data from the film is saved. This allows the CCD camera and the probe laser (2mW HeNe) to be switched off while the more time-consuming fringe analysis is being performed, prolonging the life of the camera and preserving the fringe data for visual inspection should a particular point measurement fail. The two-dimensional Fourier transform is calculated by performing a Fast Hartley transform [23] on the rows and then on the columns of the digitised data. This gives a significant reduction in the computation time over a Fast Fourier Transform as the data has no imaginary part on starting the calculation. Subtraction of the fringe pedestal prior to transformation zeroes the d.c. component and significantly aids the resolution of low fringe frequencies [24]. Location of the discrete signal peak is then a simple search for maximum data point in the transform plane. The peak is the sum of a number of peaks associated with the individual particle pairs. The average position of these contributory peaks is found by calculating the centre of mass of the data in the vicinity of the maximum. The position k_x, k_y calculated in this way gives the spatial frequency components in the horizontal and vertical directions which when multiplied by a calibration value and divided by the illumination interval gives the horizontal and vertical components of velocity. The visibility of the fringes is also calculated from the height of the signal over the area under the fringe intensity data, allowing an estimate of the measured velocity's reliability.

Figure 12 illustrates the fringe aquisition apparatus, which analyses photographic negatives under computer control.

Within each set of data generated from a flow photograph there is a subset of measurement points which are not consistent-with those velocity values about them. Their orientation and/or magnitude may differ significantly from neighbouring values because their fringe frequency values are anomalous and generated by detection of a peak other than the peak due to the separated particle images. The reasons for such failures are noted above and occur more frequently the poorer the quality of the fringes. The success rate quoted above from Huntley [22] is consistent with measurements made with the system described but a significant fraction of fringes measured from wave records have visibilities well below 7%. By considering the measured fringe visibility and the fringe frequency and orientation it is possible to identify most of the spurious vectors. These values are removed and in places where sufficient numbers of valid neighbours exist an interpolated value substituted.

5 Results and Conclusions

Figure 11 contains an overlay of experimentally measured and numerically generated surface profiles, at equivalent phases, as the wave approaches breaking. While the overall match of position and size is good, the detail around the plunging tip is not. It was found, during the replication of the numerical wave, that the exact form of the breaking wave was very sensitive to changes in the generated wave spectrum, so that the discrepancies in figure 11 could be explained by a 1% error in the wavegauge calibration. In future experiments the sensitivity to small changes will be explored and the drive signal to the wavemaker modified until a good match of surface profiles is acheived at the plunging phase.

Despite the inexact match of the surface profiles the photographic records of the internal velocities were analysed and a typical example is plotted in figure 13. For comparison numerically generated internal velocities for an earlier phase of the wave, with a similar surface profile, are plotted in figure 14.

6 Acknowledgement

The authors gratefully acknowledge the funding provided by the Marine Technology Directorate U.K. for this project. They also wish to thank Prof. D.H. Peregrine et al of the Mathematics Dept., Bristol University who developed the time-stepping computer program and allowed the authors to run this at Edinburgh.

References

[1] Longuet-Higgins, M.S. and Cokelet, E.D. (1976) *The Deformation of Steep Surface Waves in Water. A Numerical Method of Computation.* Proc. Royal Soc. London, A. 350, 1-26.

[2] Dold, J.W. and Peregrine, D. P. (1986) *Numerical Methods for Fluid Dynamics II.* Authors Morton, K.W. and Baines, M.J. Oxford University Press, 671-679.

[3] Dommermuth, D.G., Yue, D.K.P., Lin, W.M., Rapp, R.J., Chan, E.S. and Melville, W.K. (1988) *Deep-water Plunging breakers: a comparison between potential theory and experiments.* J. Fluid Mech., 189, 423-442.

[4] Van Dorn, W.G. and Pazan, S.E. (1975) *Laboratory Investigation of Wave Breaking, Part 2, Deep Water Waves.* Research Report, Advanced Ocean Engineering Laboratory, Scripps Institute of Oceanography, University of California, San Diego, S10 Ref. No. 75-21, AOFL Report £71.

[5] Kjeldsen, S.P., Vinge R. and Brevig, P. (1980) *Kinematics of Deep Water Breaking Waves.* Proc. 12th Annual Offshore Technology Conference, Texas, 317-325.

[6] Easson, W.J. and Greated, C.A. (1984) *Breaking Wave Forces and Velocity Fields.* Coastal Engineering, 8, 233-241.

[7] Easson, W.J. (1987) *Velocity and Force Measurement in the Splash Zone.* J. of Strain, Feb, 15-18.

[8] Gray, C. Greated, C.A. and Fancy, N.A. (1987) *The Application of PIV to Measurements Under Waves.* 2nd Int. Conf. on Laser Anemometry, Strathclyde.

[9] Gray, C. and Greated, C.A. (1988) *The Application of PIV to the Study of Water Waves.* Optic and Lasers in Engineering, 9.

[10] Salter S.H. (1982) *Absorbing Wave Makers and Wide Tanks.* Proc. Conf. Directional Wave Spectra Applications, ASCE, 185-200.

[11] Kjeldsen, S.P. (1982) *2 and 3 Dimensional Deterministic Freak Waves.* Norwegian Hydrodynamic Laboratories Report, 1983.

[12] Greenhow, M., Vinje, T., Brevig, P. and Tanylor, J. *A theoretical and experimental study of the capsize of Salter's Duck in extreme waves.* J. Fluid Mech., 118, 221-239.

[13] Hyun, J.S. (1976) *Theory for Hinged Wavemakers of Finite Draft in Water of Constant Depth.*

[14] Lourenco, L. (1986) *Theory and Application of Particle Image Displacement Velocimetry.* in Lecture Series 1986-09, Von Karman Inst. of Fluid Dynamics, Brussels.

[15] Sharpe, J.P., Gray, C., Greated, C.A. and Campbell, M. (1989) *Measurements of Acoustic Streaming using PIV.* Acoustica.

[16] McCluskey, D.R., Easson, W.J., Greated, C.A. and Glass D. (1989) *Use of Particle Image Velocimetry to Study Roping in Pneumatic Conveyence.* 4th European Symposium in Particle Characterisation, Nuremberg, W.Germany.

[17] Gray, C. and Greated, C.A. (1988) *A Scanning Beam System for the Two Dimensional Illumination of Flow Fields.* Von Karman Inst. of Fluid Dynamics, Belgium.

[18] Sinha, S.K. (1988) *Improving the Accuracy and Resolution of Particle Image or Laser Speckle Velocimetry.* Experiments in Fluids, 6, 67-68.

[19] Burch, J.M. and Tokarski, J.M.J. (1968) *Production of Multiple Beam Fringes from Photographic Scatters.* Optica Acta, Vol 15, No. 2, 101-11.

[20] Robinson, D.W. (1983) *Automatic Fringe Analysis with a Computer Image Processing System.* Applied Optics, 22, 2169-2176.

[21] Moraitis, C.S., Buchlin, J.M. and Reithmuller, M.L. (1987) *Improved Autocorrelation Analysis of Fringe Images for Laser Speckle Velocimetry.* ICIASF June 22-25, 1987.

[22] Huntley, J.M. (1986) *An Image Processing System for the Analysis of Speckle Photographs.* J. Physics. E. Sci. Intrum., 19.

[23] Bracewell, R. N. (1986) *The Fourier Transform and its Applications.* McGraw-Hill.

[24] Pickering, C.J.D. and Halliwell, N.A. (1985) *Particle Image Velocimetry: Fringe Visibility and Pedestal Removal.* Applied Optics, Vol 24, No. 6, 2474-2476.

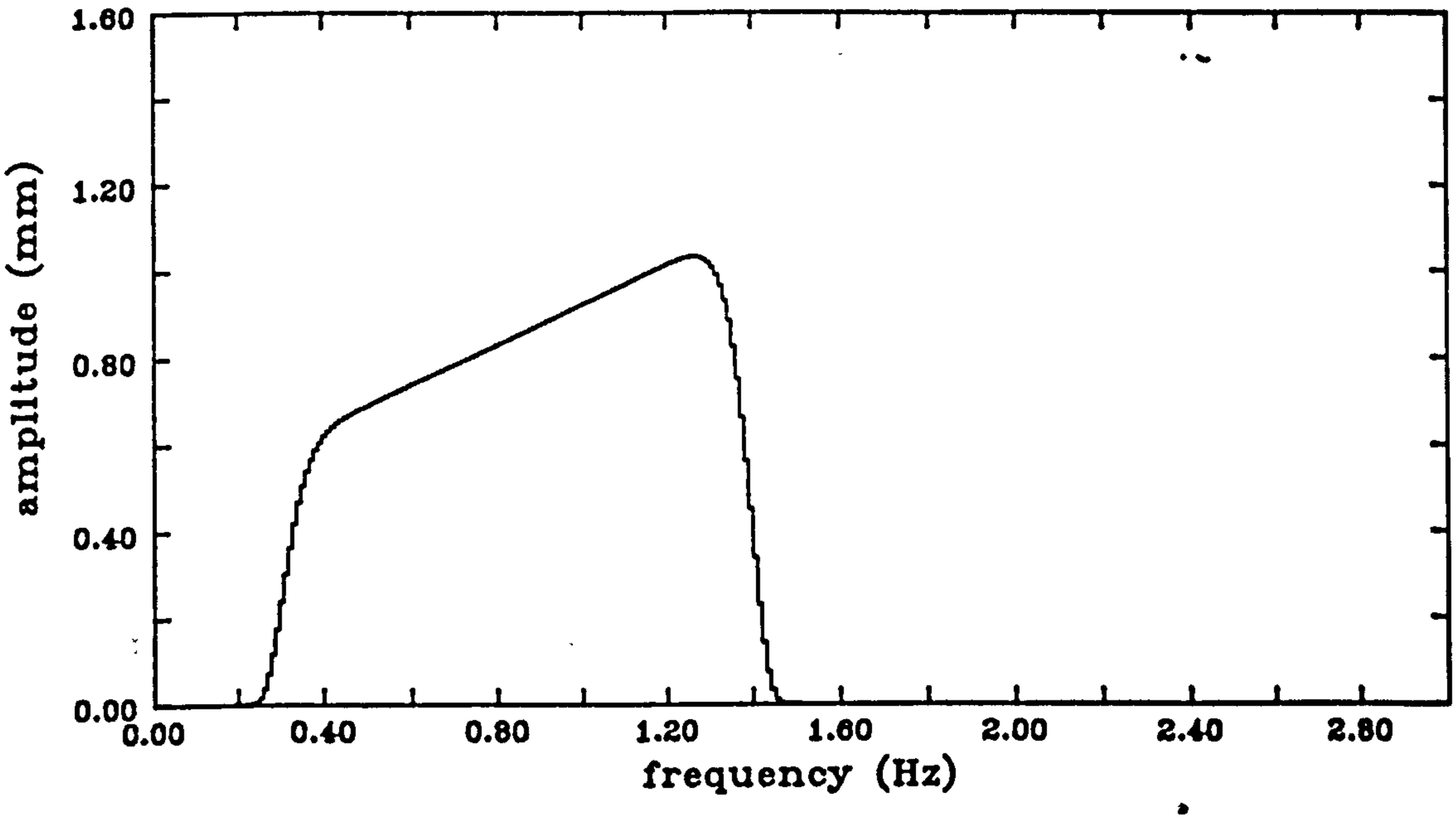

Figure 1: Wave amplitude spectrum found to produce a suitable numerical breaker.

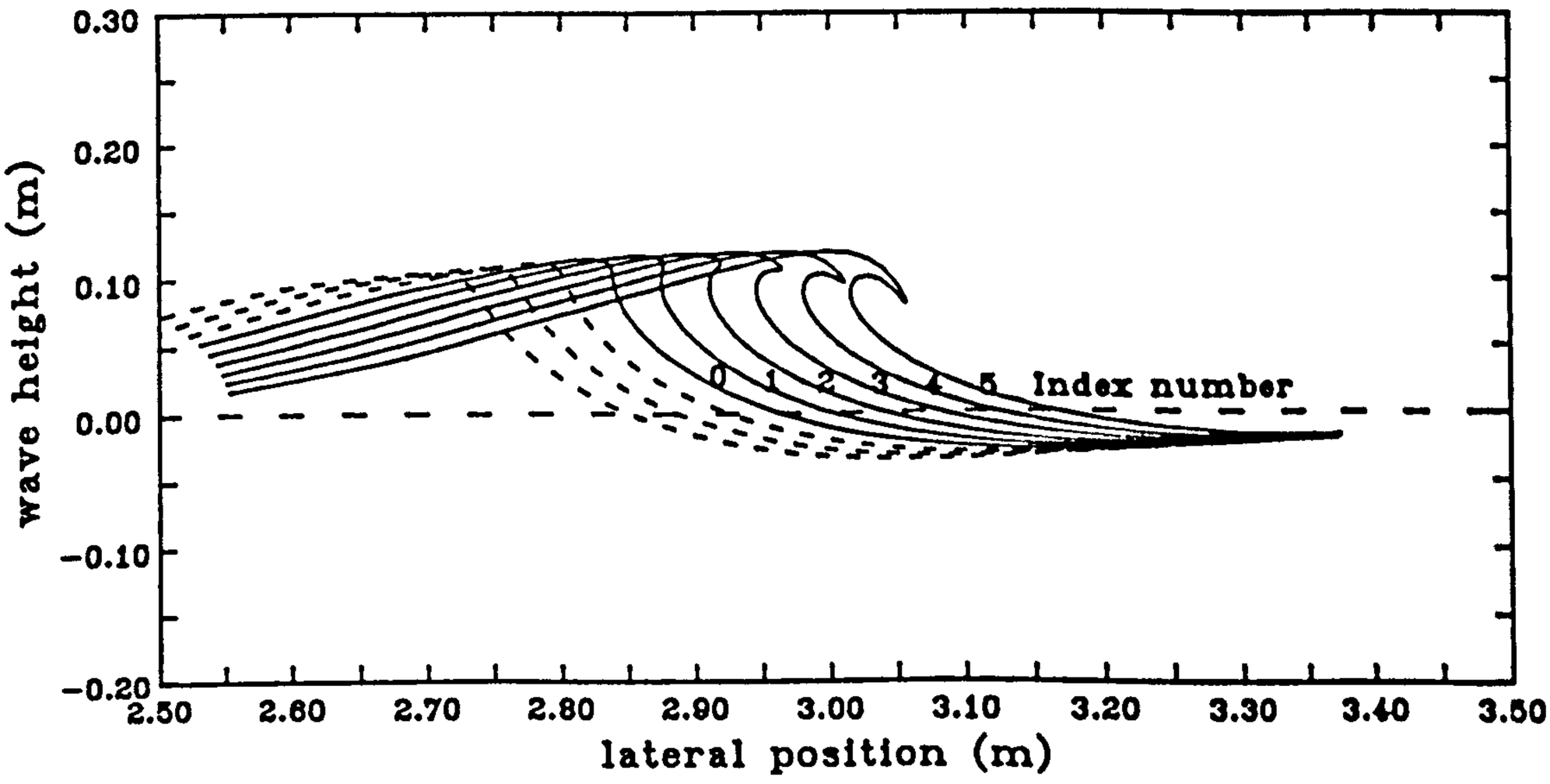

Figure 2: Numerical profile as wave approaches breaking.

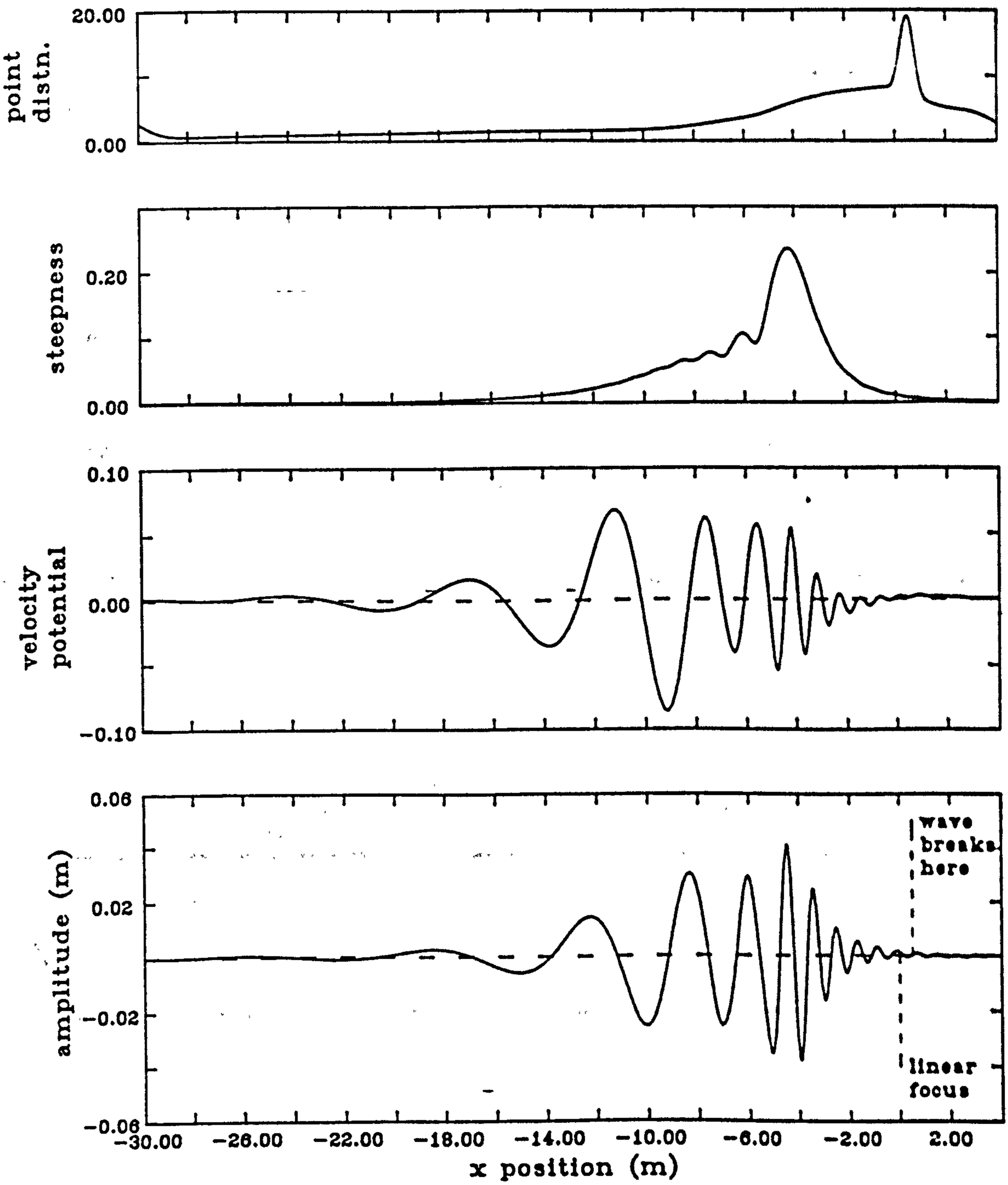

Figure 3: Starting profile and velocity potential calculated by linear theory 6 seconds before expected linear focus.

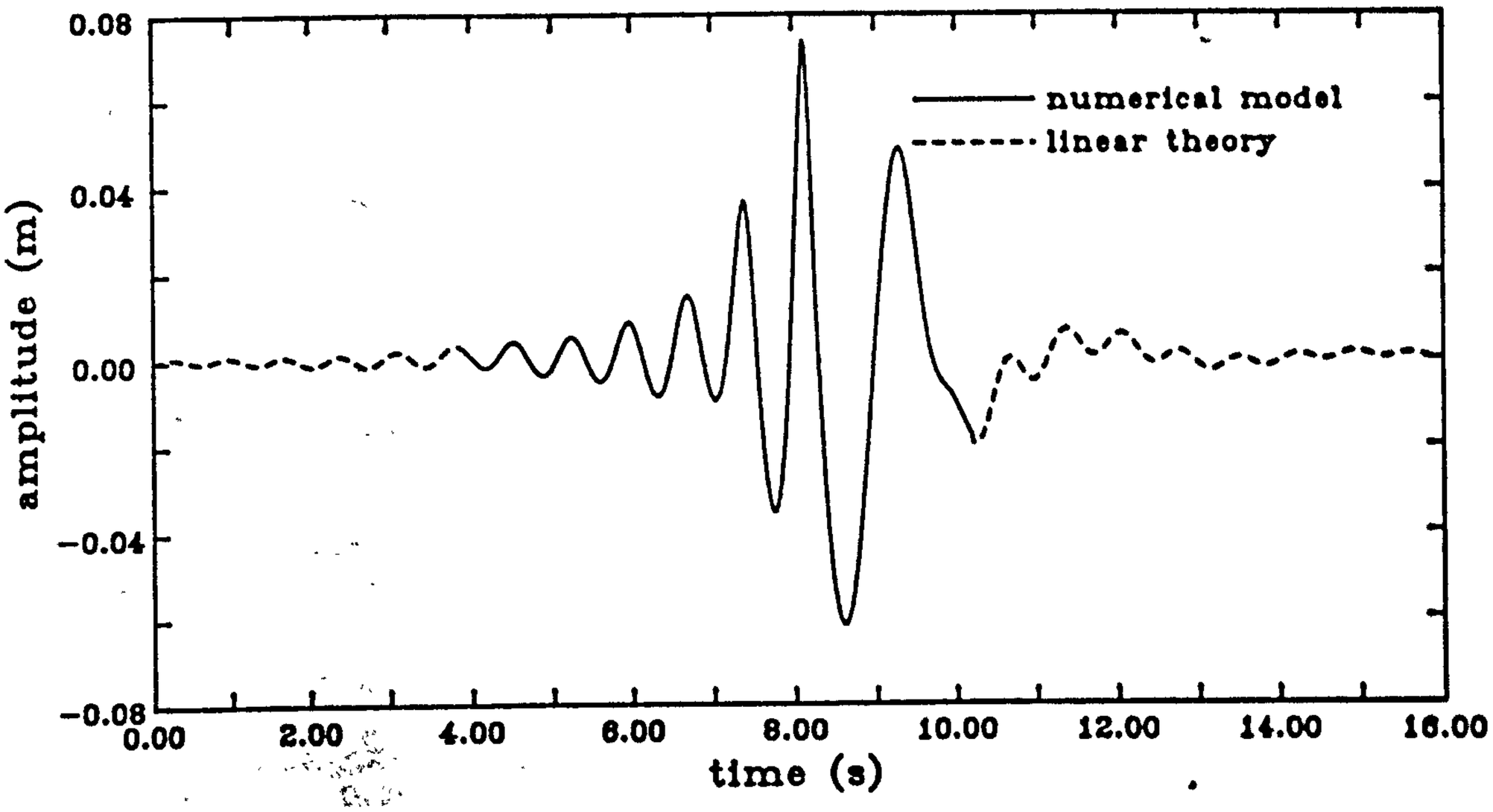

Figure 4: Composite wave amplitude timeseries from the numerical model and linear theory.

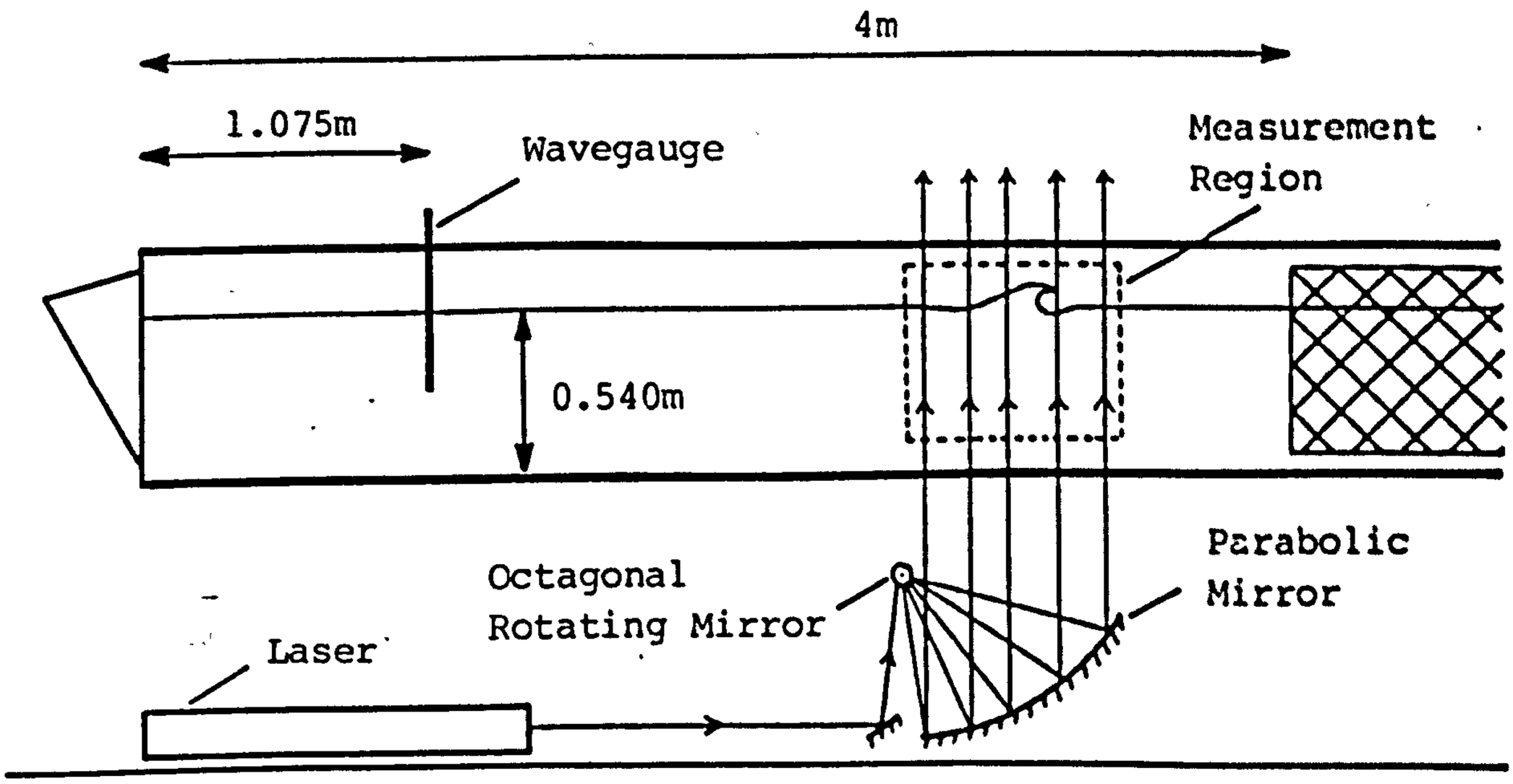

Figure 5: Wave flume used for the PIV analysis of breaking waves.

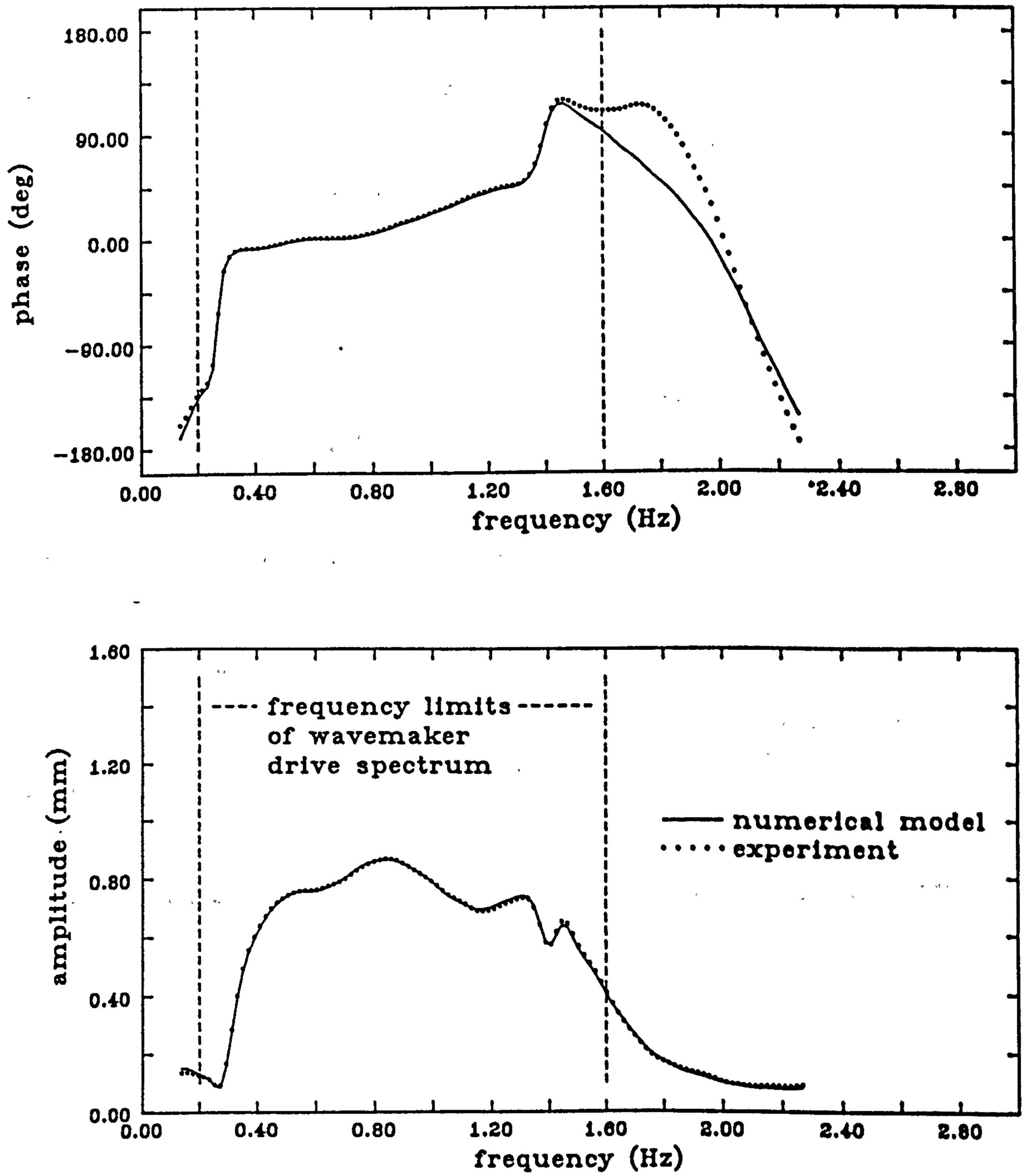

Figure 6: Experimental wave spectrum found by iteration compared to required spectrum.

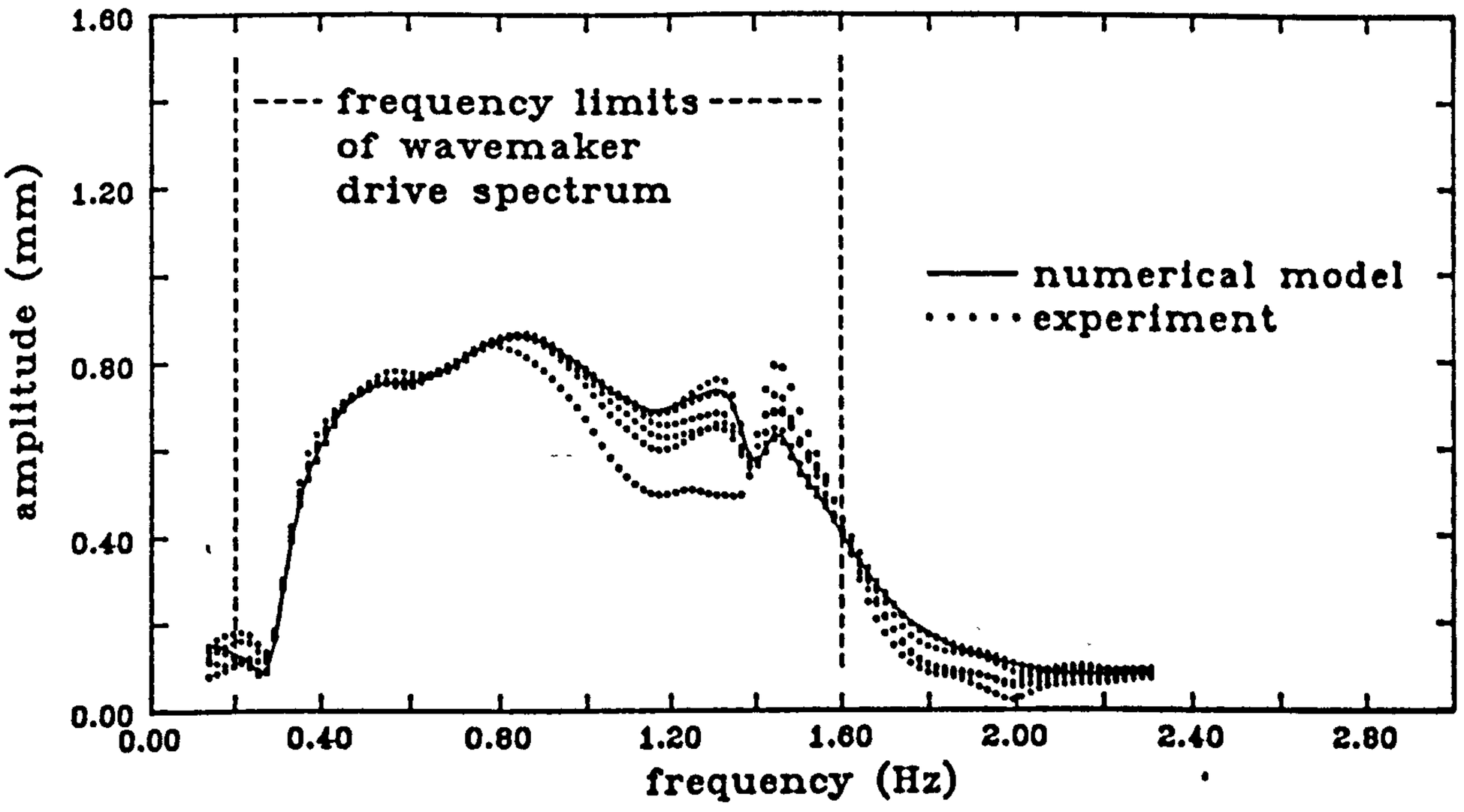

Figure 7: Experimental iterations towards the required wave amplitude spectrum.

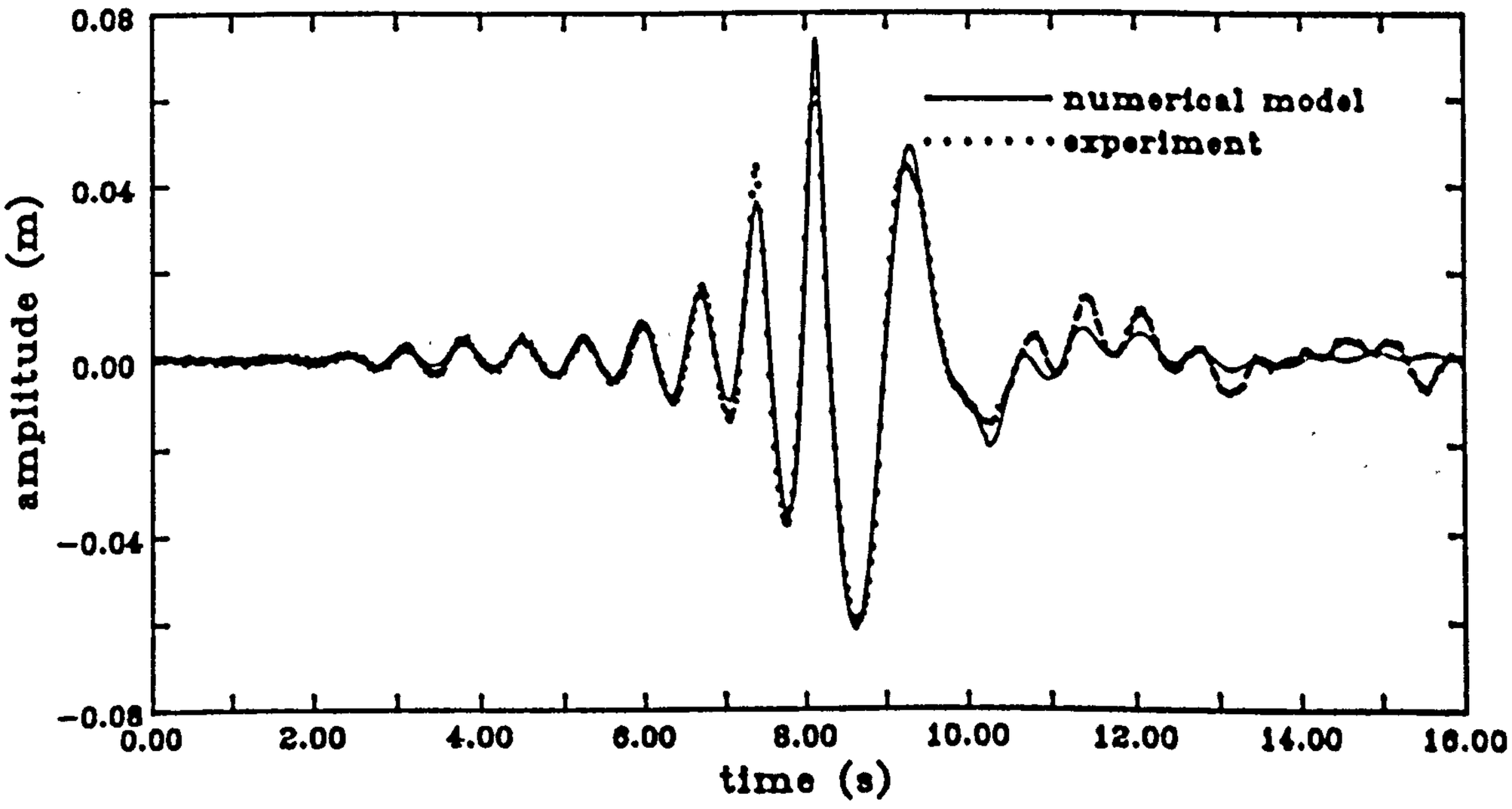

Figure 8: Experimentally achieved wave amplitude timeseries compared to the timeseries generated by the numerical model.

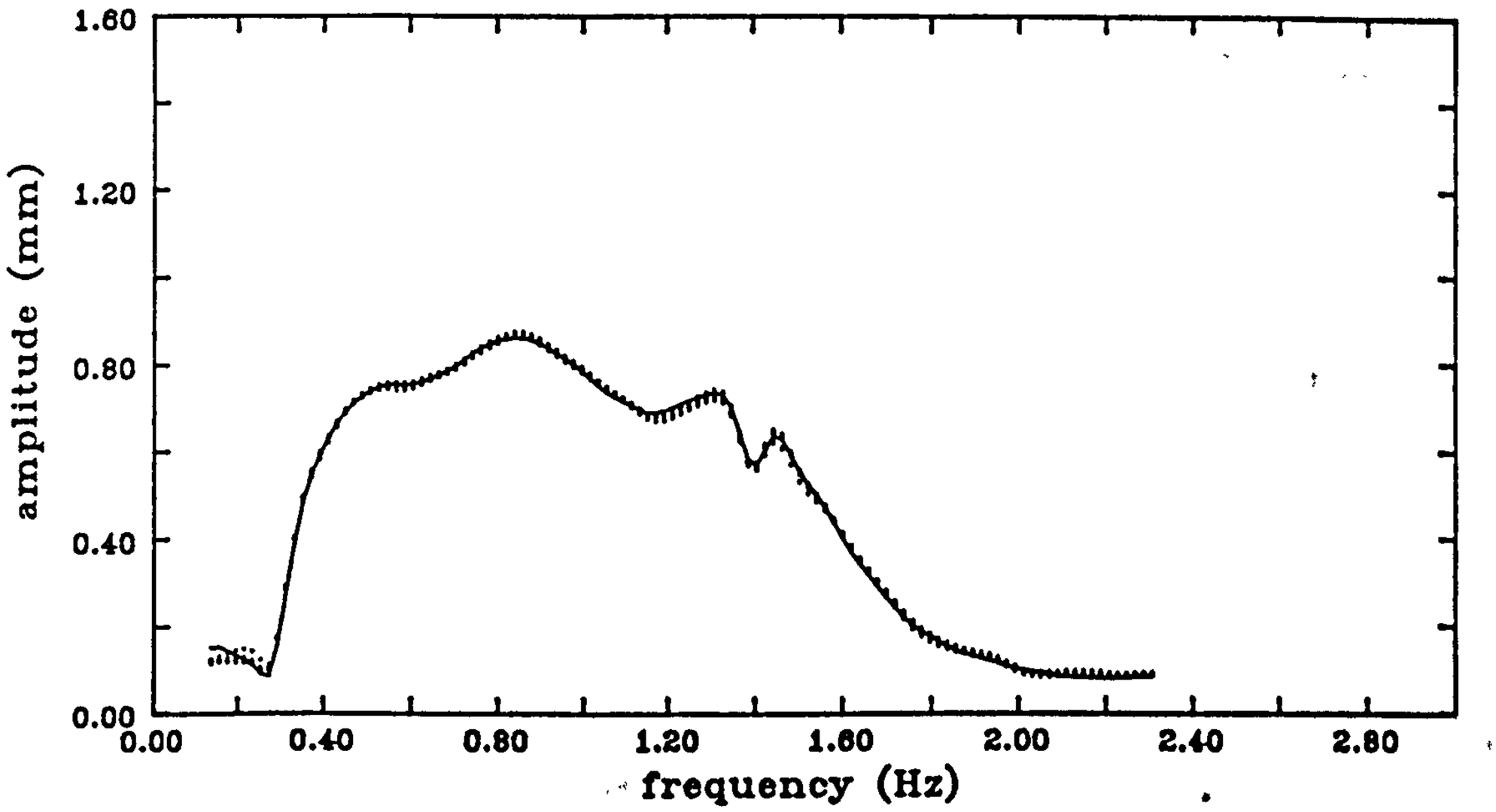

Figure 9: Repeatability of the experimentally measured wave spectrum.

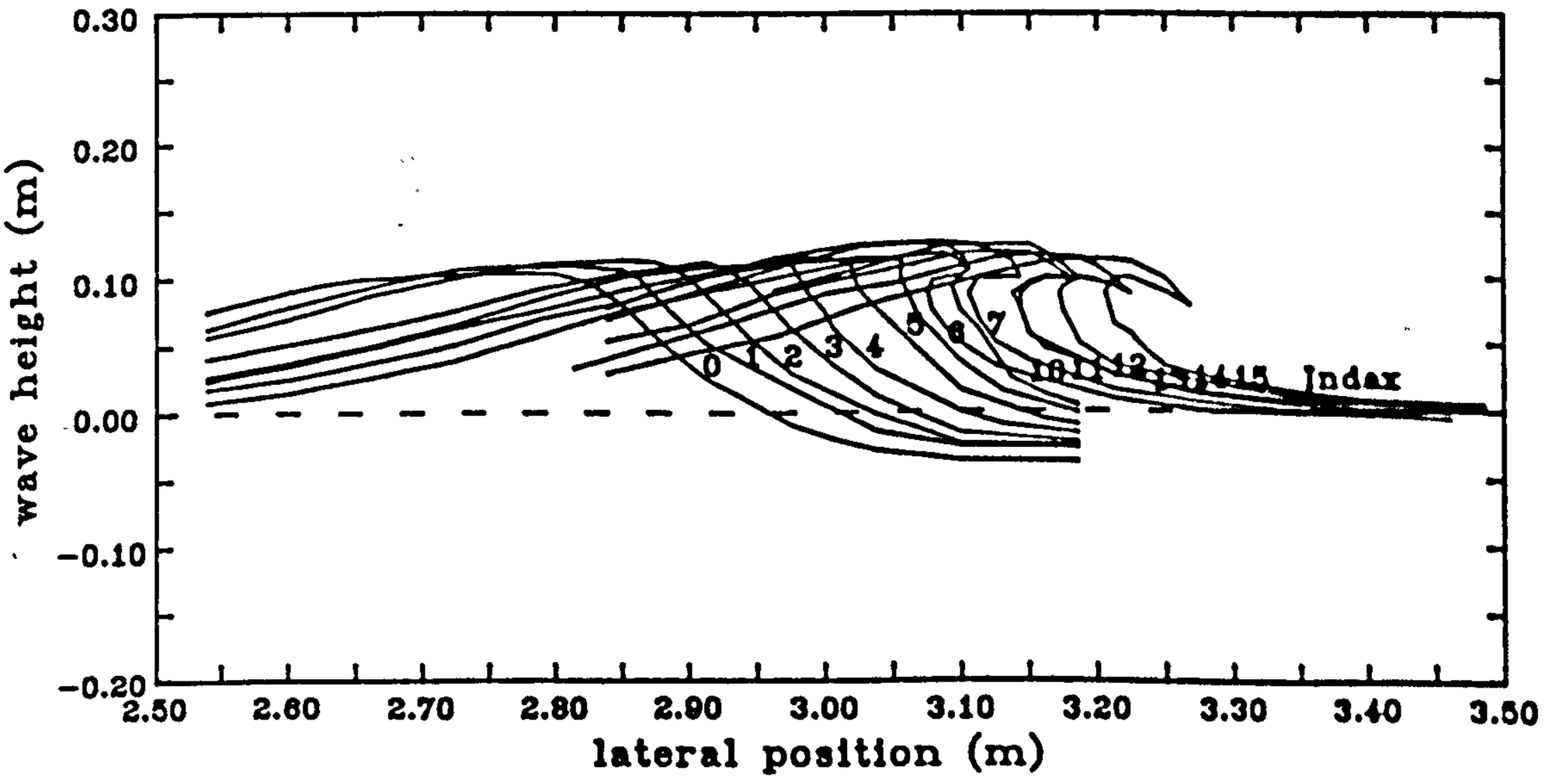

Figure 10: Experimentally measured profile of the wave approaching breaking.

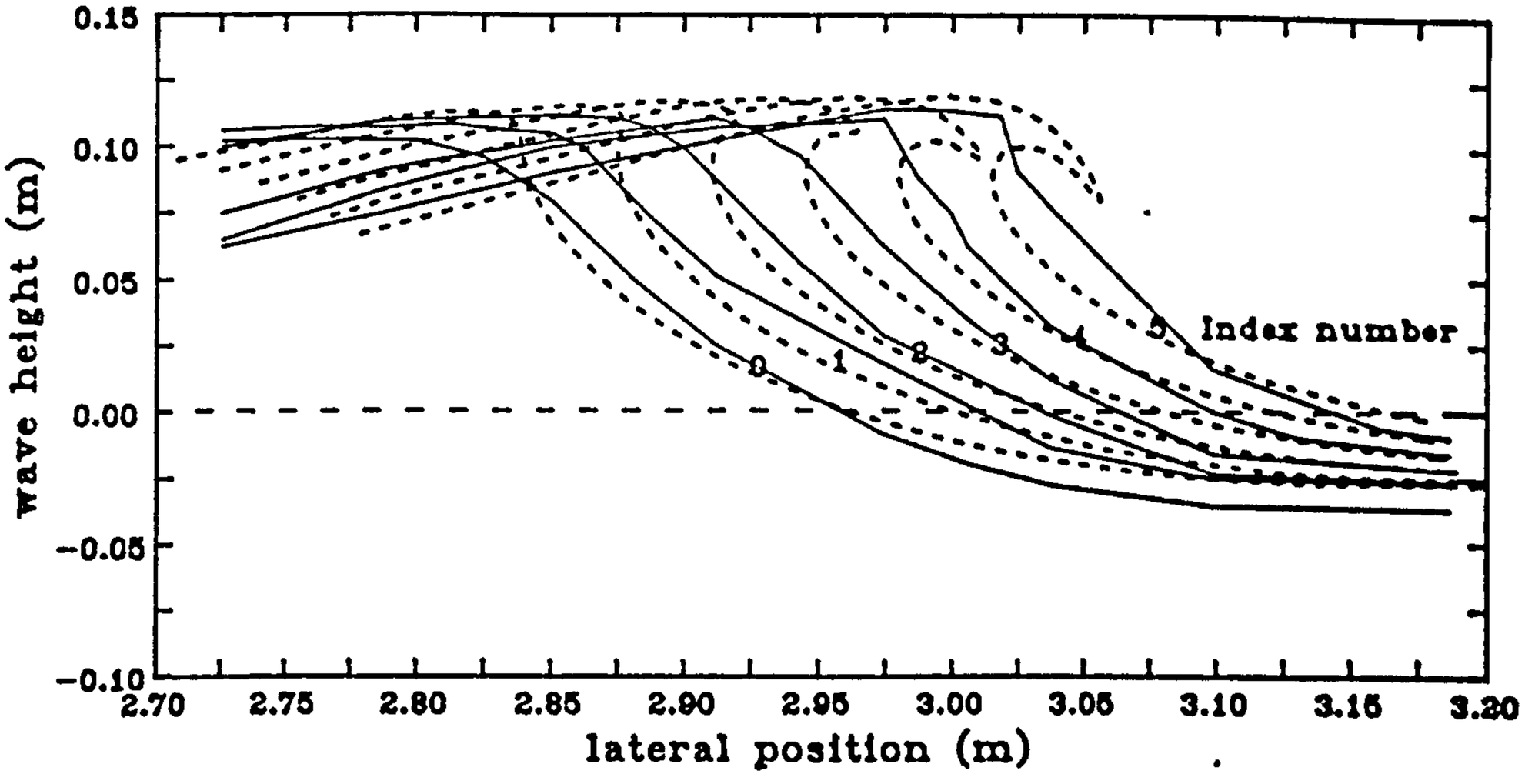

Figure 11: Overlay of numerical and experimental wave profiles.

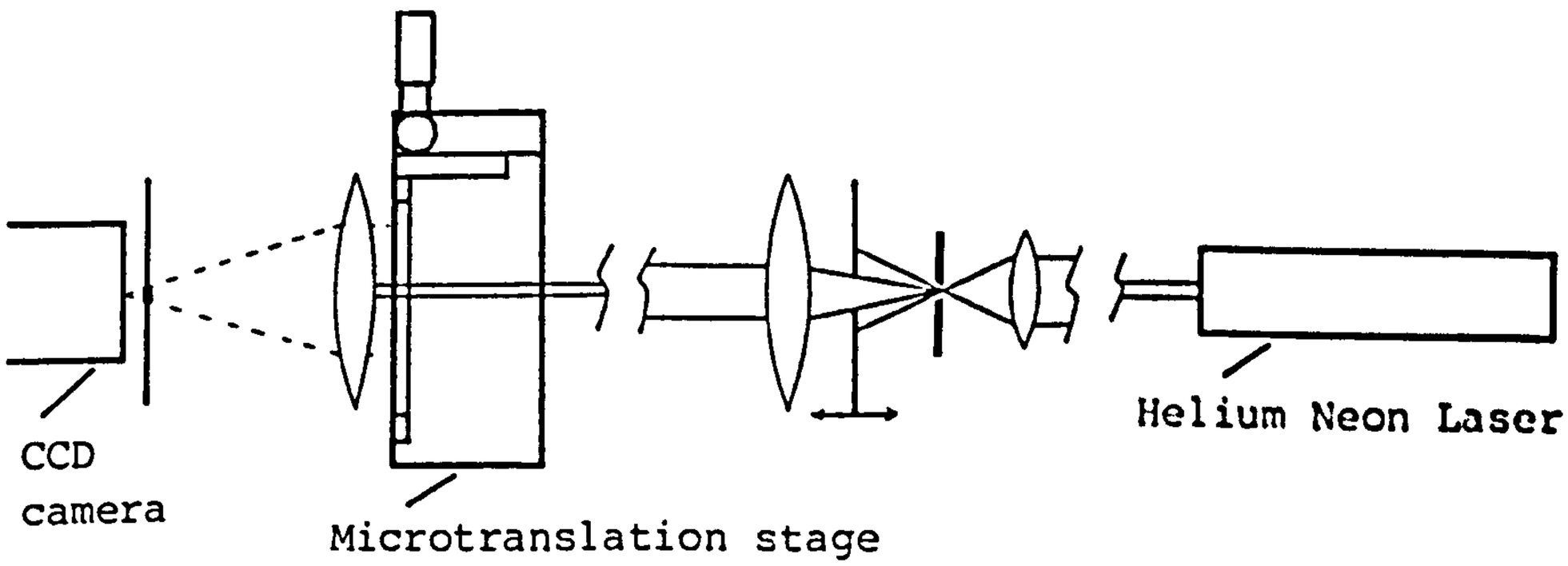

Figure 12: Generation of the speckle displacement fringes and digisation in the Fourier plane of the lens.

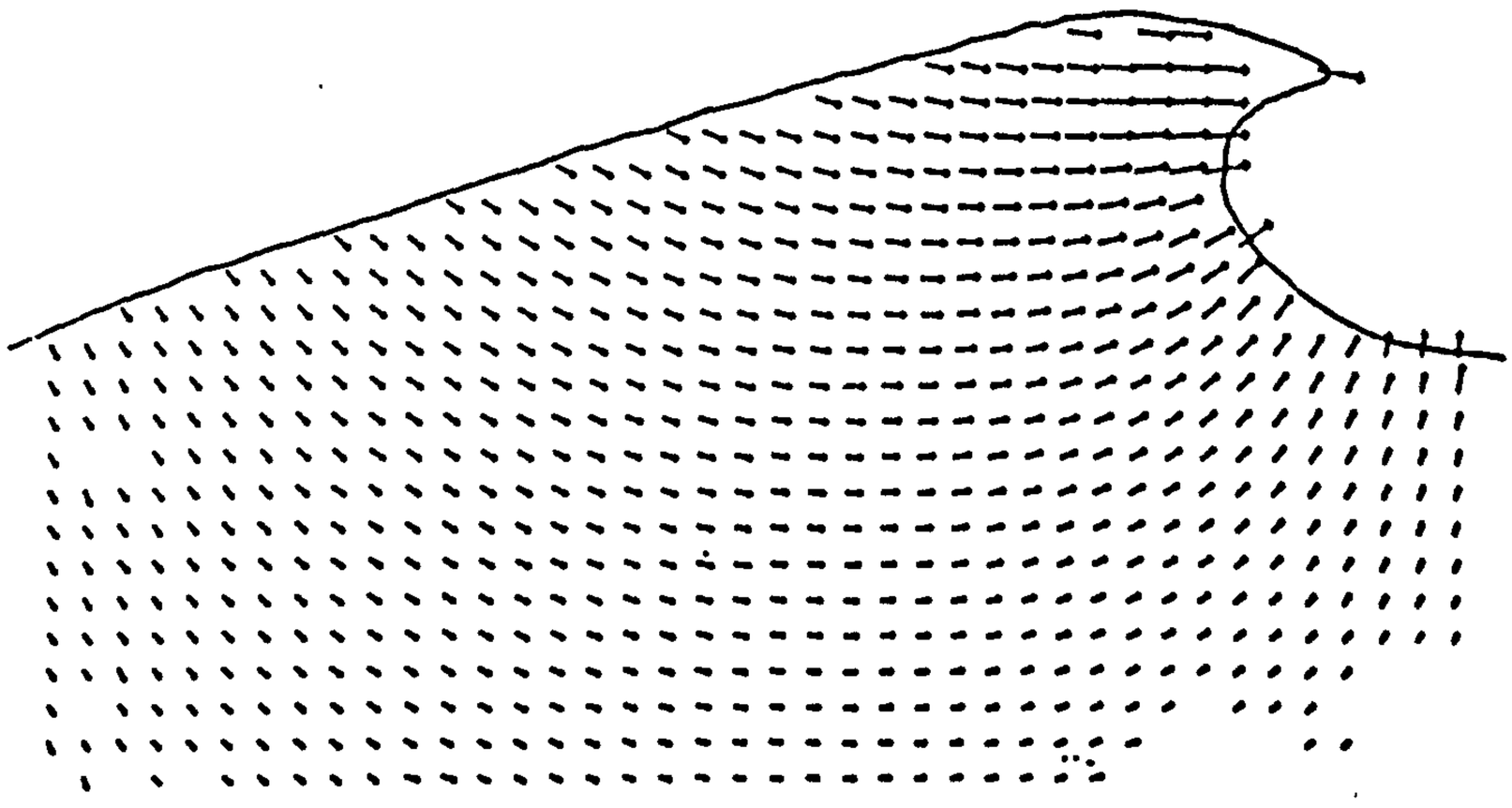

Figure 13: Velocity field measured experimentally by PIV.

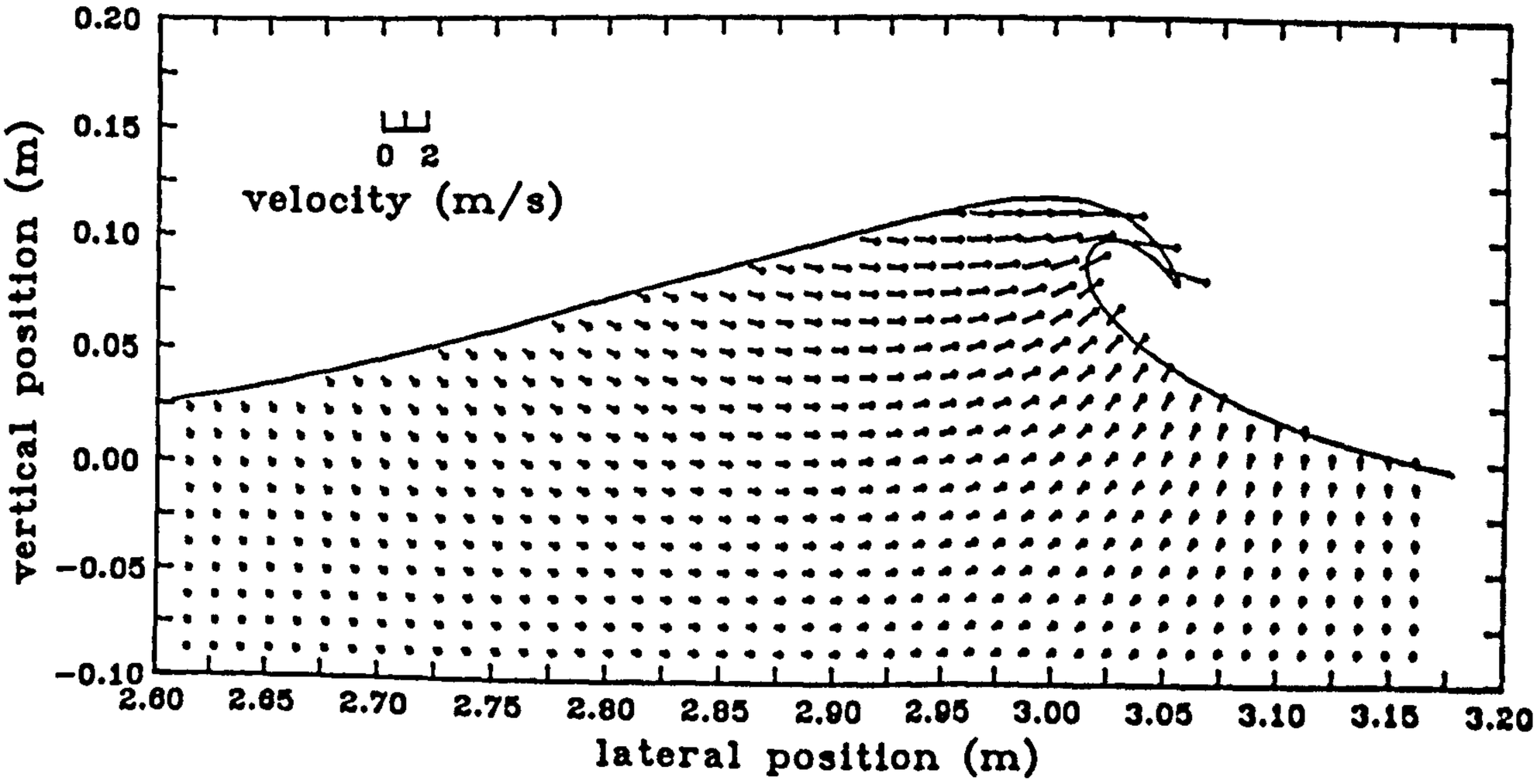

Figure 14: Numerically generated velocity field for an *earlier phase* of the wave.

Sonderdruck aus / Reprint from

ACUSTICA

JOURNAL
INTERNATIONAL
D' ACOUSTIQUE
sous le patronage du
Groupement des Acousticiens
de Langue Française

INTERNATIONAL
JOURNAL
ON ACOUSTICS
recognized by the Institute
of Acoustics of Great Britain

INTERNATIONALE
AKUSTISCHE
ZEITSCHRIFT
unter Mitwirkung
der Deutschen
Physikalischen Gesellschaft

S. HIRZEL VERLAG · STUTTGART

ACUSTICA
Vol. 68 (1989)

Although the chopper (Scitec Model 300 CD) came with its own electronic display to indicate the frequency of rotation, this was found to be unreliable at the low chopping speeds used. Consequently a photodiode and storage oscilloscope were employed to give a more precise frequency reading.

The camera used was a 35 mm Nikon with a 50 mm flat focus lens at a magnification of 0.773. This type of lens was found to be essential if one wanted to avoid distortion of the image in the off axis region. The film used was Kodak T-Max 400 which provided good sensitivity (400 ASA) and adequate resolution ($\sim$ 100 lines/mm depending on contrast). During actual experimental runs the laboratory was always illuminated with extremely subdued light and the photograph taken against a black background to increase contrast.

The amount of distortion in the image plane due to the curvature of the glass tube was estimated by putting a piece of graph paper in the tube, photographing it, and examining the developed film with a travelling microscope. A negligible amount of distortion was found except at approximately 1 mm or so from the tube wall. Since the amount of flare from the wall tended to make any measurement in this region impossible, it was not necessary to calculate correction factors for this effect.

5. Measurements and results

The apparatus was set up as indicated in Fig. 4. Sound of frequency 2460 Hz was introduced into the tube (length 450 mm, internal diameter 23.3 mm) using a horn loudspeaker with the horn removed. The tube was sealed at the other end with a rubber bung which had a tightly fitting metal plate attached to its inside face to ensure a rigid termination. The sound field thus corresponded to the 7th normal mode of the air column. A probe microphone, (Bruel & Kjaer type 4166 with 2 mm i.d. probe attachment) inserted through the rigid end monitored the pressure. The probe microphone had previously been calibrated to within 0.5 dB using an acoustic coupler. Although the intensities required to produce streaming were near the limits of the microphone's range [12] they were still within the 10% distortion limit – leading to an extra possible error of around 1 dB. So, although the pressure measurements were not highly accurate they did provide a useful independent check on the streaming velocities.

Tobacco smoke was introduced into the tube to render the flow visible and streaming was set up, the field having a pressure at the rigid end of 151 dB (re 20 μPa). Because of the limited dynamic range of the P.I.V. technique (see section 3) the streaming velocity was first estimated by eye and the chopper then set to provide pulses with a separation of 0.114 second and duration 0.0057 second. It is necessary to have the ratio of pulse separation to duration as large as this because one only wants information about particle separations and, if the particle displacements and separations are of a similar order, they will give rise to similarly sized contributions in the spatial frequency domain, which will lead to a loss of velocity information. Such details of the technique are well discussed in [8]. The shutter, set to 0.5 second, allowed 4 pulses through.

Photographs were taken near a velocity node and a print of the film used to provide the measurements quoted here is shown in Fig. 5. The individual particle images can be clearly seen. In fact, measurements could not be made far from the velocity nodes because, at the frequencies and intensities used here, the vibrational displacement amplitudes became of the same order as the particle displacements required to give fringes. This is quite an important point and will be returned to and discussed at some length in section 6.

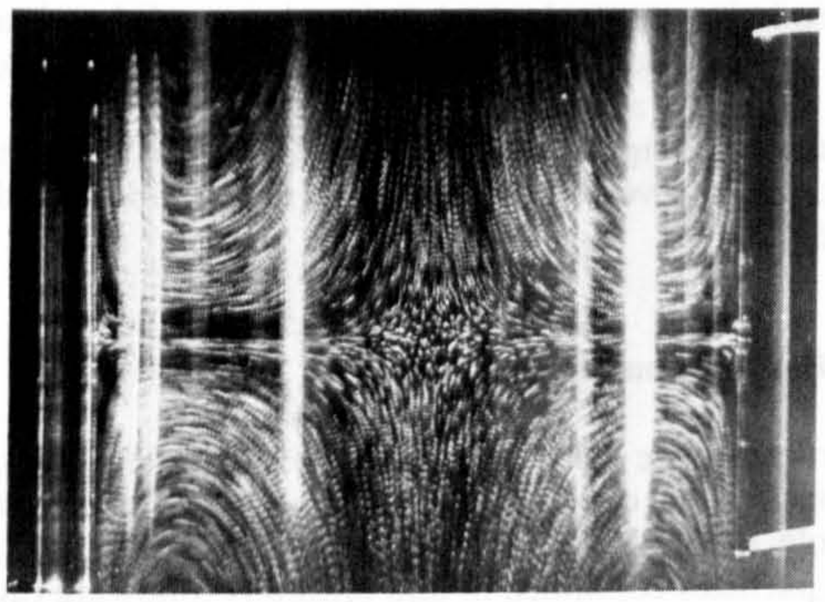

Fig. 5. Print of P.I.V. transparency used to provide measurements.

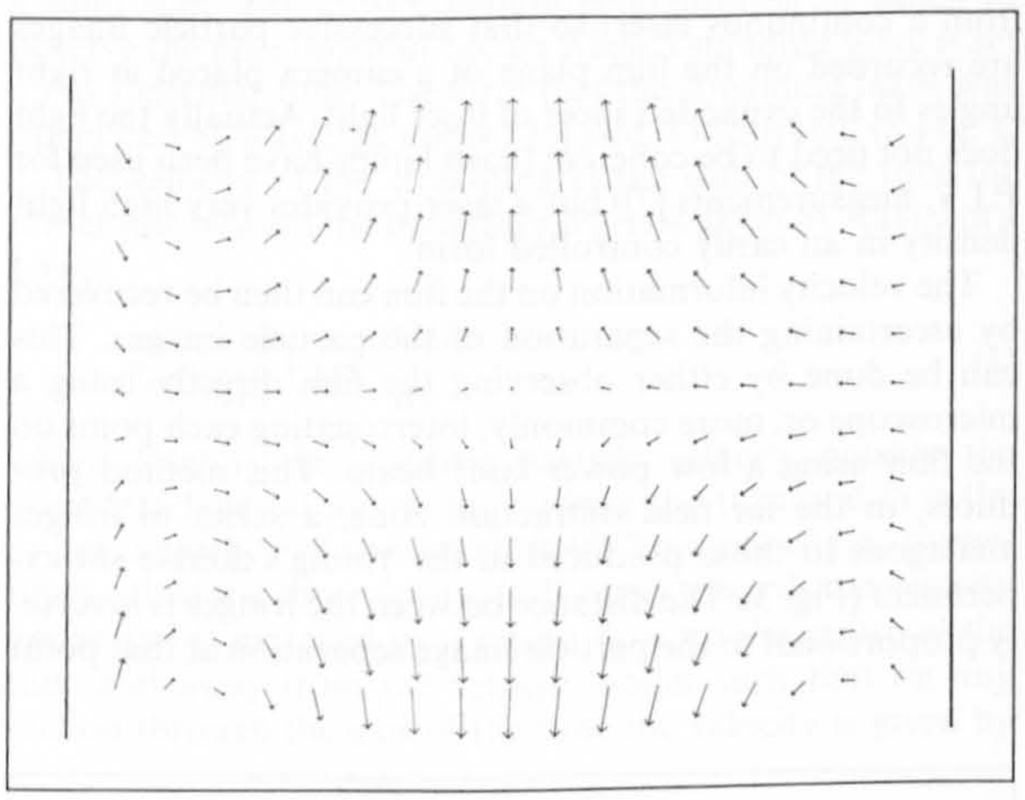

Fig. 6. Smoothed velocity map (1 cm = 4.37 mm/s).

The film was analysed in the fashion indicated in section 3. It is clear from Fig. 5 that not all areas of film yielded a velocity measurement, due either to flare from the tube walls or uneven seeding. The latter is a problem in all P.I.V. measurements and seems to be more difficult to overcome in air than in water. This may be due to the larger convective currents found in air, coupled with its lower viscosity.

The measurements were transferred to a computer which, after interpolating missing points and smoothing the velocities using a third order Chebyshev interpolation routine, drew a velocity map (see Fig. 6). As can be seen, the measurements look slightly asymmetric with the velocities in the upper left vortex seeming to sweep over too much to the right. This was probably due to outside air currents.

As a check on the accuracy of the measurements it is noticed from eq. (2) that the axial velocity should be parabolic across any section of the tube with maximum velocity given by eq. (1) and zeroes at distances $r = 0.707\,a$ from the axis of the tube. Axial velocities were therefore computed from the original unsmoothed data for three separate lines across the tube (Fig. 7). The solid parabolae were fitted using the measured velocity maxima and the theoretical zero points. The fits are quite good though the velocities do show some deviation near the left crossover point, reflecting the assymmetry mentioned earlier. A calculation using (3) and a value of 151 dB for the maximum pressure indicates a maxi-

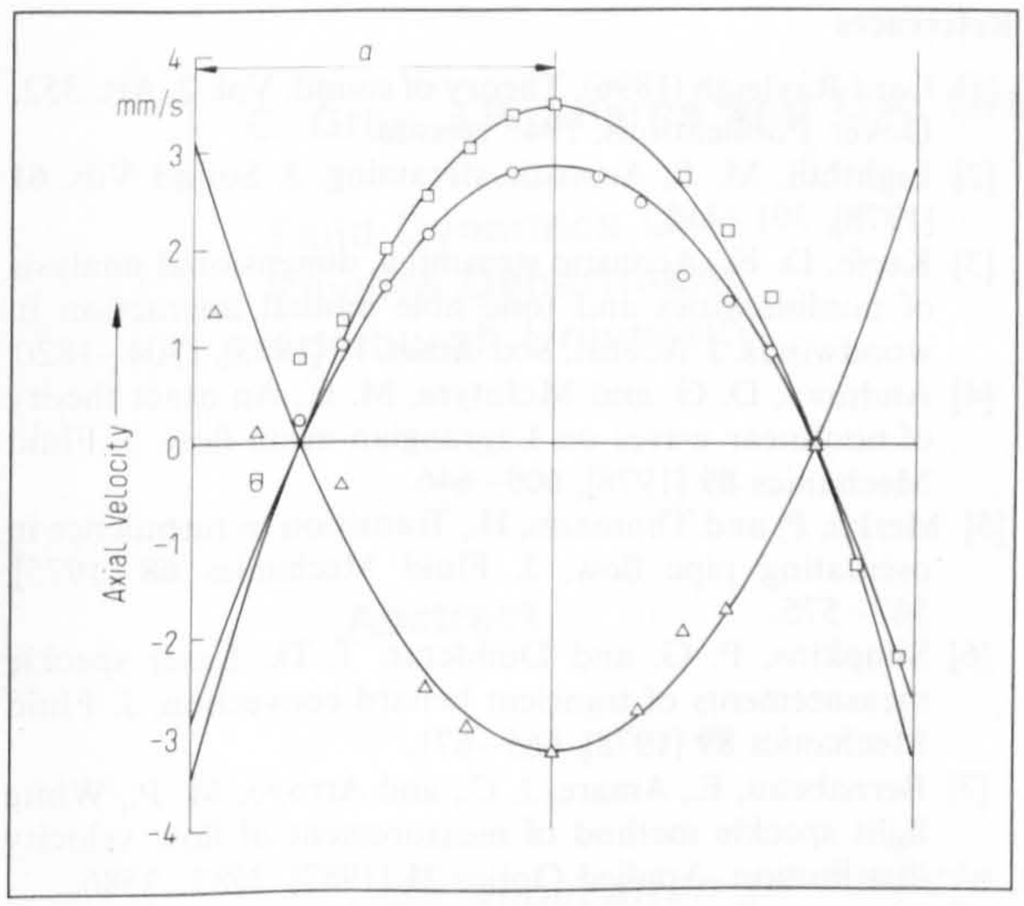

Fig. 7. Axial velocities in tube (symbols) and theoretical values (solid lines).

mum slip velocity of ~ 6.5 mm/s, giving the corresponding maximum axial velocity a few millimeters from the velocity node to be of the order of $3 \cdots 4$ mm/s – in agreement with Fig. 7. The cross sectional velocity measurements agree with the theoretical curves to within about 10% in the region of the central return velocity but deteriorate in the outer regions. This is due not only to extraneous air currents but to the fact that small positional errors in the interrogating laser beam lead to large velocity errors because of the large velocity gradient in these regions.

Inaccuracies also occur due to the finite area of the interrogating laser beam. That is, in regions where the seeding is quite sparse, the particle images which produce the fringe pattern may not lie on average at the centre of the laser beam which is where the velocity is taken to be measured. The measured velocities in Fig. 7 also show some scatter about the theoretical lines and this reflects a basic problem in P.I.V.: because the measurement is taken effectively instantaneously, effects such as particle diffusion and random particle distributions which can upset an individual velocity measurement are not averaged out. It is impossible thus to assign a statistical measure (in terms of these effects) to each separate velocity. It is however possible to assign a measure in terms of the point's nearest neighbours, because we know that the flow is continuous. This is our justification for using the velocity smoothing routine mentioned earlier.

6. Discussion and conclusions

It has been demonstrated that P.I.V. can accurately measure acoustic streaming effects; an area that cannot be tackled using conventional probe devices. Also, in contrast to the more common optical technique of Laser Doppler Anemometry (L.D.A.), it can measure "instantaneously" over a whole field. To make the type of measurements described in this paper using L.D.A. would require a two component L.D.A. system, a carefully controlled environment to prevent changing ambient conditions from upsetting the streaming over the time (many hours) that would be required to make the measurements, and some method of traversing the L.D.A. measuring volume accurately to each point in the flow.

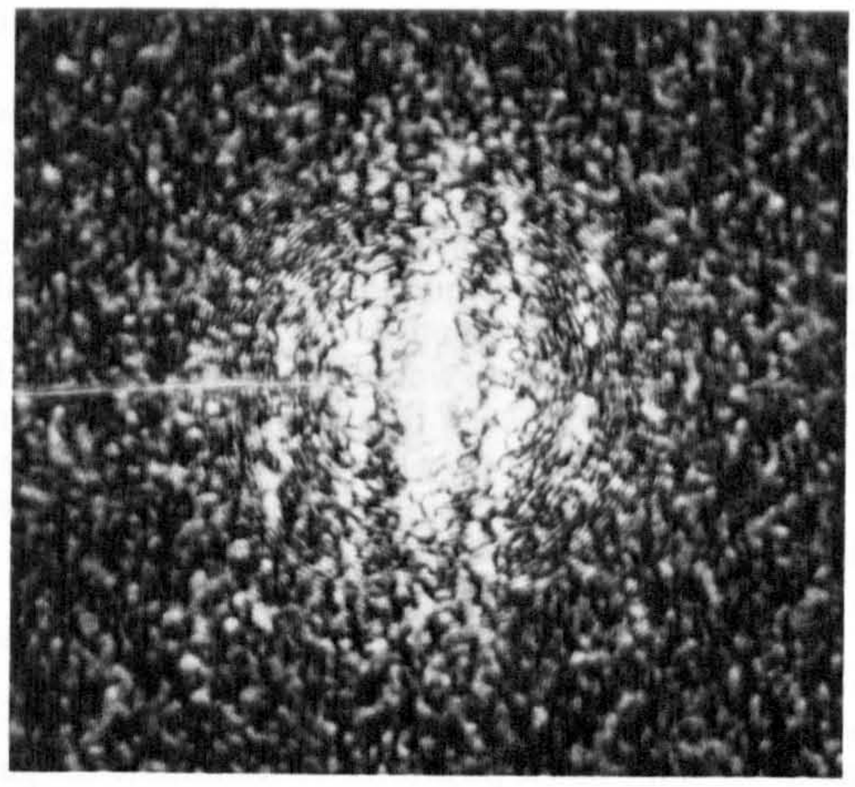

(a)

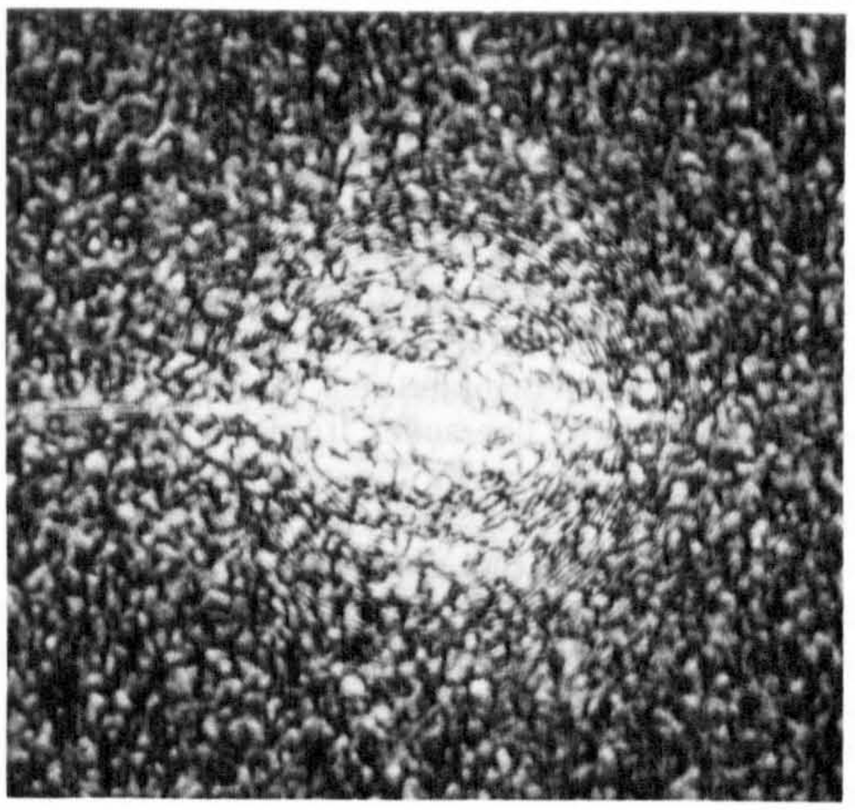

(b)

Fig. 8. P.I.V. fringe patterns. Acquired near velocity node (a) and a few millimeters away from velocity node (b).

There are however several limitations to the P.I.V. technique. Firstly, any flows measured must be essentially two dimensional: if there is too much out of plane motion then the particle images will become decorrelated and no velocity information can be extracted. Secondly, and just as importantly for acoustic streaming, if the vibrational displacement of the sound field becomes too large then it can effectively swamp the velocity displacement images (the particle images become streaked and overlap). Such an effect was noticed in this work (Section 3). Furthermore, in regions not too far from the velocity node the streaking of the particles causes the circular halo, in which the fringes are confined, to become elongated and outer lobes to become visible (see Fig. 8). This can have serious implications for the fringe analysis system since, in our implementation, an average circular halo is subtracted from each fringe pattern in order to remove low frequencies which could otherwise swamp the fringe frequency [9]. Clearly it is impossible to define such a halo if it changes for different portions of the film. We avoid this problem by instructing the computer to make measurements on successive lines perpendicular to the tube axis across which the vibrational amplitudes are constant. The computer can

then gather an average halo from each of these lines and use it to remove the low frequencies for that line.

In fact the particle streaks are dumbell shaped due to the particles moving more rapidly at the centre than at the extremities of their displacements. The halo (in the direction parallel to the particle displacements) then takes the profile of a squared zero order Bessel function from which it would be possible to estimate the magnitude of the particle displacements [15]. Such estimates would probably however be of quite low accuracy and such measurements would perhaps be of little practical use. It may however be of interest to note that, knowing the sound field and the particle density, it would be possible in principle to deduce the particle sizes from their displacement amplitudes.

A way round the above problem would be to pulse the laser fast enough to "freeze" the particle images, the pulse former being triggered from the sound field to capture the images at the same phase positions. To illuminate the particle for say 1/10 of its period would require, for frequencies of the order we have here, laser pulses lasting only small fractions of a millisecond. This would then require (if we scale up the intensities used here) laser powers of the order of several-watts. Such lasers are not uncommon though their use does entail certain difficulties and hazards. It may be noted however that more effective use can be made of available laser light by employing scanning beam technology [13] or by using more sensitive films and sacrificing resolution.

However, despite these limitations the technique should be of considerable interest both to acousticians and fluid dynamicists. It may also be noted that in other areas the technique would perhaps not suffer from the aforementioned difficulties. For example, in the regions of much higher frequencies, say 20 kHz upwards, the vibrational amplitudes can become quite small though the streaming effects are very large [2, 14]. The authors feel that the P.I.V. technique complements their earlier work on the optical measurement of acoustic velocities [16], and hope to go on to apply both techniques to the measurement of practical acoustic situations (e.g. the acoustics of musical instruments).

Acknowledgements

This work is supported by the SERC and British Telecom. J. P. Sharpe and C. Gray are grateful to the Dept. of Education for N. Ireland and the SERC respectively for studentships.

References

[1] Lord Rayleigh (1896), Theory of sound, Vol. 2, Art. 352. Dover Publications, 1945 reissue.
[2] Lighthill, M. J., Acoustic streaming. J. Sound Vib. **61** [1978], 391–418.
[3] Keefe, D. H., Acoustic streaming, dimensional analysis of nonlinearities and tone hole mutual interaction in woodwinds. J. Acoust. Soc. Amer. **73** [1983], 1804–1820.
[4] Andrews, D. G. and McIntyre, M. E., An exact theory of nonlinear waves on Lagrangian-mean flow. J. Fluid Mechanics **89** [1978], 609–646.
[5] Merkli, P. and Thomann, H., Transition to turbulence in oscillating pipe flow. J. Fluid Mechanics **68** [1975], 567–575.
[6] Simpkins, P. G. and Dudderar, T. D., Laser speckle measurements of transient benard convection. J. Fluid Mechanics **89** [1978], 665–671.
[7] Bernabeau, E., Amare, J. C., and Arroyo, M. P., White light speckle method of measurement of flow velocity distribution. Applied Optics **21** [1982], 2583–2586.
[8] Meynart, R. and Lourenco, V. K. I., Digital image processing in fluid dynamics. Von Karman Institute for Fluid Dynamics Lecture Series 1984-03.
[9] Gray, C. and Greated, C. A., Application of P.I.V. to measurement under water waves. Optics Lasers Engineering (submitted).
[10] Robinson, D. W., Role for automatic fringe analysis in optical metrology. SPIE Vol. 376.
[11] Huntly, J. M., An image processing system for the analysis of speckle photographs. J. Physics E. **19** [1986], 43–49.
[12] Bruel & Kjaer, Condenser microphones and microphone preamplifiers for acoustic measurement. B & K Data Handbook 1982.
[13] Gray, C. and Greated, C. A., A scanning laser beam system for two-dimensional illumination of flow fields. Proc. Particle Image Displacement Velocimetry Conference. Von Karmen Institute for Fluid Dynamics, Belgium 1988.
[14] Bergmann, L., Ultrasonics. G. Bell & Sons Ltd., London 1938.
[15] Tiziani, H. J., Application of speckling for in-plane vibration analysis. Optica Acta **18** [1971], 891–902.
[16] Sharpe, J. P. and Greated, C. A., The measurement of periodic acoustic fields using photon correlation spectroscopy. J. Physics D (Applied Physics) **20** [1987], 418–423.

Fringe Analysis for PIV measurements in Acoustic Streaming

C. Gray, J.P. Sharpe and C.A. Greated

Fluid Dynamics Unit
Physics Department
Edinburgh University

Abstract

The application of Particle image velocimetry to the measurement of Rayleigh acoustic streaming within a circular tube is described. The streaming motion is the result of the interaction of a high intensity standing wave sound field with the boundary layer of the tube wall. Multiple exposure photographic recordings of seeding particles within the flow appear as extended streaks due to the oscillatory motion of the air column supporting the standing acoustic wave. The complications imposed upon the analysis of the flow record by the position dependent lengthening of the particle images is described. Final measurements of the streaming at a node are presented with a quantitative comparison of these measurements with the theoretical values.

Introduction

Acoustic Streaming, which may be described here as the generation of non-zero mean motions by a sound field, has been a subject of investigation since the time of Rayleigh [1]. Although, as pointed out by Lighthill [2], the topic has been neglected of late, it is still of considerable interest to acousticians and fluid-dynamicists interested in Lagrangian mean flows [3,4]. The phenomenon typically arises when a

sound field is attenuated or dissipated due to its interaction with the medium of propagation or with the boundary layer when a solid wall is present. Quite a body of theoretical work has been produced on the subject [see above references] but experimental work is scarce. This lack of measurement is not difficult to appreciate when one considers that in the regimes of acoustic amplitude and frequency where streaming takes place there can be considerable interaction between the sound field and any measurement device introduced into the flow [5]. Consequently, one sees in the literature qualitative statements about "strong" or "weak" streaming and comparison with theory made on the basis of flow visualisation [3,4].

We present here the application of a non intrusive optical technique (Particle Image Velocimetry) to the measurement of Rayleigh streaming. This form of streaming was chosen since it is well understood and its magnitude can be independently estimated from pressure measurements of the sound field causing it. Particle Image Velocimetry (PIV) is a velocity measuring technique which can simultaneously record the instantaneous velocity distribution over a whole plane within a flow [6]. Small particles contained in and faithfully following the flow under investigation are photographed using an intense sheet of laser illumination throught the region of interest. Pulsing of the illumination (either by Q-switching, mechanical or optical modulation of a continuous beam, or by a scanning technique) results in two or more successive particle images being recorded at the film plane of a camera positioned perpendicularily to the illumination plane. The light source used does not have to be coherent (flash lamps have been used for PIV measurements [7]) but a laser provides a convenient high intensity collimated beam.

The velocity information on the film can then be recovered by ascertaining the separation of related particle image pairs. This can be done manually by microscopic inspection of the film but more commonly by automated optical and digital analysis. Analysis of the multi-exposed photographs presented here was performed by interrogation of the film over a number of points with a low powered laser beam. This produces a series of fringes in the back focal plane of a lens whose orientation and periodicity are related directly to the flow direction and particle image separation respectively [8]. The lower and upper limits of particle image separation are governed by the particle image diameters and the diameter of the probe laser beam. The limitations imposed on the dynamic range of the technique are discussed in [9].

A typical region requiring analysis can contain from fifty to several thousand points and so it is necessary to analyse the fringes automatically. Precise digitisation of the fringe pattern resulting from each probe position provides the information in digital form allowing a computer to extract the velocity information. Such a system has been developed at our institution [10] based upon two-dimensional Fourier transformation of the fringe intensity data. Other approaches to determining the fringe orientation and periodicity are well documented in the literature [11,12,13] describing the speed, accuracy and reliability of the procedures.

Rayleigh streaming

Rayleigh streaming occurs when an acoustic standing wave is dissipated in the boundary layer generated by a solid wall. The most common configuration in which to observe the phenomenon occurs

when a standing wave is set up in a circular tube.

The velocity of the streaming at the wall of the tube (or rather just beyond the boudary layer) is given by Rayleigh's law,

$$u_s = \frac{-3}{4\omega} V(x) \frac{dV(x)}{dx} \qquad [1]$$

where $V(x)$ is the acoustic particle velocity outside the boundary at any point x along the tube and ω is the radial frequency of the sound field. This velocity u_s (sometimes called the slip velocity) is directed towards the velocity nodes such that on any section through the axis of the tube the velocity is given by,

$$u = u_s \left(1 - \frac{2r^2}{a^2}\right) \qquad [2]$$

where r is the distance from the tube axis and a is the tube radius.

If the acoustic particle velocity of the sound field is given by

$$V(x) = a_m \sin\left(\frac{2\pi x}{\lambda}\right) \qquad [3]$$

where a_m is the velocity amplitude then, inserting this into (1) yields

$$u_s = \frac{-3a_m^2}{8c} \sin\left(\frac{4\pi x}{\lambda}\right) \qquad [4]$$

where c is the speed of sound. It may be noted that (4) does not depend on the viscosity of the medium. Thus, using the relationship between the velocity and pressure in a standing wave, it is possible to estimate the magnitude of the slip velocity at any point in the tube outside the boundary layer.

Experimental apparatus

A diagram of the experimental arrangement is shown in Fig.1. Light from a 32mW He-Ne laser (λ=633nm) was expanded into a

two-dimensional sheet using the lens l and the two cylindrical lenses c1 and c2. When the sheet entered the tube, cutting the axis, it was approximately 2cm high and 1mm wide. It was noticed while conducting the experiments that the streaming motions could be greatly affected by small temperature gradients. To minimise this effect, the tube was lagged with polyurethane foam at all points except the working section and baffles were placed around the apparatus to reduce air movement. The shutter was placed between the lens L and the laser while the chopper was placed at the focus of L. The chopper, which was a slotted rotating disc formed the pulses of light while the shutter could be adjusted to allow a preset number of pulses through. The use of an external shutter rather than the cameras own shutter was to reduce vibration to a minimum. The chopper came with its own electronic display, but was found to be unreliable at the low chopping speeds used. Consequently a photodiode and a storage oscilloscope were used to give a more precise frequency reading. The camera used was a 35mm Nikon with a 55mm Macro lens used at a magnification of 0.773. This type of lens was found to be essential if distortion of the image in the off axis regions was to be avoided. The film used to record the streaming was Kodak T-Max 400 which provides good sensitivity (400ASA) and adequate resolution (100 lines/mm depending on contrast). During actual experimental runs the laboratory was illuminated with extremely subdued light and the photographs taken against a black background to increase contrast.

The amount of distortion in the image plane due to the curvature of the glass tube was estimated by inserting a piece of graph paper into the tube, photographing it, and examining the developed film with a travelling microscope. A negligibe amount of distortion was found

except at approximately 1mm from the tube wall. Since the amount of flare from the wall tended to make any measurement in this region impossible, it was not necessary to calculate correction factors for this effect.

Measurement and results

The apparatus was was set up as indicated in Fig.1. Sound of frequency 2460Hz was introduced into the tube (length 450mm, internal dia. 23.3mm) using a horn loudspeaker with the horn removed. The tube was sealed at the other end with a rubber bung which had a tight fitting metal plate attached to its inside face to ensure a rigid termination. The sound field thus corresponded to the 7th normal mode of the air column. A probe microphone, (Bruel & Kjaer type 4166 with 2mm i.d. probe attachment) inserted through the rigid end monitored the pressure. The probe microphone had previously been calibrated to within 0.5dB using an acoustic coupler. Although the intensities required to produce streaming were near the limits of the microphone's range [14] they were still within the 10% distortion limit leading to an extra possible error of around 1dB. So, although the pressure measurements were not highly accurate they did provide a usefull independent check on the streaming velocities.

Tobacco smoke was introduced into the tube to render the flow visible and streaming was set up, the field having a pressure at the rigid end of 151 db. The streaming velocities were first estimated by eye and the chopper set to provide pulses with a separation of 0.114 second and a duration of 0.0057. The shutter was set to 0.5 second allowing an average of 4 pulses through.

Photographs were taken near a velocity node and a print of the film

used to provide measurements here is shown in Fig.2. The individual particle images can be clearly seen. Close inspection reveals that the particle images at a distance from the velocity node are recorded as streaks rather than points. This is due to the rapid oscillations imposed upon the smoke particles by the high intensity sound field. In fact, the particle images are dumbell shaped due to the particles moving more rapidly at the centre than at the extremitles of thier motion. This factor imposes certain difficulties in the analysis of the flow photographs and will be discussed in the next section.

Fringe analysis

The exposed and developed film was analysed over a regular grid of approximately 200 points covering a large proportion of the flow shown in Fig.2. The beam used to probe the photograph was passed through a spatial filter to reduce the amount of noise in the fringe plane. This arrangement also incorporates a movable circular aperture used to control the diameter of the laser beam which for this application was set at 0.5mm in order to achieve high positional resolution. This is particularily important when measuremets are taken over large velocity gradients as a large probe diameter will cover a large range of particle pair separations ultimately reducing the visibility of the fringes to an unmeasureable degree [15]. However, the use of a small probe region increases the speckle noise due to the small number of particle image pairs contained within the analysis area. Consequently, the fringes generated from the streaming photograph are of relatively low visibility and contain a high degree of speckle noise Fig.3.

Digitisation of the fringe intensity pattern was performed using a Panasonic CCD camera coupled to a Watford Electronics image digitiser

which is incorporated into the processing computer as a slot-in card. This set-up enables the fringe patterns to be digitised in a geometrically precise manner with rapid communication of the data to the computer fig.4. The fringe intensity data was sampled over a grid of 256*256 and then averaged over 4*4 pixel blocks to reduce the data to a 64*64 array of 6 bit intensity values without danger of any high frequency speckle noise interfering with the lower frequency fringe signal.

The low fringe visibilities resulting from the streaming photograph is reflected in the choice of numerical processing for the fringes. Two-dimensional Fourier analysis of speckle displacement fringes has been shown to be both reliable and accurate for fringe visibilities down to 7% [16], which represents fringes on the point of not being visible to the eye. The main disadvantage associated with this method of analysis is the large amount of computation required to transform the fringe intensity data to the 2-D spatial frequency domain, $2N^2\log_2 N$ multiplications and additions. To reduce the time taken for transformation of the fringe data the 2-D Fourier transform was performed by multiple 1-D Hartley transformation of the rows and then columns of the fringe data. There is no complex part to the fringe intensities therefore Hartley transformation is approximately twice as fast as an FFT. A further reduction in computing time is made from the realisation that the Fourier plane of the real data is symmetrical about the centre thus requiring processing of only half of the columns.

It has been shown that for low fringe densities (less than 5 visible fringes) the diffraction halo can influence the detected position of the fringe frequency. Kaufmann [17] showed that this effect was less pronounced when Fourier analysis of the fringe frequencies was used but was still significant. In cases where the fringe frequency is

extremely low the finite width of the central dc peak in the Fourier plane can completely obscure the signal peak [18]. The most usefull means of reducing the effects of the halo from the Fourier plane is by subtraction. The halo function is not additive to the fringes but halo division tends to magnify the noise at the edges of the fringe pattern where the halo is reduced in intensity. Halo subtraction removes the central peak and if the halo function can be estimated precisely most of the low frequencies associated with the halo can also be removed . However, this aspect of the fringe analysis is complicated by the streaked nature of the particle images on the streaming photographs. As mentioned, this is a result of the rapid motion of the particles in the time of the exposure. For points on the film away from the standing wave nodes the vibrational amplitude is quite large, resulting in a marked distortion of the halo in the vertical direction. This has serious implications for the analysis of the flow record as the fringe halo will vary in geometry as the film is probed in different vertical positions.

For conventional applications of the 2-D Fourier analysis system the halo shape is approximated by averaging a number of diffraction halos from a single exposure photograph of the seeded area in the flow to be measured [10]. This approach was used to try and approximate the average halo from the whole film in the hope that the subtraction of such a function would reduce the zero and low frequencies in the Fourier plane to allow detection of the signal peak by a search for the maxima. However, an excessivly high failure rate was found to occur using this approach. Investigation of the transformaed data on one of the failed measurements showed large amplitude peaks on either side of the dc position. This indicated that the halo subtraction scheme was highly sensitive to difference in the shape of the fringe and subtracted

halos. This effect combined with the relatively low visibility of the fringes resulted in the anomalous peaks being located rather than the fringe peak. This is illustrated in figures 5,6. Figure 5 shows a fringe pattern with 24% visibility and ovality 0.65, where ovality is taken to be the ratio of the vertical width of the fringe halo to the horizontal width. A halo of ovalality 0.8 was subtracted from this fringe pattern and transformed. The resulting spatial frequency data is shown in fig. 6. The two anomalous peaks nearest the centre of the Fourier plane become reduced in height the more matched the subtracted halo gets to the fringe pattern. Fig.7 shows the same fringe pattern with a 0.75 ovality halo subtracted.

Successfull analysis of the streaming photograph was achieved by subtraction of a "matched" diffraction halo from each fringe pattern. A singly exposed photograph of the standing acoustic wave in the tube was taken at the same position. The halo then subtracted from each line on the multi- exposed photograph was obtained by averaging the diffraction halos obtained from the corresponding line on the single exposure photograph. Because the halo shape only varies in the vertical direction all the halos obtained from a horizontal line will be of similar dimensions allowing an average smooth halo to be calculated for use in the analysis of the corresponding line on the displacement photograph.

The measurements resulting from the above analysis are shown in fig.8. As can be seen there are a number of missing values where a measurement failure occured. Such points are removed from the data set on the basis of continuity with neighbouring points and their measured visibility. The missing data points are filled in by interpolation using a third order Chebyshev polynomial. The results from this are shown in Fig.9 . As can be seen, the measurements look slightly

asymmetric with the velocities in the upper left vortex seeming to sweep over too much to the right. This was probably due to outside air currents.

As a check on the accuracy of the measurements it is noticed from eq.2 that the axial velocity should be parabolic across any section of the tube with a maximum velocity given by eq.1 and zeroes at distances $r = 0.707a$ from the axis of the tube. Axial velocities from the measured data at three separate lines across the tube were plotted against the corresponding theoretical values (fig.10). The solid Parabolae were fitted using the measured velocity maxima and the theoretical zero points. The fits are quite good although the velocities do show some deviation near the left crossover point, reflecting the assymmetry mentioned earlier. A calculation using eq.4 and a value of 151dB for the maximum pressure indicates a maximum slip velocity of about 6.6mm/s, giving the corresponding maximum axial velocity a few millimeters from the velocity node to be of the order 3....4mm/s - in agreement with fig.10. The cross sectional velocity measurements agree with the theoretical curves to within about 10% in the region of the central return velocity but deteriorate in the outer regions. This is not only due to extraneous air currents but to the fact the particle pairs carrying the velocity information are distributed randomly within the finite probe area which will cover a range of velocities due to the large velocity gradient. The mean velocity measured for any particular point will thus have a degree of uncertainty associated with it due to the variance of the mean particle separation measureable from that region.

Discussion

It has been shown that PIV can accurately measure acoustic

streaming effects; an area that can be tackledonly with difficulty using conventional probe devices. Also, in contrast to the more common optical technique of Laser Doppler Anemometry (LDA), it can measure the instantaneous velocity over an extended region in a flow field. To make the type of measurements described in this paper using LDA would require a two component LDA system, a carefully controlled environment to prevent changing ambient conditions from upsetting the streaming over the time (many hours) that would be required to make the measurements, and some means of traversing the LDA measuring volume accurately to each point in the flow.

There are however several limitations to the PIV technique. Firstly, any flows measured must be essentially two-dimensional ; if there is too much out of plane motion then the particle images will become decorrelated between exposures an no velocity information can be extracted. Secondly, and importantly for acoustic streaming, if the vibrational displacement of the sound field becomes too large then it can effectively swamp the velocity displacement image (when the particle images become streaked and overlap). For vibrational amplitudes less than this velocity measurements can be made but the analysis is made more complicated by the elongated particle images.

A way around the above problem would be to pulse the laser fast enough to "freeze" the particle images, with the pulse being triggered by the sound field to capture the images at the same phase positions. To illuminate the particle for say 1/10th of its period would require, for frequencies of the order used here, laser pulses lasting for a small fraction of a millisecond and a corresponding increase in the illuminating intensity to provide the same exposure value. This is not a problem as high powered pulsed lasers or CW laser combined with a

scanning beam system could be used to provide the requisite intensity and pulse duration. The difficulty exists in ensuring that the illumination is pulsed at precisely the same frequency as the sound field so that gross errors due to the oscillating motion of the sound field contributing to the mean motion measurement are avoided.

Acknowledgements

This work is supported by the SERC and British Telecom. J.P. Sharpe and C. Gray are grateful to the Dept. of Education for N. Ireland and the SERC respectively for studentships.

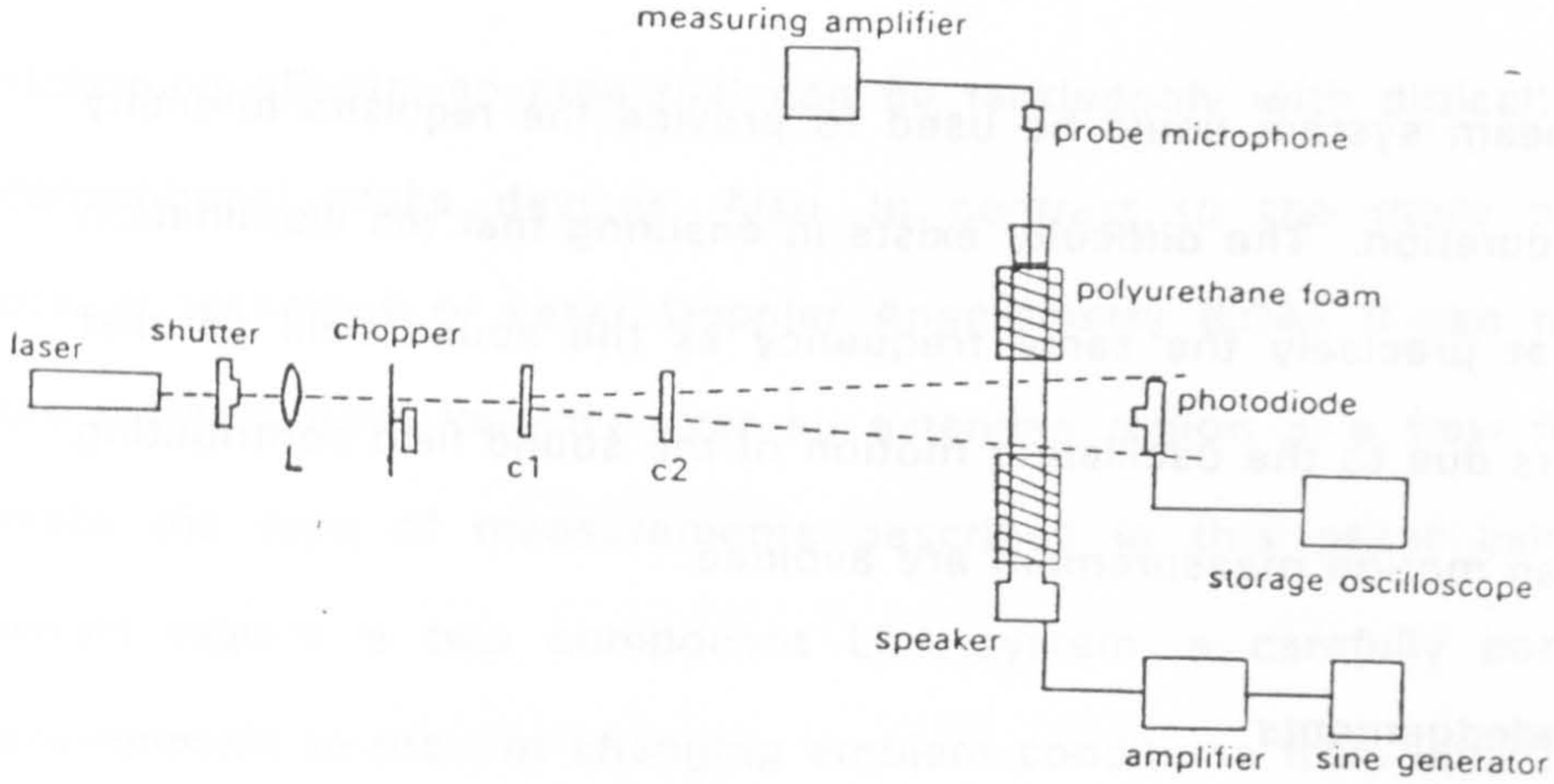

Figure 1. Schematic diagram of P.I.V. setup.

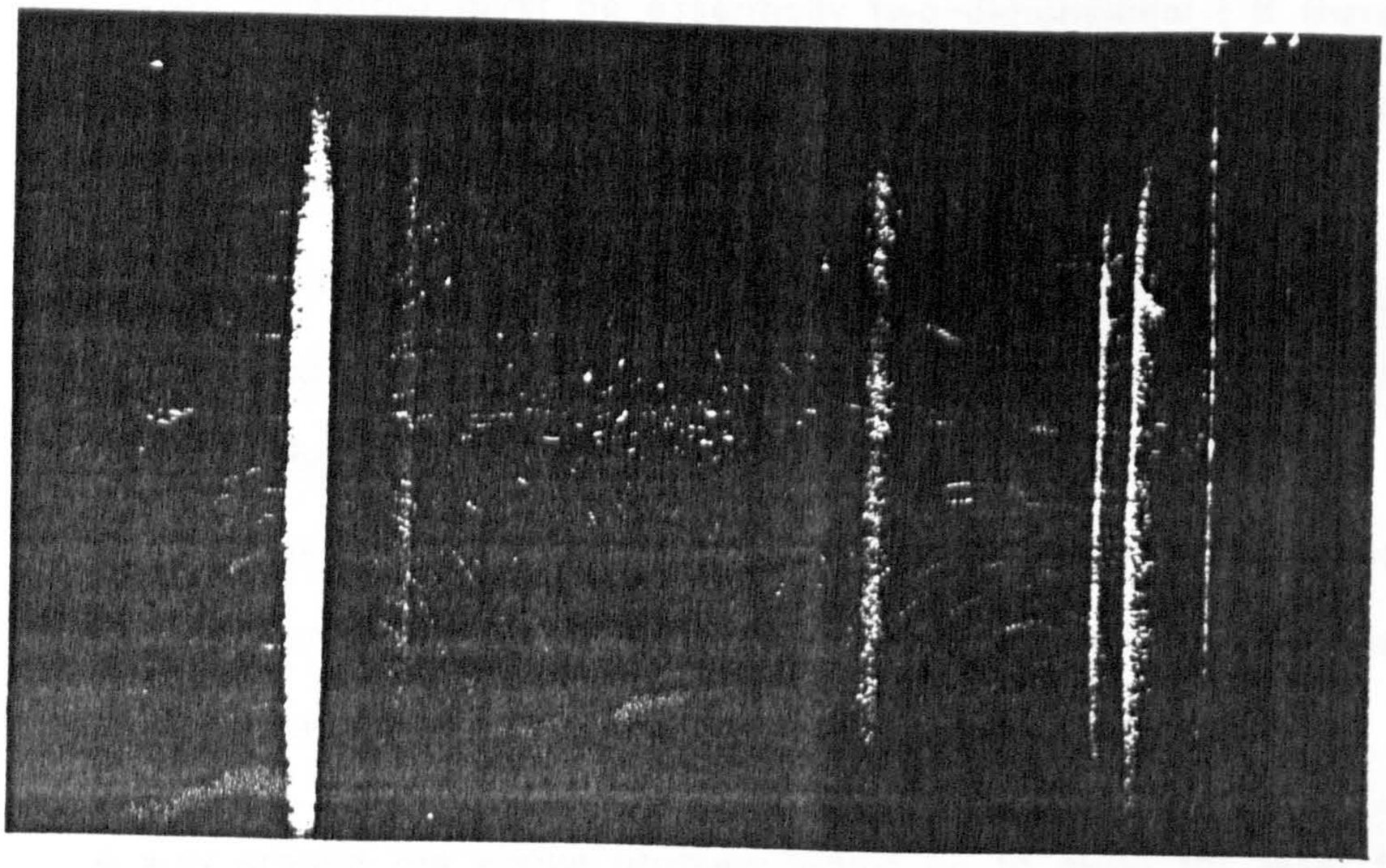

Figure 2. Print of P.I.V. transparency of Rayleigh streaming used for velocity analysis.

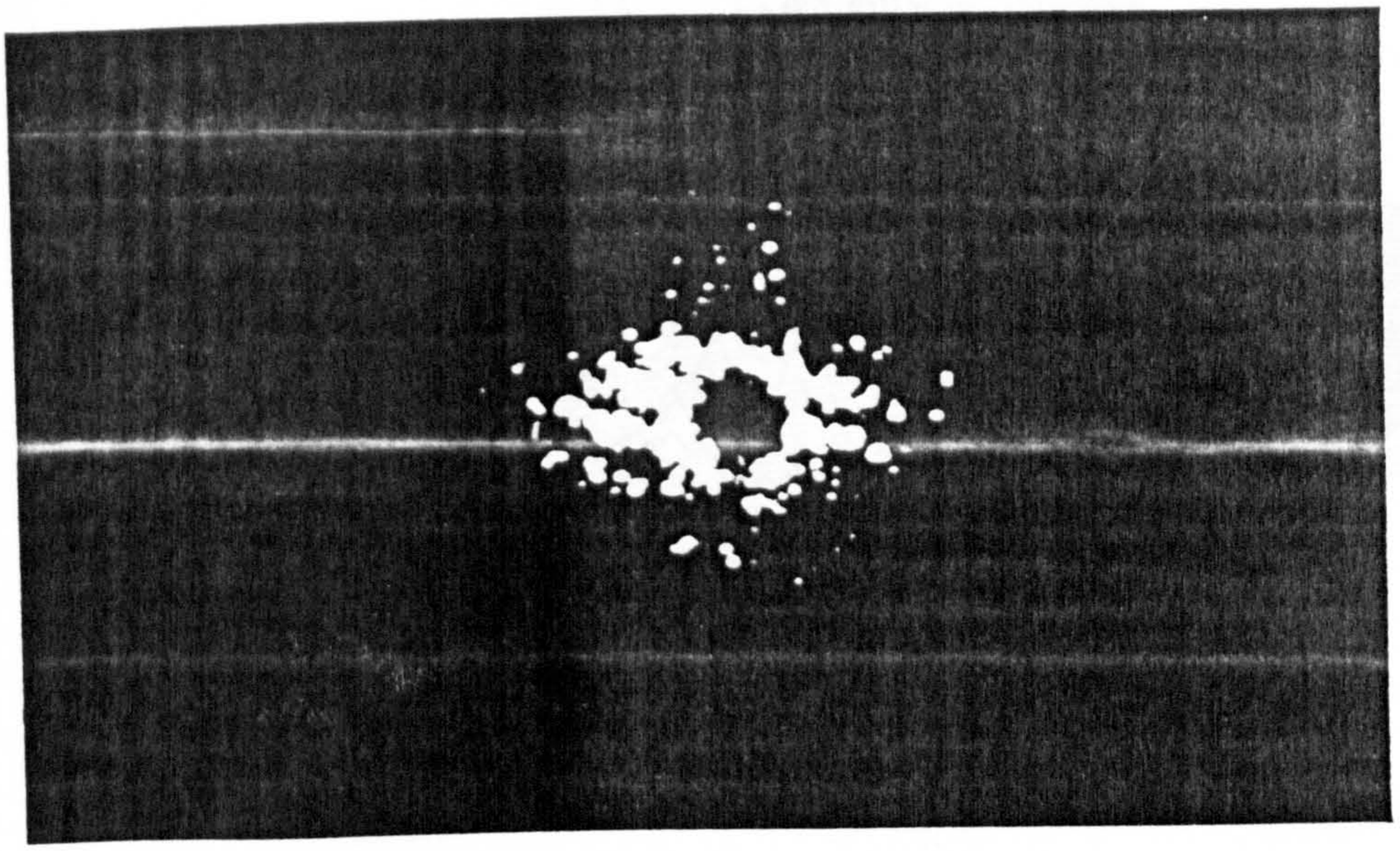

Figure 3. Typical fringe pattern generated from streaming photograph.

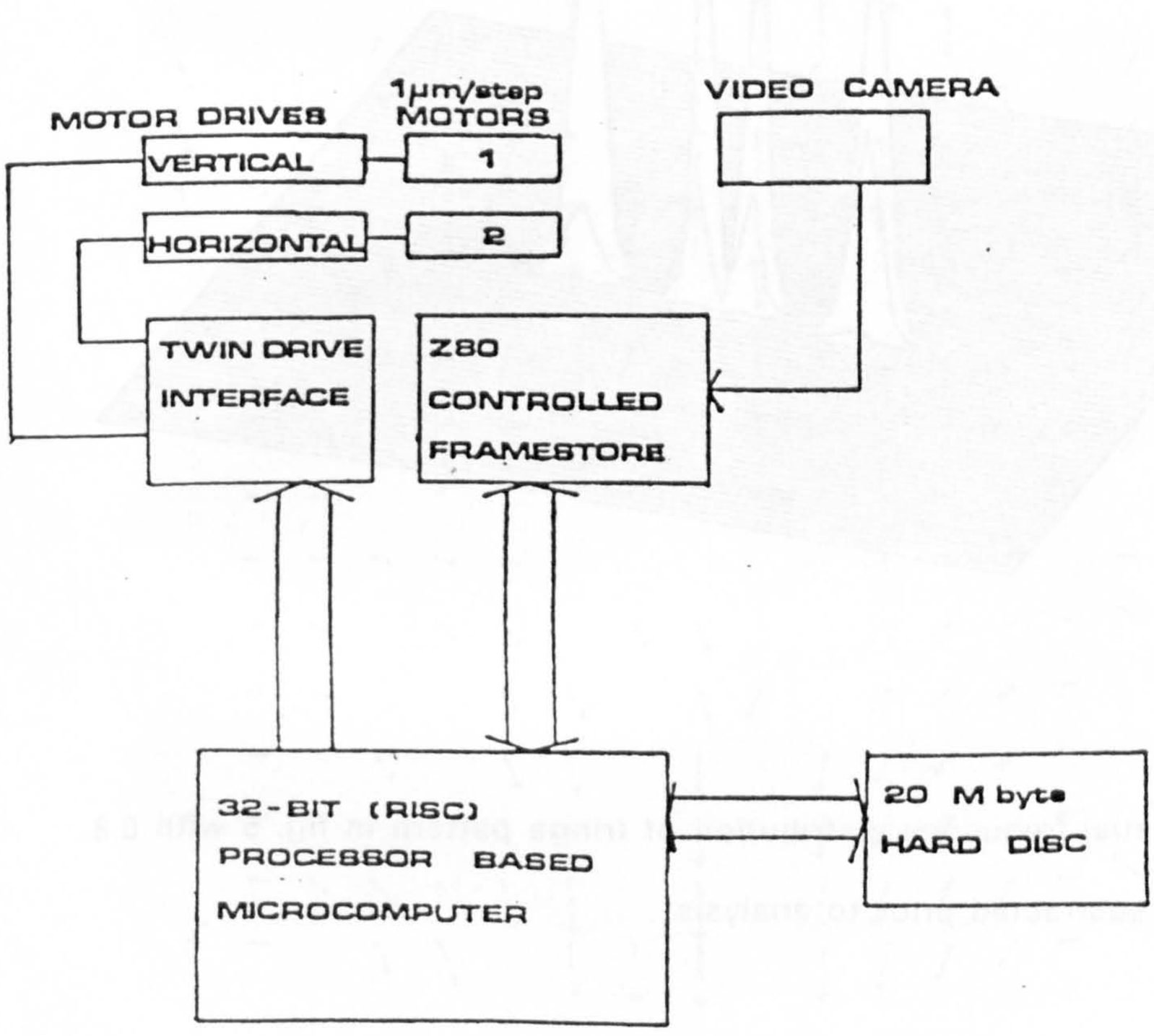

Figure 4. Automatic fringe digitisation and analysis system.

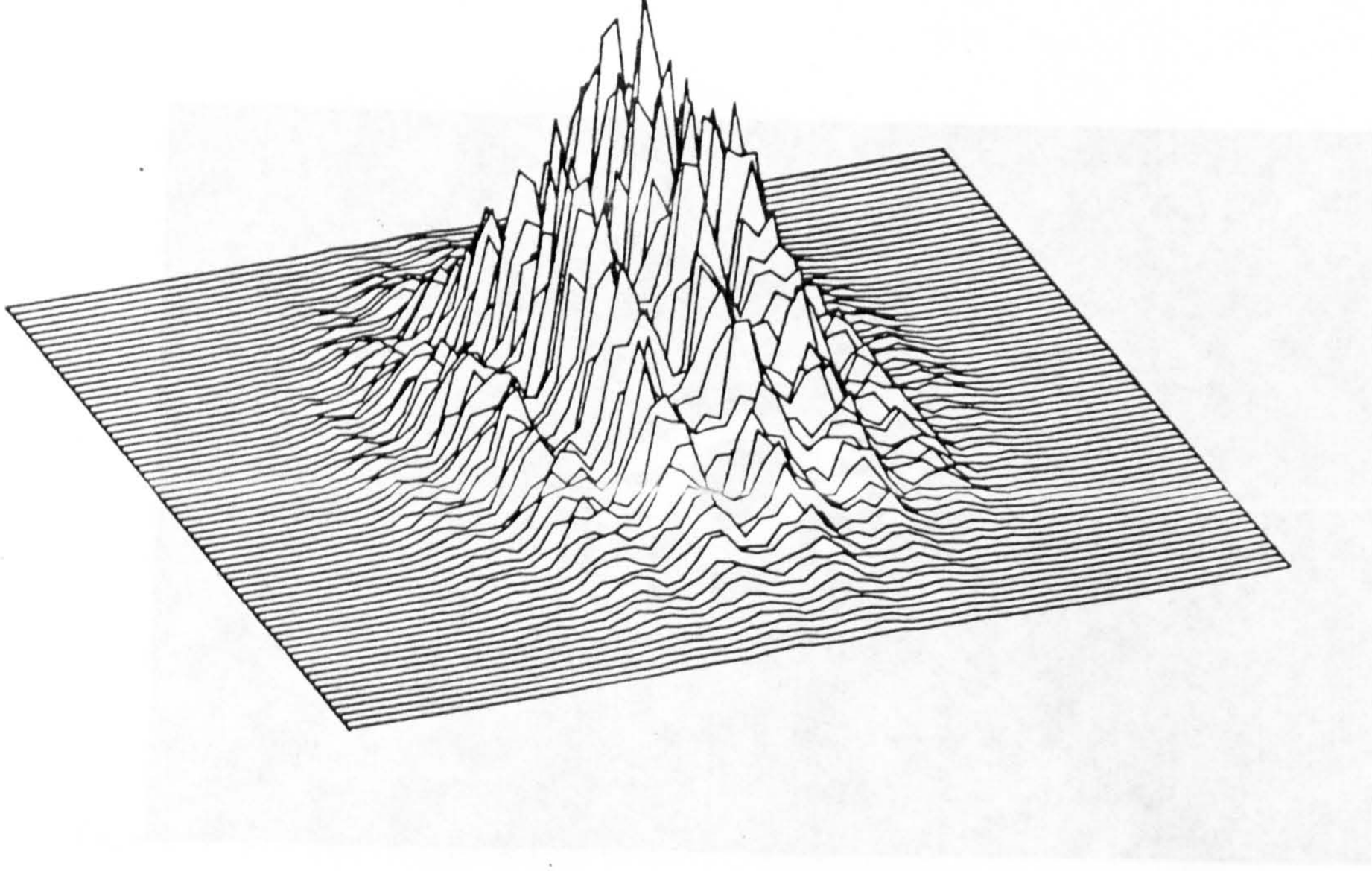

Figure 5. Fringe pattern intensity distribution

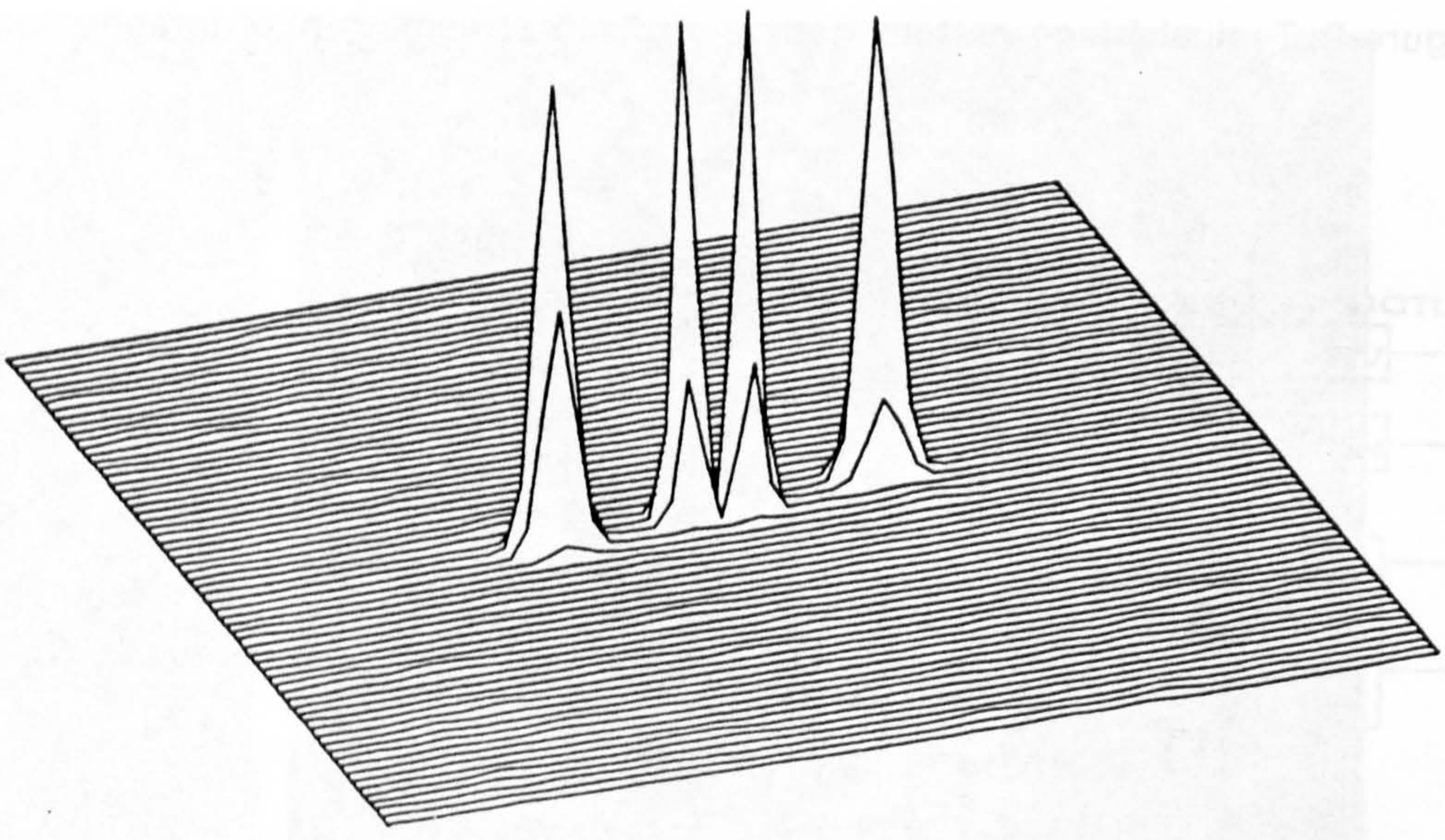

Figure 6. Spatial frequency distribution of fringe pattern in fig. 5 with 0.8 ovality halo subtracted prior to analysis.

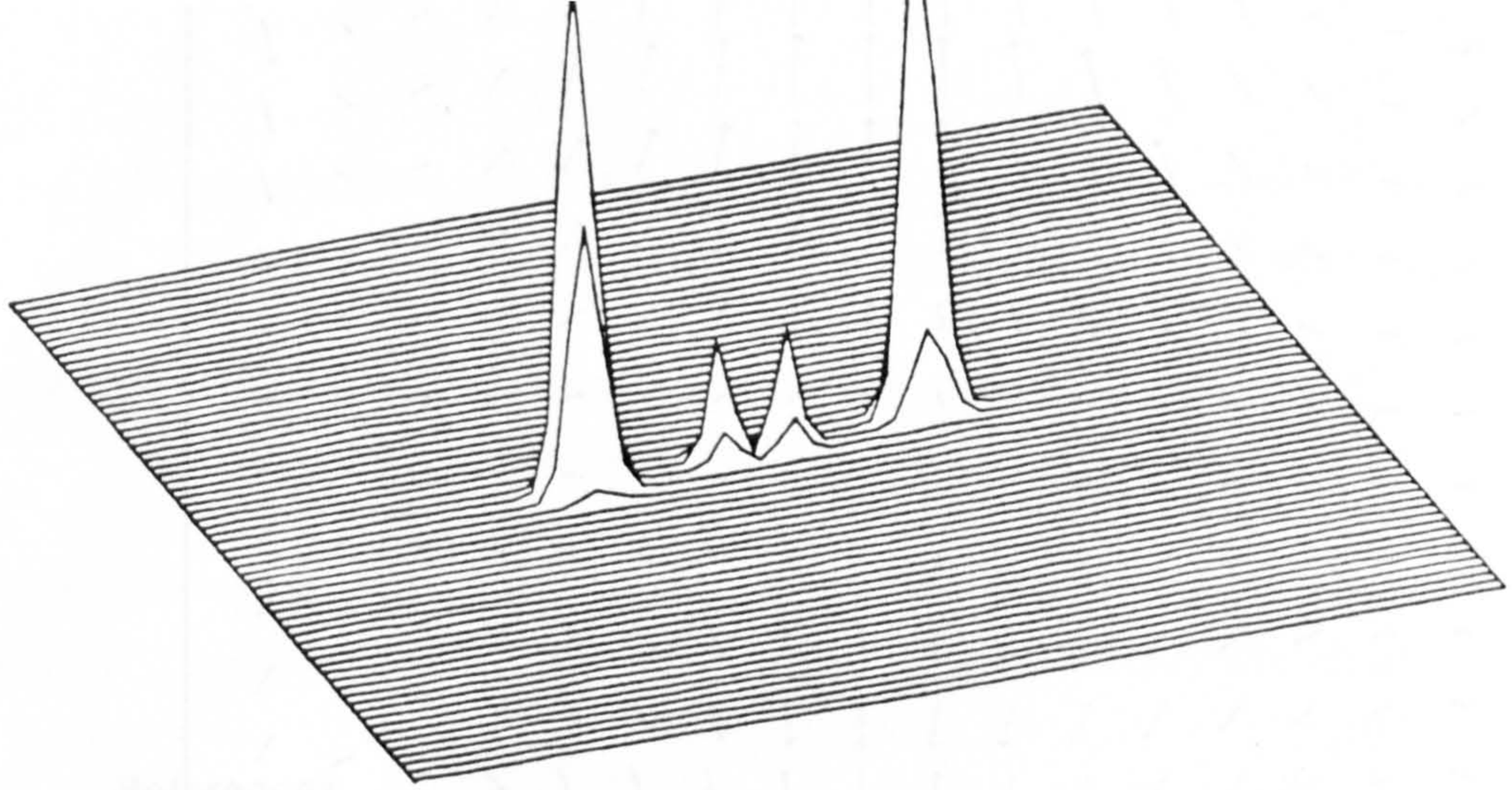

Figure 7. Spatial frequency distribution of fringe pattern in fig. 5 with 0.75 ovality halo subtracted prior to analysis.

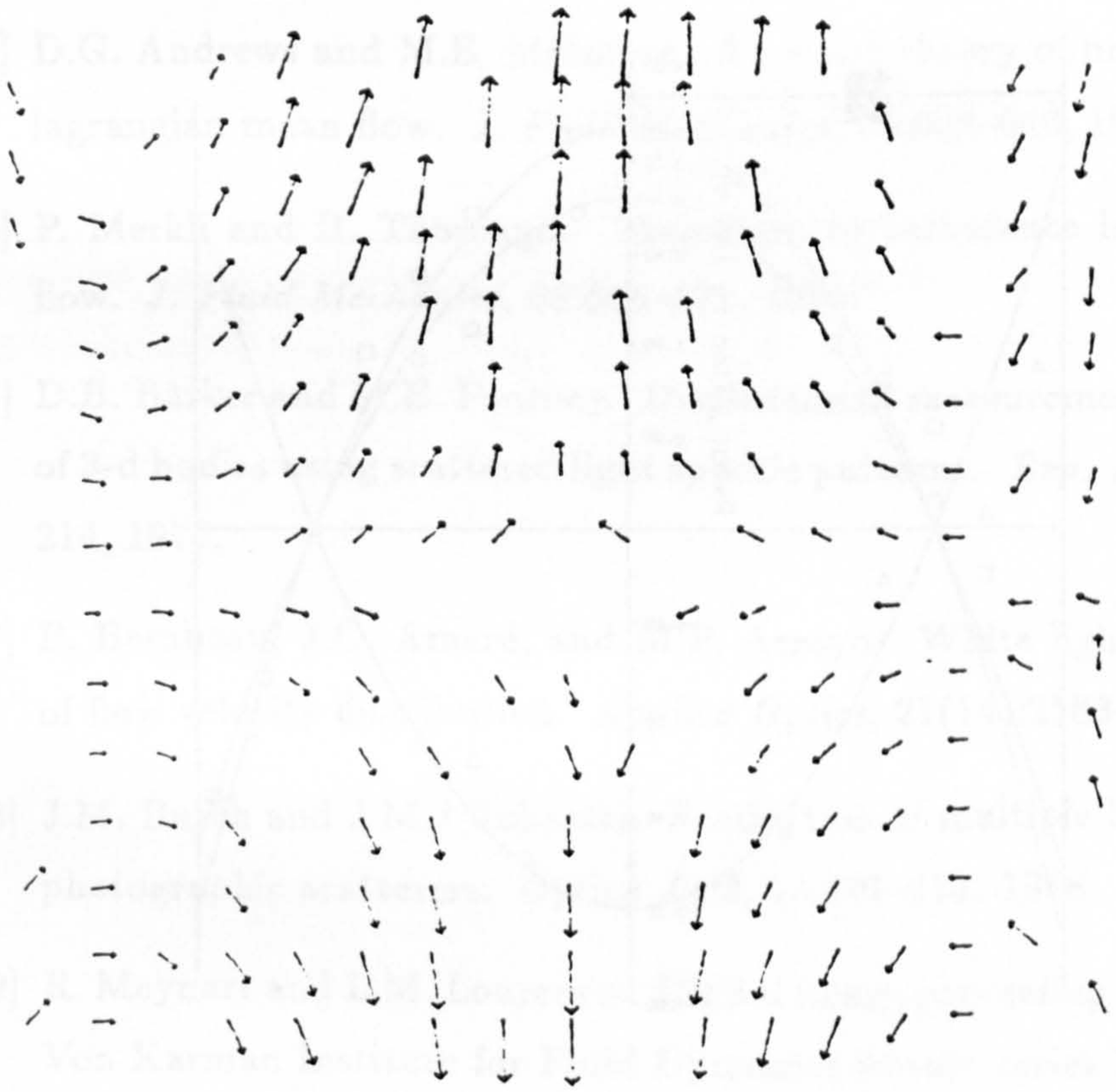

Figure 8. Velocity distribution derived from flow photograph in fig. 2. Anomalous values have been removed.

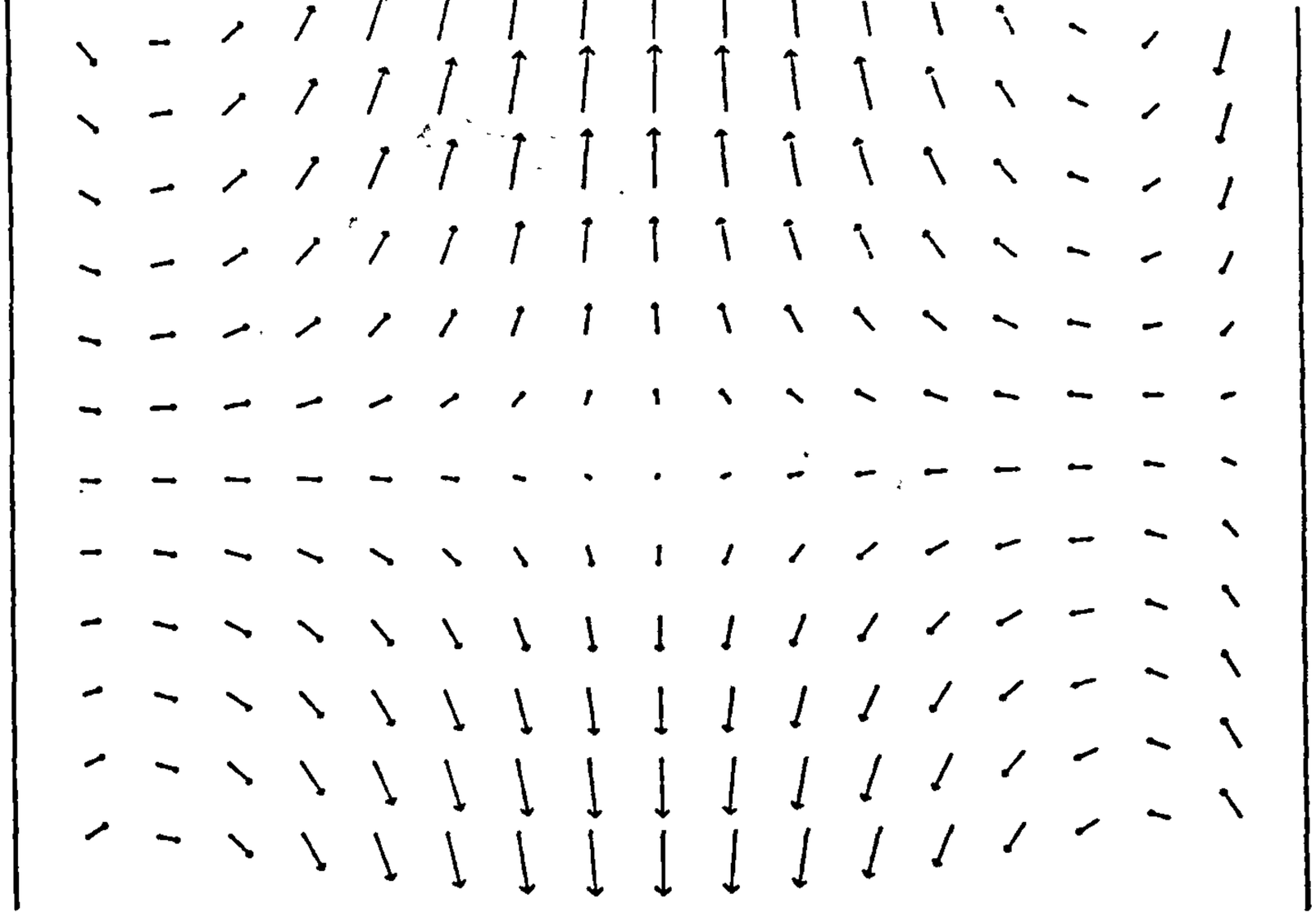

Figure 9. Velocity distribution with interpolated values.

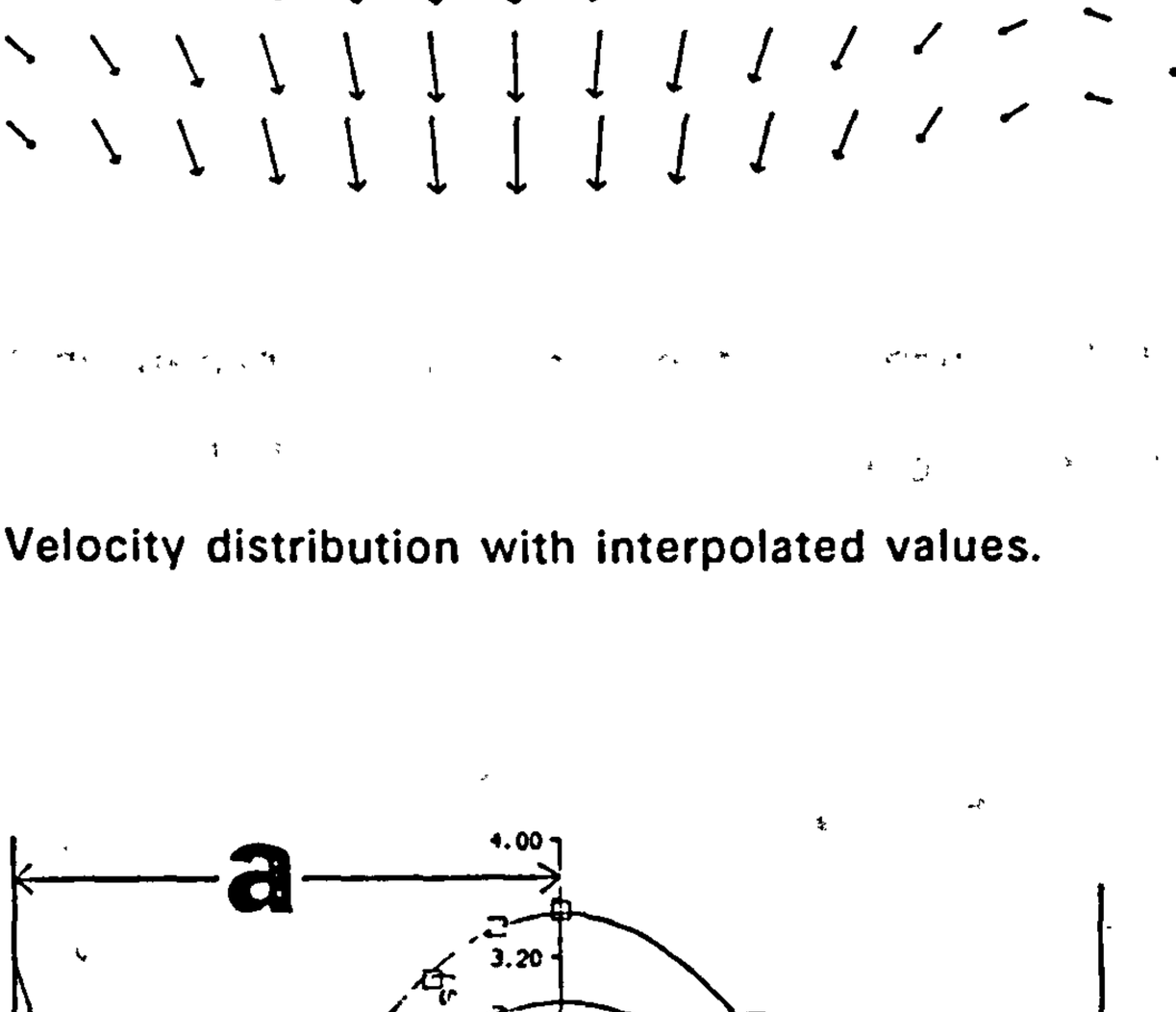

Figure 10. Axial velocities in tube (symbols) and theoretical values (solid lines).

References

[1] Lord Rayleigh. *Theory of sound.* Volume 2, Dover Publications, 1945.

[2] M.J. Lighthill. Acoustic streaming. *J. Sound Vib.*, 61:391–418, 1978.

[3] D.H. Keefe. Acoustic streaming, dimensional analysis of nonlinearities and tone hole mutual interaction in woodwinds. *J. Acoust. Soc. Amer.*, 73:1804–1820, 1983.

[4] D.G. Andrews and M.E. McIntyre. An exact theory of nonlinear waves on lagrangian mean flow. *J. Fluid Mechanics*, 89:609–646, 1978.

[5] P. Merkli and H. Thomann. Transition to turbulence in oscillating pipe flow. *J. Fluid Mechanics*, 68:665–671, 1975.

[6] D.B. Barker and M.E. Fourney. Displacement measurements in the interior of 3-d bodies using scattered light speckle patterns. *Exp. Mech.*, 16(6):209–214, 1976.

[7] E. Berabeau, J.C. Amaré, and M.P. Arroyo. White light speckle method of flow velocity distribution. *Applied Optics*, 21(14):2583–2586, 1982.

[8] J.M. Burch and J.M.J Tokarski. Production of multiple beam fringes from photographic scatterers. *Optica Acta*, 15:101–111, 1968.

[9] R. Meynart and L.M. Lourenco. Digital image processing in fluid dynamics. Von Karman Institute for Fluid Dynamics lecture series 1984-03, 1984.

[10] C. Gray, D. Skyner, and C.A. Greated. The measurement of breaking waves using particle image velocimetry. In *Proc. ICALEO*, pages 166–177, 1988.

[11] R. Erbeck. Fast image processing with microcomputer applied to speckle photography. *Applied Optics*, 24(22), 1985.

[12] D.W. Robinson. Automatic fringe analysis with a computer image processing system. *Applied Optics*, 22(14):2169–2176, 1983.

[13] A. Kirita and C.J.D. Pickering. Particle image velocimetry: Automatic fringe analysis by cross correllation. *Optical Engineering*, 27(3):188–192, 1988.

[14] *Condenser microphones and microphone preamplifiers for acoustic measurement.* 1982.

[15] k. Hinsch, W. Schipper, and D. Mach. Fringe visibility in speckle velocimetry and the resolution of random flow components. *Applied Optics*, 23(24), 1984.

[16] R.N. Bracewell. *The Fourier Transform and its Applications.* McGraw Hill, New York, 1986.

[17] G.H. Kaufmann. Numerical processing of speckle photography data by fourier transform. *Applied optics*, 20(24):4277–4280, 1981.

[18] C.J.D. Pickering and N.A. Halliwell. Particle image velocimetry: Fringe visibility and pedestal removal. *Applied Optics*, 24(16):2474–2476, 1985.